Truly Mould free Carbon fibre reinforced polymer (CFRP) manufacturing by double-point incremental forming (DPIF) and direct electrical cure (DEC)

Yunlong Tang

A thesis submitted in partial fulfilment of the requirements for the degree of Doctor of Philosophy

The University of Sheffield
Faculty of Engineering
Department/School of Mechanical Engineering

June 2024

Declaration

I confirm that the thesis is my own work. I am aware of the University's Guidance on the Use of Unfair Means (www.sheffield.ac.uk/ssid/unfair-means). This work has not previously been presented for an award at this, or any other, university.

This project was supervised by Prof. Patrick Fairclough and Dr Christophe Pinna from the University of Sheffield. from November 2020 to June 2024.

Acknowledgement

First of all, I would like to express my deepest gratitude to my academic supervisor, Pro. Patrick Fairclough. I will be forever grateful to him for giving me an opportunity to develop my research skills at a higher research institution, the University of Sheffield. In addition, he helped me with simulating suggestions and encouragement, coordinating my project, and writing this thesis. This work would not be possible without his positive attitude and enthusiasm.

Moreover, I would also like to thank the support of my colleagues in the research office, like Fernando Cepero Mejias, Mohammed S Alotaibi, Abdullah F Alzayed, Jack Leach, Paul Mattinson, and Pablo Jaramillo. They helped me with a lot of professional knowledge and skills. In addition, several technical and support staff from the University of Sheffield played essential roles throughout the work and provided valuable guidance.

I also want to mention the friends I made from different countries in my PhD study. I am grateful for the opportunity to share many experiences with these vibrant and joyful people. These experiences will be unforgettable forever.

Finally, I would like to thank my family and friends in China. To my parents, thank you for your patience and understanding during my PhD study and for supporting me in achieving my PhD dream. To my friends for helping me to enjoy the world outside the PhD journey.

Abstract

Carbon fibre-reinforced polymers (CFRPs) have been widely used in a variety of high-performance fields, such as aerospace, automotive and sport. CFRP manufacturing methods require extended curing times and moulds. The mould is used to define the shape of the composite. Moulds are expensive and add considerably to the costs for small production runs. Additionally, autoclaves and ovens have high running costs due to the indirect heating of the part.

This thesis proposed a novel mould-free CFRP manufacturing method, double-point incremental forming (DPIF) with direct electrical curing (DEC). To achieve this, the conductivity of the CFRP is increased by adding conductive nanoparticles into the matrix (epoxy resin). First, carbon nanoparticles, including carbon black (CB), carbon nanotubes (CNTs), and graphene, were dispersed into the epoxy resin system. Compared with CNTs and graphene, CB shows good dispersion. With a CB loading of 2wt.%, the composite shows optimal performance in terms of electrical and mechanical properties.

Then, CFRP with 2 wt.DEC manufactured % CB with four different electrical contact arrangements. Here, the top-bottom mode (current through the laminate) has the best performance, which established a solid foundation for DPIF research.

For DPIF, CFRP with 2 wt.% CB was used. Experimental and finite element analysis methods are used to evaluate the DPIF process. The result indicates that DPIF can cure the sample in a short time without fibre damage. In addition, DPIF has the same performance in terms of mechanical properties and DoC as traditional manufacturing methods (oven and autoclave) but with much lower energy consumption. DPIF achieved fast localised consolidation and curing without a mould.

Nomenclature

CFRP	Polymer fibre-reinforced polymer
CB	Carbon black
CNT	Carbon nanotube
SWCNT	Single-wall carbon nanotube
MWCNT	Multi-walled carbon nanotube
AM	Additive manufacturing
FDM	Fused deposition modelling
SLCOM	Selective lamination composite object manufacturing
SPIF	Single-point incremental forming
CNC	Computer numerical control
DPIF	Double-point incremental forming
DoC	Degree of cure
DC	Direct current
DEC	Direct electrical curing
RTM	Resin transfer moulding

VARTM	Vacuum-assisted resin transfer moulding
Tg	Glass transition temperature
SEM	Scanning electron microscope
TEM	Transmission electron microscopy
ΔG	Gibbs free energy change
ΔH	The enthalpy change
ΔS	The entropy change
T	Temperature
UCST	Upper critical solution temperature
DSC	Differential scanning calorimetry
AT30S	AT30 slow hardener
τ	The torque (N·m)
FEM	Finite element method
FEA	Finite element analysis
β	Heating rate in DSC
T_p	The peak temperature

$\rho_{particle}$	The particle density
ρ_{bulk}	The bulk density of composites
CT	Compact tension test
DIC	Digital imaging correlation
RoM	Rule of mixture
K_{IC}	The plane-strain fracture toughness
G_{IC}	The critical strain energy release rate
DLS	Dynamic Light Scattering
RIPS	Reaction-induced phase separation

Contents

LIST OF FIGURES

LIST OF TABLES

Chapter 1 Introduction

1.1 Background

Carbon fibre reinforced polymer (CFRP) has been widely used in a variety of fields, such as aerospace, automotive and sport, due to its excellent strength-to-weight ratio. For example, the aerospace industry has achieved significant weight reductions in aircraft by increasing the use of composite materials in the airframe. In terms of Boeing 787, almost half the fuselage is composed of CFRPs and other composite materials. Compared with traditional aluminium design, this design can reduce the weight by 20 % [1]. In addition, it also offers high corrosion resistance and damage tolerance to fatigue [2], [3].

Though CFRPs can be manufactured by a variety of methods, most of these are high-cost and relatively slow. In addition, traditional manufacturing methods (autoclaves and ovens) need specific moulds depending on the product requirements. These moulds are usually made of aluminium, steel, or other metals, which have long service lives, high cost, and environmental impacts [4]–[7]. As a result, in terms of low-volume or custom products, the cost of mould will be a significant part of the final costs.

To address these issues, researchers started to explore alternative manufacturing methods. Additive manufacturing (AM) is a famous novel manufacturing method. AM can directly manufacture CFRP parts without any mould. It has a wide variety of production processes, such as fused deposition modelling (FDM) [8]–[11] and selective lamination composite object manufacturing (SLCOM) [12], [13]. However, AM also has limitations when manufacturing continuous carbon fibre reinforcement polymer. They are often characterized by low fibre volume fractions [8], [14], high void rate [15]–[17], or simple layups that do not allow the fibre direction to be tailored to complex stress fields [14], [18].

Considering the above issues, single-point incremental forming (SPIF) of composites was proposed. Initially, SPIF was used in the sheet metal forming [19]–[22]. The workpiece is fixed by a clamp above the net-shaped mould (open mould). A tool stylus is controlled by a computer numerical control (CNC) system and incrementally compresses the workpiece with a specified load until the desired shape is achieved [23]. In terms of research on SPIF on FRPs, Emami *et al.* [24] employed SPIF in conjunction with a ceramic

infrared heater positioned beneath the sample to fabricate glass fibre-reinforced polymer. Okada *et al.* [25] documented a SPIF of CFRPs using forming punches and localized optical heating. Cedeno-Campos *et al.* [26] utilized a copper tool equipped with a heater controlled by a CNC system to accomplish SPIF manufacturing of CFRPs. The system employed force feedback control to apply uniform curing pressure on samples. Compared with traditional manufacturing methods, SPIF uses net-shape moulds to replace closed moulds, which can effectively reduce mould costs. Moreover, in SPIF manufacturing, the heating resource directly works samples without air and mould heating [24], [26]. As a result, it can significantly save energy, especially small-size samples.

While SPIF reduces the cost of mould, it is still not genuinely mould-free. To achieve this aim, double-point incremental forming (DPIF) is proposed [26]. In DPIF, the net-shape mould in SPIF is replaced by a tool stylus. A CNC system also controls it and can be regarded as a support tool. Compared with SPIF, two tools in DPIF can offer more process control, especially in terms of surface quality, formability, and geometric accuracy of the part. DPIC can directly manufacture metal with complicated shapes without refastening the workpiece [27]. Though DPIF is very popular in sheet metal forming, its study in FRP is still a blank.

In addition, in SPIF, FRPs are heated and cured by contacting the heated tool or mould. The sample collects heat energy from the tool or mould by contact heat conduction. However, due to the low heat conductivity of FRPs, the tooling mainly heats the surface of FRPs. The temperature in the middle is far lower than the surface temperature. The exothermic curing polymerisation reaction in FRP manufacturing releases heat, which causes a high increase in the rate of heat release in FRPs. This positive feedback process can lead to over-curing, degradation of the resin and even combustion in extreme cases. Meanwhile, due to the lower temperature rate in the middle area of the sample, the degree of cure (DoC) could be very low when the surface has been fully cured. Thus, the heated contact DPIF is a slow process with poor control.

To solve this problem, direct electrical curing (DEC) is used to replace the traditional tool heating method. The positive and negative probes of a direct current (DC) power supplier connect the two tools across the composite in DPIF, respectively. When the tools compress the CFRP sample, an electric circuit is completed, electrical current can pass

through the sample, and Joule heating provides a more uniform temperature across the sample. This DEC can be leveraged to produce a low-energy, highly controllable curing process that directly heats the composite part [28]–[30]. However, due to the high insulation of the matrix (epoxy resin), in terms of CFRP samples with a woven fabric, the resistivity along the fibre R11 and R22 are far lower (0.022 mΩ·m) than while through the ply stack, R33, the resistance is much higher (310 mΩ·m) [31], [32]. To decrease the resistivity of the epoxy resin, conductive carbon nanoparticles were added to the epoxy resin to reduce the resistivity of epoxy resin [33], [34].

1.2 Aims and Objectives

Aim: To investigate the use of a novel double-point incremental forming with direct electrical (Joule) heating (DPIF-DEC) process to manufacture carbon fibre (CFRP) panels. These panels will include a dispersed carbon black phase to improve through thickness conductivity. So, a secondary aim is to investigate the dispersion and reaction-induced segregation of the carbon black as the composite is cured.

The cost of creating a mould for a CFRP part considerably outweighs the price of the fibre or resin of the individual part. Thus, it is expensive to produce small numbers of parts or to prototype [35], [36]. This work addresses this issue by creating a novel flexible carbon fibre manufacturing process. To achieve this, the following objectives for this project have been defined as:

- The dispersion of carbon nanoparticles in epoxy resin

In this section, the carbon nanoparticles (carbon black (CB), carbon nanotubes (CNTs), and graphene) are dispersed in epoxy resin by different methods. The dispersion is assessed by an optical microscope and electron microscope, as well as the resistance of the carbon nanocomposite. In addition, the relationship between the curing temperature and the resistance of the samples is discussed.

- The influence of carbon nanoparticle concentration on CFRPs

In this section, the influence of carbon nanoparticle concentration on CFRPs is studied. The electrical, mechanical, and thermal properties of CFRPs are examined.

- Using direct electrical curing (DEC) method to manufacture CFRP laminate.

In this section, the DEC method with the four different contact arrangements is applied to manufacture the CFRP laminate. The temperature distribution of the samples with the four different contact arrangements is studied. In addition, the CFRPs manufactured by DEC are compared with those manufactured by traditional manufacturing methods. The mechanical properties and energy consumption in the manufacturing process are discussed.

- Using DPIF method to manufacture CFRP laminate.

In this final section, the above processes are combined, delivering DPIF with DEC, which is used to manufacture CFRPs. The temperature distribution during the manufacturing process is observed by an IR camera and numerical analysis by Abaqus. In addition, the CFRPs manufactured by DPIF are compared with those of traditional manufacturing methods in terms of mechanical properties and DoC. The mechanical properties and energy consumption in the manufacturing process are discussed.

Chapter 2 Literature Review

This literature review introduces carbon fibre-reinforced polymers (CFRP), carbon-based nanomaterials, and the different manufacturing methods for CFRP, including traditional and novel manufacturing methods.

2.1 Carbon fibre reinforced polymer (CFRP)

Carbon fibre-reinforced polymer (CFRP) is a composite material. The main components are polymer and carbon fibre. Epoxy resin is a common thermosetting polymer used in CFRP, which provides the binding matrix to protect the fibres, hold them together and provide some toughness. Carbon fibre provides the high strength and stiffness for the material [37]–[39]. Due to CFRP's advantages of high strength, durability, design flexibility, and low density [40]–[42], CFRP is widely used in many fields, such as aerospace, automotive, chemical industries, civil engineering, and sports equipment [43]–[47]. This section described the principal components (epoxy resin and carbon fibre), manufacturing methods (hand layup and infusion (Resin transfer moulding (RTM) and Vacuum-assisted resin transfer moulding (VARTM)), and the application of CFRP.

2.1.1 Epoxy resin

Epoxy resins have been extensively used in many industrial applications as adhesives, protective coatings, and matrix polymers in composites. These applications derive from their outstanding bonding and chemical resistance [48]–[52]. As early as 1891, Lindmann synthesised a resin by the condensation reaction of hydroquinone and epichlorohydrin [53]. In 1909, Prileschajew discovered that an organic peracid could be used as an oxidant to oxidise olefins and form an epoxy compound [54]. Although more than 100 years have passed, these two reactions are still the main synthesis routes. In 1947, the United States Devoe-Raynolds company opened up epichlorohydrin-bisphenol A resin technology history, and the epoxy resin industry started to develop [55].

2.1.1.1 The classification of epoxy resins

Due to the variety of applications and diverse polymeric nature of epoxy resins, there is no official classification. At present, the famous classification is to classify epoxy resin into glycidyl and non-glycidyl epoxy resins according to their chemical structure; glycidyl epoxy

includes glycidyl-ether, glycidyl-ester and glycidyl-amine [53]. Non-glycidyl epoxies have two types. They are cyclic aliphatic and acyclic aliphatic [56].

- Glycidyl epoxy resin

Bisphenol A glycidyl ether (DGEBA) resin is a popular glycidyl epoxy resin [53]. It makes up a high percentage of the industrial epoxy resin market [57]–[60].

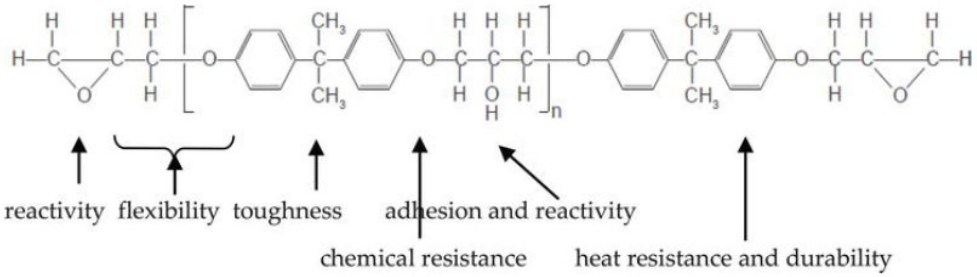

Figure 2.1 The chemical structure and critical features of DGEBA resin [58]

Figure 2.1 shows the chemical structure and critical features of DGEBA resin. The characteristic of DGEBA resin depends on the number of n. This number, n, is the number of repeating units, commonly known as the degree of polymerisation. With the degree of polymerisation increasing, the molecular weight will increase. Generally, the range of n is 0 to 25. The n value of epoxy resins with low molecular weight usually is less than 2, and the softening point is below 50 ℃. When the temperature is higher than this point, epoxy resin will be soft. For medium molecular weight, the n value is between 2 and 5, and the softening point is between 50 and 95 ℃. When the n value is higher than 5, and the softening point is higher than 100 ℃, these epoxy resins are termed high molecular weight resins. As a result, the heat resistance is improved [58].

Phenolic epoxy resin is also known as F-type epoxy resin (see Figure 2.2). The long chains in epoxy resin and the curing reaction result in higher crosslinking density and viscosity in the resin. The cured phenolic epoxy resin has excellent heat resistance, chemical resistance, and solvent resistance. Because of these properties, phenolic epoxy resins can improve the glass transition temperature (Tg), heat resistance, and properties of epoxy blends[61]. As a result, phenolic epoxy resins can be used as modifiers for primary epoxy resin or multi-resin systems. In addition, these resins are also used in the manufacture of various structural parts and electrical parts [62], [63].

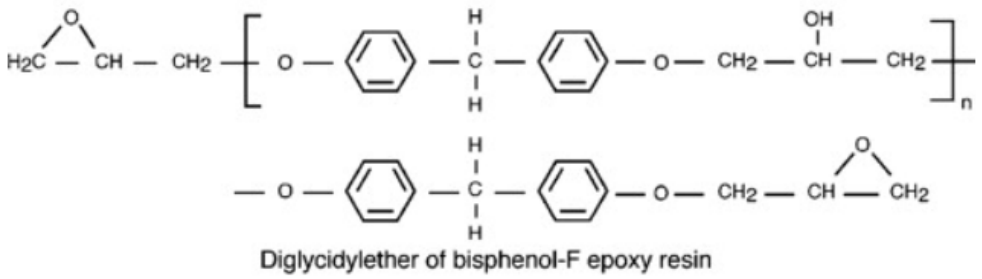

Figure 2.2 The chemical structure of phenolic epoxy[64]

- Non-glycidyl epoxies

In terms of non-glycidyl epoxies, the cycloaliphatic resin (see Figure 2.3)is a cyclic structure whose molecule has an epoxy group. The standard cyclic aliphatic resins include vinyl cyclohexene dioxides and dicyclopentadiene dioxides. The acyclic aliphatic resin is a linear structure where an epoxy group adheres. Acyclic aliphatic resin can be divided into epoxy diene polymers, epoxidized oils and polyethene glycol dicyclic oxides [56].

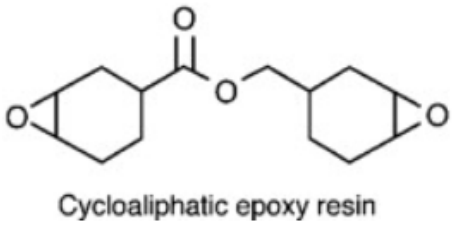

Figure 2.3 The chemical structure of cycloaliphatic epoxy resin [64]

2.1.2 Carbon fibre

Carbon fibres are the priority choice fibres in the industry due to their low density, high strength, good heat and electrical conductivity, and high thermal and chemical stability [65]–[67]. In 1897, Thomas Edison [68] carbonized cotton at high temperatures and obtained carbon fibres, which were used in incandescent light bulb experiments. Then, in 1958, Roger Bacon [68] produced carbon fibre by heating artificial filaments and carbonizing them. However, the carbon concentration of produced fibre was only 20%. In the early 1960s, Dr. Akio Shindo used polyacrylonitrile (PAN) as a raw material and invented a new carbon fibre manufacturing process. In this process, the carbon concentration was increased to over 55%. The modulus of this material is higher than 140 GPa. In 1963, Dr William Watt oriented the PAN chain parallel to the fibre axis through

tension in the early stage of pyrolysis and prepared high-strength carbon fibre. The PAN high-performance carbon fibres invented by Shindo and Watt dominate the world market to date [69]. In addition, in a search for alternative raw materials, in the 1960s, pitch from oil was used to produce carbon fibre. At room temperature, the pitch has both a high viscosity and carbon concentration [70]. Pitch is a mixture of hundreds of aromatic hydrocarbons and heterocyclic compounds with an average molecular weight of 300-400 u (1 u is the be 1/12 of the mass of one atom of carbon-12). The carbon concentration of pitch can be higher than 80%. As the aromaticity increases, the quality of carbon fibre will increase [71].

2.1.2.1 The structure and properties of carbon fibre

Carbon fibre is provided in the form of continuous tows wound onto spools. One tow is a bundle of thousands of continuous carbon filaments bonded together and protected by organic coatings such as polyethene oxide (PEO) or polyvinyl alcohol (PVA). This process is termed fibre sizing. The graphitic structure of carbon is not reactive, so sizing is required to give good adhesion to the epoxy resin matrix. The surface chemical properties of fibre depend on the sizing component. Sizing is defined as a thin chemical coating applied to the surface of a fibre during the manufacturing process to protect the fibre during handling and processing and to promote adhesion between the fibre and the polymer matrix [72]. The tow is conveniently unwound from the spool to use. Each carbon filament in the tow is a continuous cylinder of 5-10 um diameter.

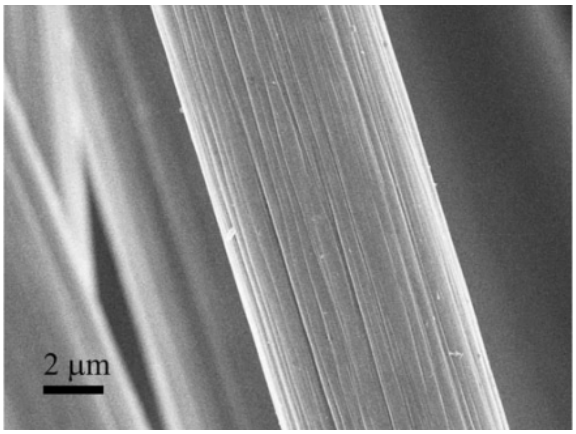

Figure 2.4 Micrograph (SEM) of a carbon filament with a 7.0 µm diameter [73]

The atomic structure of carbon fibres is carbon atom sheets (graphene sheets) arranged in a regular hexagonal pattern (see Figure 2.5). According to the precursor to make the

fibre, the structure of carbon fibre can be turbostratic or graphitic or have a hybrid structure with both of them. In turbostratic structure, carbon atom sheets fold or wrinkle together. This structure happens in carbon fibre processed from PAN. However, if the precursor is pitch, the carbon fibre structure will be graphitic after the heating process at over 2200 ℃ temperature [74]–[76].

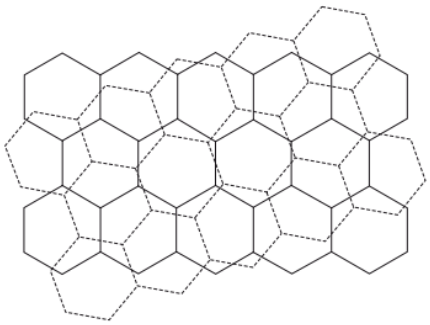

Figure 2.5 Carbon atom sheets (graphene sheets) arranged in a regular hexagonal pattern [77]

Because of the different structures of carbon fibre, the mechanical performances of PAN and pitch-based carbon fibre are different. The modulus of carbon fibre depends on the carbonization/graphitization temperature. The heating process can improve the modulus of PAN, but its strength will decrease [77].

2.1.2.2 The drapability and application of different carbon fibre

Generally, carbon fibre is classified as weave fibre (plain, twill, harness satin weave, etc) and unidirectional (UD) fibre. UD fibre does not use interlocking tows, which has poor drapability, as the fibres tend to separate over objects with curvature in 2 dimensions. As a result, UD is used for flat plates or longitudinally in cylindrical parts.

The following simplest structure of the fibre, commonly available, is plain weave (Figure 2.6). Plain weave carbon fibre is a symmetrical structure with a checkerboard appearance. The tows are woven in an over-and-under pattern. The short space between the interweaving gives the fibre a high level of stability, which refers to the ability of the fibre to maintain its weave angle and fibre orientation. Due to the high level of stability, the drapability of plain weave fibre is low. As a result, plain weave is less suitable for products with complex contours. Therefore, it is usually used to manufacture flat sheets, tubes, and shallow 2D curve products [78], [79].

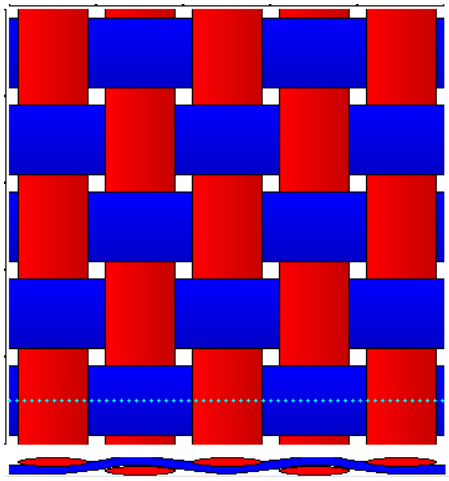

Figure 2.6 Plain Weave Carbon Fibre Cloth from TexGen

Twill weave fibre serves as a bridge between a plain weave and the satin weaves (Figure 2.7). 2×2 twill weave fibre is a commonly recognisable twill weave fibre used in industry. As the 2×2 name implies, each tow will pass over 2 tows and then under two tows. Compared with plain weave fibre, the distance between the tow interlaces in twill weave fibre is longer, which indicates less crimping. Thus, there is less stress concentration at the cross-over points. As a result, the drapability of the twill weave is higher than that of the plain weave. It is commonly used in more complex parts such as racing parts such as hoods and fenders, as well as interior components [78], [79] that show curvature in 2 dimensions.

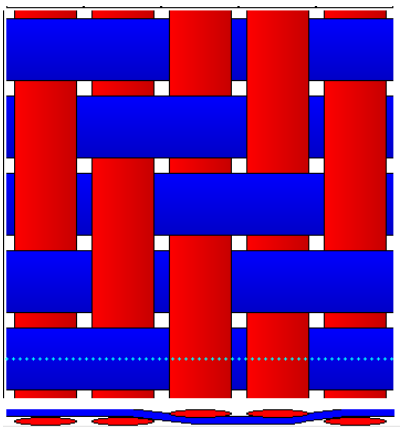

Figure 2.7 2x2 Twill Carbon Fibre Cloth from TexGen

Compared with the above two weaves, harness satin weave has the highest level of drapability. Harness satin (HS) weave fibre is characterised by four or more fill or weft yarns floating over a warp yarn or vice versa. There are several types of HS weave fibre,

including 4HS, 5HS, and 8HS. The number represents the total number of tows passed over and then under. For instance, a 4HS weave fibre consists of three tows passed over, and then one passed under (Figure 2.8). As the HS number increases, the flexibility and stability decrease. Due to the high drapability, HS weave fibre is usually used in products with complicated shapes, such as luxury car interiors, exterior car body panels, and various sporting equipment [78]–[80].

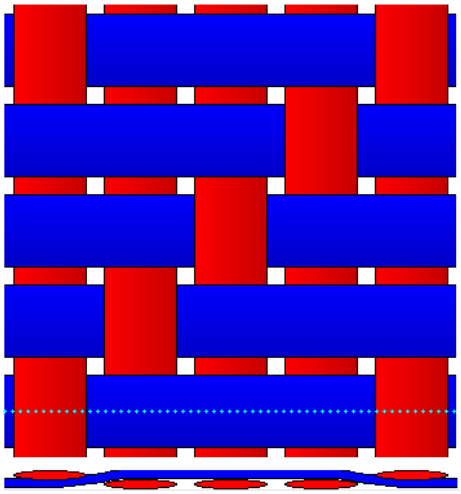

Figure 2.8 4HS weave carbon fibre cloth from TexGen

2.1.3 Advantages and disadvantages of CFRP

In this section, the advantages and disadvantages of CFRP are discussed.

2.1.3.1 Advantages

Compared with metals, it has high strength and stiffness with lower density. As a result, when the strength and stiffness of two products are the same, the weight of the product with CFRP is far lower than that with metal [81]. In addition, CFRP is radiolucent, which is transparent to X-rays. Due to its excellent anti-fatigue performance, CFRP is gradually replacing metal alloys in medical devices [82]. CFRP also has good corrosion resistance performance. Compared with conventional materials like metals, it can withstand most chemical solutions, such as acids, alkalis, solvents and salts. It also will not rust or corrode when exposed to moisture or oxygen [83].

2.1.3.2 Disadvantages

First of all, energy intensity and cost remain significant barriers, especially for large-scale products. Carbon fibre production is estimated to be about 14 times more energy-

intensive than conventional steel production [84]. The price of carbon fibre depends on the category of carbon fibre and the size of the fibre tow. Second, the manufacturing process of CFRP is complex, takes a long time, and requires specific equipment [85], [86]. In addition, CFRP is brittle, particularly when subject to impact. When CFRP is subjected to tensile stress, it can fail by cracking along the fibre direction or by debonding between the fibre and the matrix. In these failure modes, there is low deformation or energy absorption before fracture [87], [88]. Due to the high brittleness, the maintenance and inspection frequency is high. Currently, there is no accepted recycling method for carbon fibre. Parts can be recycled into short fibre composites by resin extraction or burn as energy recovery [89].

2.1.4 Application

Because of its excellent performance, CFRP has been widely used in various fields, such as aerospace engineering, automotive engineering, civil engineering, and sports goods.

2.1.4.1 Aerospace engineering

Due to its low weight, high-tensile strength, stiffness, and excellent fire protection capabilities, CFRP has been widely used in aerospace engineering. For example, from Boeing 767 to Boeing 787, the percentage of the composite increased from 3 wt.% to 50 wt.%. The material of airframes, main wings, and tail wings is replaced from aluminium to CFRP. Compared with the Boeing 767, the weight of the Boeing 787 has a significant decrease, which can save 20-22% of fuel [90].

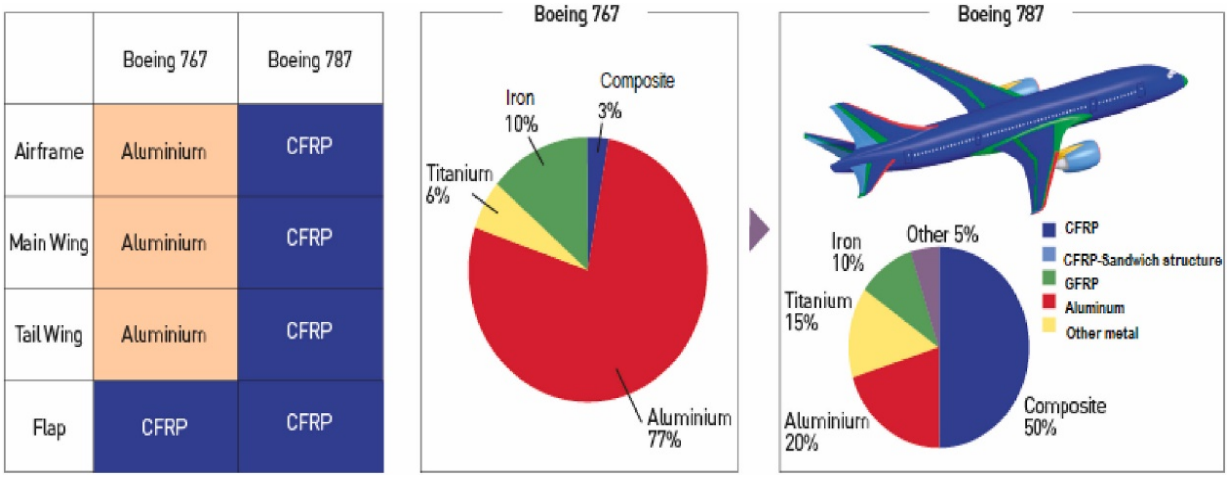

Figure 2.9 Comparison of materials used in Boeing 767 and Boeing 787 [90]

2.1.4.2 Automotive engineering

Due to its low weight, high strength, and stiffness, the industry has been focused on the potential of CFRP as a new automotive part material. In theory, compared with traditional vehicles with steel, the weight of vehicles with CFRP can be reduced by 60 wt.%. Fuel efficiency can increase by 30%, and CO_2 emissions be reduced by 20% [91].

In addition, A project funded by the European Union involving three car companies, Volkswagen, Renault and Volvo, has developed an automotive CFRP floor. In this project, the number of parts was reduced by 30%, and the weight of the vehicle was reduced by 50%. 50 units of CFRP floor can be produced by this technology one day by a single press [92].

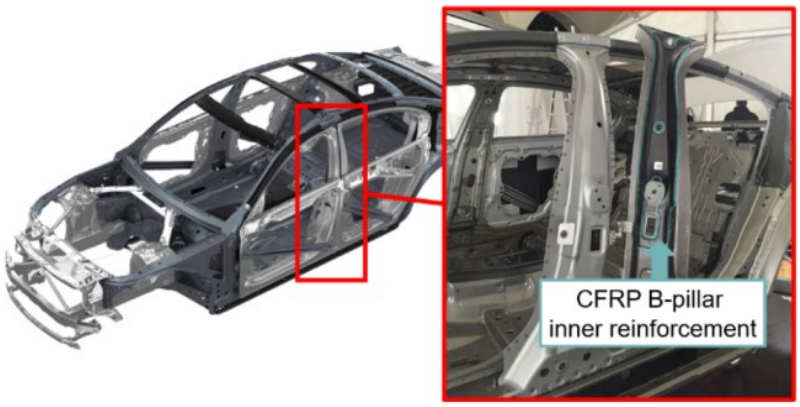

Figure 2.10 The application of CFRP on the B-pillar of the car [93]

2.1.4.3 Civil engineering

From 2004 to the present, the requirement for CFRP in civil engineering has had a noticeable increase. In 2025, the CFRP used in civil engineering could reach 6.2 kilotons. The application of CFRP in civil engineering includes the strengthening of buildings and bridges, the repairment of tubes, bridge decks, cables, etc. 80%-90% of CFRP is used in enhancing and repairment of deteriorating infrastructure such as external bonding of CFRP sheets, the addition of composite strips or tendons, and near-surface mounting of composites [94]–[96].

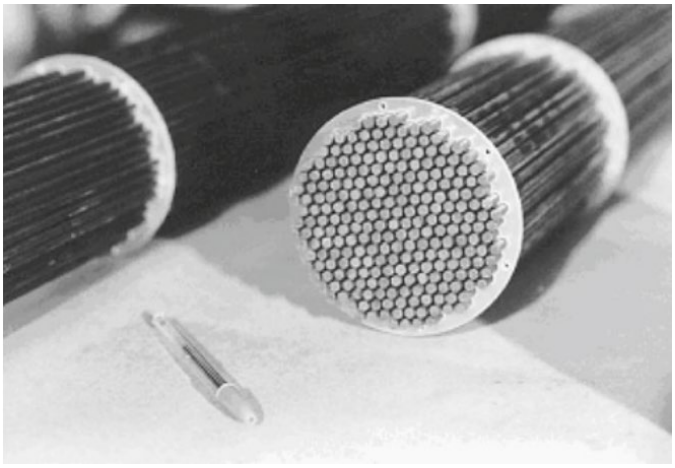

Figure 2.11 CFRP used in electrical cables with12 MN load capacity [97]

2.1.4.4 Sports

Compared with other fields, the scale of products in the sports field is smaller. So, it is one of the earliest industries to use CFRP. CFRP's main products include golf clubs, fishing rods, and tennis rackets. Compared with other products, golf clubs and bicycles are the largest consumers of CFRP. For golf clubs, CFRP improved the stiffness with lower weight to increase durability. In terms of bicycles, due to their low weight and high strength, bicycles can be used in various harsh conditions [98], [99].

Figure 2.12 The bicycle frame with CFRP [100]

2.2 Carbon nanomaterials

In general, carbon nanomaterials are described as carbon materials with nanoscale dimensions, which have specific optical, electronic, thermo-physical or mechanical

properties [101]–[105]. The three main carbon nanomaterials discussed are carbon black (CB), carbon nanotubes (CNTs), and graphene.

2.2.1 Carbon black

2.2.1.1 Introduction

Carbon black (CB) is an amorphous carbon particle. It is the product of incomplete combustion or thermal decomposition of carbon-containing substances such as coal, natural gas, and fuel under insufficient air. Carbon makes up 98% of all the chemical elements in CB. To improve its solubility, dispersion, cohesion or other properties, there may be other elements in CB, such as oxygen, nitrogen, and sulphur [106]. CB is marketed as black powder or particles. More than 90% of CB is used in rubber products [107].

2.2.1.2 Morphology

The carbon particles form a hexagonal plate. Three to five of these plates form a crystallite. The arrangement of carbon atoms is orderly in each carbon crystallite. However, the arrangement of carbon in adjacent crystallites is uncorrelated. So, while CB plates are crystalline, CB particles are quasi-crystalline [108]. The microstructure of aggregated CB is shown in Figure 2.13.

The structure of CB is often divided into two levels, a primary and a secondary structure. The primary structure of CB is of spherical particles created from small graphitic sheets of carbon. These particles are formed during the incomplete combustion of coal tar, vegetable matter, or petroleum products. The primary particles of CB are tiny, typically measuring 10-500 nm in diameter [109], [110].

The secondary structure of CB refers to aggregating the primary spherical particles into larger "agglomerates." These structures show a random fractal structure with a wide range of sizes and shapes. However, this structure is unstable and can be readily disrupted under the influence of mechanical strain [109].

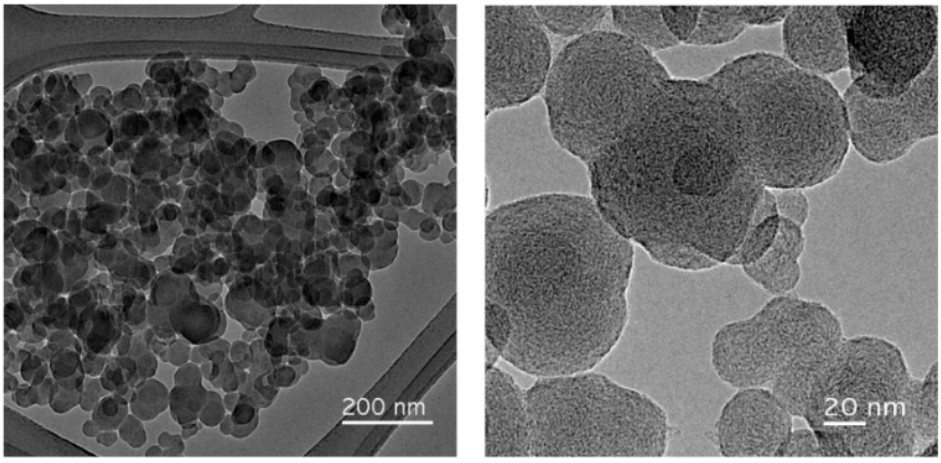

Figure 2.13 The structure of aggregated CB under TEM [111]

2.2.1.3 Electrical conductivity

The conductivity of CB depends on their surface properties. Highly conductive CB has a low aspect surface area, and their volume resistivity is between 0.1- 0.01 Ω·cm [112]. In addition, in the manufacturing process of CB, their surfaces often produce function groups, such as hydroxy groups and carboxyl groups. These polar functional groups can attract electrons and impede the movement of free electrons to affect conductivity. In general, the pH value can indicate the surface chemical properties of CB. The pH value is smaller when more polar functional groups are present. Therefore, the lower the pH, the lower the conductivity[113].

2.2.1.4 Mechanical properties

CB is often used as a filler and added to other matrices, such as natural rubber, to increase the conductivity of materials. Compared with other conductive fillers, CB has some advantages. At first, CB has a lower cost than most other conductive additives. In addition, CB can adjust the conductivity of composite materials over a specific range by changing the concentration of CB. For insulating matrices such as ink and natural rubber, the conductivity of the composite materials depends entirely on fillers. As the concentration of CB increases, CB particles will move from disconnected to partial connection and finally complete connection. Finally, CB atoms will form continuous paths. These paths are called percolating networks, and they affect the magnitude of conductivity [103].

2.2.2 Carbon nanotubes (CNTs)

2.2.2.1 Introduction

In 1952, Russian scientists LV Radushkevich and VM Lukyanovich published clear TEM images showing carbon nanotubes (CNTs) [114]. CNTs are tubular cylinders connected by a group of hexagonal carbon atoms, essentially a rolled sheet (or sheets in Multiwalled CNTs). Each carbon atom connects three adjacent carbon atoms by a covalent bond [115]. CNTs have high aspect ratios. CNTs have had a significant influence on carbon nanotechnology, optoelectronics, carbon nanocomposites and other fields [116].

2.2.2.2 Morphology

CNTs can be classified as single-wall carbon nanotubes (SWCNTs) and multi-walled carbon nanotubes (MWCNTs). SWCNTs, as their name implies, have a single layer of carbon atoms forming the tube. Their diameter is around 1.4 nm, and their length can be over 200 nm. SWCNTs have excellent mechanical and electrochemical properties [117]. Compared with SWCNTs, MWCNTs consist of multiple carbon layers, and their diameter is higher than 10 nm. SWCNTs and MWCNTs have good electrochemical properties [118]. However, due to the different structures of SWCNTs and MWCNTs, the former are flexible, while the latter are strict and rigid, rod-shaped structures [119]. The TEM images of them are shown in Figure 2.14.

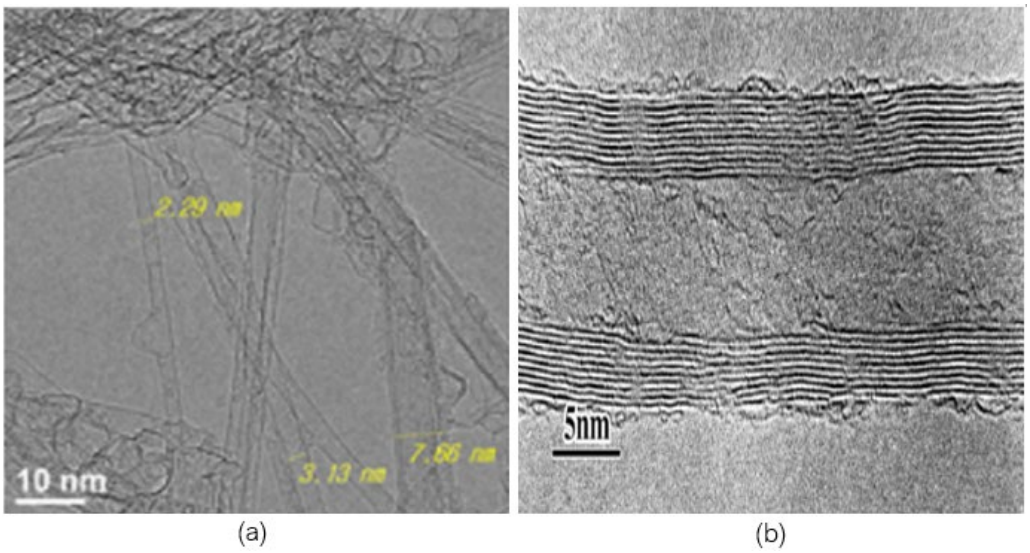

Figure 2.14 (a) TEM image of SWCNTs [120] (b) TEM image of MWCNTs [121]

2.2.2.3 Electrical conductivity

SWCNTs manifest either metallic or semiconductor electrical conductivity depending on the hexagonal lattice orientation of the nanotube central axis. In contrast, MWCNTs predominantly display metallic electrical conductors [122]. The resistivity of SWCNTs can range from 10^{-6} to 10^{-2} Ω·cm, and for MWCNTs, the range varies from 10^{-5} to 10^{-3} Ω·cm [123].

2.2.2.4 Mechanical properties

When external forces are exerted on them, the internal tubes of CNTs will move, allowing for a higher strength. Their tensile elastic modules can reach 1 TPa, which is similar to that of diamonds and is five times that of steel [124].

2.2.3 Graphene

2.2.3.1 Introduction

Graphene is a single layer of graphite. It is a two-dimensional carbon layer arranged in the hexagonal lattice of carbon atoms. Three million layers of graphene are stacked together and would be 1 mm thick. In 2004, Andre Geim and Konstantin Novoselov, physicists at the University of Manchester, successfully isolated graphene from graphite by micromechanical stripping [125]. Meanwhile, graphene was recognised as the basic building unit of sp2 carbon allotrope, including graphite, carbon nanotubes and fullerene. Graphite is a stack of graphene which is held together by weak Van der Waals forces [126]. In addition, graphene can wrap and roll up to form fullerenes and carbon nanotubes [127].

2.2.3.2 Morphology

The arrangement of carbon atoms in graphene is the same as that of the single atomic layer of graphite. There are four electrons in the outermost layer of a carbon atom, and three of them generate a sp2 bond, with each carbon atom contributing an unbonded electron located in the P track. The P-track of adjacent atoms is perpendicular to the plane to form a p bond. The bond length between each two adjacent carbon atoms is 1.42×10^{-10} m, and the bond angle is 120°. The P track perpendicular to the layer plane of each carbon atom can form a large polyatomic p bond, like a benzene ring. Therefore,

graphene has good conductive and optical properties [128], [129]. The graphene structure under transmission electron microscopy (TEM) is shown in Figure 2.15.

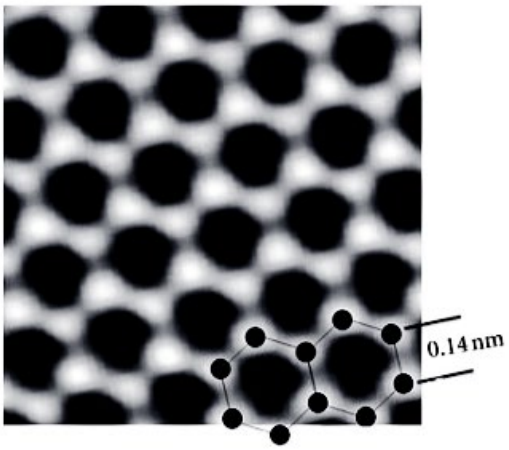

Figure 2.15 The two-dimensional honeycomb structure of carbon atoms in graphene along with the transmission electron microscopic (TEM) image [130].

2.2.3.3 Conductivity

In graphene, each carbon atom has 4 bonding electrons. In a two-dimensional plane, three electrons bond with the other three adjacent carbon atoms, and this leaves one electron that produces electronic conduction along the plane of the sheet. These highly mobile electrons are p electrons, which are above and below the graphene sheet. The electron mobility of graphene is very high and up to 15 000 $cm^2/V{\cdot}s$ at room temperature. The resistivity is about 10^{-6} $\Omega{\cdot}cm$ [131]. Therefore, graphene has excellent conductivity [132] compared with copper.

2.2.3.4 Mechanical properties

Due to the structure of graphene, as discussed above, graphene has good performance in terms of mechanical properties. However, the in-plane bending stiffness is very low and bending deformation occurs easily. The literature shows that graphene's strength and elastic moduli are 125 GPa and 1TPa, respectively [105]. Its strength is 100 times as high as that of carbon steel. In addition, its density is much lower than that of steel and other metallic materials. Therefore, graphene has been used as a typical two-dimensional reinforcement in composite materials [132].

2.2.3.5 Graphene nanoplatelets

Graphene nanoplatelets (GNPs) are flat sheets of multiple graphene layers. It is generally produced by the exfoliation of graphite, a layered material, using mechanical or chemical methods. [133]. The lateral dimensions are a few hundred nm to a few thousand nm, and the thickness of GNPs is generally under 100 nm, depending on the production method. The aspect ratio of GNPs can reach up to several thousand [134]. Like other carbon nanomaterials, GNPs have excellent thermal and electrical conductivity. In terms of thermal conductivity, unlike CNTs or carbon fibres, the platelet morphology provides a lower contact thermal resistance at lower loading levels, resulting in higher thermal conductivity [135]. Due to the high electrical conductivity, GNPs can substantially improve the electrical conductivity of GNPs/polymer composites. Because of the high aspect ratio, they also can form effective conductive networks at low loading levels, 1-5 wt.%, in most polymeric materials [136]–[138].

2.2.4 The application of carbon nanomaterials in CFRP

Epoxy resin, as the matrix of CFRP, has a highly crosslinked structure. As a result, CFRP is brittle, which limits structural ability [139]. In addition, due to the low heat capacity and conductivity of epoxy resin, the performance of CFRP is limited [140]–[142]. Therefore, well-dispersed nanoparticles are introduced into the matrix (epoxy resin) to improve the performance of CFRP [143]–[150]. In this section, the application of carbon nanoparticles (CB, CNTs, and graphene) in CFRP is introduced.

Compared with pristine CFRP, CNT-modified CFRP has better performance for mechanical properties such as higher compressive strength, bending strength, bending modulus, and tensile strength. In addition, CNT-modified CFRP has higher electromagnetic interference shielding ability [143], [148]–[150]. Due to the high electrical conductivity, MWCNTs can enhance the electrical conductivity of CFRP to allow structural health monitoring, primarily via the thickness direction [151]. When graphite oxide and graphene nanoplatelets are added to the matrix, the additional toughening mechanisms (crack bifurcation/pinning and separation between layers) are improved, which can enhance the fracture properties of CFRP [146].

However, there are comparatively few papers discussing the influence of CB on CFRP, which is one of the research focuses of this project. However, there are some papers discussing the influence of CB on epoxy resin, which can indirectly indicate the impact of CB on CFRP. For example, Blackburn *et al.* [152] dispersed CB and silica nanoparticles into epoxy resin. As the concentration of CB nanoparticles increases, the electrical conductivity of the composite shows significant improvement. In addition, the conductivity has a high sensitivity to the bending angle. Dungani *et al.* [153] collected CB from biomass waste and blended it with epoxy resin. When CB concentration is between 1 wt.% and 5 wt.%, the fracture strength has obvious improvement. Ma *et al.* [154] manufactured CB/epoxy resin composite by the blending-casting method. As CB wt. % increases, the tensile strength will increase until 2 wt. % CB.

2.3 The dispersion of carbon nanoparticles in the matrix

The poor dispersion of carbon nanomaterials in the matrix is the main reason that composite materials do not show the predicted performance. If the dispersion is low, i.e. the nanoparticles aggregate together in the matrix, then they do not improve the mechanical properties. In extreme cases, high aggregations can reduce the strength of components due to the formation of stress concentrators [155]–[157]. Eshelby-Mori-Tanaka made a simulation model which suggests that at a volume fraction of SWCNTs of 10% and along the fibre direction, Young's modulus (E) of the composite material should be more than 20 times higher than that of the matrix [158]. However, the experimental E is far lower than the predicted value. In addition, Gong and Dutaa carried out similar tests with the same result, which was that the mechanical properties of composite materials could t reach the predicted values [159], [160]. Both above samples have poor nanoparticle dispersion. During the manufacturing of composite materials, carbon nanomaterials show secondary agglomeration. In addition, when a load is applied to the composite, stress will concentrate on the agglomerated carbon nanomaterials, and the mechanical properties of the composite material will decrease [161]. As a result, improving the dispersion of carbon nanomaterials in matrixes is critical. In this section, the dispersion energy, re-aggregation, percolation, phase segregation, and quantitative analysis of the dispersion are discussed.

2.3.1 The dispersion energy

Dispersing nanomaterials into epoxy resin is a challenge. The Gibbs free energy can explain it. The Gibbs free energy is a thermodynamic function that determines the direction of a process in a thermodynamic sense. The Gibbs free energy change is introduced to judge whether the process is spontaneous, expressed in Equation 2.1.

$$\Delta G = \Delta H - T \cdot \Delta S$$

Equation 2.1

Where ΔG is Gibbs free energy change, ΔH is the enthalpy change, T is the temperature, and ΔS is the entropy change. When DG is negative, the process is spontaneous.

In the mixing process, the mixing entropy contribution from the nanomaterial is generally tiny. The main reason is the suspension is not a solution or mixture on a molecular basis. Because of the high aggregation and low saturation, the diameter of nanoparticle agglomerations in the mixture is between 1 and 100 nm. As a result, the nanomaterial cannot have the same combinatorial relationship within the fluid as a solute has on a molecular basis [162]. The nanomaterial is dispersed in another material, such as a colloid. If the mixing process is to be spontaneous, the change of Gibbs free energy should be negative. However, the entropy change DS is low when nanoparticles are dispersed in epoxy resin. Therefore, the mixing process of epoxy resin and carbon nanomaterials is not spontaneous. The mixing energy can be improved by using compatible agents such as surfactants or high-speed stirring. However, surfactants can lead to a weak interface [163].

2.3.2 The percolation of carbon nanoparticles

Broadbent and Hammersley proposed percolation theory in 1956 [164]. This model described the movement of fluid in a disordered porous media. It was extended in 1973 when the Kirkpatrick-Zallen percolation theory described the formation of a conductive network in mixtures of conductive and non-conductive particles [165]. When the volume fraction of conductive nanoparticles is small, the conductive particles are isolated (if uniformly distributed in the matrix). Therefore, the composite material is insulating. With the volume fraction of conductive nanomaterials increasing, the conductivity of the composite material has a negligible increase, as the particles are still isolated. However, when the volume fraction of conductive nanoparticles increases to a critical value, the

conductive particles start to contact each other, and the conductive network is formed at this stage. As a result, the conductivity of the composite material increases suddenly, and the value change can reach ten orders of magnitude. Strictly speaking, since the conductive process occurs via electron tunnelling [166], the particles do not need to touch but only need to be sufficiently close for the tunnelling probability to be high.

All of this assumes that the particles are uniformly distributed. This sudden change is the "percolation region", and this critical volume fraction is the "percolation threshold". After the percolation region, there is a slight change in conductivity as the volume fraction of conductive nanoparticles increases. This model indicates that for spherical particles, a minimum of 28 vol.% is required for percolation. However, the threshold concentration depends strongly on the aspect ratio of the particles, and higher aspect ratios achieve percolation at lower concentrations.

Taherian introduced a model to predict the electrical conductivity of polymer-based carbon composites [167]. This model accounts for the changes in conductivity due to the aspect ratio, the arrangement of the particles and the surface energy between particles and the matrix. However, the above models do not consider the effect of electron tunnelling. Payandehpeyman proposed a mean field, which is based on a tunnelling model between nanoparticles [168] to address the above issue. In addition, this model can predict the composite conductivity with random, segregated, or agglomerated structures by changing the aspect ratio of the complex nanoparticles.

The above is demonstrated in polymer-carbon conductive composites, such as with CB, CNTs, and graphene. When the concentration of the filler is low, there is no significant change in the composite conductivity. However, when the concentration of filler reaches the percolation threshold, the conductivity significantly increases, showing a sharp increase in conductivity (6-10 orders of magnitude) [169]. Therefore, the percolation threshold concentration is where the composite has a continuous conducting path throughout the sample. In the percolation region, the conductivity (σ) follows Equation 2.2 and Equation 2.3 [170].

$$\sigma = a \cdot (p - p_c)^t \qquad \text{Equation 2.2}$$

$$\sigma = a \cdot e^{-e^{-t \cdot (p - p_c)}}$$ Equation 2.3

Where t is a critical exponent, p is the concentration, and p_c is the percolation threshold concentration.

2.3.3 Re-aggregation and phase segregation

Literature shows that powerful interparticle van der Waals forces exist in CB, CNT and graphene nanomaterials. Due to the strong van der Waals force, when carbon nanomaterials are dispersed into the epoxy resin, they will have a noticeable tendency to reaggregate in the matrix. The primary size of carbon nanomaterials can affect their re-aggregation after dispersion. For example, if the primary size of carbon nanomaterial is small, the carbon nanoparticles will have a high specific surface area. As the surface area increases, the interaction energy will increase. As a result, it will need more energy to avoid re-aggregation. In addition, the dispersion degree is influenced by concentration. With the concentration of the carbon nanomaterial increasing, the inter-aggregate attractive forces are lower. Therefore, the carbon nanomaterial is a challenge to re-aggregate and has good dispersion in high concentrations. Besides the nanoparticle size and concentration, viscosity also can affect re-aggregation. Epoxy resins generally have high viscosity, which can reduce the re-aggregation speed of the nanomaterials [171]–[173].

In addition, epoxy resins are thermosetting polymers. When the epoxy resin is heated, the viscosity will be reduced, and the re-aggregation of nanoparticles will be increased. However, the curing process of epoxy resin will accelerate at the same time due to the high temperature [174].

The re-aggregation of carbon nanoparticles in the epoxy resin during the curing process can be explained by phase segregation, which is an upper critical solution temperature (UCST) type phase behaviour (see Figure 2.16) as curing proceeds from low molecular weight oligomers to high molecular weight polymer, as indicated by the arrow. As the system cures and the monomer is converted to polymer, the configurational entropy rapidly decreases as the monomer is incorporated into the chain. Thus, the entropy of polymer molecules is vastly smaller than that of the monomers from which it was made. This loss of entropy drives phase segregation as polymer forms. There is thus a critical molecular weight, where the carbon nanoparticles are no longer miscible in the resin. The

phase segregation is also influenced by the method of polymerisation. For step-growth, as in epoxy-amine systems, the monomers are converted to dimers and trimers, and then trimers and tetramers and the total number of molecules decreases as the mass of the molecules increases. This results in no longer being a sea of monomers present, and no large polymers are created until high conversions occur. Consequently, in a step-growth polymerization, phase segregation is generally seen at the late stages of the reaction, where viscosity has a significant impact on the kinetics of phase segregation. The most pinned phase-separated structures, such as polyurethane, are seen in step-growth systems[175].

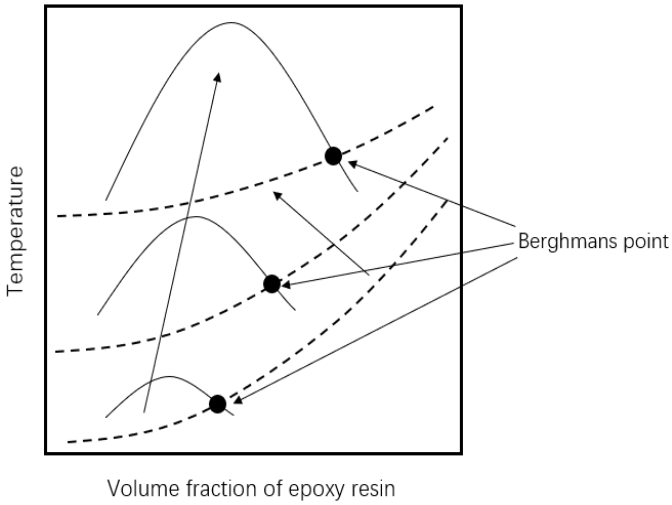

Figure 2.16 The schematic representation of carbon nanoparticles/epoxy resin in the phase diagram (solid line) and Tg(dashed line)

Meanwhile, during the curing process, the two-phase region will expand, and the critical point in the UCST will increase. At some point, the critical temperature will pass the experimental temperature and phase segregation will start. In addition, the Flory-Fox equation indicates that the glass temperature will increase on curing [176]. The crossover point between the UCST line and the Tg line is Bergman's point [177]. Once the composition reaches this point, there will be no further phase segregation between carbon nanoparticles and resin as the system is now vitrified into a glass.

2.3.4 Quantitative analysis of the dispersion of carbon nanoparticles: fractal dimension analysis.

Researchers used different methods to analyse carbon nanoparticle dispersion quantitatively. For example, Luo and Koo [178] calculated the statistical distribution of

nanoparticles by integrating the probability density function (PDF). The larger the spacing between integration boundaries indicates the better distribution. Bryan *et al.* measured the free-path spacing between nanoparticles and particle dimensions to analyse the dispersion quantity and agglomeration quantity, respectively [179].

In this project, a mathematical model, fractal dimension analysis, is used to quantify the dispersion. Some researchers have used this model in the study of nanoparticle dispersion[180]–[182].

2.3.4.1 Introduction of fractal geometry

Fractal dimension analysis focuses on fractal geometry. Fractal geometry is different from classical Euclidean geometry, where all shapes are regular, like squares, rectangles, triangles, circles, etc. Fractal geometry is a new branch of geometry that describes irregular shapes observed in nature, such as snowflakes, clouds, and leaves. All these shapes can be regarded as the result of continuous division according to a specific iteration. Figure 2.17 shows Classic fractal geometry, which is evident in the Sierpinski triangle. In the second triangle, there are three reduced copies of the first triangle. In the third triangle, there are three reduced copies of the second triangle. This rule is used in all later triangles [183].

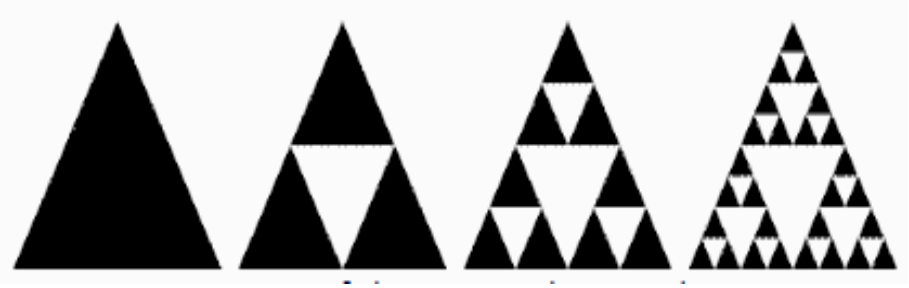

Figure 2.17 Stages of the Sierpinski triangle adapt from [184]

The features of fractal geometry [184]:

Fractals have infinite detail, can be constantly enlarged, and have fine structure.

1. Fractals have similarities. Fractals can be seen as composed of many similar parts but different in size.

2. They are not combinations of regular shapes. They cannot be described by

Euclidean geometry.

3. Simple recursive and iterative methods can usually generate fractals.

As a result, carbon nanoparticles can be described by fractal geometry. Fractal dimension analysis can be used to analyse the dispersion of carbon nanoparticles.

2.3.4.2 Introduction of fractal dimension

In classic geometry (Euclidean geometry), the dimension of an object is integer and specific. However, this is inappropriate for fractal objects that do not have integer dimensions. In 1919, Hausdorff proposed the Hausdorff dimension, which defines non-integer dimensions for fractal geometry [185]. Compared with classic Euclidean geometry, a fractal's most striking property is that it possesses structure at all scales, no matter how far one zooms in. The object's fractal dimension can quantify its geometry's complexity, scaling properties, self-similarity, and the effective ratio of surface area to volume [186]. In 1967, Mandelbrot [187] used fractals to determine the degree of geometric irregularity present in the coastline of Britain.

The Fractal dimension is a measure of complexity, which quantifies how a fractal pattern's detail changes with the scale at which it is measured. When the fractal dimension increases, the fractal geometry fills up more space. When the fractal dimension is between 1 and 2, the fractal pattern changes from a straight line (fractal dimension is 1) to a wiggly line (fractal dimension is 2). This wiggle can fill a 2D-dimensional plane. For example, a Koch snowflake's fractal dimension is 1.2619 [188]. However, when the fractal dimension is between 2 and 3, the object is usually three-dimensional but does not fill space. It is more space-filling than a flat surface (fractal dimension is 2) but less complex than a solid volume (fractal dimension is 3). For instance, the fractal dimension of broccoli, a 3D percolation-by-invasion cluster, and the regular Brownian surface are between 2 and 3 [189]–[191].

Mass fractal dimension and surface fractal dimension

Generally, the fractal dimension can be classified into a mass fractal (Dm) or a surface fractal (Ds). A mass fractal dimension measures how the mass of a fractal structure changes with its size. It is always less than the dimension of the fractal object's space.

Therefore, the value of Dm lies between 0 and 3. With the fractal structure growing, the growth speed of the mass is lower than that of the volume. As a result, the density of a fractal object is not constant but decreases with increasing size [192].

In terms of a surface fractal (D_s), this measures how the surface area of a fractal changes with its size. If a surface structure is constant and not affected by length scale, it is self-similar, and this surface can be considered fractal. In this case, the surface area of an object with radius (r) is proportional to D_s. D_s is between 2 and 3 for a surface fractal in three-dimensional space. The former means that the surface is very smooth, and the latter means that the surface is filled [192], [193].

In conclusion, the D_m quantifies the change in the mass of a fractal with its size, while the D_s indicates the change in the surface area of a fractal with its size. In other words, D_m gives the density of the fractal filling space, while D_s gives the roughness of the surface [192].

2.3.4.3 The application of fractal dimension in the dispersion quantification of nanoparticles

As fractal dimension can be used to describe irregular objects, it can also describe dispersion [194]. As the fractal dimension increases, the dispersion of nanoparticles is more space-filling. Literature shows how the fractal dimension can be used to quantify the dispersion of nanoparticles. For instance, Karasinski [195] reported the dispersion of zinc oxide in epoxy resin. Kanniah [196] examined the aggregation of titania and ceria in ethanol. Liang [194] discussed the influence of dispersants on the dispersion of CNTs in water. Morozov [197] analysed the dispersion of CB in rubber.

The fractal dimension serves as a simple approach for quantifying the dispersion of nanoparticles. Its adaptability allows for analysing optical and electron microscopy images across multiple length scales. This innovative method sidesteps the drawbacks of previous techniques, including excessive dependence on diverse probability distribution functions and reference samples [198].

2.3.4.4 The application of fractal dimension in the dispersion quantification of nanoparticles

The fractal dimension is usually used to describe irregular objects. For instance, it can be used to characterize the morphology and surface roughness of material cross-sections. It can reflect whether a particular structure is dense, dispersed, compact or dispersed [199]. The dispersion of nanoparticles is often related to the size, shape, and distribution of nanoparticles in the system. Therefore, it is inferred that the fractal dimension is related to dispersion [194]. With the fractal dimension increase, the dispersion of nanoparticles is better. Some literature uses the fractal dimension to quantify the dispersion of nanoparticles. For instance, Karasinski [195] reported the dispersion of zinc oxide in epoxy resin. Kanniah [196] examined the aggregation of titania and ceria in ethanol. Liang [194] discussed the influence of dispersants on the dispersion of CNTs in water. Morozov [197] analysed the dispersion of CB in rubber.

The fractal dimension serves as a simple approach for measuring the distribution of nanoparticles. Its adaptability allows for precise analysis of both optical and electron microscopy images with multiple scales, such as micro, meso, and nano levels. This innovative method sidesteps the drawbacks of previous techniques, including excessive dependence on diverse probability distribution functions and references [198].

2.4 The curing technology

2.4.1 Introduction

Curing adds curing agents into epoxy resins to transform their linear structure into a 3D crosslinking network. As a result, the molecular weight, morphology and crosslinking density of the epoxy resin will be changed, and the physical and chemical properties will be improved [200].

2.4.2 Arrhenius relationship for chemical reactions.

As the curing process of CFRP involves non-isothermal kinetics, the n-th order kinetic model (see Equation 2.4). In 1899, the Swedish chemist Svante Arrhenius created the Arrhenius equation depending on activation energy and the Boltzmann distribution law.

The Arrhenius equation is a function that shows the influence of temperature on reaction rate [201], [202]. The Arrhenius equation is shown in Equation 2.5.

$$\frac{d\alpha}{dt} = k \cdot (1-\alpha)^n \qquad \text{Equation 2.4}$$

$$k = A \cdot e^{-\frac{E_a}{RT}} \qquad \text{Equation 2.5}$$

Where *k* is the reaction rate constant; A is a constant value; Ea is the amount of energy reaction required; R is the ideal gas constant (8.3145 J/(mol·K), and T is the temperature in Kelvin.

The equation shows that as the temperature increases, the reaction rate will increase. Because at higher temperatures, the probability of two molecules colliding is higher [203]. Another way to improve the reaction rate is to decrease the activation energy. In a chemical reaction, Ea is the height of the potential barrier separating the products and reactants [204]. Catalysts can effectively ''reduce'' Ea value without being consumed. As a result, when reactants react with catalysts, the required Ea is lower than that in the original reaction. In addition, the same quantity of consumed catalysts is produced during the reaction process[205], [206].

As a result, high curing temperatures and catalysts can effectively reduce the curing cycle.

2.4.3 Traditional manufacturing methods

In this section, there are some traditional curing methods are discussed, including room temperature curing and heated curing methods (Oven and Autoclave)

2.4.3.1 Room temperature curing

Resins can be cured at room temperature. The cure time depends on the type of resin and hardener, as well as the mould size. In the curing process, the resin and hardener are mixed, and the viscosity of the mixture quickly increases. The state will change from liquid to sticky and to stiff. Finally, the resin will be cured at room temperature [200]. However, the curing cycle is very long at room temperature, which commonly takes 1-2 days.

2.4.3.2 Oven

An industrial curing oven is used for heat treatment. By accelerating the chemical reaction rate, ovens can improve the properties of materials. If the resin maintains a high

temperature in the oven, the cure time of the resin will sharply decrease, and the resin will be more robust and more stable [207].

- Advantages

Firstly, ovens can provide high temperatures with lower energy consumption compared to autoclaves, as they generally have a lower thermal mass than an autoclave with an equivalent internal volume [208]. Secondly, ovens usually cost much less than autoclaves. Finally, the service and maintenance costs of an oven are far lower than those of autoclaves [209].

- Disadvantages

Compared to autoclaves, samples cured in an oven, even under vacuum, have higher void content. As a result, mechanical properties are inferior [210]. Compared to other curing mechanisms, ovens also have a higher energy requirement and slower cycle times than hot presses.

2.4.3.3 Autoclave

Autoclaves are primarily of two different types: medical autoclaves and composite autoclaves. Medical autoclaves use pressurised steam to sterilise surgical instruments at high temperatures, 120-140 ℃ [211]. Compared with dry heat, moist heat is more reliable in destroying microorganisms and spores as it transfers heat more effectively. These sterilisation autoclaves are widely used in hospitals, universities and manufacturing facilities [212].

However, composite autoclave is used to manufacture composites. Under the vacuum state, the autoclave uses procedures such as heating, pressurization, and insulation to provide a uniform and high temperature and pressure to manufacture composite products with complex shapes and large volumes [213]–[215].

Autoclave moulding is a manufacturing process for thermosetting composite materials. The heat and pressure needed in the curing process are from autoclaves. During manufacturing, fibres and thermoplastic matrices are laid on the mould in a specific sequence. Fixing glue is sprayed on the surface of each fibre sheet to ensure materials will not move. Then, laminate materials are put into a vacuum bag to expel the entrapped air between the layers. The whole assembly is moved to the autoclave, where the matrix

can be evenly and effectively dispersed to complete the curing process by increasing temperature and pressure [216], [217]. The inside and outside structures of autoclaves are shown in Figure 2.18.

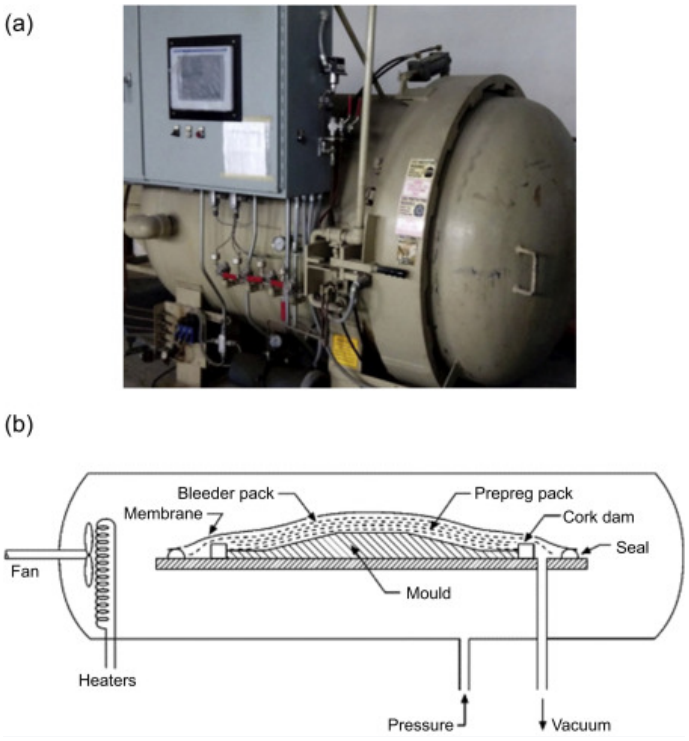

Figure 2.18 The (a) outside and (b) inside the structure of autoclaves [216].

- Advantages

Compared with ovens, autoclaves have some advantages. At first, autoclaves can reduce void components to less than 1%. In addition, when permeable high-viscosity resins are used in the manufacturing process, better surface quality, high interfacial adhesion, and wettability of reinforced fibres can be achieved [210].

- Disadvantages

However, autoclaves also have disadvantages. The cost of an autoclave is very high, and the size is limited. The cycling time is long, and the labour intensity is high, which leads to low production efficiency. Besides the high cost of manufacture, autoclaves need to have a good heating and pressurising system or the composite materials cannot be cured well [210]. During the manufacturing process, the original materials and mould must be able to endure high pressure and temperature.

2.5 New manufacturing methods - Direct electrical curing (DEC)

Direct electrical curing (DEC) for manufacturing conductive composite materials has been developed. Conductive composites (carbon fibre) have good electrical conductivity. When the current goes through the “resistance”, it will create Joule heat, which can provide energy and successfully cure the material from the inside of the material. The use of nanocarbon composite resins as conductive composite matrices for electrical curing has increased in recent years. The experiment results from Joseph and Viney [30] show that current going through carbon fibre can produce heat that can successfully cure carbon fibre/epoxy resin composite materials. Mas *et al.* recently developed a method of thermosetting curing by joule heat of nanocarbon for fabrication, repair, and welding of composite materials [218].

Direct electric cure, or Joule heating, is the process whereby the intrinsic conduction of the carbon fibre allows the fibre to act as a resistive heater. As current passes along the fibre, it heats up, curing the matrix. Whilst most studies have naturally concentrated on passing current along the fibre [29], [219], it is possible to pass currently perpendicular to the fibres without incorporating conductive nanoparticles [28].

Lee [220] reported that DEC achieved a 99% energy saving compared with autoclave with no noticeable change in the cured samples' physical or mechanical properties. Fukuda *et al.* [28] introduced DEC (or Joule Heating) to fabricate thermoset CFRP parts. Utilising two different contact arrangements and vacuum consolidation, they performed through thickness and edge-to-edge heating. Collinson *et al.* [219] used DEC to cure prepreg with vacuum consolidation for large areas. A sample size of 700 × 2000 mm with 16 plies thick prepreg was prepared.

2.5.1.1 Working principle

Electrodes are connected to the ends of an epoxy resin containing conductive particles, and electric power is applied to it. When the current passes through the epoxy resin, the network of conductive particles will generate heat. As a result, the temperature of the composite sample (epoxy resin containing conductive particles) will increase. The increase in temperature can be controlled by adjusting the power transferred to the conductive particles, such as by changing the voltage and current. [218].

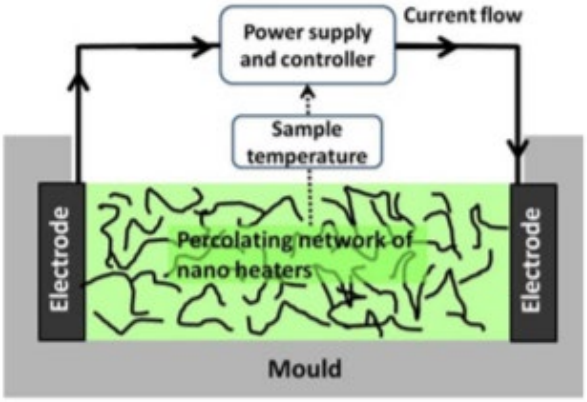

Figure 2.19 Schematic of electrical curing working principle [218]

2.5.1.2 Advantages

Compared with autoclave and oven curing, in DEC, most of the heat energy converted from electrical power can be applied in the curing of samples. However, in the autoclave and oven curing process, there is energy loss by conduction and convection in mould and samples [30], [218]. In addition, compared with the other two curing methods, electrical curing can heat the matrix more evenly, and a more even distribution of the matrix can be found. It is possible to achieve a crosslinking gradient near each fibre. The three-point bending test shows that electrically cured samples can maintain about twice the fracture strain and have stronger energy absorption [29].

2.5.1.3 Disadvantages

Compared with traditional manufacturing methods (oven and autoclave), DEC has specific requirements for operation and materials. Electrically insulated tools are required for operation. The electrodes should come into contact with or within the materials to create an electrical circuit [29], [221], [222].

DEC generates Joule heat to cure samples. So, the material should be conductive. In the electrical curing process, there may be an uneven temperature distribution. The temperature of positions close to electrodes is often higher. In addition, the resin flow in uncured CFRP samples can affect the thickness distribution and resistance distribution. As a result, the power distribution will be influenced, which will lead to a non-uniform distribution of DoC in the sample. In addition, during the curing process, the resin will generate lots of heat. Due to the non-uniform distribution of cure speed, the non-uniform

distribution of DoC will be more and more obvious, especially in large components [223]–[225].

2.6 New manufacturing methods with open mould or non-mould.

Traditional manufacturing methods of CFRPs, including autoclaves and ovens, must use specific moulds tailored to product requirements, which are typically constructed from aluminium, steel, or other metals and are characterized by their long service life, high cost, and environmental impact [4]–[7]. Consequently, for low-volume or custom products, the mould costs can be a significant cost of the product. It presents a substantial challenge in the cost-effective production of CFRPs.

Alternative and innovative manufacturing methods have been investigated to overcome the above issues. In this section, two manufacturing methods are introduced: additive manufacturing (AM) and incremental forming, including single-point, SPIF, and double-point, DPIF.

2.6.1 Additive manufacturing (AM)

Additive manufacturing (AM) is one of the famous novel manufacturing methods. Additive manufacturing can directly create CFRP parts without moulds. A wide variety of production processes for continuous fibres have been used. Fused deposition modelling (FDM) [8]–[11] and selective lamination composite object manufacturing (SLCOM) [12], [13] are two popular methods in AM. Therefore, these two methods are discussed in this section.

2.6.1.1 Working principle

Here, the working principles of FDM and SLCOM are discussed.

- The working principle of the FDM method

There are two different approaches. The first one is the conventional FDM process (see Figure 2.20). Prepreg filament is supplied in spools and fed into the extrusion head. The extrusion head has a temperature controller that can help heat the prepreg and convert it into a semi-solid state. The material is then printed layer by layer to create the desired

geometric features. Because there are few changes compared with the traditional FDM, it is regarded as the simplest method [11].

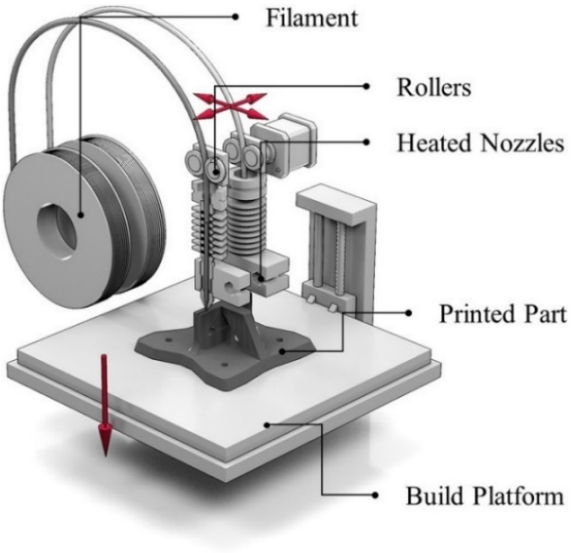

Figure 2.20 Schematic illustration of conventional FDM Process [11]

Besides the conventional FDM process, there is a new method (see Figure 2.21). The fibres and matrix are separated until reaching the printing head. The two materials are mixed in the printing head. This new method makes mixing flexible. However, it comes with a challenging printhead setup. Air entrainment should be avoided through precise control during fibre penetration [10].

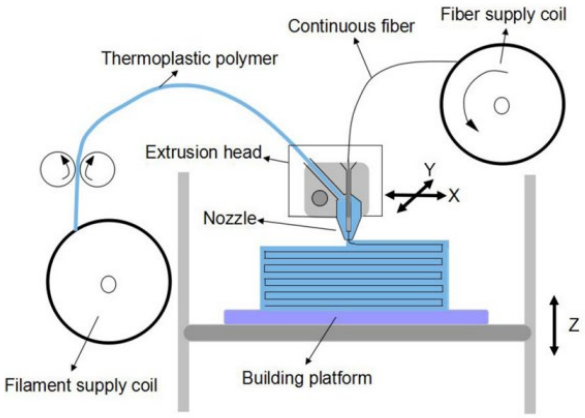

Figure 2.21 Schematic of the new FDM for CFRPs [10].

- The working principle of the SLCOM method

The preheated thermoplastic matrix roll is fed into the print bed and cut cleanly with an ultrasonic cutter. A nozzle sprays the waxy substance on areas which do not require

lamination. A heated pressure roller melts the thermoplastic matrix to ensure complete impregnation and applies pressure to consolidate the layers. Then, the feed roller is advanced so that the waste material from the cutting is wound onto the take-up roller, and the new material can be placed on the bed. The above steps are repeated until the required plys are reached. Finally, all areas with the waxy substance are removed, and the fine products can be collected [12].

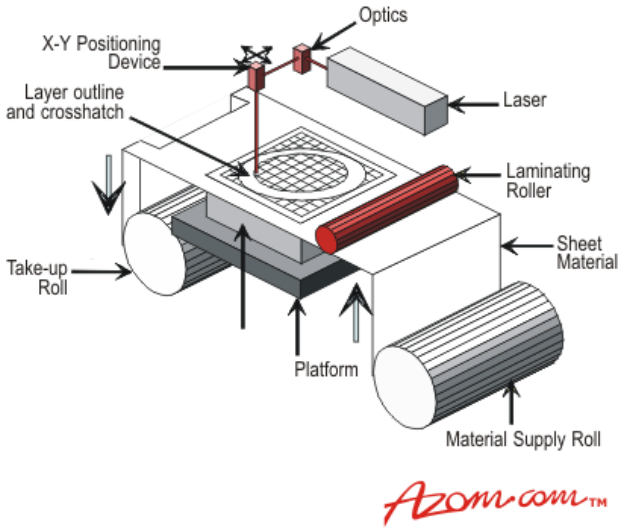

Figure 2.22 Schematic representation of SLCOM [12]

2.6.1.2 Advantages

First of all, there is no requirement for moulds, which can save a lot of money. As a result, the products can be customized easily. In addition, the complicated inside structure of products can be manufactured by AM. AM can maximize material utilization due to zero-waste manufacturing. It can significantly reduce the manufacturing time and energy consumption [226].

2.6.1.3 Disadvantages

Compared with the traditional manufacturing methods, the fibre volume fraction of CFRPs manufactured by FDM is lower. Because the high fibre volume fraction will clog the nozzle and cause the building process to fail [227]. Due to the occurrence of triangular gaps between the printed track, a high void rate is common in FDM [17], [228]. In terms of SLCOM, besides the high void rate, due to the low adhesion between the layers, the possibility of delamination between layers is increased [13].

2.6.2 Single-point incremental forming (SPIF)

The single-point incremental forming (SPIF) method is a novel manufacturing method that uses cheap open moulds instead of expensive closed moulds. In 1967, Leszak [229] proposed it and filed the patent. After that, SPIF is widely used in sheet metal forming [19]–[22]. Nowadays, more and more research on SPIF in FRPs is being conducted. For example, Emami *et al.* [24] used SPIF with a ceramic infrared heater under the sample to manufacture polyamide 6 (PA6) sheets reinforced by glass fibres (GF). Okada *et al.* [25] reported a SPIF of CFRPs using forming punches and localized optical heating. Cedeno-Campos *et al.* [26] used a copper tool with a heater controlled by a CNC system to achieve SPIF manufacturing CFRPs.

2.6.2.1 Working principle

In the SPIF process, computer-aided design models and computer numerical control (CNC) codes are used to form various parts with different geometry. Then, the workpiece is clamped with a fixture. The CNC machine tools are implemented by moving tools along a specific path, which is formed by CNC codes [230]. The schematic of the SPIF process is shown in Figure 2.23.

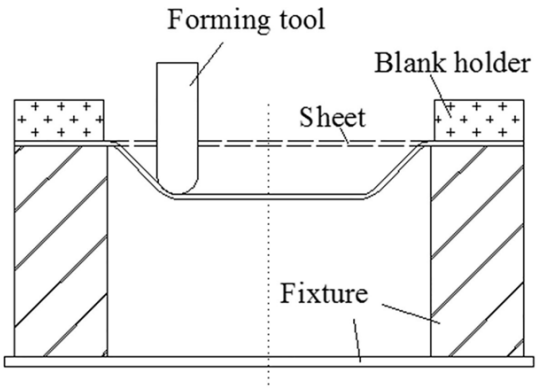

Figure 2.23 The schematic of the SPIF process [230]

2.6.2.2 Advantages

Single incremental forming can quickly and cost-effectively manufacture CFRP parts with different complicated geometry, which does not need high cost in the mould and setup time [231]. In addition, due to direct contact, energy consumption is significantly lower than that of traditional manufacturing methods [232].

2.6.2.3 Disadvantages

However, though SPIF does not require expensive closed moulds, it still needs open moulds to support the materials and avoid bad deformation during the manufacturing process [20].

2.6.3 Double-point incremental forming (DPIF)

To achieve mould-free, as with the improved SPIF technology, double-point incremental forming (DPIF) is proposed. It has been widely used in sheet metal forming and is matured [27], [233]–[235].

2.6.3.1 Working principle

In the DPIF working principle, the open mould in SPIF is replaced by a tool stylus, which is the same as the top one. It is used to support the material. The top tool is a forming tool, which has the same function as that in SPIF.

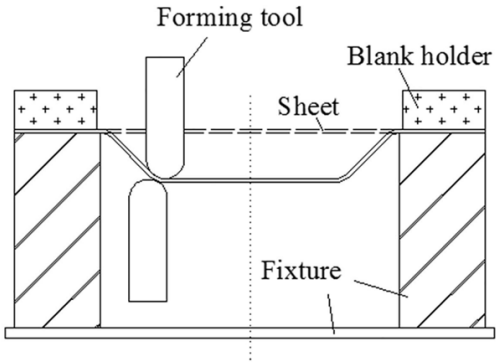

Figure 2.24 The schematic of the DPIF process [230]

2.6.3.2 Advantages

Compared with SPIF, DPIF can deliver CFRP manufacturing without any mould. In addition, two tools in DPIF can provide more process control, especially in terms of surface quality, formability, and geometric accuracy of the part.

2.7 Conclusion

Though the application of DPIF in sheet metal forming is matured [27], [233]–[235], the study of it in FRP is absent. As a result, this thesis discusses the study of DPIF

manufacturing in the CFRPs. In addition, due to the limitation of heating the bulk with heated tools, an electrical curing method is considered. Two tools in DPIF and a DC power supplier form a DEC system. Carbon fibre is inherently conductive and can act as its own heating element. This DEC can be leveraged to produce a low-energy, highly controllable curing process that directly heats the composite part [28]–[30]. However, due to the high insulation of matrix (epoxy), the resistivity along fibre R11 and R22 (0.022 mΩ·m) is much lower than that when passing through laminated layers of R33(310 mΩ·m) [31], [32]. Carbon nanoparticles are added to improve the electrical conductivity of the epoxy resin. Due to the influence of carbon nanoparticles, the dispersion of carbon nanoparticles in epoxy resin is discussed first. Then, the impact of carbon nanoparticle concentration on CFRPs and the DEC in CFRP sheets is discussed. The detail is shown in the next section (methodology).

Chapter 3 Methodology

In this section, the raw materials, different composite manufacturing methods, and different properties testing experiments are discussed.

3.1 Raw materials of CFRP

In this project, there are three main components in CFRP. They are epoxy resin as a matrix, carbon nanomaterials (CB, CNTs, and graphene) as fillers, and carbon fibre as a reinforcement.

3.1.1 The epoxy resin system

The epoxy resin has two reagents, epoxy and hardener, which are termed part A and part B. They need to be mixed by a specific ratio for the cure. The cured material is commonly termed “epoxy resin”.

- The epoxy (part A)

The epoxy used in this project is IN2 epoxy infusion resin (IN2 resin) from Easy Composites Ltd. It is a modified infusion epoxy resin. The main components of it are Bisphenol A diglycidyl ether and phenolic epoxy resin F-44. Compared with traditional monomer epoxy, it has extremely low viscosity to ensure that it can quickly and effectively infuse through a range of reinforcements. Due to comparatively low viscosity, the carbon nanomaterials can be easily dispersed into the resin. In terms of physical properties, IN2 resin is a viscous liquid at room temperature but becomes significantly less viscous upon heating it.

- The hardener (part B)

The epoxy resins are polymerized by curing hardeners. In this project, the AT30 slow hardener (AT30S) is chosen as the curing hardener from Easy Composites Ltd. The main components of it are Isophoronediamine and Poly(propylene glycol) bis(2-aminopropyl ether). Compared with the AT30 fast hardener, it has a lower viscosity, though the cure time is longer. It is liquid at room temperature and is easy to incorporate into the resin. At room temperature, IN2 resin/AT30S can be cured in 24 hours. AT 60 ℃ and 100 ℃, it takes 6 hours and 3 hours, respectively (the data is from the supplier [236]).

3.1.2 Carbon nanomaterials

This work has researched three main carbon nanomaterials as fillers in the matrix. They are carbon black, carbon nanotube, and graphene.

- Carbon black (CB)

CB used is ''Carbon black, acetylene, 100% compressed'' from Alfa Aesar Ltd. The CAS number is 133-86-4. The density of CB is about 2.1 g/cm^3 at 20 ℃. The electrical conductivity is about 5.58×10^{-2} Ω·m [237].

- Carbon nanotubes (CNT)

The CNT used is MWCNT-COOH 95% with 10-20nm outer diameter (OD), and the CAS number is 308068-56-6. The density of CNTs is about 2.2 g/cm^3 [238]. The electrical conductivity is about 10^{-4} Ω·m [239].

- Graphene

The graphene used is PureGRAPHTM 20 from First Graphene Ltd, CAS number 1034343-98-0. The graphene's platelet size is about 20 um. The tapped density of this graphene is 0.251 g/cm^3 [240].

The electrical conductivity of carbon nanomaterials is affected by temperature, pressure, structure and other factors. So, the above electrical conductivity data is merely a guide.

3.1.3 Carbon fibre

The carbon fibre used is 2x2 twill 3k carbon fibre cloth carbon supplied by Easy Composites Ltd. The carbon fibre is a TR 30S 3L manufactured by PYROFIL™ [241]. Its areal weight and density are 210 g/cm^2 and 1.79g/cm^3 respectively. The filament diameter is 7 μm. The manufacturer's data sheet gives the tensile strength and modulus as 4120 MPa and 234 GPa, respectively [242].

In terms of DPIF manufacturing, because the CFRP products manufactured are flat plates, the requirement of drapability is low. As a result, the 2×2 twill weave carbon fibre is used in this project. A high drapability weave such as harness satin weave would be preferable in future work.

3.2 Carbon nanomaterial/epoxy resin composite sample preparation

To analyse the different methods to disperse carbon nanomaterials in epoxy resin, CB is dispersed into IN2 resin/AT30S with four different methods (manual stirring, magnetic stirrer, overhead stirrer, and ultrasonication) and different mixing times. Finally, the optimal combination (mixing method and time) was used in the dispersion of CNTs and graphene in epoxy resin.

3.2.1 The fabrication process of CB/IN2 resin composite

The 30 g IN2 resin was added to a disposable plastic cup. CB was weighed out and added to the IN2 epoxy resin. The IN2 and CB were mixed by manual premixing for 30 seconds. In this process, the CB particles can be wet out, and particle splashing can be avoided. Then, the dispersion method is given for the specified time. After that, a 9 g AT30S was added to the mixture and remixed for the specified time. The detail can be seen in Table 3.1. For example, 1+1 mins indicates adding CB to IN2 resin and mixing for 1 minute. Then AT30S was added to the mixture and mixed for another 1 minute. Subsequently, the mixture with well-dispersed CB nanoparticles is degassed in a vacuum chamber for 10-30 minutes until no bubbles are seen in the mixture. Finally, it is poured into specific moulds (see Figure 3.6(a)) and heated in the oven (UT 6200 Thermo Fisher Scientific Inc. Waltham, USA) for a specific time and temperature. The preparation process is shown schematically in Figure 3.1.

Finally, the optimal combination of the mixing method and mixing time in CB dispersion was used to disperse CNT and graphene into IN2/AT30S. In terms of the mixture with well-dispersed carbon nanoparticles, the fabrication is the same as that in CB/IN2 resin.

Table 3.1 The table of the different mixing times and methods.

Mixing methods	Speed	CB+IN2 stirring time (mins)	CB+IN2+AT30S stirring time (mins)
Manual	-	1	1
		2	2
		4	4
Magnetic stirrer	1200 rpm	3	3
		6	6
		12	12
Overhead stirrer	900 rpm	1	1
		2	2
		3	3
Ultrasonicator	40% (amplitude)	1	1
		2	2
		4	4

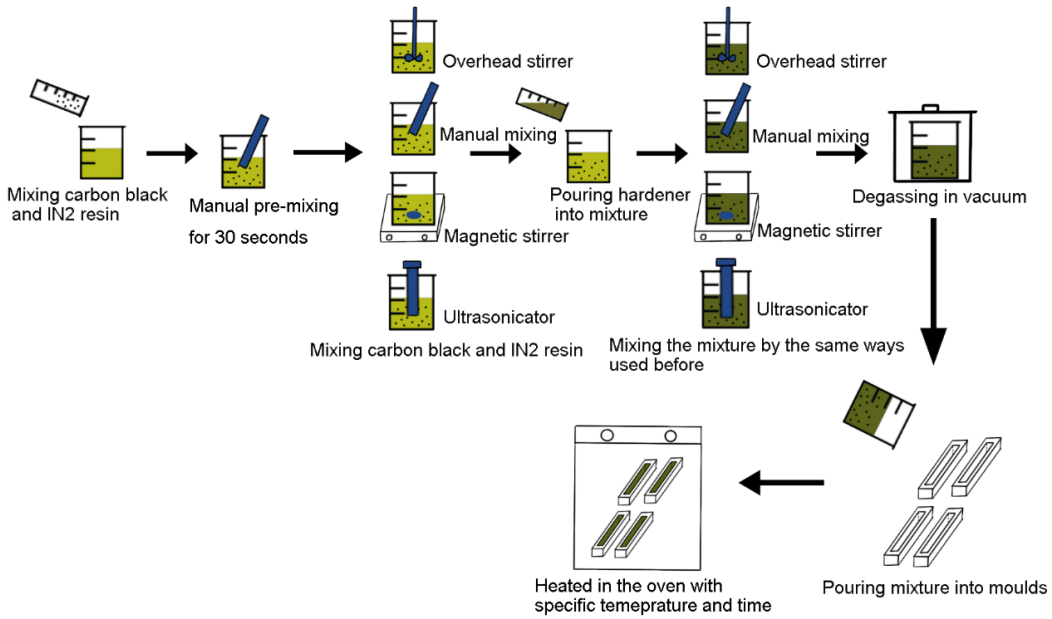

Figure 3.1 The fabrication process of CB/IN2 resin composites.

3.2.2 The four different mixing methods

This work discussed the four different dispersion methods (manual stirring, magnetic stirrer, overhead stirrer, and ultrasonication) used in this project. The fabrication process can be seen in Figure 3.1. Before using different mixing methods, the IN2 and CB were mixed by manual premixing for 30 seconds to avoid particle splashing.

- Manual stirring

The IN2 resin and carbon nanomaterial are mixed in a plastic cup by a wooden stirrer for 1, 2, or 4 minutes with hands. Then, the hardener is added to the mixture and remixed for the same stirring time.

- Magnetic stirrer

The magnetic stirrer is one device for mixing the mixture. It is combined with a magnetic stirring bar and a mechanical plate [243]. The mechanical plate is composed of an electromagnet driver and a heating element. The electromagnet driver can drive the magnetic stirring bar to rotate in liquid and mix the mixture. The magnetic stirring bar is generally bar-shaped, whose cross-section is usually octagonal or circular. There are also various special shapes for magnetic stirring bars to mix in different containers stably and

efficiently. To avoid contamination or reaction with the mixture, a PTFE coating is applied to the bars. When PTFE is not suitable due to high temperature or chemical attack, glass will be an alternative [244]. In addition, the heating element can heat the liquid during the mixing process to increase the mixing efficiency [245].

In this work, the magnetic stirrer used is a CD162 hot plate stirrer (see Figure 3.2) from Stuart Ltd. In the mixing process, a 1 cm length magnetic stirring bar is placed in a plastic cup to mix the mixture. The stand support fixes the cup. First, the CB/IN2 resin mixture is mixed by the stirring bar at 1200 rpm for 3, 6, and 12 minutes. Then, AT30S is added to the mixture, and the mixture is remixed to the same stirring speed and time.

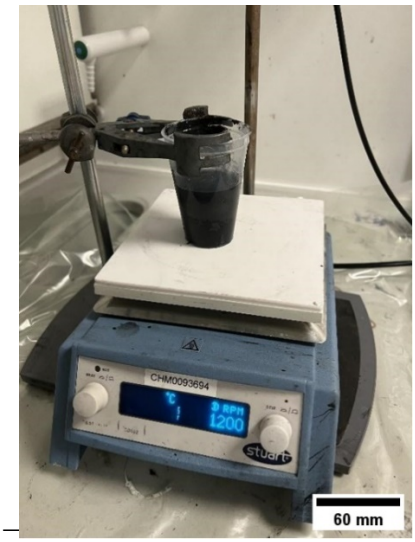

Figure 3.2 CB is dispersed into IN2 resin by the magnetic stirrer.

- Overhead stirrer

An overhead stirrer is a mechanical stirrer used to stir solutions. One overhead stirrer consists of a stand and a motor which controls the stirring time and speed. The motor is connected to a stirrer and drives it to stir the liquid. According to the different requirements, the stirrer is anchor, bladed, flat blade turbine, split blade, etc. Under the high rotation speed, the overhead stirrer can generate a very high shear speed. Meanwhile, there will be a vortex that draws agglomerates and aggregates into the cutting head and breaks them with shear force [246]. The experiment showed that the shear mixing technology is more energy-saving and efficient than ultrasonication technology.

In this work, the overhead stirrer used is ''Hei-TORQUE Value 100'' from Heidolph Instruments. The stirrer is pitched-bladed.

In this project, the steel propeller stirring bar was used to mix carbon nanomaterials and IN2 resin. The carbon nanomaterials and IN2 resin were added into a plastic cup with a specific weight. Then, the top of the stirring bar was immersed in the mixture at about 1 cm distance from the bottom of the cup. The overhead stirrer stirred the mixture at 900 rpm for 1, 2, or 3 minutes (see Figure 3.3). Then AT30S was added to the mixture and remixed for the same stirring speed and time.

In addition, Equation 3.1 can calculate the output power of the overhead stirrer.

$$P = \tau \cdot (\frac{60}{2\pi} \cdot n) \qquad \text{Equation 3.1}$$

Where τ is torque (N·m), and n is the rotation speed (rpm).

The rotation speed in this project is 900 rpm. The torque is about 550 N·cm maximum torque at 900rpm. So, the output power is about 51.8W for this project.

Figure 3.3 CB is dispersed into IN2 resin by the overhead stirrer

- Ultrasonication

Ultrasonication is a common dispersion technology in the preparation of polymer composites. It disintegrates agglomerates and aggregated fillers into small particles and disperses these in the polymer [247]. The ultrasonic mixer has a metal probe with piezoelectric materials at the tip. The metal probe is placed in the liquid, and when an

electric current is applied to the detector, it begins to vibrate and causes cavitation. Ultrasonic cavitation refers to the dynamic process of growth and collapse when the sound pressure reaches a specific value [248]. In this process, sound waves propagate into the liquid medium in alternating high-pressure (compression) and low-pressure (rarefaction) cycles. In low-pressure cycles, tiny bubbles will form. However, in high-pressure cycles, these bubbles will collapse and create local shock waves, which release large amounts of localised mechanical and thermal energy [249]. Cavitation can produce a high-velocity liquid jet of up to around 600 mph. The high-pressure jet liquid between particles can separate particles. In addition, small particles will move violently under the shock of jet liquid and collide with surrounding particles, which can result in the decomposition of particles [250]. In conclusion, ultrasonication can effectively disperse, deagglomerate, and fine-grind nanoparticles.

In this work, the ultrasonicator used is a "model 120 sonic dismembrator" from Fisherbrand™. Using Equation 3.2 can convert amplitude to power.

$$P_{real} = P_{max} \cdot A^2 \qquad \text{Equation 3.2}$$

Where P_{real} is the real (actual) ultrasonication power applied to the sample, P_{max} is the maximum ultrasonication power that the ultrasonicator can use, and A is the amplitude of ultrasonication.

The maximum ultrasonication power of the model 120 sonic dismembrator is 500W. In this work, the amplitude of ultrasonication used is 40%. So, the actual ultrasonication power is 80W. When an ultrasonicator mixes carbon nanomaterials and epoxy resin, it will generate heat. However, this heat will accelerate the curing reaction of the epoxy resin. To avoid this situation, the mixing vessel was placed in a room temperature or ice water bath, and a thermocouple monitored the temperature of the mixture. A duty cycle was employed with an "on time'' set to 20 seconds and "off time" set to 10 seconds (a 67% duty cycle) to avoid a high temperature of the mixture. In addition, the mixture container was placed in an ice water bath and mixed by the magnetic stirrer at 1200 rpm speed to boost water flow around the mixture container and increase heat transfer speed. The detail is shown in Figure 3.4.

Figure 3.4 CB is dispersed into IN2 resin by ultrasonicator.

In this work, the carbon nanomaterials and IN2 resin are added into a plastic cup with a specific weight. Then, the top of the ultrasonicator bar is immersed in the mixture at about 1 cm distance from the bottom of the cup. The ultrasonicator mixed the mixture at 40% amplitude for 2, 3, or 4 minutes (see Figure 3.4). Because the ultrasonicator releases lots of heat, the mixture is stirred again for 2 minutes to avoid high temperatures and the composite curing. During the ultrasonication process, the ultrasonicator degasses the mixture. There are no bubbles in the well-blended mixture. It can be directly poured into silicone moulds without the degassing process, and the moulds are placed in the oven to finish the curing process.

After mixing, except for the mixture mixed by ultrasonicator, all well-blended mixtures were degassed by a vacuum pump. Finally, they were poured into specific moulds and cured in an oven with a specific temperature and time.

3.2.3 Measuring the conductivity of the carbon nanomaterial/resin composite

- The silicone mould design

Initial measurements of the resistance were made via a resistance probe on the surface of the fully cured sample. However, when IN2/AT30S resin with carbon nanoparticles is cured, there is a layer of insulating resin at the top surface. Thus, this method is therefore ineffective. (This suggests the epoxy resin has the lower surface energy.) Therefore, a new method is proposed.

First, 3D printing is used to print an ABS mould, which is shown in Figure 3.5. CR1 Easy-Lease Chemical Release Agent (Easy Composites Ltd, Stoke-on-Trent) was sprayed on the inside surface of the mould to avoid sticking. Then, the AS40 addition cure silicone rubber (Easy Composites Ltd., UK) was mixed by hand with the AS40 catalyst in a plastic cup with a wooden spatula for 1 minute. The component ratio was 10:1. A vacuum pump degassed the mixture, and the degassed mixture was poured into moulds and left at room temperature for one day to cure.

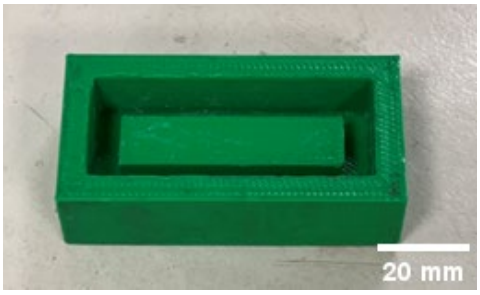

Figure 3.5 An ABS positive mould printed by 3D printing

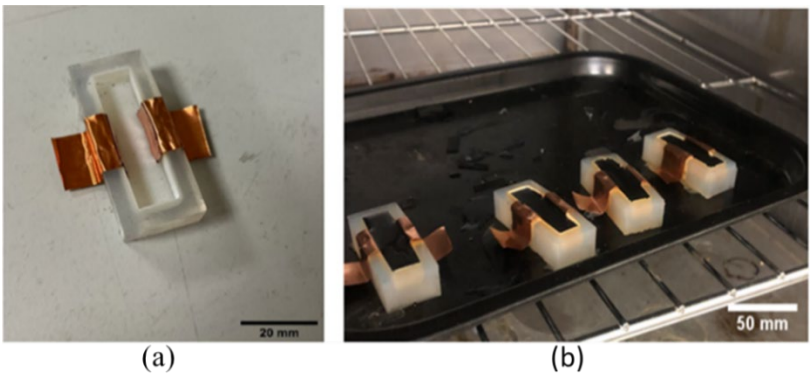

Figure 3.6 (a) The silicone mould without the composite and (b) with the composite in the oven.

The degassed IN2/AT30S/CB epoxy mixture is poured into silicone moulds, where the copper sheets are preplaced at the two sides (see Figure 3.6(a)). The width of the copper sheet is 16mm; this is sufficiently wide to allow for a reproducible electrical connection between the terminals and the carbon black in the resin. Additionally, a wider strip is preferred to determine the cross-sectional area between the contacts without significant fractional uncertainty. The flow of electrons is expected to follow the electric field lines and, as such, will diverge a little in the middle of the sample. A wider strip means this deviation does not significantly contribute to the conductive path. Thus, the resistivity can be calculated based on the cross-sectional area of the contact. When the sample is

cured, there is a large connection between the copper sheets and the sample (see Figure 3.6(b)). Therefore, the average resistivity can be figured out. The profile size of the mould is 50×20×12 mm (L×W×H), and the inside size is 40×10×7 mm (L×W×H).

- The measurement of resin resistance

When the ohmmeter measures resistance, all resistance in the circuit is measured, including the sample resistance and resistance of the electrical cable between the sample and the ohmmeter. Generally, the wire resistance can be ignored (a few ohms per 100 meters). However, if the connection cable is very long or the resistance of the subject is very small, the resistance wire will cause a large measure error [251]. To solve this problem, four-terminal sensing is introduced. In four-terminal sensing, there are four cables. Four cables create two circuits. One circuit measures the current, and another circuit measures the voltage. The end of each of the two cables is connected with an alligator clamp. The half jaws of clamps are insulated from each other, and only subject resistance is in contact with the tip of the clamp. Therefore, the current through the "current" jaw does not pass the "voltage" jaw, and there will not be any induced resistance along its length [252]. Compared with traditional two-terminal sensing, four-terminal sensing separates the current and voltage electrodes to eliminate the influence of resistance of connection wires [253].

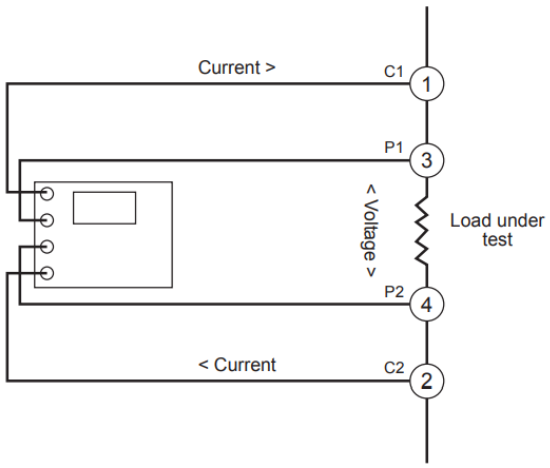

Figure 3.7 The four-terminal sensing setup for measurement [254]

In this project, a BK Precision 2841 ohmmeter (see Figure 3.8) is used to measure the resistance of the sample via the four-terminal sensing principle. This ohmmeter has an extensive measurement range between 1μΩ and 100 MΩ with a high precision of 0.01%.

In addition, its temperature measurement range is between -10 ℃ and 99.9 ℃, with an accuracy of 0.3%.

Figure 3.8 BK Precision 2841 resistance meter

Electrical resistivity is introduced to analyse the electrical property of a material, which is a fundamental property of a material that estimates how strongly it resists electric current. Equation 3.3 converts resistance to resistivity.

$$\rho = R \cdot \frac{A}{L} \qquad \text{Equation 3.3}$$

Where ρ is the resistivity of the sample, R is the resistance of the sample, A is the cross-sectional area of the sample, and L is the length of the sample.

3.3 The resistance and temperature measurement methods for CB/IN2/AT30S nanocomposites

In this section, the resistance and temperature changes of CB/IN2/AT30S nanocomposites during the curing process are discussed.

3.3.1 LabVIEW to record resistance and temperature changes.

In this project, the resistance is measured by the BK Precision 2841 resistance meter, and temperatures are measured by K-type thermocouples, which are connected to the Pico USB TC-08 Thermocouple Data Logger. To record the change of resistance and temperatures of samples during the curing process, the resistance meter and data logger

are connected to the PC and controlled by a LabVIEW program. This program (see Figure 3.9) can record the resistance and up to 8 position temperatures every 2 seconds.

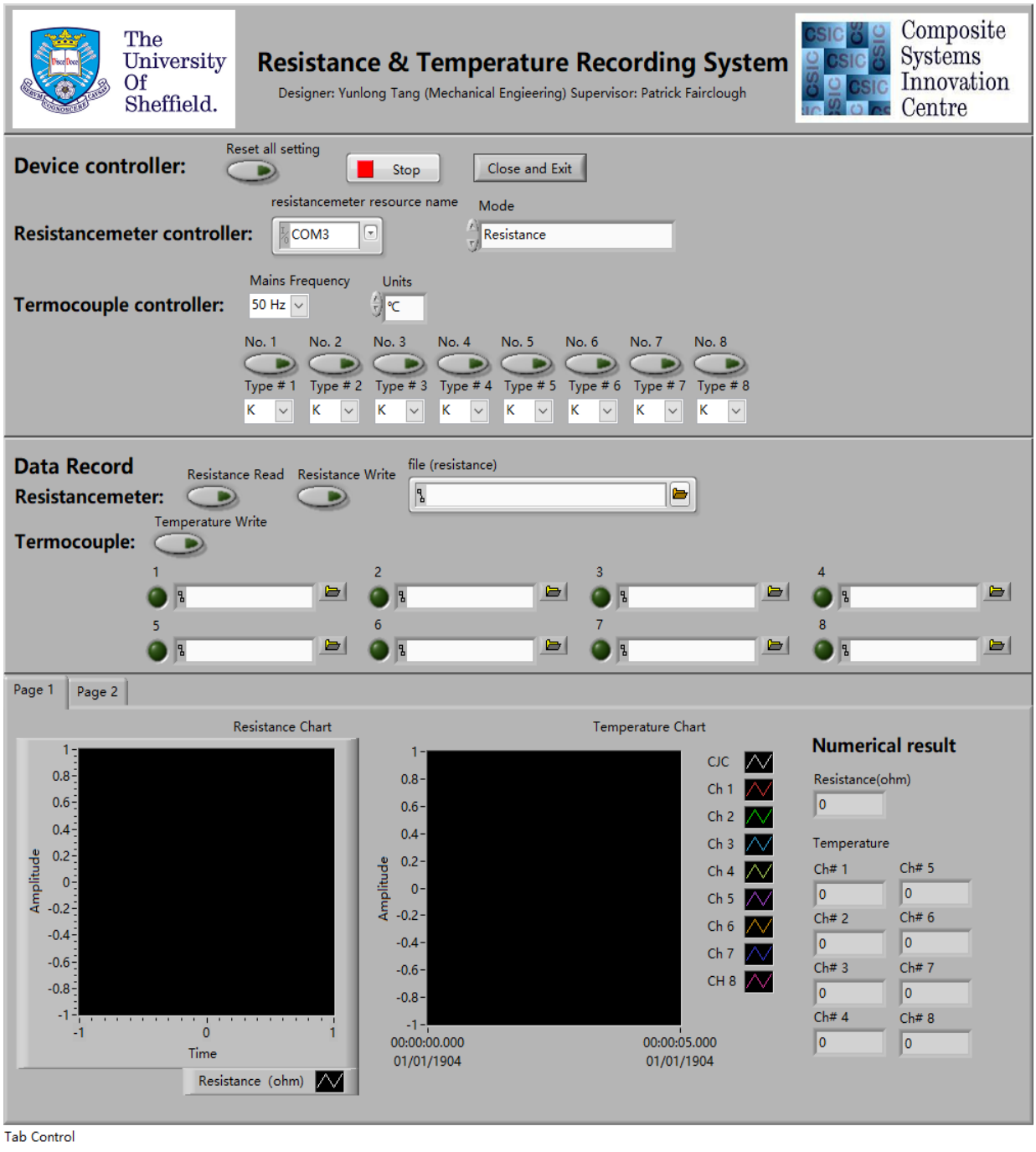

Figure 3.9 The front panel of the resistance and temperature recording LabVIEW program

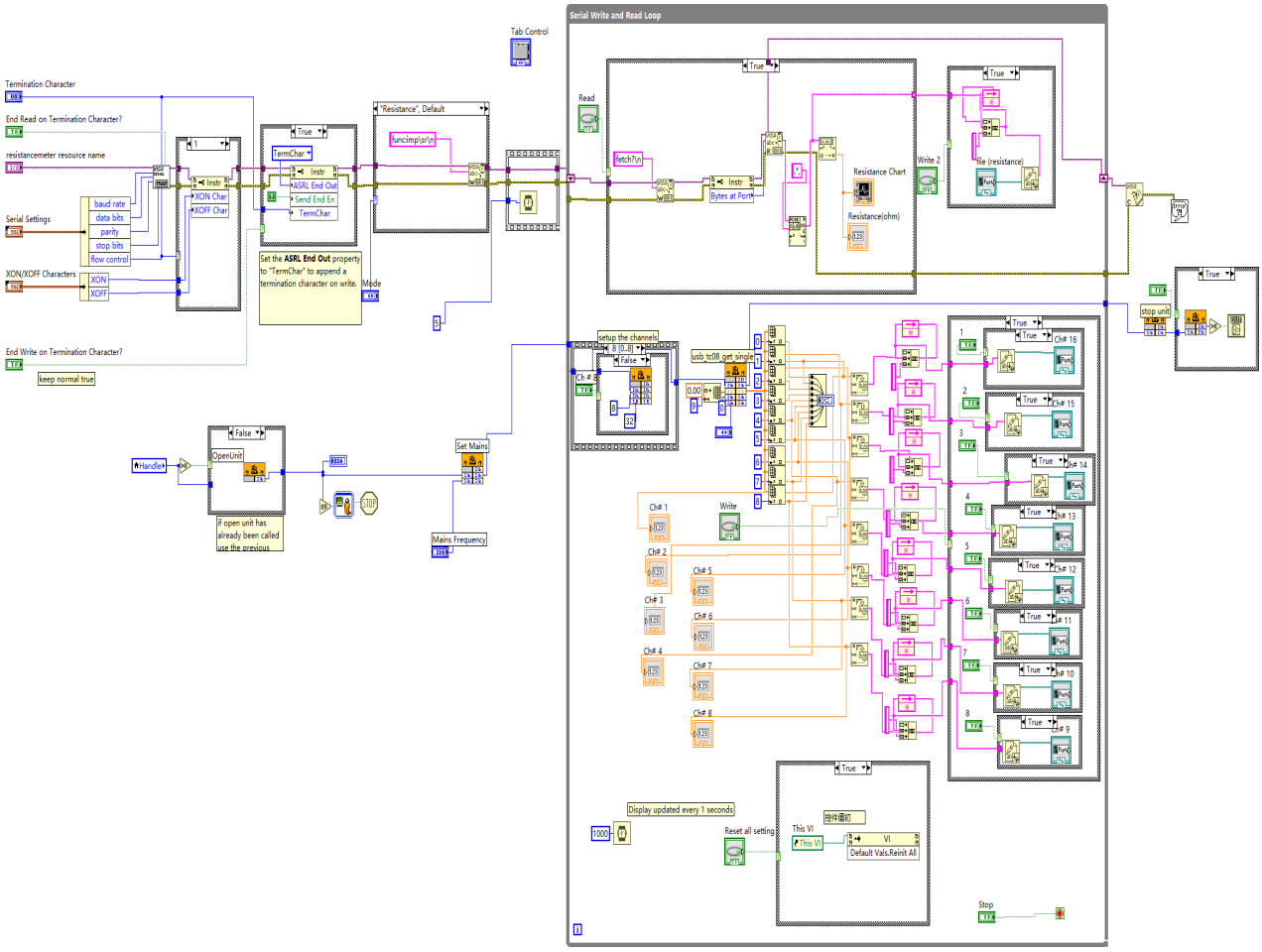

Figure 3.10 The project code of resistance and temperature recording LabVIEW program

3.3.2 The resistance and temperature changes of carbon nanomaterial/IN2 resin composite during the curing process

To discuss the influence of temperature on composite resistivity in the curing process, four different isothermal curing temperatures (70, 130, 150, and 170 ℃) are examined. Two cables are connected to the two copper sheets at the two sides of the silicone mould, and one thermocouple wire is inserted into the mould, as shown in Figure 3.11(a). Another end of the cables and thermocouple wire is connected to the resistance meter and data logger to record the resistivity and temperature changes along the curing cycle (see Figure 3.11(b)), which is recorded by the LabView program (see section 3.3.1).

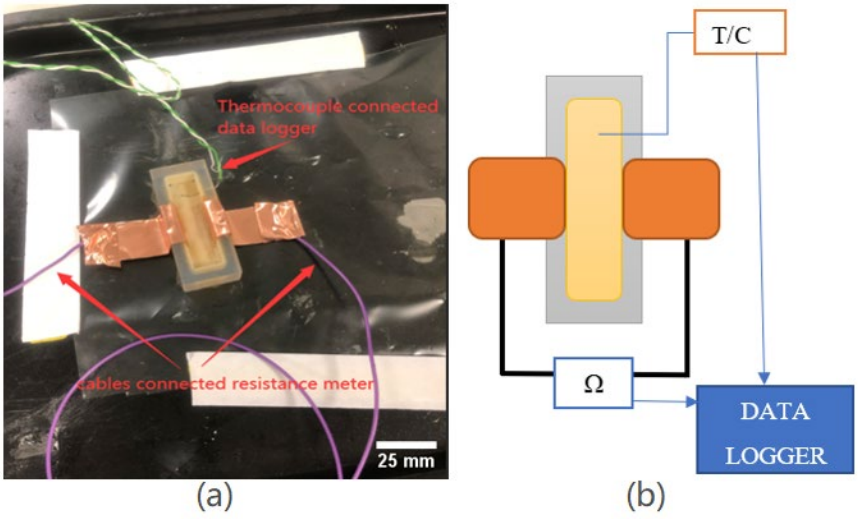

Figure 3.11 (a) The setup of temperature and resistance recording of sample in the oven (b) diagram of the set-up employed.

3.3.3 The influence of stirring temperature on resistance of carbon nanomaterial/IN2 resin composite

To determine the stability of carbon nanomaterials in IN2 and AT30S, the carbon nanomaterials are mixed with IN2 and AT30S in a glass beaker in an oil bath at three different temperatures (85, 115, and 130 ℃). Two thin copper cables are placed at opposite two sides of the beaker and held in place by clips. An overhead stirrer stirred the mixture at 900 rpm for 8 minutes, and the resistance was measured. The mixing is subsequently stopped, and the evolution of the resistance is monitored. The critical factor here is the stability of the resistance in the resin components, not the absolute value of the resistivity. Figure 3.12 shows the test setup. As neither the effective cross-sectional area of the wires nor the effect of the conductive path around the non-conductive stirrer can be determined, accurate resistivity values cannot be reported.

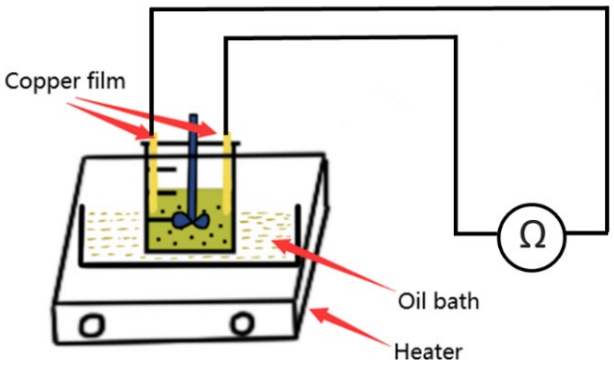

Figure 3.12 The setup of the stirring temperature influence test.

3.4 The prepreg of CFRP with different CB wt.%

This section includes two parts (matrix modification and hand layup for prepreg) to manufacture the prepreg of CFRP with different CB wt.%. The schematic of the manufacturing process is shown in Figure 3.13.

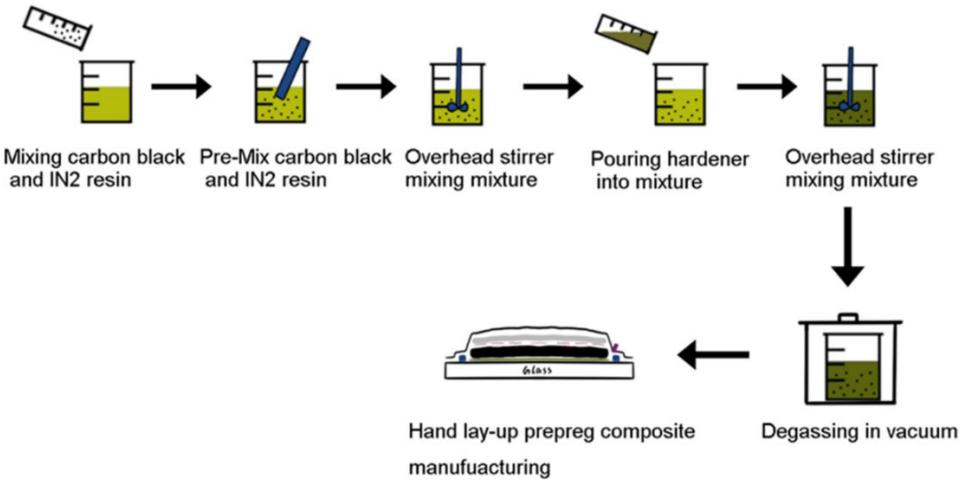

Figure 3.13 The schematic of matrix modification and prepreg manufacturing process

3.4.1 Matrix modification

The 100g IN2 resin was mixed with 0,1,2,3 wt.% CB in epoxy matrix. First, a wooden stirrer was used to combine 100g IN2 resin and CB in a disposable plastic beaker for 30 seconds to avoid aerosolizing the CB and wetting out the particles. The CB/IN2 resin mixture was mixed by an overhead stirrer ("Hei-TORQUE Value 100" (Heidolph Instruments, Germany)) at 900 rpm for 10 minutes. Then 30g AT30S (30% of the IN2

resin) was added to the mixture and mixed for 3 minutes at the same speed with the overhead stirrer. Before the hand layup operation, this mixture was degassed under vacuum for about 30 minutes until no bubbles could be seen in the mixture.

3.4.2 Prepreg manufacturing

Hand layup was used to manufacture the composite “prepreg”. Compared with infusion, hand layup has clear advantages, such as a simple process and low infrastructural requirements. However, hand layup suffers from poor repeatability in terms of fibre volume fraction. Therefore, the sample was subjected to vacuum consolidation to improve repeatability in fibre-volume fraction. Resin infusion could have allowed the fibres to filter out the CB to some extent, which may cause the CB particles to spread out unevenly. In hand layup method, first, to avoid the laminate sticking, CR1 Easy-Lease Chemical Release Agent (Easy Composites Ltd, Stoke-on-Trent) was sprayed on the surface of the glass sheet. Then, one layer of carbon fibre (160×160 mm) was placed at the surface of the glass. A brush uniformly spread the prepared degassed CB/IN2/AT30S nanocomposite out on the surface of the carbon fibre. The last two steps were repeated until the required layers of carbon fibre were stacked (4 layers for tensile tests and 15 layers for bending tests) since the thickness requirement of the two tests is different. Finally, 170 x 170 mm release film and vacuum breather were placed on the top sample in order. A vacuum bag was used to cover the whole mould, and vacuum tape was used to seal it. A vacuum pump degassed the sample for about 15 hours (overnight) at room temperature and de-moulded it to collect the prepreg. The carbon fibre is 2x2 twill 3k carbon fibre cloth carbon. The DoC of “prepreg” is 62%, as measured by DSC (see section 3.16). Figure 3.14 shows the schematic of the hand layup setup.

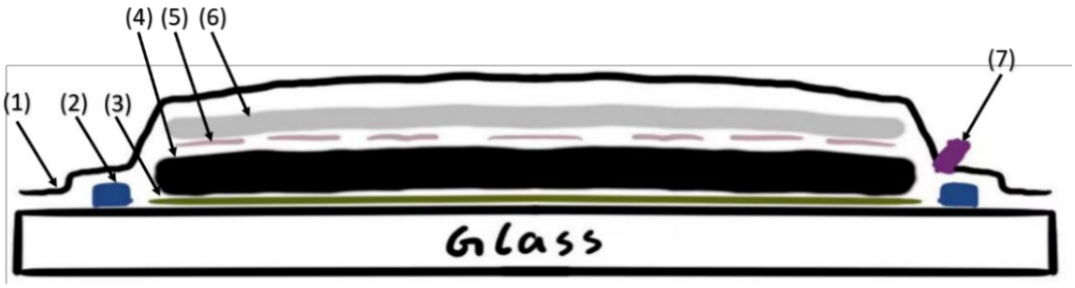

Figure 3.14 The schematic of the hand layup setup (1: vacuum bag, 2: vacuum tape, 3: release agent, 4: hand layup composite sample, 5: release film, 6: vacuum breather, 7: vacuum inlet)

3.5 The traditional manufacturing methods

In this section, three different traditional manufacturing methods (oven, autoclave, and heat press) were introduced to cure epoxy resin and CFRP samples.

3.5.1 Oven

The oven is UT 6200 (see Figure 3.15) from Thermo Fisher Scientific Inc. (Waltham, USA). This unit is ideal for laboratory, prototype, and industrial composite production, with a temperature range of up to 300 ℃. UT 6200 features an enhanced digital control system to ensure accuracy and reliability. The interior dimension of the oven is 50×65×55 cm (L×W×H).

Figure 3.15 The UT 6200 oven

When curing the epoxy resin and CFRP samples, the curing temperature and time are different according to the various requirements. The temperature increase rate is 3 ℃/min. When curing the CFRP samples, an external vacuum pump reduced the pressure in the bagged samples to consolidate them. As determined by the dial gauge, a pressure of -0.8 bar gauge, 0.2 bar absolute, was maintained throughout the heating cycle.

3.5.2 Autoclave

The autoclave used in this project is AC052 Autoclave (see Figure 3.16) from Premier Autoclaves Service and Solutions.

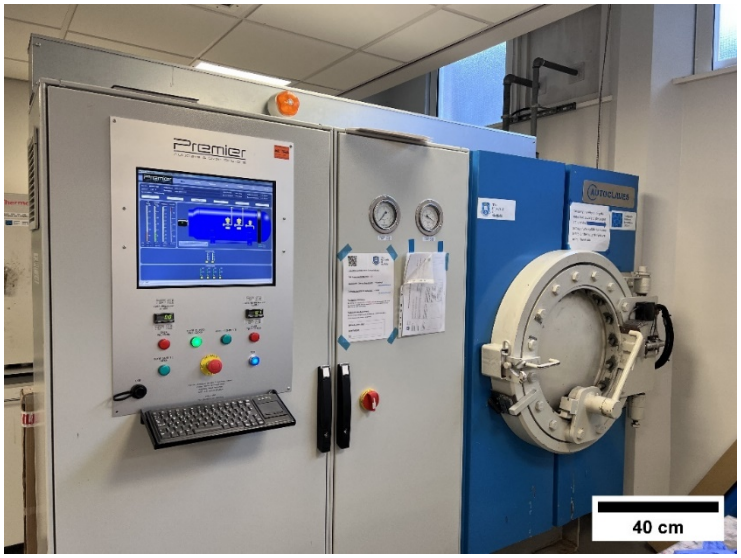

Figure 3.16 The AC052 Autoclave

According to the different requirements, the curing temperature and time for CFRP manufacturing are different. The temperature increase rate is 3 ℃/min. The pressure of the sample is 6 bar.

3.5.3 Heat press

The heat press used is Moore Hydraulic Heated Platen Press (George E Moore & Son Ltd, UK), which provides 20 tons maximum load. West 6100+ digital temperature controller (Gurnee, America) is the heat resource controller to heat the steel plates that contact the top and bottom surface of samples and heat them, which is shown in Figure 3.17.

Figure 3.17 The heat press

In this case, when curing CFRP samples, the pressure of the sample is 2.1 MPa to control the thickness to about 4mm. According to the requirements, the curing temperature and time are adjusted. The temperature ramp was 3 ℃/min.

3.6 Direct electrical curing (DEC) with different electrode contact

A PS1540S SMPS (Rapid Electronics, UK) (see Figure 3.18) provided electrical power to the DEC, which can provide a 15V maximum voltage and 40A maximum current. The voltage was manually adjusted to around 10-15V to maintain the sample temperature of 60-70 ℃. A hydraulic press (section 3.5.3) gives a 2.1 MPa pressure to samples by compressing to increase the carbon fibre fraction and reduce the void rate of the sample.

Figure 3.18 The PS1540S SMPS

Four different configurations were tested to study the effect of contact arrangement on conductive resin DEC. Copper sheets were inserted to a depth of 1 cm to create contact with the samples, and then the electrode cables were connected to the copper sheets. Figure 3.19 illustrates the schematic of the various electrode contact arrangements, as well as the positive and negative electrodes of the power.

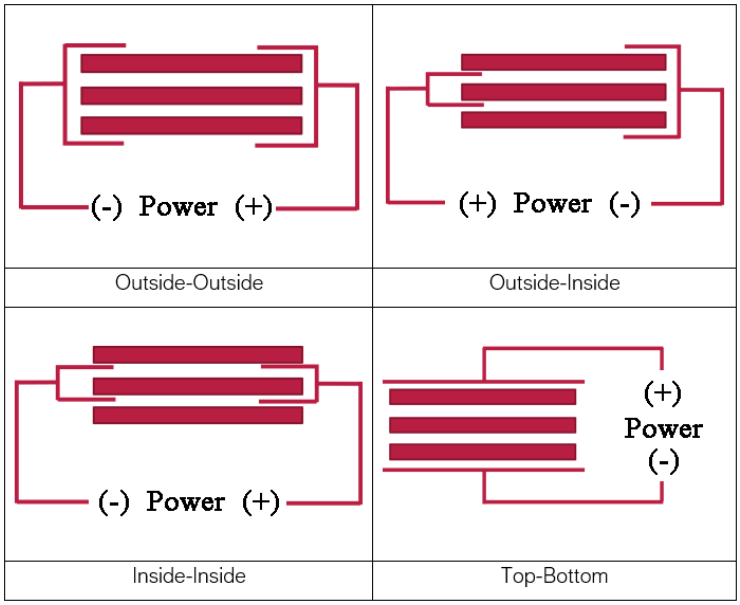

Figure 3.19 The schematic of different contact arrangements in DEC manufacturing (one thick red bar in the schematic is 5 layers of carbon fibre and conductive resin). The gaps between the layers are not present in the samples. They are shown to aid clarity in the positioning of the electrodes. The thin red lines are copper sheets and copper wires)

3.7 The resistance and temperature measurement methods for CFRP with 2 wt.% CB in the matrix during the DEC process

3.7.1 Resistance measurement during the DEC process

In the DEC process, the bench power supply PS1540S SMPS has a digital screen to show the voltage and current. According to Ohm's law, the resistance (R=U/I) of specimens can be calculated. Due to the low resistance, the resistance influence of copper sheets and cables is ignored in the calculation.

3.7.2 Temperature measurement during the DEC process

To study the temperature distribution during the DEC process in four different contact modes, there are 7 thermocouples (one is in the centre of the top surface, one is in the centre of the bottom surface, and five are in the middle layer) were used to record temperature change with time by USB TC-08 thermocouple data logger (Pico Technology, UK). The schematic is shown in Figure 3.20.

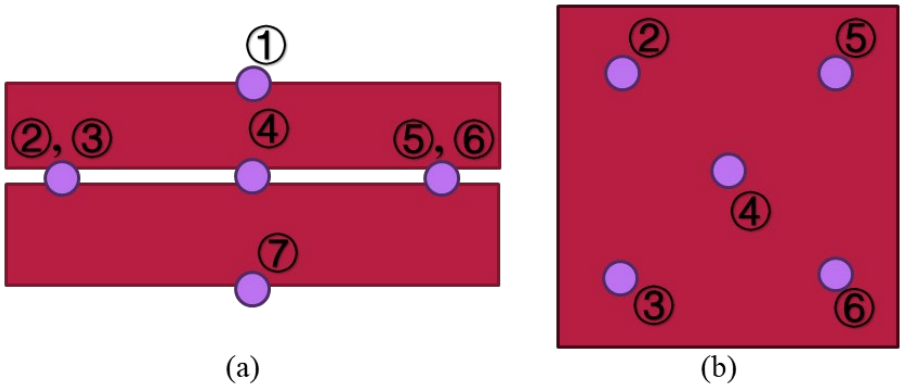

Figure 3.20 The schematic of thermocouples distribution in samples at (a) middle cross-section (b) middle layer (the thin and thick red bars are 7 layers and 8 layers laminate respectively, and purple circles are thermocouples (1-top centre, 2,3-left middle, 4-centre middle, 5,6-right middle, 7-bottom middle)).

3.8 Double-point incremental forming (DPIF) machine

3.8.1 Introduction

Dr. Victor M. Cedeno-Campos and Dr. Pablo A. Jaramillo created the CNC prototype and original control code. The CNC prototype was designed to control the movement and temperature of forming tools by a CNC machine and transfer heat energy to the sample by compressing. In theory, when forming tools that apply heat to a single point, heat

transfer causes the temperature of the surrounding area to rise, initiating the curing process. When the forming tools move to this area, the area is fully cured, or the DoC is very high. In addition, this CNC machine can manufacture different shapes of thermosetting material without a mould by adjusting the external pressure at various positions.

However, this CNC prototype has some drawbacks in this curing method. Due to the low heat conductivity of CFRPs in the through laminate direction, when heating the surface of CFRPs, the increasing temperature in the middle is far lower than that in surfaces which connect the heat resources. The exothermic curing polymerisation reaction in CFRP manufacture releases heat. As a result, the heat release on the surface of CFRPs will increase due to a high increase in the rate of temperature. This positive feedback process can lead to over-curing, degradation of the resin and even combustion in extreme cases. Meanwhile, due to a low increase rate of temperature in the middle area of samples, the DoC could be very low. Thus, curing was slow, and DoC control was difficult.

As a result, electrical curing is used in this project. According to the project requirement, the bench power supply, load cell, and thermocouple were added to the machine. In the new DPIF machine, there are some components (structural frame, CNC controller, communication, data acquisition, force control, temperature monitor, clamp, and power supplier). Figure 3.21 shows the components and structure of DPIF.

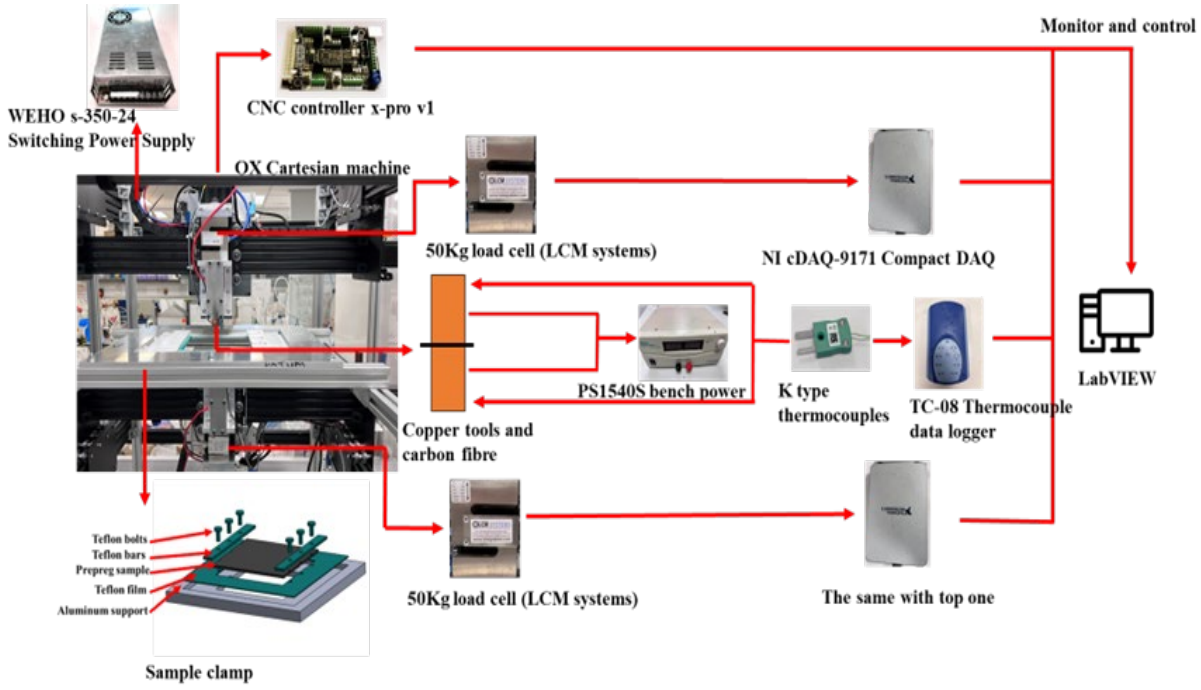

Figure 3.21 The component and structure of DPIF (the red arrows represent physical connections between elements)

3.8.2 Structural frame

The structure of movement tracks is made of aluminium extrusion with V slots, where the wheels can stand on the slot (see Figure 3.22). Compared with an electrical rail guide, it is actuated by mechanics, which makes it easy to operate and has low-cost advantages. All wheels are driven by three different-direction step motors, which are connected to a CNC controller. However, positional accuracy is sacrificed for speed of operation.

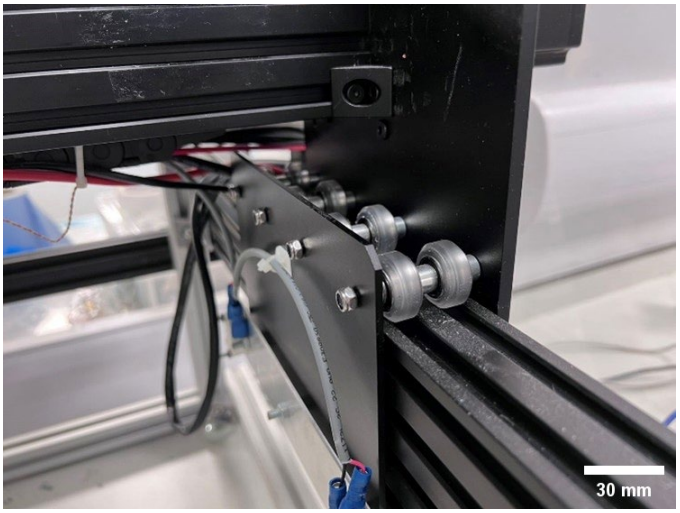

Figure 3.22 The wheels on a V slot frame

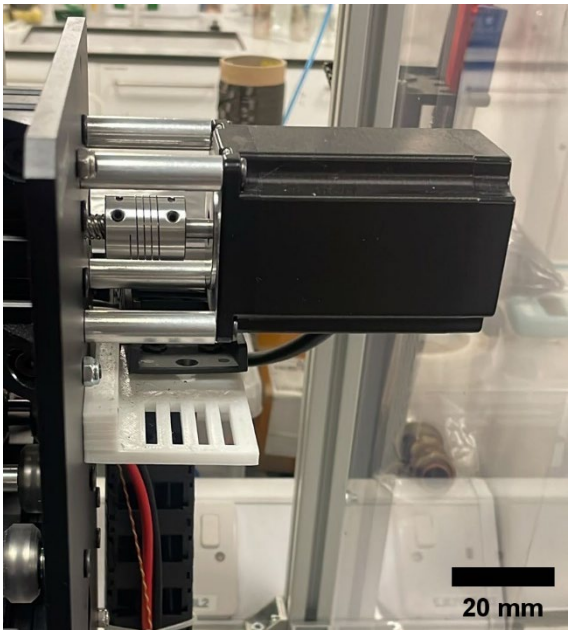

Figure 3.23 MT-2303HS280AW motor (MOTECH MOTOR CO., LTD., China)

3.8.3 CNC controller

The CNC control panel is the core component of the CNC machine. It controls all stepper motors, and each stepper motor derives movement in one direction. There are two kinds of controllers (open-loop and closed-loop controller), which are used to monitor the movement trajectory of motors. Compared with the closed-loop control panel, the open-loop control panel does not have a feedback function. But it has easy operation and low cost [255]. In this project, the controller is xPro V1. xPro V1 (see Figure 3.24) is a new open-loop GRBL-compatible all-in-one stepper driver board with 4 motor controllers for XYZ and 1 clone [256]. GRBL is an embedded, high-performance software designed to control the motion of machines that move, create, or both. In addition, G code can be interpreted by GRBL and generate motion control signals for the CNC machine [257]. As a result, in this project, the CNC motion is controlled by G code. The interaction between the software and the controller is facilitated via a USB port, which is accessible on any computer.

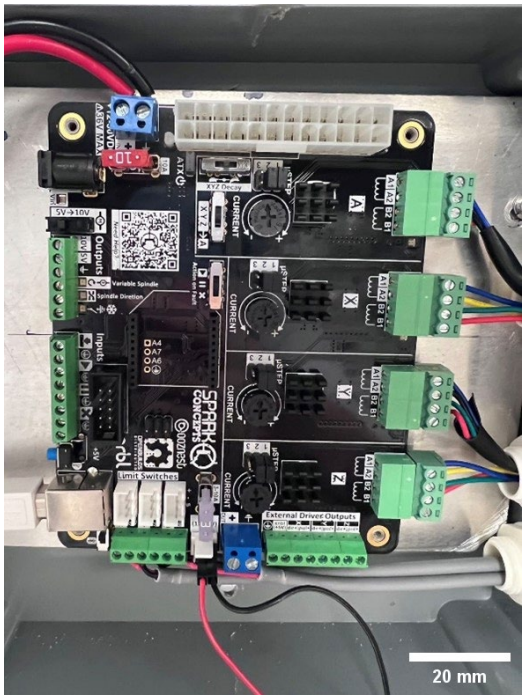

Figure 3.24 xPro V1 driver board

3.8.4 Communication-LabVIEW software

LabVIEW software was used to achieve the communication between the G code and the CNC controller. The G code can be sent to the CNC controller to be executed by LabVIEW serial communications functions (e.g., Visa Configure Serial port). For instance, when sending a G code ("G21 G91 G0X10") to the controller, the tool will move 10 mm on the X-axis. Figure 3.25 shows the generation of the command. It is only a simple command to show the working principle. The actual commands are more complicated than this one, which will be shown later. In this way, it is possible to control the machine to perform displacements and set different parameters, such as speed or the origin of the work coordinate system.

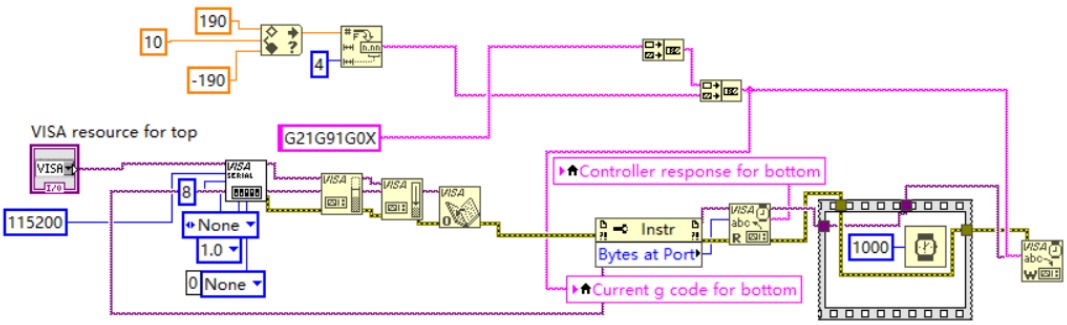

Figure 3.25 The G code command for 10mm movement in the x direction in LabVIEW

In this project, there are two modes (manual control and automatic control) in communication. Dr. Pablo A. Jaramillo provides the primary codes. According to the project requirements, the codes are modified.

- Manual control

In manual control, the speed and acceleration of tool movement and the original point of tools in the XYZ direction can be set. In addition, tools can move a specific distance in XYZ direction. The relative G code will be shown in the execution window when it is executed. The control panel can be seen in orange boxes in Figure 3.26. Figure 3.28 shows the block diagram of manual control for the top tool. The bottom tool uses the same block diagram.

- Automatic control

In the Automatic control, the movement path of tools (G code) can be created as a txt file when the txt file is imported into LabVIEW. The tools will automatically move according to the movement path provided by the txt file. Considering the importance of pressure and cure time in the curing process, this project added the load monitor and feedback in the system, which is discussed in section 3.8.6. After tools move to a specific position in the XY plane, the tops will move in the Z direction to compress the sample until the target load is reached and keep it for a specific duration. Then, the tools will move in the Z direction to release pressure and move in the XY plane to the next point. Figure 3.27 shows the front panel of automatic control. The XY graph can monitor the movement path of tools in the XY plane. Due to the complexity of the block diagram of this automatic process, it is not shown.

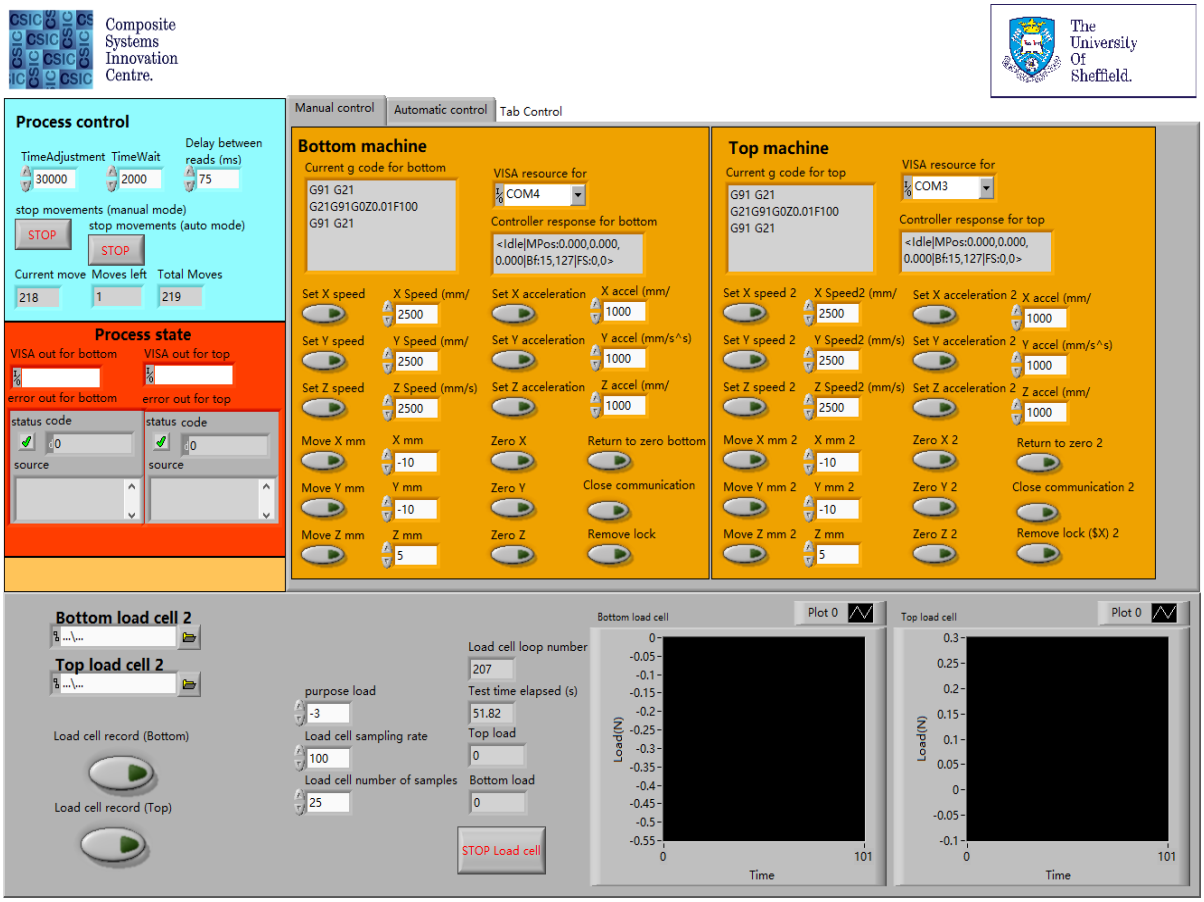

Figure 3.26 The front panel of the manual control in LabVIEW

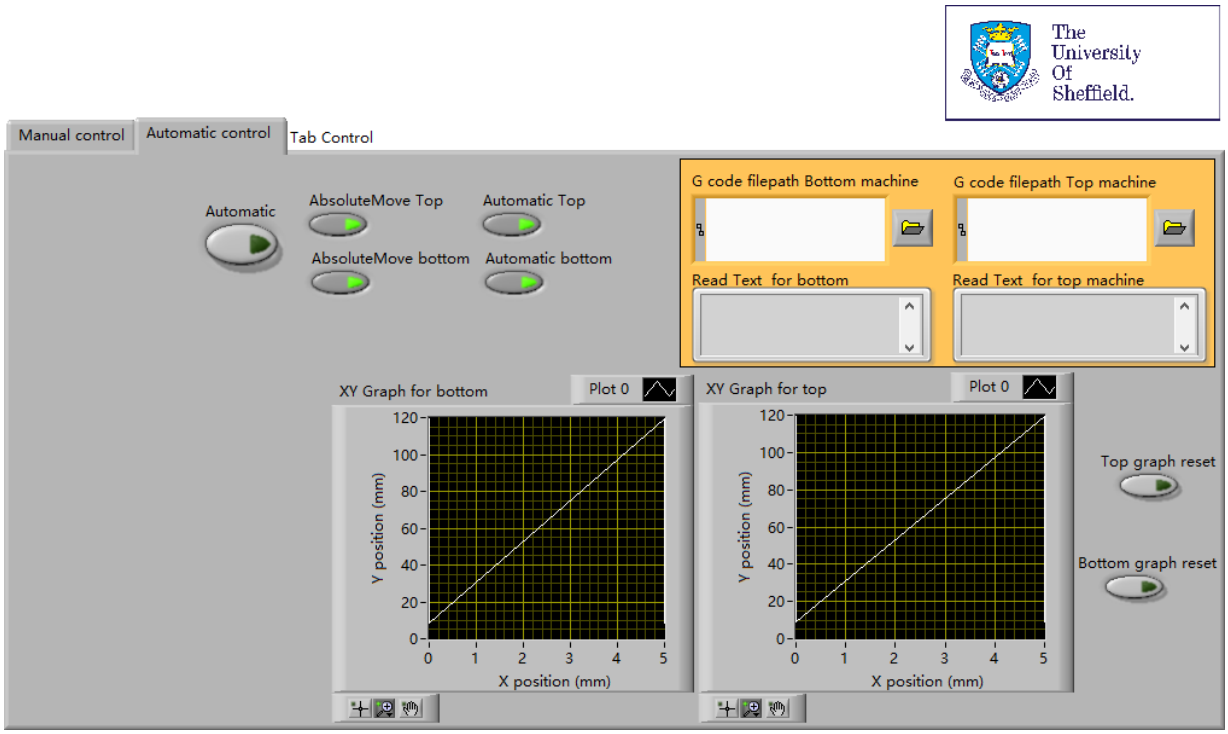

Figure 3.27 The front panel of the automatic control in LabVIEW

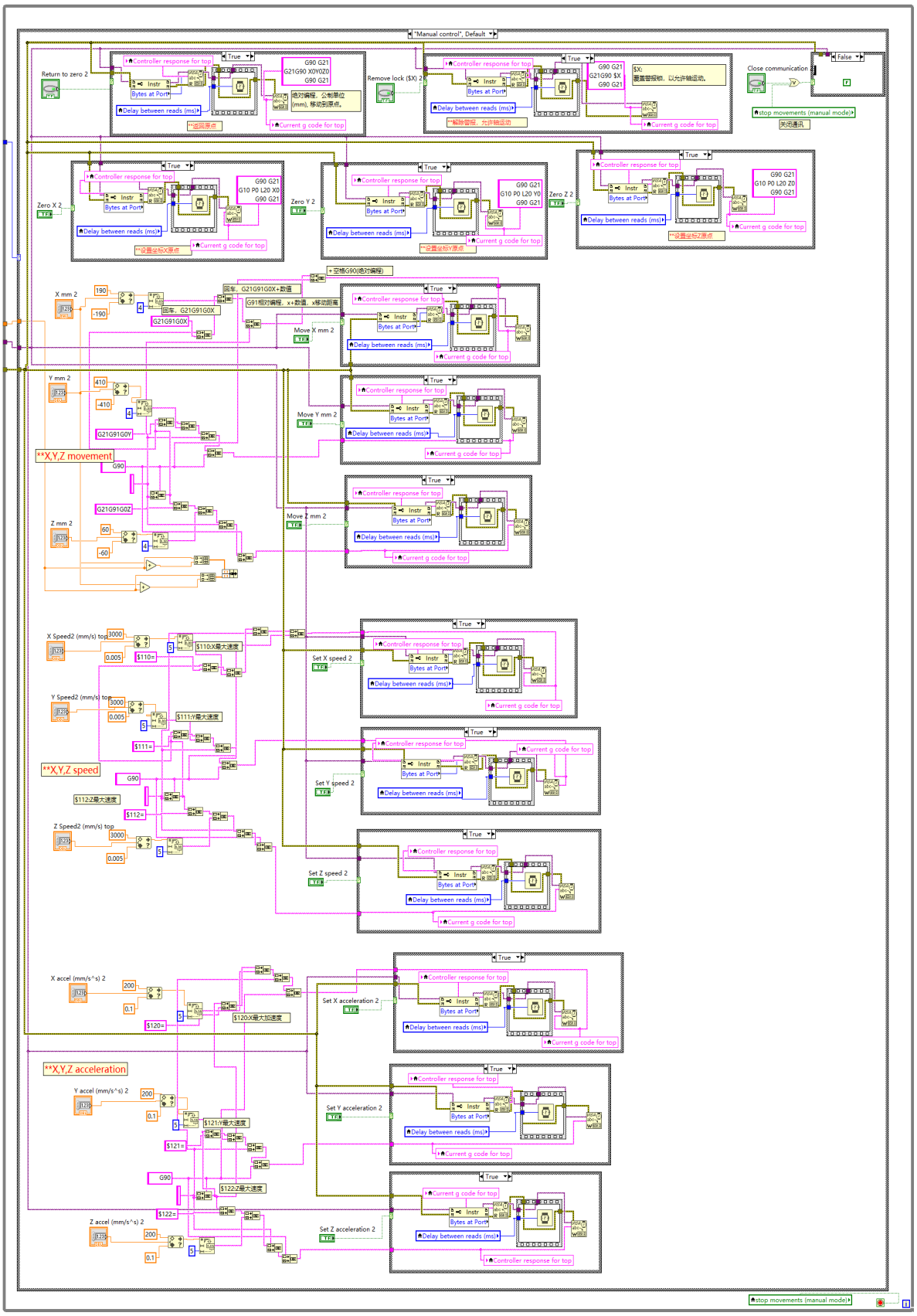

Figure 3.28 The block diagram of manual control for the top tool (it is the same for the bottom tool) in LabVIEW.

3.8.5 Data acquisition

Generally, a data acquisition system has a sensor, data acquisition hardware, and a PC with relative application software. A sensor is a device that converts physical changes like temperature and load to measurable analogue signals. However, these signals cannot be read by a PC. Therefore, data acquisition is used as the bridge between the PC and the sensors. It can convert analogue signals to digital signals that the PC can recognize. Finally, these signals are analysed by application software to visualize and store measurement data [258]. In this project, two data acquisition systems (load and temperature) were used, which are discussed in section 3.8.6 and section 3.8.7, respectively.

3.8.6 Force control

Generally, the load data acquisition needs a combination of hardware and software, which includes a load cell, signal conditioning to amplify the signal, and a data acquisition device to measure and digitalize the signal. Commonly, data acquisition devices integrate both signal conditioning and data acquisition into a single hardware unit. National Instruments offers readily accessible and user-friendly DAQs specifically designed for force-sensing applications [259].

In this project, a 50Kg STA-4 (LCM systems, UK) was connected to the copper tool to monitor the pressure value of the copper tool. This load cell is based on a piezoelectric sensor, which will generate a proportional voltage when it is deformed under an external load. Compared with traditional sensors, it has higher accuracy, a wider frequency range, and a wider measurement range for the load. In addition, Piezoelectric sensors are more durable than traditional sensors. They can withstand significant impacts and extreme temperatures and operate in different environments [260]. However, the electrical charge generated from the sensor is small, which makes it difficult to measure. As a result, the signal should be amplified before being collected. NI cDAQ-9171 is a compact data acquisition which can amplify and collect signals from the sensor. LabVIEW is used to record data from DAQ.

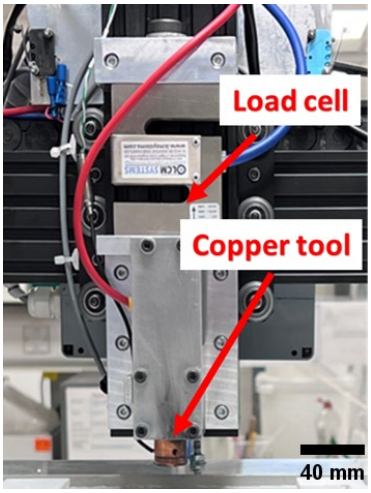

Figure 3.29 The copper tool connected with a 50 Kg STA-4 load cell.

3.8.7 Temperature monitor

Two K-type thermocouples were inserted into the top and bottom of the copper tools (see Figure 3.30) to avoid high temperatures of the copper tools and the sample burning. The basic principle of K-type thermocouple temperature measurement is that two conductors of different compositions form a closed loop. When there is a temperature gradient across the circuit, current will flow through the loop. According to the relationship function between thermoelectric electromotive force and temperature, the temperature can be determined[261]. To avoid shorting when the electrical current is applied, the exposed part of the thermocouples is generally covered by heat shrink tubing to get insulation.

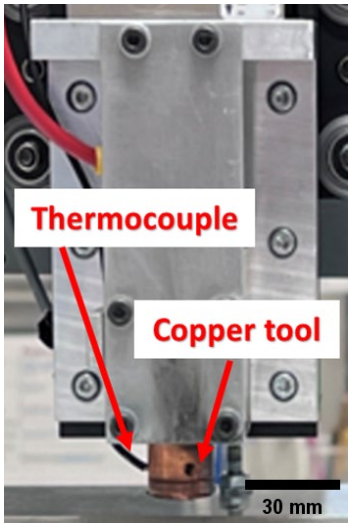

Figure 3.30 The top copper tool is inserted with a K-type thermocouple (the structure is the same as the bottom copper tool). The black cable is the thermocouple covered by heat shrink tubing.

The ends of thermocouples are connected to the TC-08 Thermocouple data logger (Pico Technology, UK), which can connect up to 8 thermocouples at the same time. The data logger connects a PC, and data are collected by the LabVIEW program (see Figure 3.31). In this program, the temperatures of 8 thermocouples can be monitored and recorded at the same time. In addition, based on the Arrhenius equation and n-th order curing reaction equation, this program can calculate the DoC and heat flux change depending on temperature and time. It can help monitor the DoC changes of the sample during the curing process. The establishment of the Arrhenius equation and n-th order curing reaction equation is discussed in section 3.11.

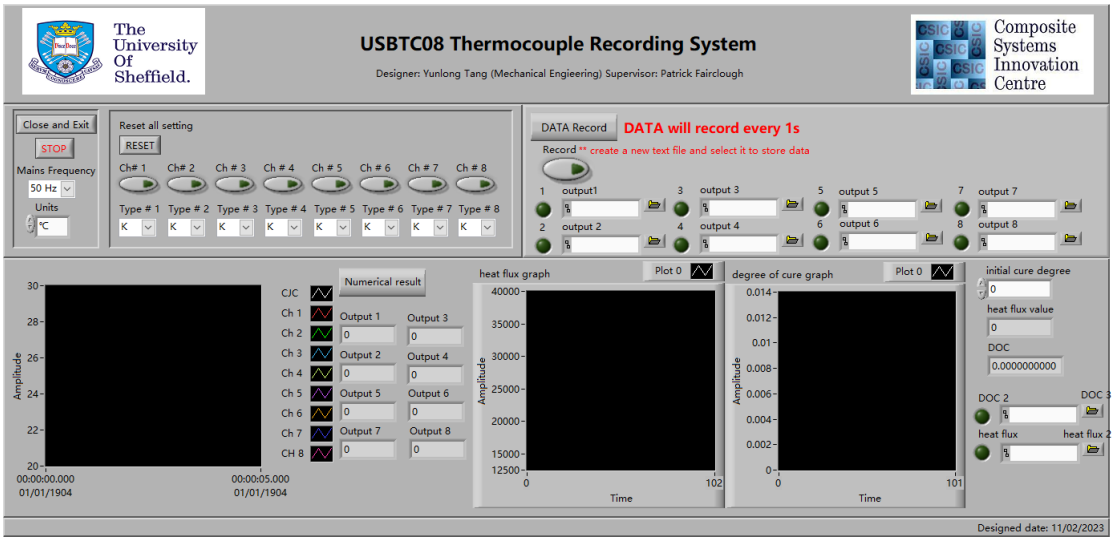

Figure 3.31 The front panel of the temperature monitoring program in LabVIEW

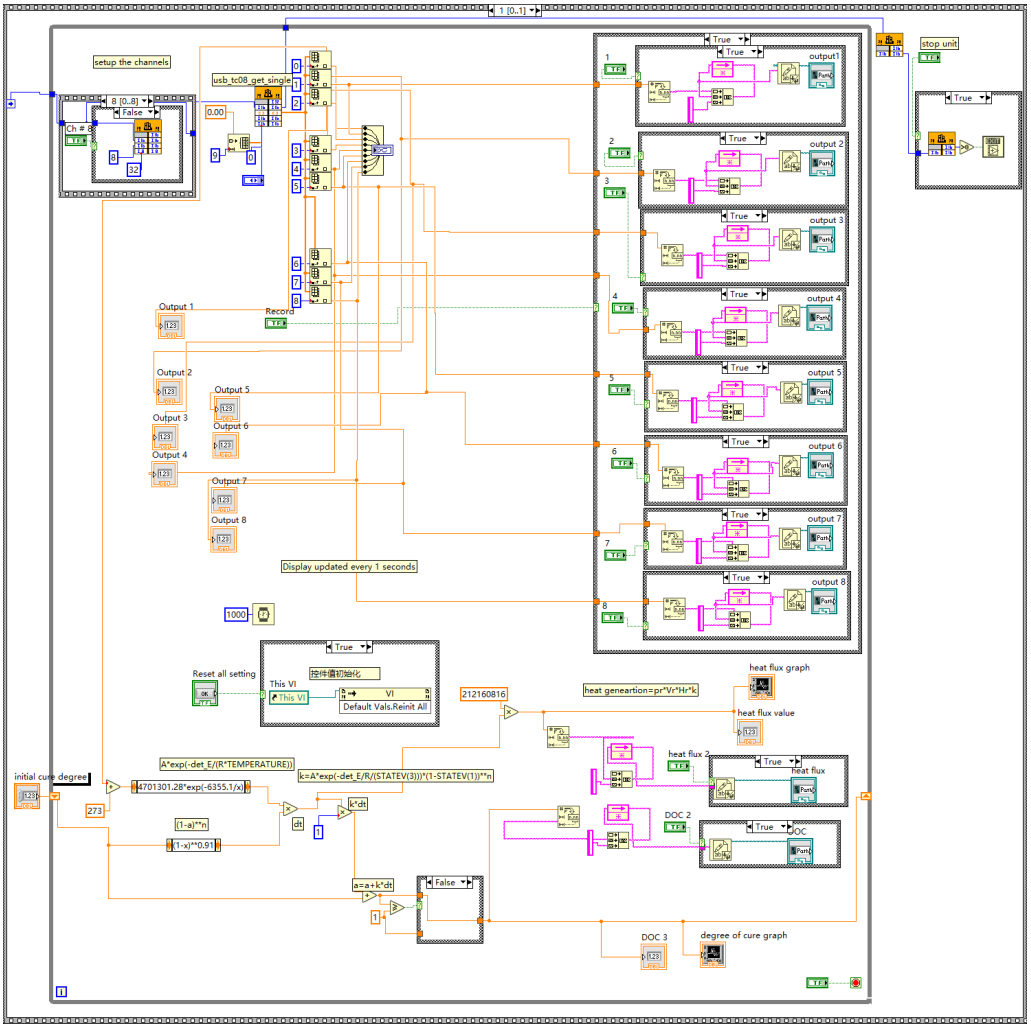

Figure 3.32 The block diagram of the temperature monitoring program in LabVIEW

3.8.8 Clamp

Thermosetting materials manufacturing systems ensure the laminate conforms to the mould using different methods. Autoclave and RTM manufacturing methods use a double mould, and VARTM uses a single mould, which constrains the laminate's freedom.

In this project, no mould was used. The left and right sides of the laminate are clamped to confirm there is no extreme deformation during the manufacturing process. In addition, the curing method used in this project is electrical curing. To avoid conductivity, all clamp materials contacting the laminate are Teflon. The bottom of the laminate contacts a Teflon film. In terms of the top, the left and right sides are fixed by Teflon bars and bolts. The laminate is supported by a steel support, which is under the Teflon film. Figure 3.33 shows the structure of the clamp.

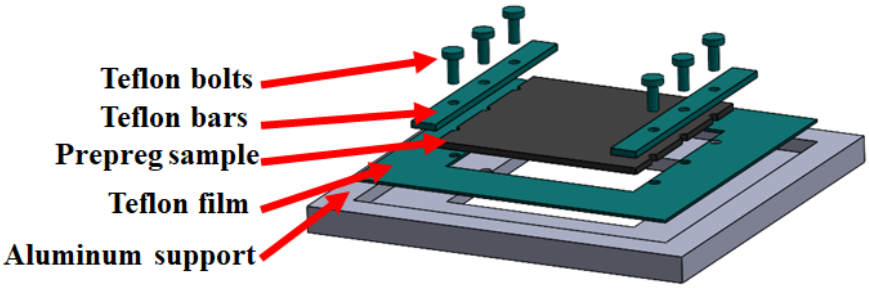

Figure 3.33 The structure of the clamp

3.8.9 Power supply

The core of the DPIF manufacturing method is electrical curing. A PS1540S SMPS power supply (Rapid, UK) is used to provide electrical power, which has a high-power switch mode power supply housed in a lightweight and compact enclosure with digital LED displays for voltage and current readings. It can provide 15V, 40A, and 600w maximum power.

In this project, the top tool and bottom are connected to the positive and negative electrodes of the power supply by red cables. There is no communication function in the power supply. According to the temperature changes, the power is manually adjusted by a knob. Figure 3.34 shows the structure of it.

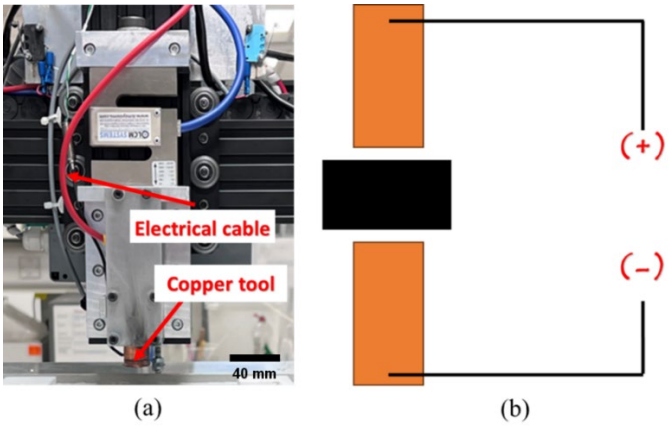

Figure 3.34 (a) The top copper tool is connected to an electrical cable, and (b) the schematic of the connection between the sample, tools, and power supply.

3.9 DPIF manufacturing

3.9.1 The manufacturing process of DPIF

Section 3.8 discussed the working principle of the DPIF machine (CNC machine). In this section, the manufacturing process of DPIF is discussed. The samples of 15 layers or 5 layers of carbon fibre samples are used to examine flexural properties or tensile properties, respectively. First, 160×160 mm “prepreg” with 2 wt.% CB in the matrix is prepared by hand layup, which has been discussed in section 3.4. The prepreg is fixed by the clamp (see section 3.8.8). Then, according to the previously imported G codes, the tools move in the XY plane. The interval between two adjacent points is 10mm, which is the radius of the tool. The movement path of tools is shown in Figure 3.35.

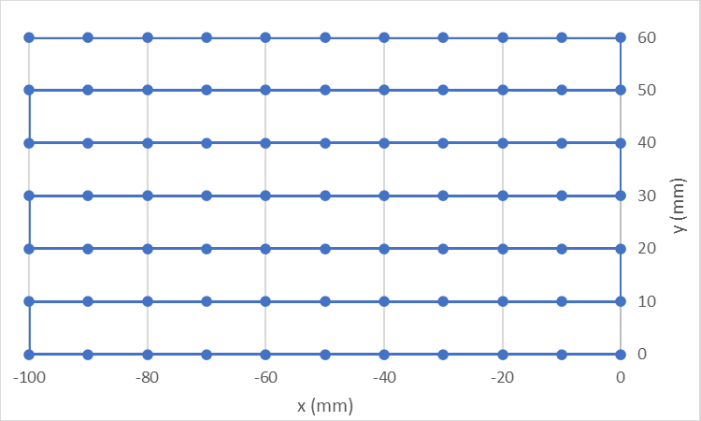

Figure 3.35 The movement path of tools

When tools move to one point, the tools will start to move in the Z direction to compress the sample until the load is over 160N. Then, the bench power provided a 6-7A current for 90 seconds to cure the sample by Joule heat. If the current is too high, the temperature of copper tools will rapidly increase and be over 1000 ℃. The samples will be burned in a few seconds. The top tool temperature rises rapidly and is held at around 80 ℃ during this process. After 90 seconds, the tools move away from the sample in the z direction, the pressure is released, and the tools move to the next cure point.

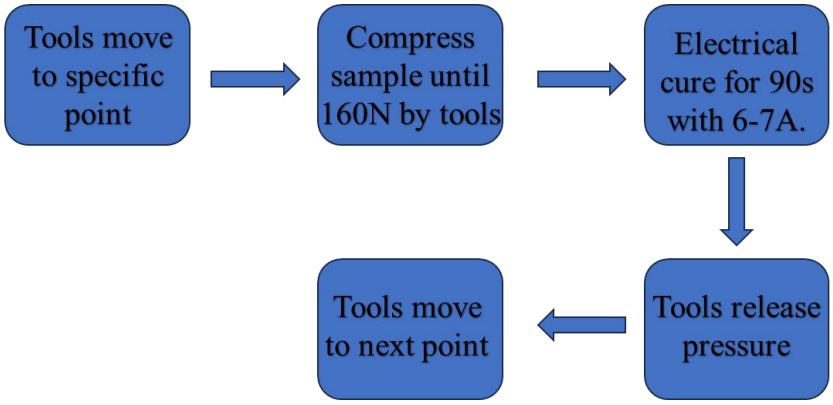

Figure 3.36 The manufacturing process of DPIF

3.9.2 Temperature monitoring during the DPIF process

Two different methods were used, K-type thermocouples and a thermal imaging camera, to monitor the temperature of the sample during the DPIF process.

- K-type thermocouples

The K-type thermocouples connect a Pico USB TC-08 Thermocouple Data Logger, whose data was collected by the LabView program, which has been discussed in section 3.8.7. There are three thermocouples placed at the top, middle, and bottom positions of a fixed point in the sample. This point is 30 mm away from the first curing point. As a result, the temperature changes at a single point can be recorded during the curing process. In addition, two thermocouples were inserted into the top and bottom copper tools to monitor tool temperature and avoid high temperatures and sample burning. Figure 3.37 shows the schematic of the thermocouple distribution.

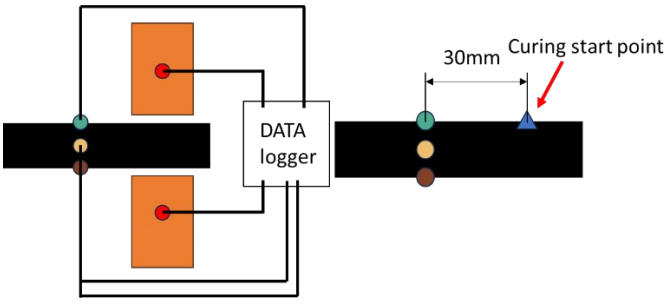

Figure 3.37 The schematic of the thermocouple distribution

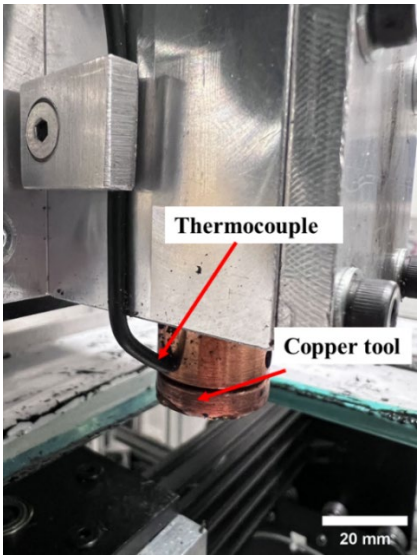

Figure 3.38 The copper tool and thermocouple (thermocouple is 10 mm away from the surface of the tool)

- Thermal imaging camera

The thermal imaging camera used in this project is an E4 thermal imaging camera from FLIR Ltd. (US), which can measure objective temperature from –20℃ to 250℃ with ±2℃. It was used to observe the temperature distribution in the sample surface during the curing process.

3.10 Numerical simulation by Abaqus

3.10.1 Introduction

Numerical simulations are calculations run on a computer that follows a procedure that implements a mathematical model of a physical system. The finite element method (FEM) is a common numerical simulation method. FEM is a general numerical method for solving partial differential equations (i.e. boundary value problems) in two or three spatial variables. To solve the above issues, finite elements subdivide large systems into smaller, simpler parts called finite elements. It is achieved by a specific spatial discretization (meshing) in the spatial dimensions, which is achieved by constructing a grid of objects: a numerical domain of solutions which has a finite number of points. The finite element method of boundary value problems culminates in a system of algebraic equations. This method approximates a function over the domain [262].

In this project, Abaqus conducted a numerical simulation to analyse the heat transfer of CFRP during the DPIF process. This section discussed how to build a finite element analysis (FEA) model.

3.10.2 The geometry of the FEA model

The geometry of the material (see Figure 3.39) is created by the "part" module. The dimension of it is 120×120×4mm (L×W×T). To set different cure points, the "partition face" function is used to separate the surface of the material into many circles with 20 mm diameter. The centre point distance between two adjacent circles is 10 mm.

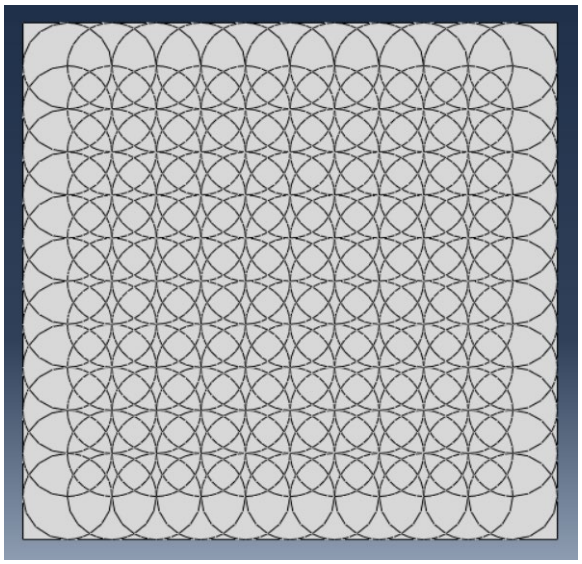

Figure 3.39 The geometry of material built by Abaqus.

3.10.3 The material properties

The properties of CFRP are shown in Table 3.2. The density data is from the physical properties section (see section 3.13). The thermal properties (heat capacity and thermal conductivity along the thickness (k_{33})) are data measured by LFA 467 Hyper Flash from NETZSCH (Selb, Germany), which is a laser flash analyser. The thermal conductivities along the fibre (k_{11} and k_{22}) are difficult to measure. As a result, this data was referred to in the literature [263]. The thermal conductivities across the fibre (k_{12} and k_{23}) are the conductivity of the resin [264].

Table 3.2 The properties of CFRP used in the numerical simulation. Values for k_{11} and k_{22} are taken from references [263], [264]

Properties	Density (kg/m³)	Thermal capacity (J/(kg·k)	Thermal conductivity (W/(m·K))
Value	1388	1440	k_{11} = 7 k_{22} = 7 k_{33} = 0.48

			k_{12} = 0.3 k_{13} = 0.3 k_{23} = 0.3

3.10.4 The boundary condition of material

To simulate the DPIF process, the boundary conditions are repeated in steps. The boundary condition refers to the experiment data. In terms of one step, the top and bottom surface temperature of a heating circle with a 20mm diameter, which is created in geometry, is from 45℃ to 160℃ in 90 seconds. Then, the heat resource moves along the specific moving path. The moving path of the heating circle (adding boundary condition) is the same as the moving path of tools in the DPIF process. The surrounding temperature is 20℃ with a 20W/(m^2·K) film coefficient.

3.11 The establishment of the curing reaction kinetic model

3.11.1 Introduction

The curing reaction dynamic model can be classified as the n-th order reaction model and the autocatalytic model. The n-th order reaction model is used in non-isothermal solidification kinetics study. However, in terms of the autocatalytic model, due to the several parameters required, it is used in isothermal solidification kinetic study. In this project, the n-th order reaction model (Equation 3.4) and the Arrhenius equation (Equation 3.5) are used to discuss the CFRP manufacturing process.

$$\frac{d\alpha}{dt} = k \cdot (1-\alpha)^n \qquad \text{Equation 3.4}$$

$$k = A \cdot e^{\frac{E_a}{R \cdot T}} \qquad \text{Equation 3.5}$$

Where k is the rate constant; R is the gas constant [8.314 J/(mol K)]; T is the temperature in Kelvin; α is the degree of reaction; t *is* the time in seconds.

3.11.2 Kissinger equation

The Kissinger equation (Equation 3.6) was used to calculate the parameters of the Arrhenius equation [265]. When n is close to 1, the model more closely represents the data. In terms of a given DSC curve with the heating rate (β), the maximum reaction rate at the peak temperature (T_p) can be observed. A Kissinger plot can be obtained by plotting

the quantity of $ln(\beta/T_p^2)$ against $1/T_p$ for a set of DSC curves with different heating rates. In this project, there are four heating rates were used (10, 15, 20, and 25 ℃/min). The slope of the Kissinger plot can be used to determine A and Ea by slope and intercept of the fit line [266].

$$\ln\left(\frac{\beta}{{T_p}^2}\right) = \ln\left(\frac{A \cdot R}{E_a}\right) - \frac{E_a}{R \cdot T_p} \quad \text{Equation 3.6}$$

3.11.3 Crane equation

When Ea/n·R >> 2Tp, the Crane equation (Equation 3.7) can be simplified as Equation 3.8, and the n value can be calculated by the slope of the fit line in lnβ against ln(1/ Tp) plot [267].

$$\frac{d\,(\ln \beta)}{d({T_p}^{-1})} = -(\frac{E_a}{n \cdot R} + 2T_p) \quad \text{Equation 3.7}$$

$$\frac{d\,(\ln \beta)}{d({T_p}^{-1})} = -\frac{E_a}{n \cdot R} \quad \text{Equation 3.8}$$

3.12 Microstructure

To analyse the microstructure of carbon nanomaterials (CB) and carbon nanomaterial (CB)-modified CFRP, electron microscopes (SEM and TEM) were used. In addition, an Optical microscope was used to observe the distribution of carbon nanoparticles in carbon nanomaterial/IN2/AT30S composites. The images from the optical microscope were analysed using the fractal dimension method to evaluate the dispersion of carbon nanoparticles.

3.12.1 TEM

An R005 300kV C-FEG TEM/STEM (Figure 3.40) from JEOL Ltd. (Tokyo, Japan) is used, which is a type of transmission electron microscope (TEM). It has two aberration correctors and a cold field-emission gun (C-FEG) to achieve ultra-high resolution and better energy resolution. It can provide a spatial resolution of nearly 0.05nm (0.5Å) for analysing materials, as well as the ability to image and perform spectroscopy on single atoms [268].

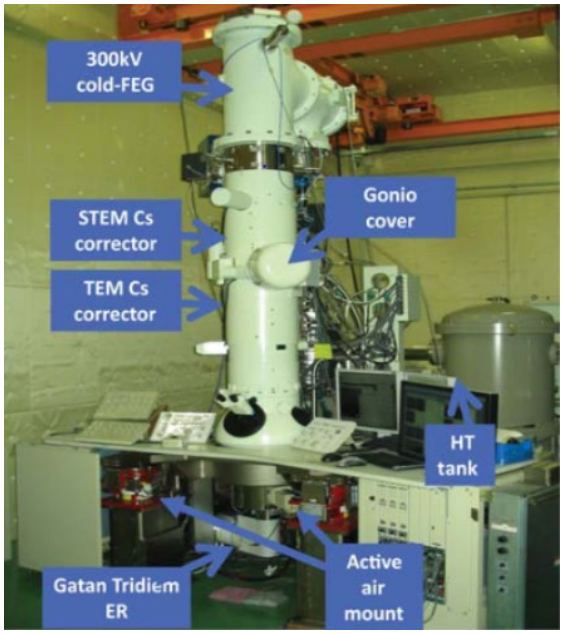

Figure 3.40 An R005 300kV C-FEG TEM/STEM [268]

The setting for analysing the microstructure of CB is shown below. A 300kV accelerating voltage, with a 35um condenser aperture, a spot 1 alpha 3 Gun, with settings of A1 at 2.9kV and A2 at 4.6kV, is employed. The sample is prepared by dispersing a few mg of powder in ethanol using a mortar and pestle. One drop of the resulting suspension is added to a 3mm diameter holey carbon support film. The solvent is allowed to dry at room temperature before insertion into the microscope.

3.12.2 SEM

An Inspect F FEG SEM from FEI company (Oregon, USA) is used to collect the SEM images. It is a stable platform for research needs, with an easy-to-use interface allowing for accurate and fast data collection. It can collect surface and compositional images, as well as perform fast elemental analysis to determine material properties and elemental composition [269].

Figure 3.41 An Inspect F FEG SEM [270]

The setting for analysing the microstructure of CB nanoparticles is shown below. The setting is a 2kV accelerating voltage, an aperture of 6 or 7 (smallest), giving a spot size of 2.5 (small). The sample is mounted by dry dispersion on a carbon adhesive pad and coated with 5nm of evaporated carbon (to ensure good electrical contact and reduce surface charging under the electron beam).

When analysing the microstructure of CB nanoparticle-filled CFRP, there are few operations for sample preparation. First, a Simplimet 1000 metallurgical mounting press (Buehler, USA) (see Figure 3.43)was used to mount CFRP. The hot mount compound used is conductive bakelite. The machine settings are shown below. The heating time is 2 minutes and 10 seconds. The cooling time is 4 minutes. The pressure is 290 bar. Finally, the cylinder samples (see Figure 3.42) with 32 mm diameter and 12 mm height were collected. Then, the surface of the sample was polished by an Automet 250 pro (Buehler, USA) (see Figure 3.43). The samples were polished with p400, p800 and p1200 grit paper for 1 minute, 27N external load and 150 rpm speed.

The sample was mounted by dry dispersion on a carbon adhesive pad and coated with 5 nm of evaporated carbon. This coating was applied to ensure good electrical contact and

reduce surface charging under the electron beam. The settings in the microscope were a 15 kV accelerating voltage, an aperture of 6 or 7 and a spot size of 3.

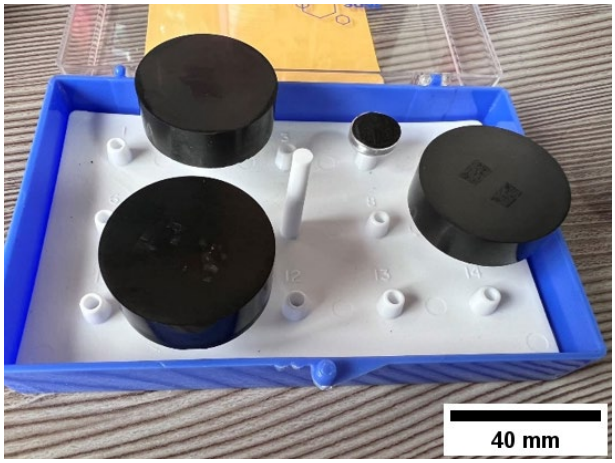

Figure 3.42 SEM samples

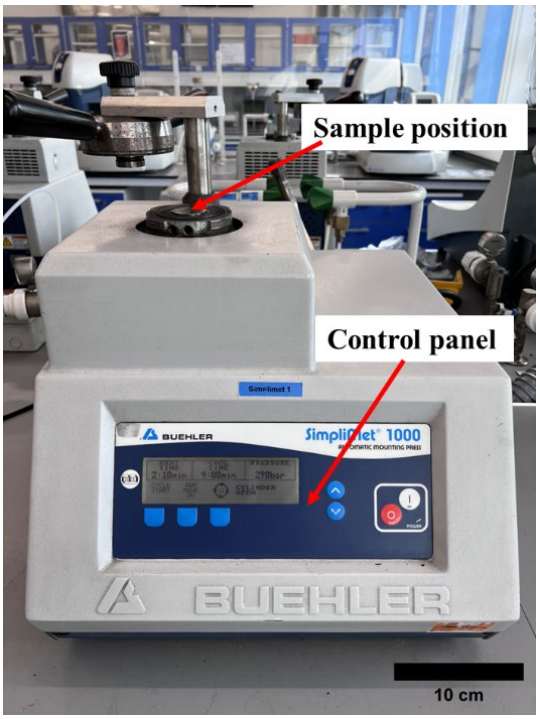

Figure 3.43 A Simplimet 1000 metallurgical mounting press

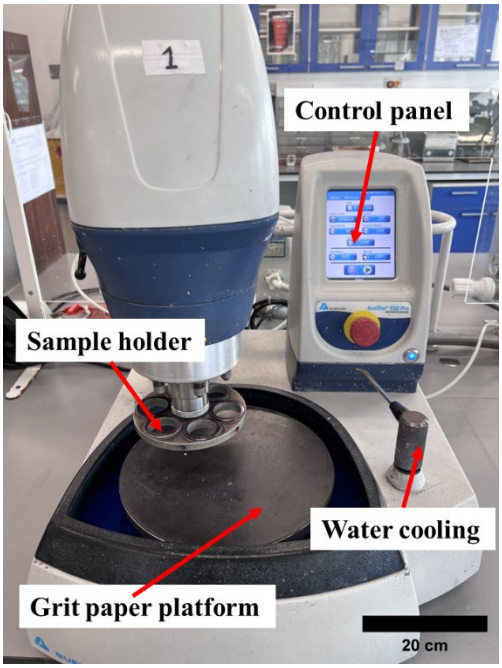

Figure 3.44 A Automet 250 pro

3.12.3 Optical microscope

A thin layer of sample is placed on a glass slide. An Olympus BX50 microscope (Olympus, Japan) with 10x magnitude is used to observe the structure of carbon nanomaterial/IN2/AT30S composites.

3.12.4 Fractal dimension method

This analysis is performed as the distribution of carbon nanoparticles in the epoxy resin could be considered a multiscale fractal system. Approximately nanoscale particles connect, forming fractal assemblies. These assemblies form aggregates which create conductive networks [271]. As a result, the fractal dimension value is used to assess the dispersion of carbon nanoparticles in epoxy resin. In addition, some researchers have used fractal dimension methods to analyse the dispersion of nanoparticles [180]–[182].

In these optical microscope images, the light area is epoxy resin rich, and the dark area is carbon nanoparticle rich. A differential box-counting method is used to calculate the fractal dimension, described below. Optical microscope images (1024×1024 pixels) are rescaled to 256 greyscale thresholds. A 3D space is created with x and y representing the position in space and z representing the grey scale value (0-255) of the corresponding (x,y) point. The images were separated into smaller grids, with the length (r) of each grid box being 2^n ($1 \leq n \leq 10$; thus x = y = 2 to 1024) pixels. As a result, there are ten images

with different grid box sizes. In each of these ten images, the maximum difference of grey value (n_r) in each grid box is calculated (see Equation 3.9).

$$n_r = \frac{max - min}{r} \quad \text{Equation 3.9}$$

Where n_r is the maximum grey value difference, max is the maximum grey value, min is the minimum grey value, and r is the size of the box.

For the smallest box size, the difference is high, and this reduces as the re-boxing averages out the contrast between the pixels.

In each image, the sum of the maximum difference grey value (n_r) or the total number of boxes is N_r. As a result, the box dimension value (D_r) under a specific grid scale can be calculated. Considering the influence of the pixel size of the image, the reciprocal of the box size is replaced by the image length (L) divided by box size, L/r (see Equation 3.10).

$$D_r = \frac{\lg N_r}{\lg \frac{L}{r}} \quad \text{Equation 3.10}$$

Finally, the least squares method was used to fit the box dimension value (D_r) under different grid scales and determine the image's fractal dimension (D).

The calculation of fractal dimension value was processed in MATLAB. The MATLAB codes are shown in Figure 3.45.

```
function fd=box_frac_dem(P);
% Difference box dimension
P=double(imread('C:\CB\CB3.5_033(before)_10x.png')); %the path of image
if size(P,1)~=size(P,2);  %M*N dimensional image, check whether M and N are equal
   error('The size of X must NxN.')
end
L=size(P,1);
if mod(log2(L),1)>0;
   error('The size of X must 2^n'); %The size of the image must be 2 raised to the Nth power
end
t=log2(L); %Assuming the image size is 256*256, then t =10
s=2.^(1:t); % s = 2,4,8,16,32,64,128,256,512,1024 Find the power of 2
Nr=zeros(1,t);
for k=1:t;
   d=s(k);   %Set grid side length
   h=L/d; % Let B instead of 256 for the size [2^nX2^n]
   for m=1:h;
       for n=1:h;
           A=P(d*(m-1)+[1:d],d*(n-1)+[1:d]);  %Divide into chunks and store to A
           mn=min(A(1:end));   %minimum grey value
           mx=max(A(1:end));  %maximum grey value
           nr=fix(mx/d)-fix(mn/d)+1;  %Integer process
           Nr(k)=Nr(k)+nr;
       end
   end
end
r=L./s;
a=log10(r)
b=log10(Nr)
plot(a,b)
p=polyfit(log10(r),log10(Nr),1); %least squares fitting
fd=p(1);
```

Figure 3.45 The MATLAB codes for fractal dimension value calculation

The experiment indicated that as the dispersion improves, the fractal dimension approaches 3, while high particle aggregation distributions provide values around 2. The process of the binarization of the microscope image and the calculation of fractal dimension is shown in Figure 3.46.

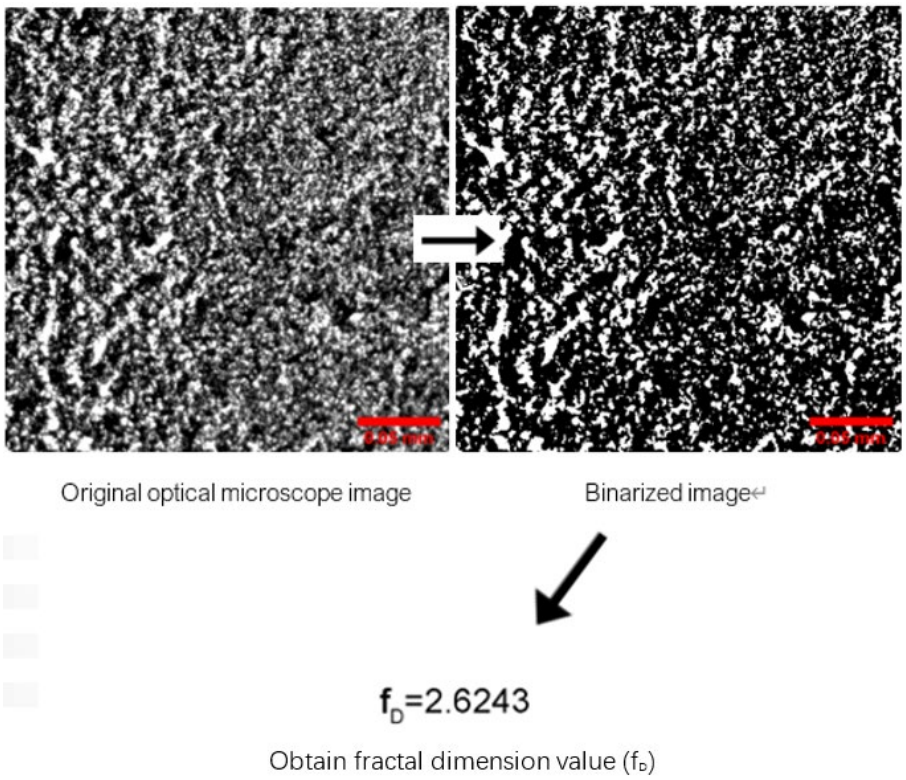

Figure 3.46 The fractal dimension analysis process when the CB is 3 wt.% (the scale bar in images is 0.05mm).

3.13 The physical properties of CFRP

Physical properties are significant and determine the performance of materials in many fields. In this project, AccuPyc II 1340 (Micromeritics Ltd, UK) (see Figure 3.48 (a)) is used to measure the density of laminates via helium pycnometry and the Archimedes principle. The pressure of purge fill and cycle fill is 19 psig (1.31 bar). The measurement of each sample is repeated five times at room temperature. Due to the high permeability of helium molecules, they rapidly fill pores as small as 0.1 nm in diameter. As a result, the calculated density can be regarded as particle density ($\rho_{particle}$). According to the density of laminate, carbon fibre, and matrix (the supplier provides the last two), the volume and mass fraction of fibre can be calculated.

Another density measurement device is density balance (see Figure 3.48 (b)), which measures the solid density by the sample weight in air and water. However, due to the surface tension of water, the water cannot fill the tiny pores in the sample. As a result, the

calculated density includes the volume of pores. The calculated density can be regarded as the bulk density of composites (ρ_{bulk}).

The void volume fraction can be figured out by bulk density and particle density as ($\Phi=1-(\rho_{bulk}/\rho_{particle})$). Because of technology limitations, when measuring the density and void, the voids in the sample that are not connected to air cannot be considered.

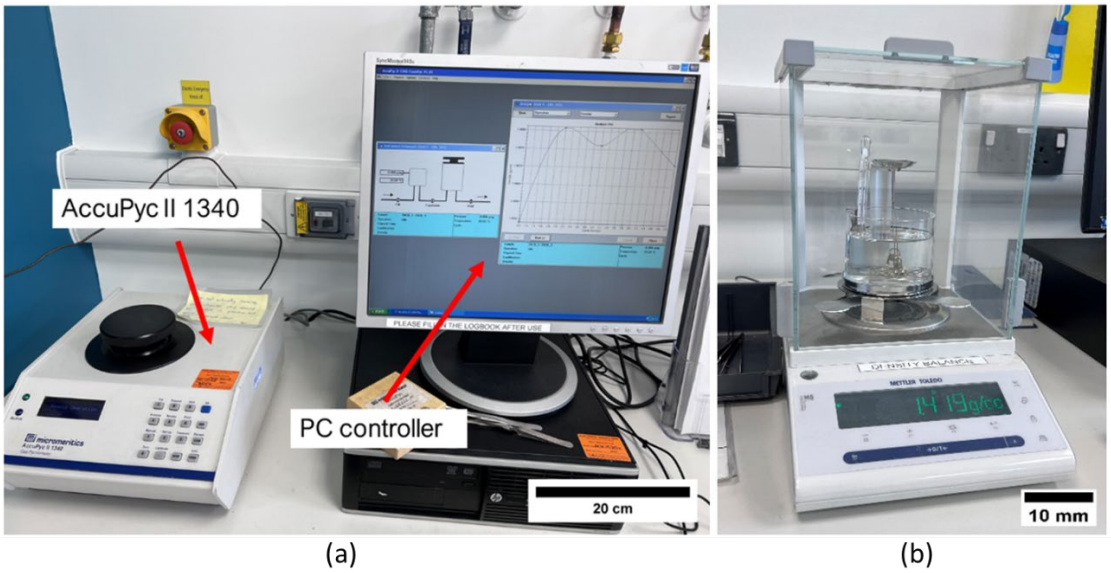

Figure 3.47 (a) AccuPyc II 1340 and (b) density balance

3.14 The mechanical properties

In this section, the mechanical properties are discussed, including the tensile test, compact tension test (CT), and four-point bending test. The test machine used is an H5KS and H25KS Benchtop Tester from Tinius Olsen (Horsham, USA), whose maximum load is 5 and 25 KN, respectively.

3.14.1 Tensile test

The tensile test is developed to analyse the influence of CB on tensile strength and Young's modulus of CB/IN2/AT30S composite and CB-modified CFRP.

3.14.1.1 Tensile test for CB/IN2/AT30S composite

The ASTM D638 standard determines the test specimen dimension and testing conditions. Samples with a gauge length of 57 mm, a width of 13 mm and a thickness of 3 mm are used. Silicone moulds are employed to prepare the tensile test samples. When preparing

the samples, CR1 Easy-Lease Chemical Release Agent (Easy Composite, UK) was coated, according to the suppliers' instructions, onto the surface of the silicone mould before pouring the mixture into the mould. Finally, samples with different CB wt.% are cured in the oven at 120 ℃ for 3 hours. Subsequently, 3 wt.% CB/IN2 resin samples are cured at oven temperatures of 70, 130, 150, and 170 ℃ for 3 hours.

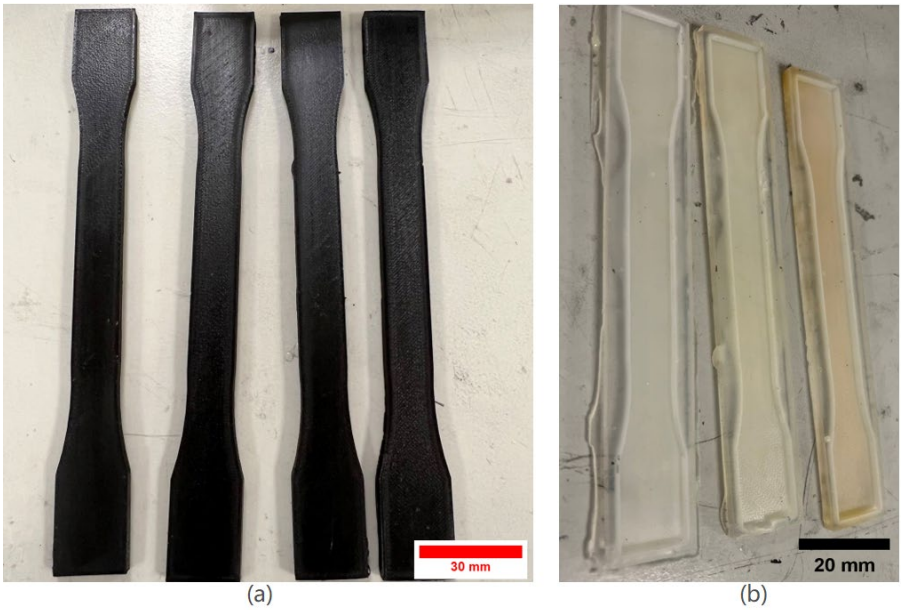

Figure 3.48 (a) The CB/IN2/AT30S composite tensile test samples (b) silicone moulds for the tensile test sample preparation

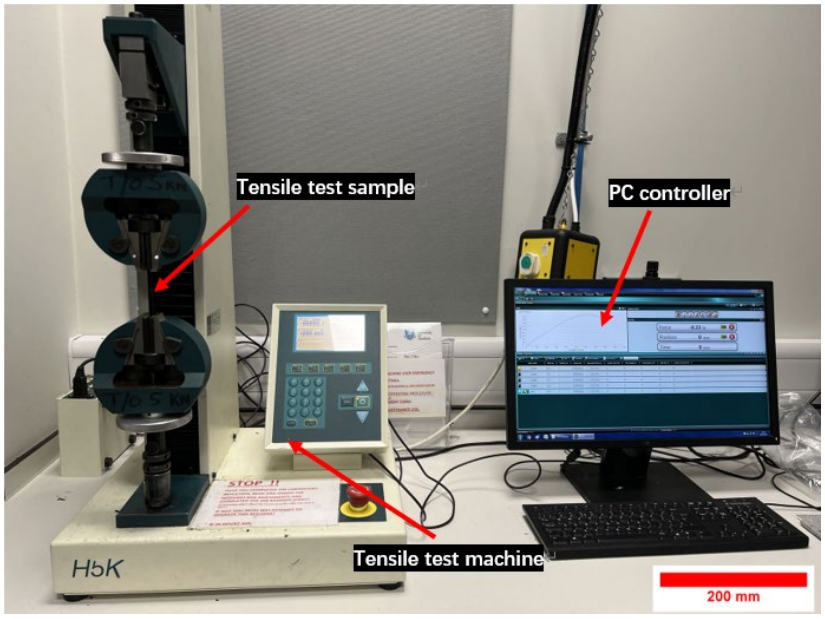

Figure 3.49 The tensile test of CB/IN2/AT30S composites

Following the ASTM D638 standard, samples are tested with a crosshead speed of 2 mm/minute in the tester. The setup of the tensile test is shown in Figure 3.49. The tensile strength and Young's modulus are calculated according to the standard.

3.14.1.2 Tensile test for CB-modified CFRP

When considering the influence of CB on the tensile properties of CFRP, the CFRP samples with 0 wt.%, 1 wt.%, 2 wt.%, and 3 wt.% CB in the matrix was examined. The test specimen dimension and testing conditions are determined by ASTM D30309 standard. The specimen dimension is 250×15×about 0.85 mm (L×W×T). In addition, when comparing the influence of DPIF and traditional manufacturing methods (oven and autoclave) on the tensile properties of CFRP, the CFRP sample with two 2 wt.% CB manufactured by different methods were examined with the same conditions. Due to the sample dimension limitation in DPIF, the specimen dimension is 150×15×≈1 mm (L×W×T). All specimens were trimmed from a large sample using a waterjet.

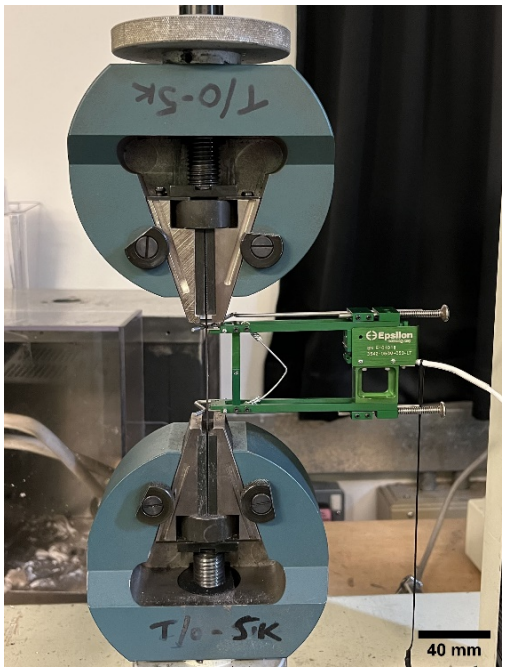

Figure 3.50 The tensile test for CFRP

Figure 3.50 shows the setup of the tensile test for CFRP. Axial Extensometer Model 3542 (Epsilon, Brackley UK) is used to measure the strain value of samples during the tensile test. Following the D30309 standard, the displacement rate is 2 mm/min in this case.

3.14.1.3 DIC camera

Digital imaging correlation (DIC) is an optical digital measurement technology that uses images from a digital camera to determine the shape, displacement, and deformation field of an object's surface under any load. It extracts the full-field information of the measured object from the digital image applied by the digital camera. From the shape of the object, its displacement and deformation, strain, velocity, and acceleration can be easily extracted [272].

In this project, a Pike F-505B/c (LIMESS Messtechnik, Germany) DIC camera (see Figure 3.51) is used, and it is equipped with a Sony Super HAD CCD sensor. At full resolution, it runs up to 15 fps. Higher frame rates can be reached by a smaller area of interest, AOI, binning (b/w), or sub-sampling [273]. The camera is connected to a PC, and the digital images are collected by Vic-Snap software. The collected images are analysed by Vic-2D software to collect the strain value in the y direction. The setting is 15 subsets and 7 steps. Finally, according to the strain and stress (data is from tensile test machine) graph, Young's modulus can be determined.

Figure 3.51 The Pike F-505B/c (LIMESS Messtechnik, Germany) DIC camera

3.14.1.4 The calculation of Young's modulus

Figure 3.52 shows an example of the stress-strain plot for CFRP. The red points show the initial tensile region and the plastic region. The black points show the elastic region. Young's modulus was calculated by a fit to the black points as drawn. The slope of fit is presented as Young's modulus.

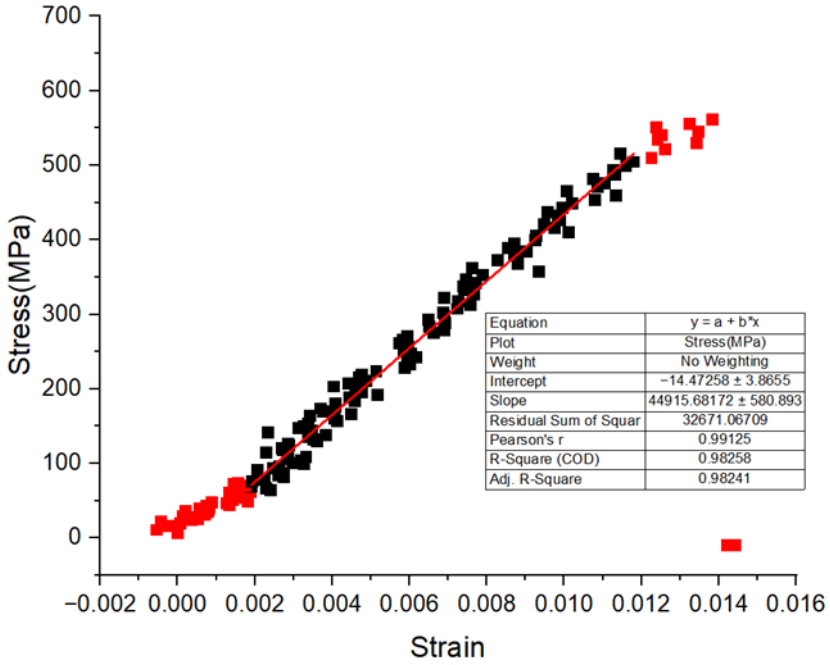

Figure 3.52 The strain and stress scattering plot of CFRP with 2wt.% CB in matrix from Origin.

3.14.2 Compact tension (CT) test

To analyse the effect of CB additives on the properties of the matrix (epoxy resin) and its contribution to the final composite performance, the fracture properties of the matrix alone were measured using a CT test. The IN2/AT30S epoxy resin with different CB wt.% was tested according to ASTM 5045. According to the literature [274], if the pre-crack line of CT samples is zigzag instead of straight, the test result will be unreliable. Therefore, a silicone mould was used to create the required shape. The dimensions of the CT samples and silicone mould are shown in Figure 3.53. The uncured CB/IN2/AT30S composite was poured into prepared CT silicone moulds and cured in the oven at 120 ℃ for 3 hours.

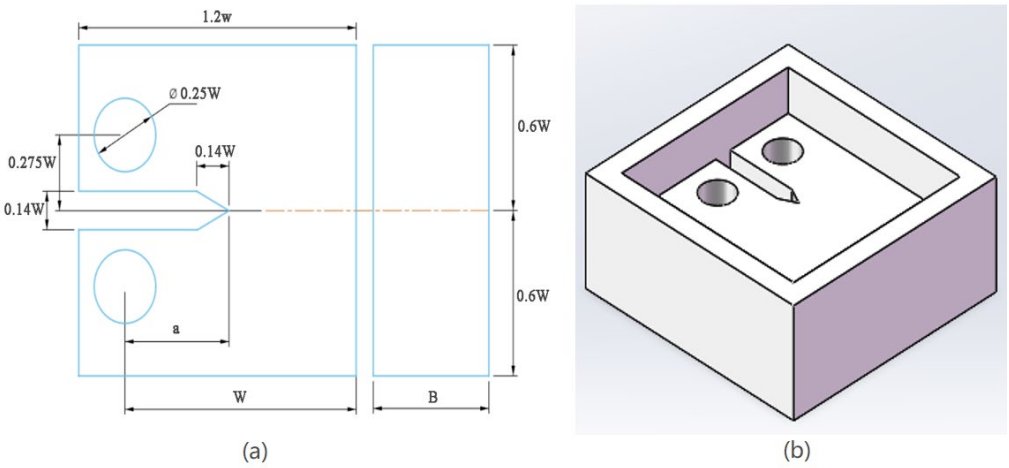

Figure 3.53 (a) The CT specimen dimension and (b) the silicone mould for CT specimen preparation drawn by SolidWorks.

Figure 3.54 The CT test for CB/IN2 resin composites

In this case, the plane-strain fracture toughness (K_{IC}) and the critical strain energy release rate (G_{IC}) were examined. According to the literature, in nanoparticle-modified epoxy resin, the K_{IC} and G_{IC} of the material are positively related to its tensile properties [275], [276]. The test was conducted using an H5KS Benchtop Tester from Tinius Olsen (Horsham, USA) with a 5KN load cell. The displacement rate was 1 mm/min. The setup of the CT test is shown in Figure 3.54.

3.14.3 Four-point bending test

The flexural properties of pristine CFRP and CB-modified CFRP with 1 wt.%, 2 wt.%, and 3 wt.% CB in the matrix is determined by four-point bending tests. In addition, when considering the influence of different manufacturing methods (heat press, autoclave, oven, DEC, and DPIF) on flexural properties of CFRP, CFRP with 2 wt.% CB was tested. ASTM D7264 Standard determines the test specimen dimension and testing conditions. The dimension of the specimens is 80×14×≈4 mm (L×W×T).

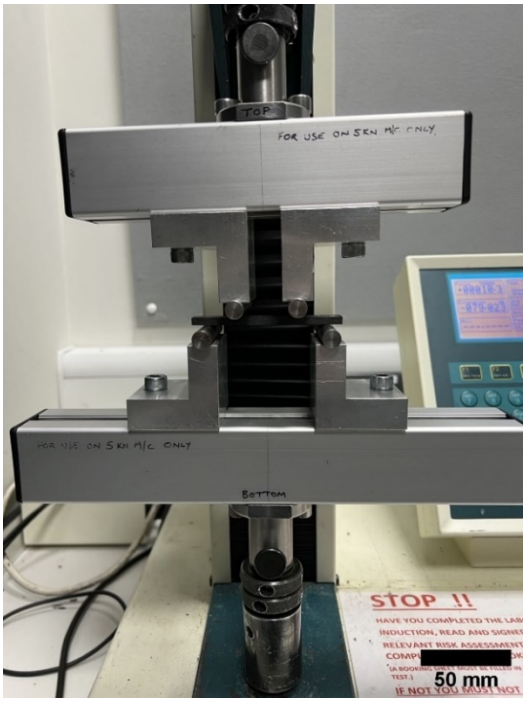

Figure 3.55 The four-point bending test for CFRP

Following the D7264 standard, the displacement rate is 1 mm/min in this case. The setup of the four-point bending test is shown in Figure 3.55. The flexural strength and flexural modulus of elasticity are calculated according to the standard.

3.15 The electrical properties

In this project, the influence of pressure and CB concentration on the electrical conductivity of CB-modified CFRP and the resistance values of CFRPs will be discussed, with 0, 1, 2, and 3 wt.% CB in the matrix under different pressures were examined.

The compression platform of an H5KS Benchtop Tester from Tinius Olsen (Horsham, USA) with a 5KN load cell is covered by insulation films. Two copper strips are placed on the surface of insulation tape and contacted with the positive probe and the negative probe of a BK Precision 2841 resistance meter (B&K Precision Corp., USA). The sample with about 1.4 cm^2 section area is placed between two copper sheets. When the tester machine compresses the sample, the resistance of the sample under different loads is recorded. When calculating the resistivity of CFRP, the thickness change during the pressing process is considered. Due to the low pressure (maximum pressure is 6 MPa), the samples are under an elastic zone during the compressing process, and there is no structural destruction in the samples. The setup of the electrical properties test is shown in Figure 3.56.

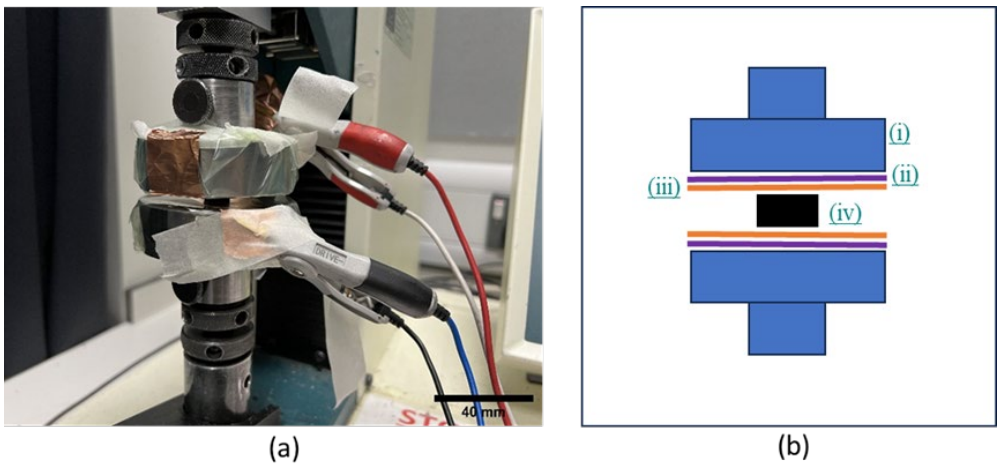

Figure 3.56 (a) The compression tests with H5KS Benchtop Tester. (b) Schematic diagram of the layout ((i) compression fixture, (ii) insulation, (iii) copper conducting plate, (iv) cured composite sample)

3.16 Differential scanning calorimetry (DSC)

A PerkinElmer DSC 4000 (PerkinElmer, USA) was used to determine the degree of cure (DoC). The cure profile of the pure resin was examined by DSC [277]. In terms of cured CFRP laminate, the samples were collected by waterjet cutting. The weight was around 10mg and followed the heating cycle from 40 ℃ to 250 ℃ with a 10 ℃/min ramp. In addition, to determine the heat produced for an uncured sample and to determine the Arrhenius equation of the resin, 7mg of uncured resin was examined. Here, the same

temperatures were used with four different heating rates: 10 ℃/min, 15 ℃/min, 20 ℃/min, and 25 ℃/min.

Figure 3.57 PerkinElmer DSC 4000

3.17 Energy consumption

In this project, novel manufacturing methods (DEC and DPIF) are compared with traditional manufacturing methods (oven, autoclave, and heat press) in terms of energy consumption. Plug-in Power Meter (Intertek, UK) was used to record the energy consumption during the curing process in the DEC, DPIF, heat press and oven. The energy consumption of the AC052 Autoclave is measured by RI-70-100-P, a 3-phase in-line power meter (Rayleigh Instruments, UK).

3.18 The thermal properties

LFA 467 Hyper Flash from NETZSCH (Selb, Germany) is a laser flash analyzer. It was utilized to examine the thermal properties (specific heat capacity and thermal conductivity) of CFRP with different CB wt.% in the matrix. CFRP samples are trimmed to 10*10*30 mm samples and placed in the laser flash analyzer. The thermal properties under 30, 50, 100, 150, 200, and 250 ℃ are examined. To avoid experimental error, the examination will be repeated 3 times at each temperature.

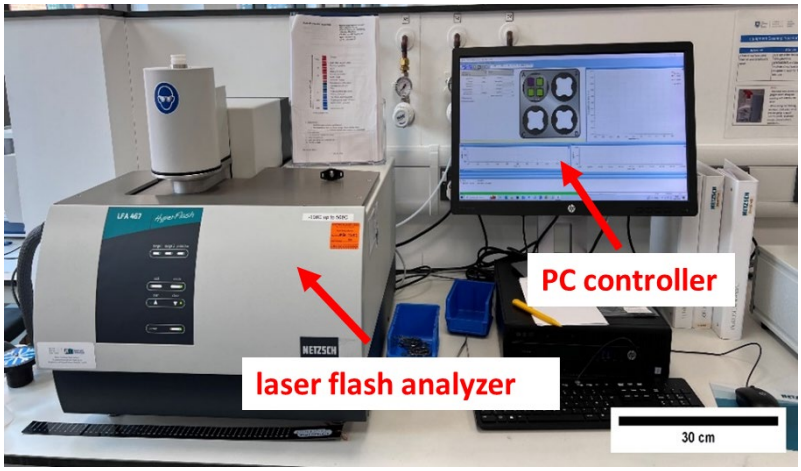

Figure 3.58 The thermal properties test of CFRP

Chapter 4 Result and Discussion Part 1 – the dispersion of carbon nanomaterials

The carbon nanomaterials (CB, CNTs, and graphene) are dispersed into IN2. In this section, the nanoparticle structure and size, the dispersion quantity of nanoparticles, and the influence of carbon nanomaterials on epoxy resin were discussed.

4.1 Carbon nanomaterial structure and size

Because the resistivity of carbon nanoparticle dispersion is controlled by electron tunnelling, the resistivity of samples depends exponentially on the distance between the nanoparticles [166]. To analyse the variation in electrical resistivity within the different curing regimes, an understanding of the carbon nanoparticle structure and size, as well as its distribution in the IN2, must first be determined. Dispersion of graphene and CNTs is difficult, and small concentrations of these particles that are well-dispersed lead to significant increases in viscosity, which makes the application and wetting of a fibre-based composite challenging as a result. Only the structure and size of CB are discussed here.

4.1.1 CB particle structure

SEM and TEM images show that CB particles tend to concentrate in high agglomerations [278], [279]. These particles are agglomerated into larger fractal structures in separated amorphous masses without a clear basic unit, as shown in Figure 4.1 (a). The visualisation of an average unitary particle's shape constitutes a cumbersome venture because the agglomeration hinders the correct detection of an isolated CB particle. In addition, it can be inferred that these particles may have a spherical shape by observing at high magnification one agglomeration's edge (see Figure 4.1 (b)). Figure 4.1 (b) reveals a circular structure.

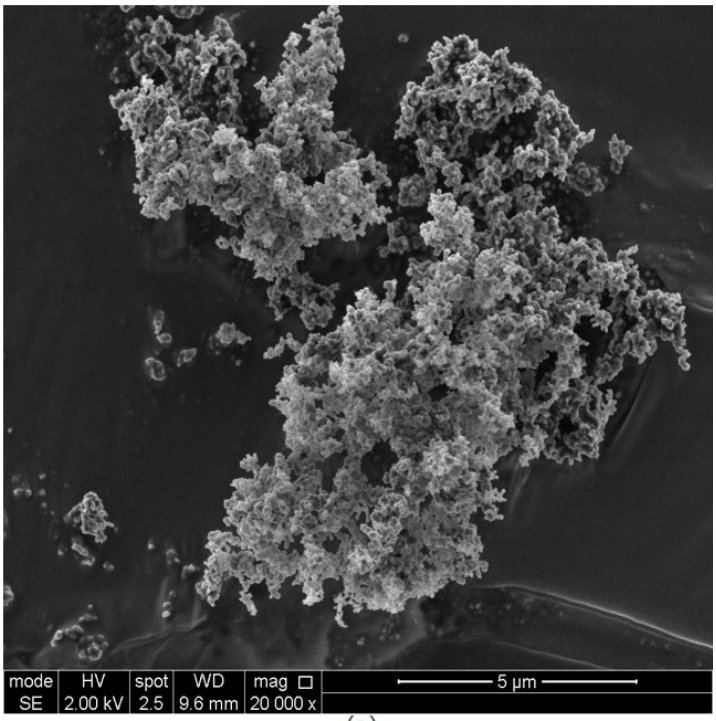

(a)

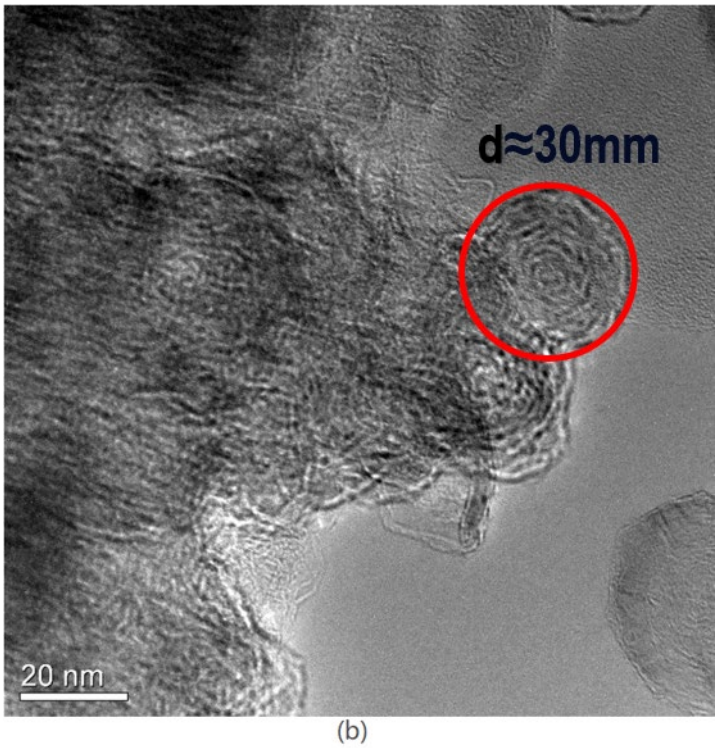

(b)

Figure 4.1 (a) SEM image of CB particle showing agglomeration of small CB particles. (b) TEM image of the individual CB nodules showing the internal structure.

4.1.2 CB particle size

Dynamic Light Scattering (DLS) analysis is performed to infer the average CB particle size. Three different solvents, such as toluene, methanol, and IPA at low CB

concentrations (0.01 wt.%) were used. The results show CB size distributions centred on 8, 90, and 400 nm diameter using toluene, methanol, and IPA solvents, respectively, as visualised in Figure 4.2. The toluene solvent hinders particle aggregation and provides an average single CB particle hydrodynamic radius value more accurately. The ensemble average particle hydrodynamic diameter from DLS analysis (9nm) is of the same order of magnitude as the single CB sphere measured by TEM in Figure 5 (b) (30nm).

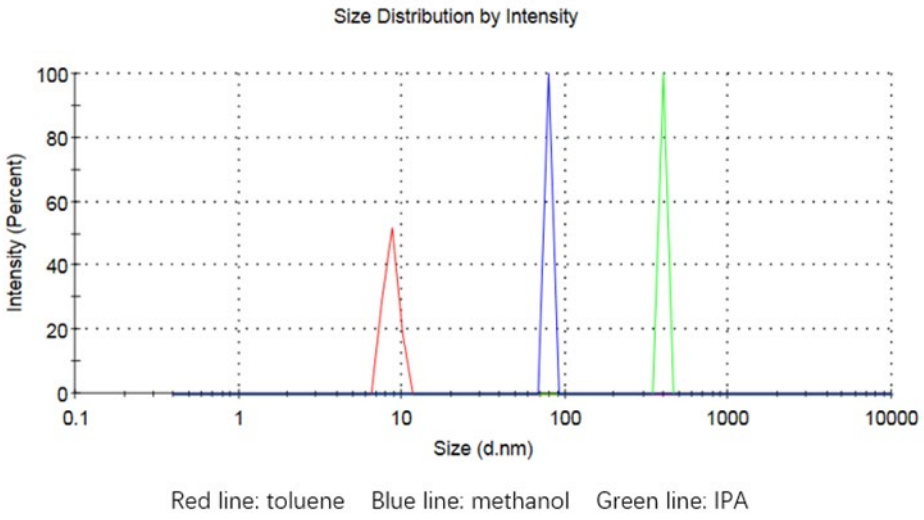

Figure 4.2 The size distribution of CB powder by intensity via DLS.

4.2 The mixing stability of carbon nanomaterials in IN2 and AT30S

In this section, the mixing stability of carbon nanomaterials (CB and graphene) in IN2 and AT30S is discussed. In this section, because neither the effective cross-sectional area of the wires nor the effect of the conductive path around the non-conductive stirrer can be determined, we cannot report the resistivity values and only report the resistance. But the container, wires, and mass of the mixture are the same. The stability is characterised by any change in resistance, and therefore, relative measures are adequate.

4.2.1 The mixing stability of CB/IN2 and CB/AT30S

Figure 4.3 describes the resistance changes for the CB mixtures (CB/IN2 and CB/AT30S with 3 wt.% CB). At 85 ℃, during stirring, the resistance of the two samples falls but stabilises after mixing. In the high oil bath temperature (115 ℃ and 135 ℃), the resistivity of samples is lower than that in the 85 ℃ oil bath. The AT30S has a high rate of evaporation at elevated temperatures. Therefore, the resistance gradually decreases over time, which

may be due to the continually increasing concentration of the CB. The resistance of the CB/AT30S is lower than that of the CB/IN2. So, the CB has better dispersion in AT30S if the resistivity and nanoparticle dispersion have an inverse relationship [280]. Here, the bad dispersion indicates the over-aggregation of nanoparticles in the initial status, not the formation of a network after dispersion.

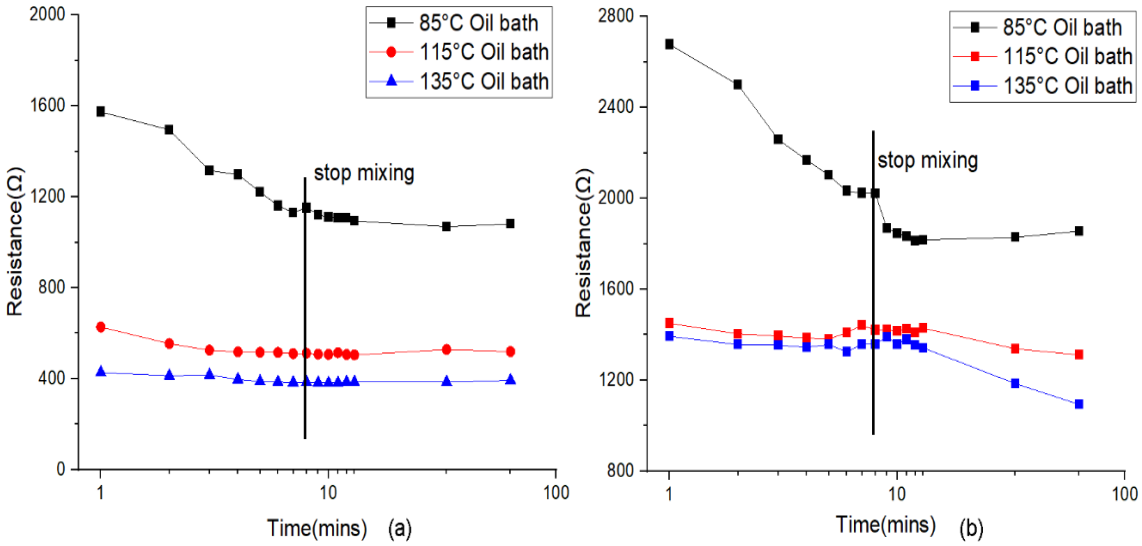

Figure 4.3 The resistivity changes of (a) 3wt% CB in pure IN2 epoxy and (b) 3wt% CB in pure AT30S at a range of temperatures (85 ℃, 115 ℃, and 135 ℃). The vertical line indicates the time when mixing was stopped. Note the x-axis is logarithmic.

4.2.2 The mixing stability of graphene/IN2 and graphene/AT30S

Because the structure of graphene, a single layer (monolayer) of carbon atoms, is unstable, the mixing stability of graphene mixtures (graphene/IN2 and graphene/AT30S with graphene 3 wt.%) in the low temperature (7 ℃ water bath), room temperature (23 ℃ water bath), and high temperature (80 ℃ water bath) are discussed. Figure 4.4 indicates that during the mixing process, the resistance change of two CB mixtures and two graphene mixtures is the same. After a few minutes, the resistance of two samples (graphene/IN2 and AT30S) is stabilized, and the resistance of the graphene/AT30S is lower than graphene/IN2. However, after mixing, the resistance of two graphene mixtures is not like that of two CB mixtures. The resistance of graphene/IN2 has a rapid increase in low temperatures (7 ℃ and 23 ℃ water bath). Only in an 80 ℃ water bath the resistance of samples is stable. In terms of graphene/AT30S, the increase of resistance only happens

at a 7 ℃ water bath. At 23 ℃ and 80 ℃ water bath, the resistance is stable. As a result, the mixing stability of the graphene/AT30hardener is better than graphene/IN2. However, the mixing stability of graphene mixtures is worse than that of CB mixtures.

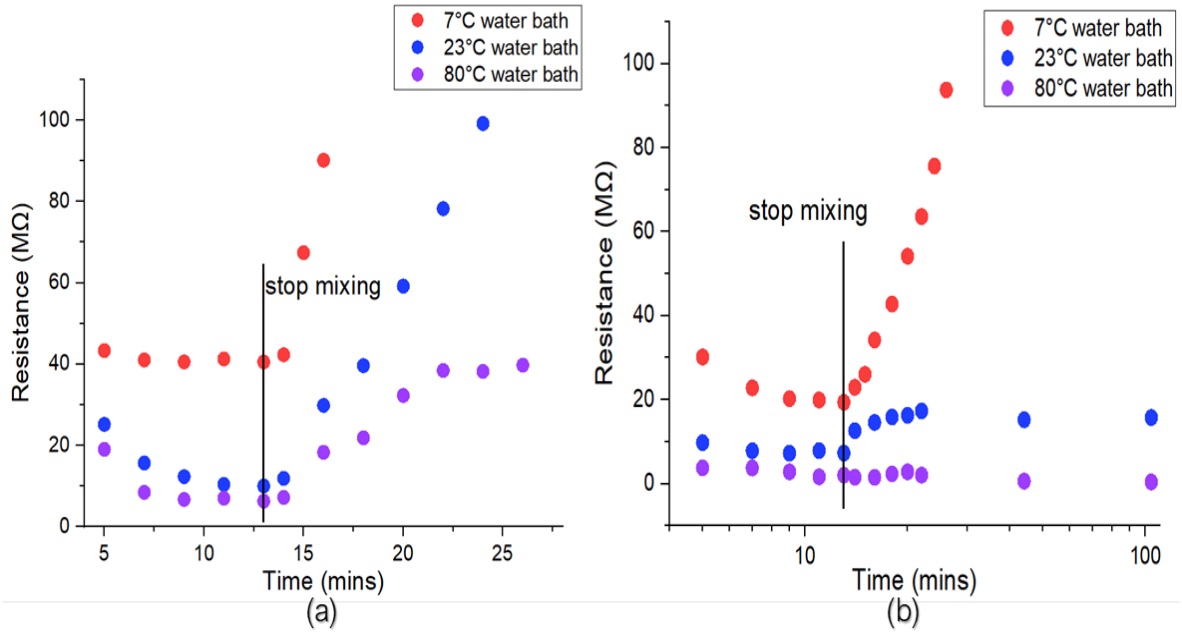

Figure 4.4 The resistivity changes of (a) 3wt% graphene in pure IN2 epoxy and (b) 3wt% graphene in pure AT30S at a range of temperatures (7 ℃, 23 ℃, and 80 ℃). The vertical line indicates the time when mixing was stopped. Note the x-axis is logarithmic in (b).

To further analyse the influence of temperature on the mixing stability of graphene mixtures, the mixtures are mixed in an 80 ℃ water bath for 10 mins until the resistance is stable and placed in different temperatures to observe the resistance change. Figure 4.4 and Figure 4.5 show similar results. In the low water bath temperature, the mixing stability of graphene mixtures is worse. The resistance of mixtures rapidly increases and is over 100 MΩ in a few minutes. In the hot-water bath, the resistance is stable. The mixing stability of graphene/AT30S is better than that of graphene/IN2.

In conclusion, due to the worse mixing stability, the research of graphene in dispersion and its influence on IN2 will not be further examined.

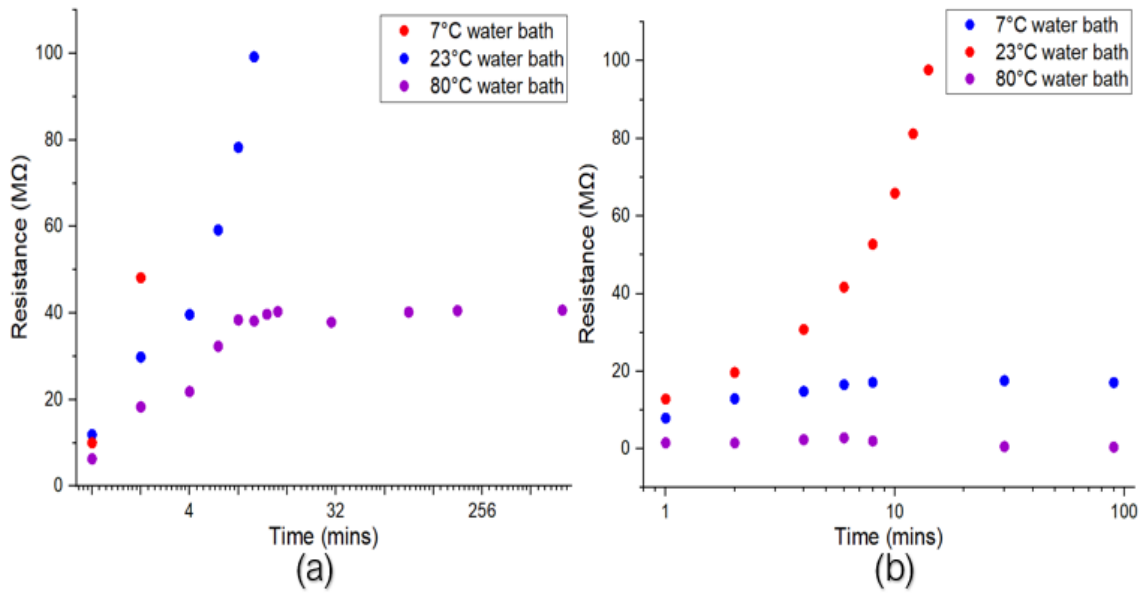

Figure 4.5 After mixing in an 80 ℃ water bath, the resistance changes of graphene/IN2 and graphene/AT30S at a range of temperatures, 7 ℃, 23 ℃, and 80 ℃. Note the x-axis is logarithmic.

4.3 The carbon nanoparticle dispersion in the IN2/AT30S resin system

In general, the carbon nanoparticle dispersion in IN2 describes how homogeneous the mixture of the carbon nanoparticles in IN2 is. In this aspect, variables such as the mixing method, carbon nanomaterials concentration and mixing temperature play a relevant role in the particle dispersion mechanism. In this research, graphene is not considered due to poor mixing stability. In addition, as Gibbs free energy explains (Equation 2.1), when the entropy change is very high, the reaction will be spontaneous and boost the stabilization of the dispersion [281]. It is irrespective of the mixing method. All the analysed samples are blended following the same mixing method, the overhead stirrer with 3+3 mins mode (see methodology), which is the optimized mixing mode in the later section (section 4.4.2). The influence of carbon nanomaterial (CB and CNTs) concentration and curing temperature on particle dispersion in the IN2/AT30S resin system are analysed by optical microscopy to determine the fractal dimension. The relevant calculation is explained in the methodology chapter. The result sections are shown below.

4.3.1 The analysis of fractal dimension error

To analyse the error in the fractal dimension, three sets of measurements for CB/IN2/AT30 composites were undertaken, which are shown below.

Case 1: Three images of the same area on a sample were analysed. As expected, this gives a low variance of the fractal dimension.

Case 2: Three different areas on the same sample (intra-sample variance) were measured.

Case 3: Three areas on different samples (inter-sample variance) were measured.

Figure 4.6 shows the standard deviation of fractal dimension in the above cases. The standard deviation of the different samples (Case 3) is higher than that of the other two groups. As a result, to improve the accuracy of experiments, Case 1 is used to analyse the variation in this project.

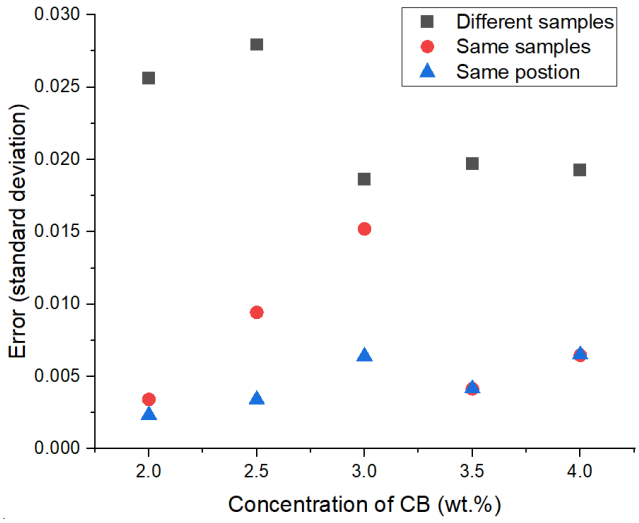

Figure 4.6 The error (standard deviation) of fractal dimensions of CB/IN2/AT30S composite in different concentrations

4.3.2 The nanoparticle dispersion in IN2/AT30S resin system with different nanoparticle concentration

This investigation analyses the fractal dimension measured in mixtures with CB concentrations of 2, 2.5, 3, 3.5, and 4 wt.% and with CNTs concentrations of 1.5, 2, 2.5, 3, and 3.5 wt.%. When the concentration is too low, the resistance of the sample is over 100 MΩ, which is beyond the range of the resistance meter.

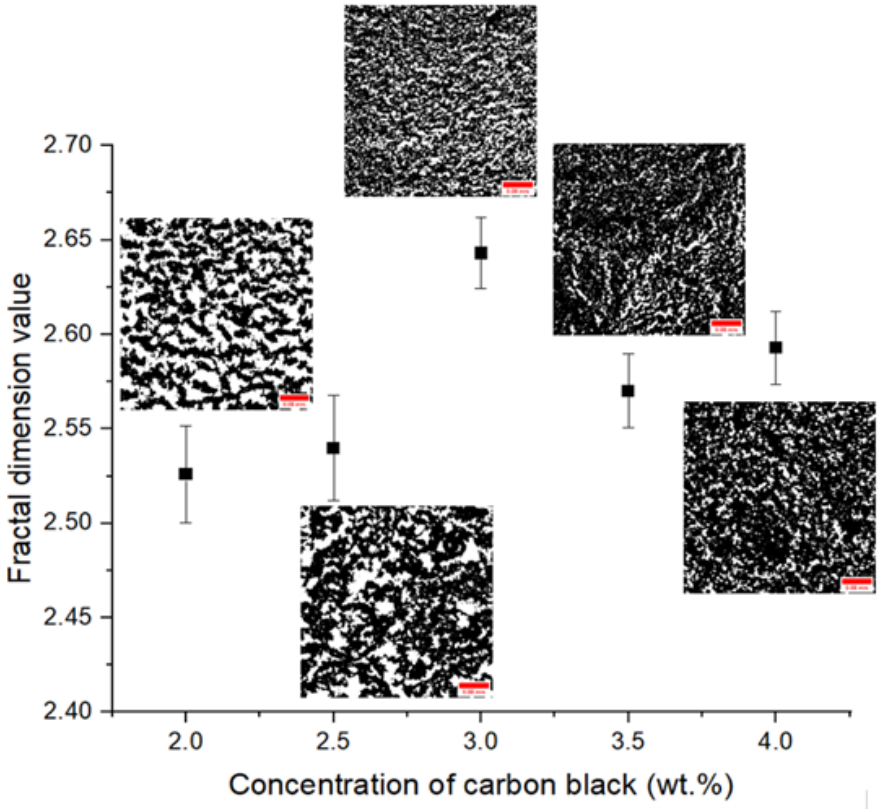

Figure 4.7 The fractal dimension value of CB/IN2/AT30S composites at different concentrations of CB. The dark regions are the phase rich in CB, and the light areas are the phase deficient in CB. The data points and errors are the average and one standard deviation of three samples. The scale bar shown in the images is 0.08mm

Figure 4.7 describes how increasing CB concentrations in the range between 2 and 3 wt.% substantially increases the fractal dimension. This trend is not observed when CB concentration is higher than 3 wt.%. Due to the nanoparticle agglomeration in high concentration, the fractal dimension values slightly fluctuate around 2.60.

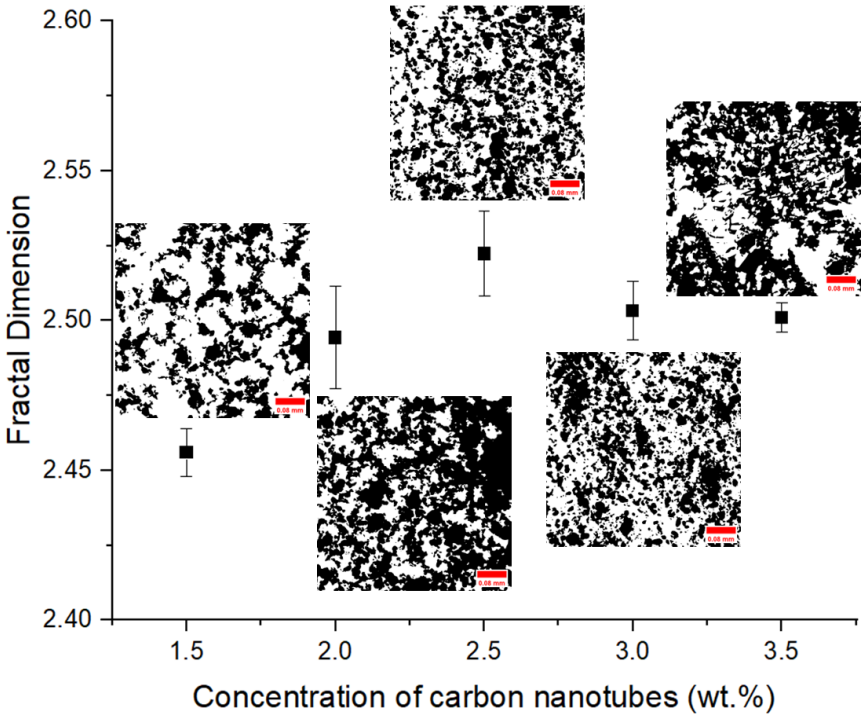

Figure 4.8 The fractal dimension value of CNTs/IN2/AT30S composites at different concentrations of CNTs. The dark regions are the phase rich in CNTs, and the light areas are the phase deficient in CNTs. The data points and errors are the average and one standard deviation of three samples. The scale bar shown in the images is 0.08mm

In Figure 4.8, the fractal dimension changes of CNTs/IN2/AT30S composites show the same tendency as that of CB/IN2/AT30S composites. When the CNT concentration is low, the fractal dimension value increases with concentration and reaches a peak point at 2.5 wt.%. When the concentration is higher than 2.5 wt.%, due to the high aggregation of nanoparticles, the fractal dimension values slightly fluctuate around 2.50.

4.3.3 The nanoparticle dispersion in IN2/AT30S resin system with CB 3 wt.% and CNTs 2.5 wt.% at different curing temperatures

To analyse the influence of curing temperatures on the nanoparticle dispersion, the fractal dimension from a dispersion's binarized microscope image of 3 wt.% CB/IN2/AT30S nanocomposite and 2.5 wt.% CNTs/IN2/AT30S nanocomposites at uncured and different curing temperatures (70℃, 130℃, 150℃ and 170℃). Figure 4.9 and Figure 4.10 shows that when the sample is uncured at room temperature (20℃), the fractal dimension has a maximum average value, which is 2.69 in CB/IN2/AT30S nanocomposites and 2.53 in CNTs/IN2/AT30S nanocomposites. Polymerisation occurs slowly, requiring over 24 hours at this temperature. The image is taken shortly after mixing.

Higher curing temperatures not only reduce the resin viscosity but also boost the rate of polymerisation, inducing carbon nanoparticle agglomeration and spinodal decomposition [282], [283]. The single phase (well-dispersed mixture) segregates into two co-existing phases: carbon nanoparticle-rich but resin-poor regions, which are the dark areas in microscope images, and resin-rich but nanoparticle-poor regions, which are the light areas. A characteristic of spinodal decomposition is the formation of a bi-continuous structure. In contrast, nucleation and growth are characterised by the formation of islands of the minority phase in the majority phase [284], [285].

However, when the curing temperature is 150 ℃ and 130 ℃, the fractal dimension value rises slightly in the CB/IN2/AT30S and CNTs/IN2/AT30S nanocomposites, respectively. Two mixing mechanisms are active. First is the mixing, which puts the energy into the system and breaks the nanoparticles up. Second is the higher temperature. After mixing, this leads to a change of Gibbs, TdS term, and so free energy decreases. As a result, the aggregation of nanoparticles is impeded. It has been explained in section 4.2.1. In addition, at sufficiently high temperatures, a mixed phase would be observed, and as such, heating beyond 150 ℃ in CB composites and 130 ℃ in CNT composites reduces phase segregation. As the curing of epoxy resin is a step-growth polymerisation, high molecular weight is created at the end of the polymerisation. Thus, phase segregation happens late in polymerisation as the viscosity rapidly rises, pinning the structure.

In summary, spinodal phase segregation is observed in all samples, creating a bicontinuous structure that reduces both the fractal dimension and resistivity (see Figure 4.19 and Figure 4.20). When the temperature is higher than 150 ℃ (CB) and 130 ℃ (CNTs), phase segregation begins to be hindered, and the fractal dimension increases marginally.

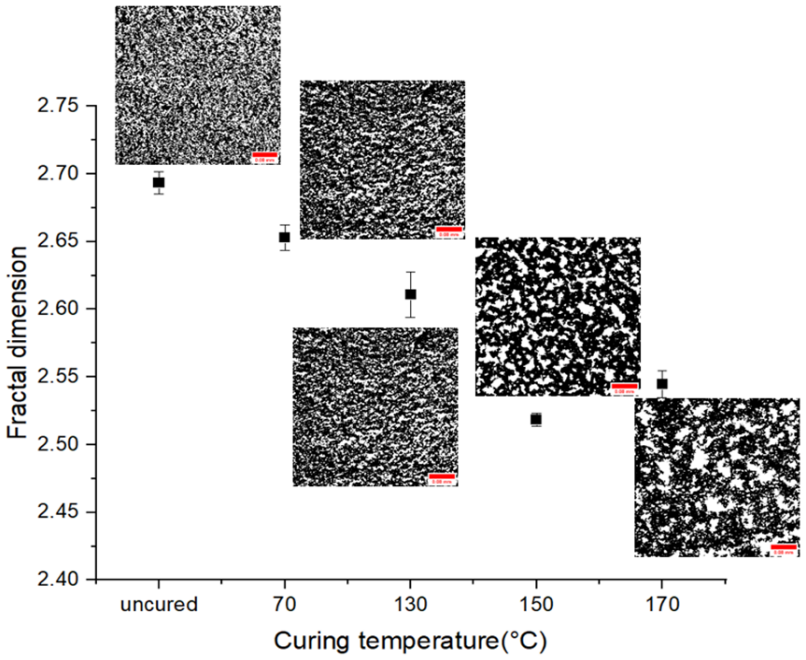

Figure 4.9 The fractal dimension of 3 wt.% CB/IN2/AT30S nanocomposites with uncured and different curing temperatures (70 ℃, 130 ℃, 150 ℃, and 170 ℃). The data points and errors are the average and one standard deviation of three samples, respectively. The scale bar shown in the images is 0.08mm.

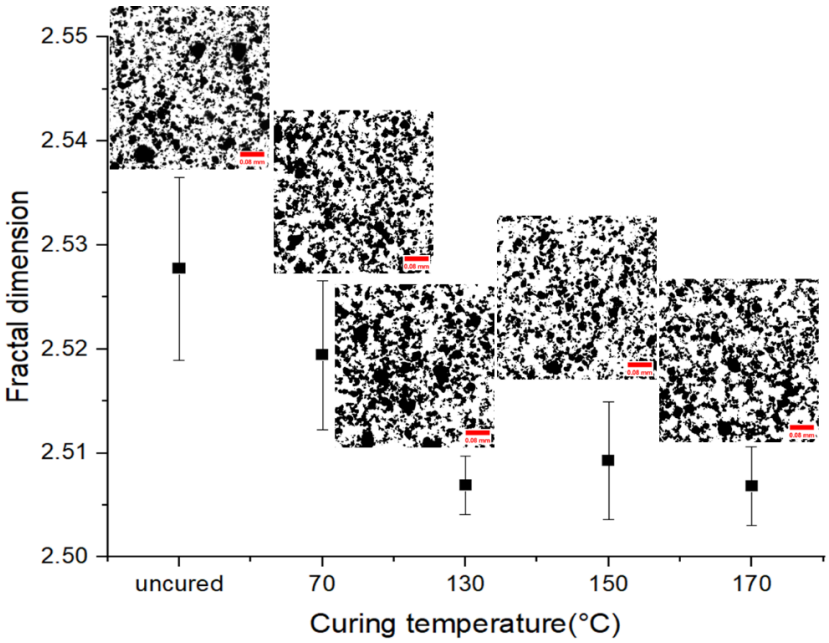

Figure 4.10 The fractal dimension of 2.5 wt.% CNTs/IN2/AT30S nanocomposites with uncured and different curing temperatures (70 ℃, 130 ℃, 150 ℃, and 170 ℃). The data points and errors are the average and one standard deviation of three samples, respectively. The scale bar shown in the images is 0.08mm.

Compared to the fractal dimension of CB/IN2/AT30S, that of CNTs/IN2/AT30S is lower in the same nanoparticle concentration and curing temperature. As a result, CB has a better dispersion in the IN2/AT30 resin system compared with CNT's.

Figure 4.11 represents the fractal dimension value changes of CB/IN2/AT30S nanoparticle composites during the curing process, where the temperature increase rate is 3℃/min. When the temperature is low (lower than 50 ℃), CB has good dispersion in the IN2/AT30S resin system, which shows a high fractal dimension value. As the temperature increases (higher than 50 ℃), the resin starts to cure, and there is phase separation in CB/IN2/AT30S nanocomposites, which leads to the aggregation of CB. As a result, the dispersion of CB is worse, and the fractal dimension value decreases. When the temperature is over 70 ℃, the curing reaction is basically completed, and there is no apparent phase separation. As a result, there is no more aggregation in CB. Figure 4.12 shows the microscope images in the curing process. When the temperature is low, there is no apparent aggregation of CB. However, with temperature increases due to the lower viscosity and polymerization reaction, there is the aggregation of CB, which is discussed in section 4.5. Nanoparticles move to areas richer in nanoparticles. As a result, the phase segregation is formed. It is formed by spinodal decomposition instead of nucleation growth. So, there is a bicontinuous structure instead of isolated nanoparticle islands.

Figure 4.11 represents the fractal dimension changes of CB/IN2/AT30S composites during the curing process, where the temperature increase rate is 3 ℃/min. When the temperature is low (lower than 50 ℃), CB has good dispersion in the IN2/AT30S resin system, which shows a high fractal dimension value. As the temperature increases (above 50 ℃), the resin starts to cure, and there is phase segregation of a CB rich from a CB poor phase, leading to CB aggregation. As a result, the fractal dimension decreases. When the temperature is over 70 ℃, the curing reaction is essentially complete, and the resin's glass transition temperature (Tg) is above 70 ℃. The system has vitrified, and there is no further phase segregation or aggregation. Figure 4.12 shows the microscope images during the curing process. When the temperature is low, there is no apparent aggregation of CB. However, as temperature increases, due to the lower viscosity and the polymerisation reaction, aggregation of CB occurs (Section 4.5). Nanoparticles move to areas richer in nanoparticles as the CB-rich phase segregates from the CB-poor phase.

As the mechanism is spinodal decomposition, instead of nucleation growth, this creates a bi-continuous structure instead of isolated nanoparticle islands. This bi-continuous structure decreases the separation of the CB nanoparticles in the CB-rich phase but maintains connectivity across the entire sample. As a result of the exponential decrease in resistivity as CB separation decreases, but only a linear dependence of the resistance on the cross-sectional area of the conductive path, the overall resistance decreases (see Figure 4.19).

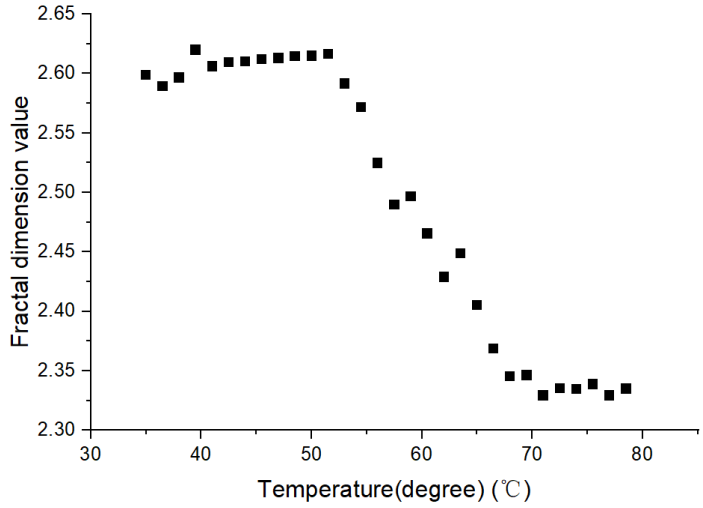

Figure 4.11 The fractal dimension value changes of CB/IN2/AT30S nanoparticle composites during the curing process

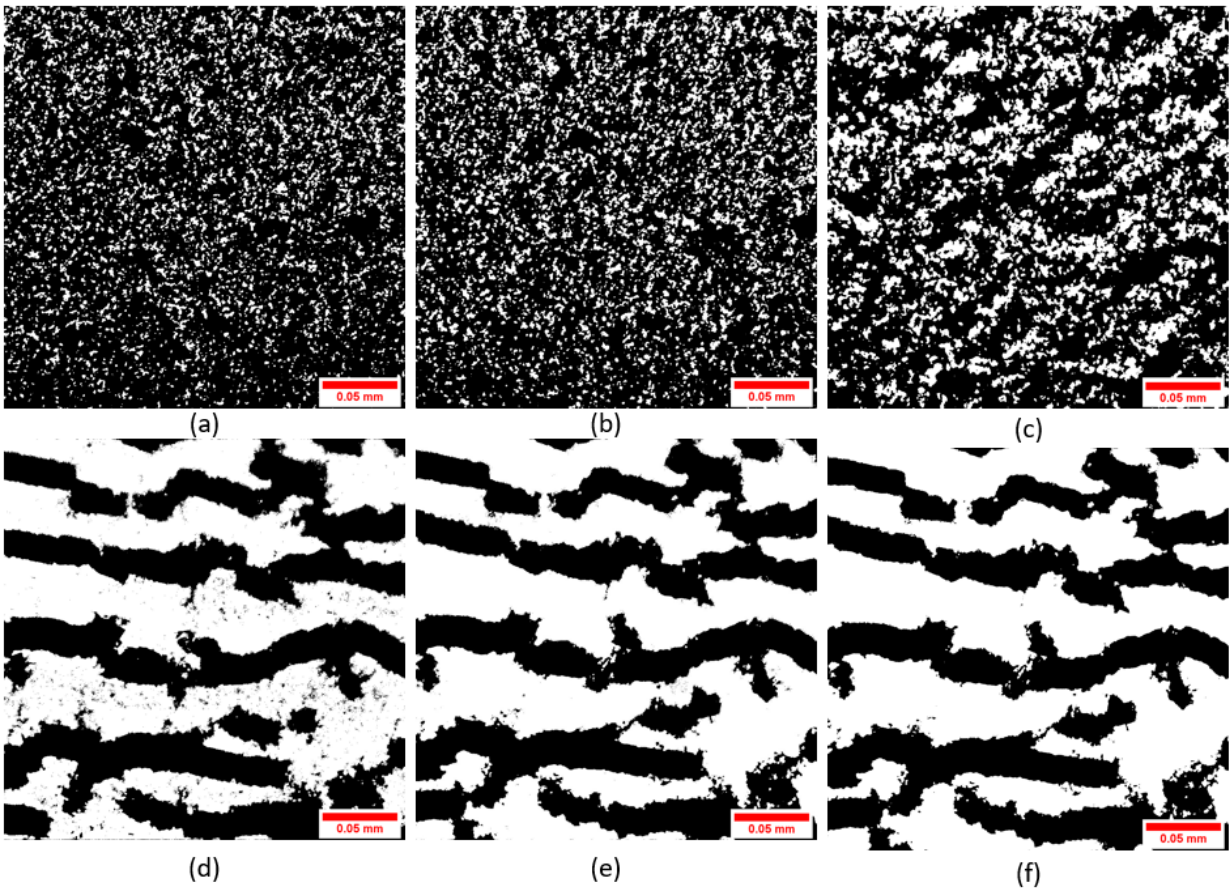

Figure 4.12 The microscope images of CB/IN2/AT30S nanoparticle composites during the curing process at different curing time (a) 0 minutes, (b) 4 minutes, (c) 7 minutes, (d) 9 minutes, (e)11 minutes, (f) 15 minutes. The scale bar is 0.05mm.

4.4 The electrical properties of the carbon nanomaterials/IN2/AT30S nanocomposites

The purpose of this section is to analyse the influence of carbon nanomaterials (CB and CNTs) on the electrical properties of epoxy resin. This section includes three main parts. The first one examines the percolation threshold of the CB/IN2/AT30S nanocomposite. The manual stirring method mixed the CB/IN2/AT30S nanocomposite with different CB concentrations and mixing time to analyse the percolation threshold value. The second one is to compare the different mixing methods at the percolation threshold concentration with different mixing time. Finally, the optimized combination of mixing method and time is used to disperse CNTs in the IN2/AT30S resin system with different CNT concentrations to analyse the percolation threshold value.

4.4.1 The percolation threshold concentration of CB/IN2/AT30S

In this section, the CB is dispersed into IN2 by manual stirring with different concentrations and stirring time. There are four samples in each composite material sample. By measuring their resistance values, the average resistivity values at different stirring time and concentrations can be determined (see Figure 4.13).

Figure 4.13 shows that at 2 minutes of stirring time and 4 minutes of mixing time, the resistivity values at some high concentrations of CB are higher than those at low concentration points. However, this result was rarely shown at 8 minutes of stirring time. In addition, compared with resistivity values at 2 minutes and 4 minutes of stirring time, the resistivity values at 8 minutes are lower at the same concentration. As expected, by increasing the stirring time, the dispersion of CB in the IN2 is improved.

According to the resistivity values at 4 minutes and 8 minutes of stirring time, the percolation threshold is around 3%. Below 3%, the resistivity decreases rapidly with concentration, and above 3%, the resistivity value plateaus.

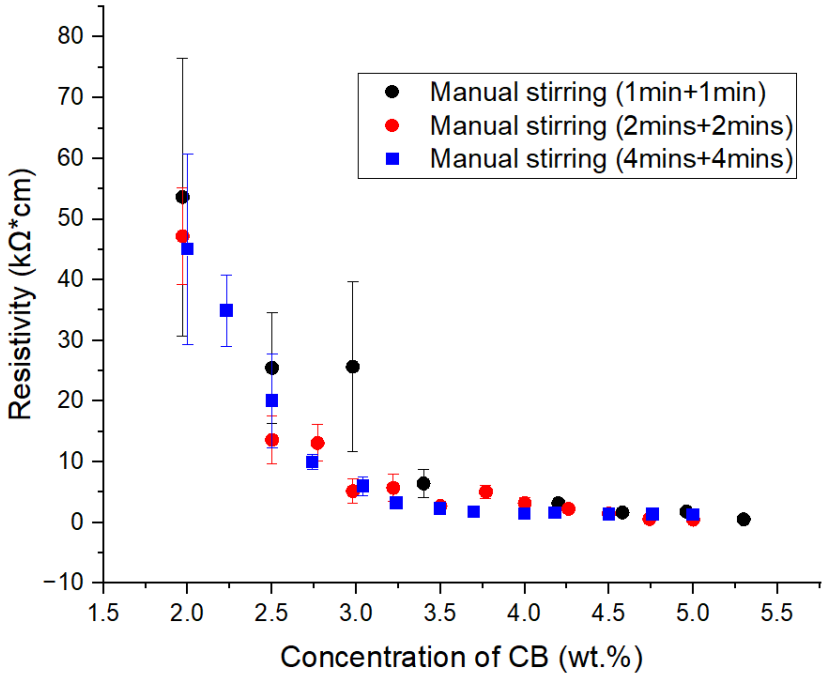

Figure 4.13 The average CB/IN2/AT30S nanoparticle composite resistivity for different manual stirring times and concentrations. The error bar is the standard deviation of 4 samples.

To further analyse the dispersion of CB, the standard deviation of resistivity was considered. The standard deviation for the samples that underwent 2 (1+1) minutes of

stirring is higher than the other two groups. The long stirring time shows a low standard deviation. The hypothesis is that the better the dispersion, the lower the standard deviation of the resistivity.

As expected, longer stirring times result in better dispersion of CB in IN2. The better dispersion of CB represents the lower range of separation in CB. As a result, the standard deviation of resistivity is lower. In addition, from the three different stirring times, the standard deviation decreases with increasing concentration. At 4 (2+2) minutes and 8 (4+4) minutes stirring time, above 3 wt.%, the standard deviation change is small.

Figure 4.14 and Figure 4.15 show the conductivity of the CB/IN2/AT30S composite with 4+4 minutes of manual stirring at different CB concentrations. In Figure 4.14, the solid red line is the fit to a percolation threshold theory function (Equation 2.2); in Figure 4.15, the red line is the fit to a Gompertz function (Equation 2.3). The data from shorter stirring times have significant uncertainty at low dispersion of CB due to poor dispersion and low conductivity, so they are not shown. Figure 4.14 indicates a percolation onset of 1.5±0.6 wt.%, and Figure 4.15 shows a percolation threshold value of 3.19±0.03 wt.%.

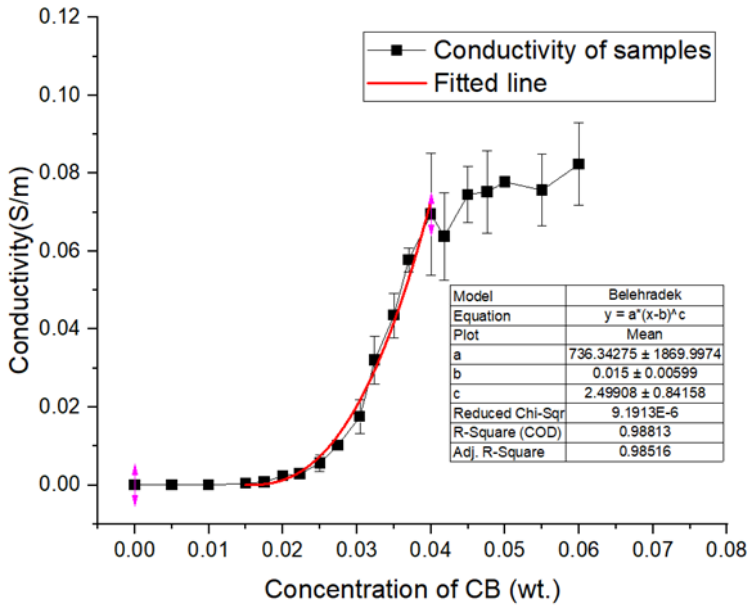

Figure 4.14 CB/IN2/AT30S composite resistivity with 4+4 minutes of manual stirring at different CB concentrations. The red line is a fit to the percolation threshold theory function (Equation 2.2).

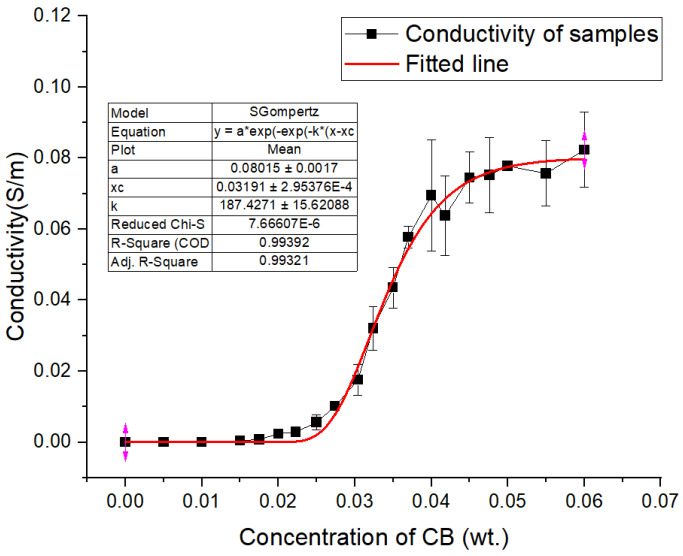

Figure 4.15 CB/IN2/AT30S resistivity with 4+4 minutes of manual stirring at different CB concentrations. The red line fits Equation 2.3, a Gompertz function. The inflection point is 3.19±0.03 wt.%.

4.4.2 The comparison of different mixing methods

This section discussed the dispersion efficiency of four different dispersion methods, which are dispersing CB into IN2 and CB, taking up 3% of the weight in the composite. Figure 4.16 shows the average and standard deviation of resistivity of 3 wt.% CB/IN2/AT30S composite (4 samples) in different stirring time by different dispersion ways.

The assumption we are making is that as the mixing improves, the variability in resistance, as measured by the standard deviation, will fall as the different samples become more similar.

Figure 4.16 shows that compared with the other three dispersion methods, the magnetic stirrer required a longer time to achieve a low standard deviation (as demonstrated by the large error bar). The magnetic stirrer requires longer than the other three dispersion ways to disperse the CB into IN2. Comparing manual stirring, ultrasonication, and overhead stirring, the standard deviation value of ultrasonication and overhead stirring is far smaller than that of manual stirring until longer stirring times. When the stirring time is 8 minutes, the standard deviation of these three methods is almost the same. In addition, comparing the four methods, the standard deviation of resistivity from the sample that was mixed by

the overhead stirrer or ultrasonicator reaches a stable value in the shortest time (about 4 minutes).

In conclusion, the overhead stirrer can effectively disperse CB in the shortest time. The ultrasonicator performs similarly to the overhead stirrer. However, the ultrasonicator generates far more heat than the overhead stirrer, which accelerates the rate of cure when the hardener is added, thus affecting the dispersion of nanoparticles and making handling and sample preparation more difficult. Manual stirring is ranked 3rd. The magnetic stirrer has the worst performance of the four dispersion methods. The magnetic stirrer needs more than 10 minutes to disperse CB into the IN2 well. As a result, the overhead stirrer with 3+3 mins mode stirring time is the best choice for the late experiments.

To some degree, the results regarding the magnetic stirrer were expected; the energy input is small, and the torque imparted is limited. What is of note is the relatively poor performance of the ultrasonicator compared to the simpler, lower-cost overhead stirrer. Literature shows that ultrasonication is more effective in low-viscosity mixtures [286].

Whilst there is a marked drop in the resistance and a visual change in the resin during the mixing process, there is no evidence to suggest that the CB is finely dispersed in the resin. There is an energy balance between the effective energy input by missing and the degree of dispersion. Thus, with higher energy input, the resistivity could fall further.

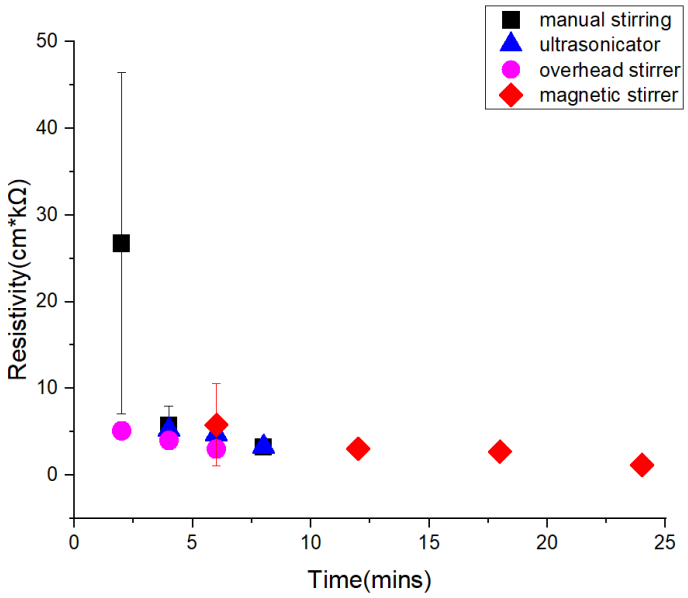

Figure 4.16 The average resistivity of CB (3 wt.%)/IN2/AT30S nanocomposite by different stirring ways with different stirring time. The error bar is (one standard deviation of 4 samples).

4.4.3 The percolation threshold concentration of CNTs/IN2/AT30S

When analysing the dispersion of CB, the optimal dispersion method and mixing time were the overhead stirrers and 3+3 minutes mode. Consequently, this combination is used to fabricate the CNT/IN2 composite.

Figure 4.17 describes the resistivity of the CNT/IN2/AT30S nanocomposites with different CNT concentrations. As the concentration of CNT increases, the resistivity of the CNT/IN2/AT30S nanocomposite decreases until the concentration of carbon nanotube is around 2.5 wt.%, where the resistivity is 259 cm·kΩ. After this point, with the concentration increasing, the resistivity plateaus. As a result, the percolation threshold value of carbon nanotube in the IN2/AT30S resin system is around 2.5 wt.%, which is far higher than the theoretical value (0.6 wt.%) [287]. The reason for this difference is the aggregation of CNTs. In addition, as the concentration of CNT increases, the error bar (standard deviation) of the resistivity decreases.

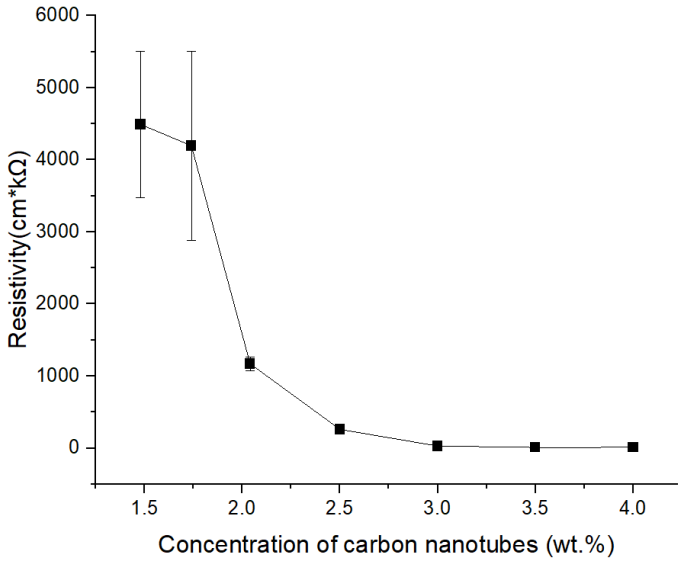

Figure 4.17 The resistivity of the CNT/IN2/AT30S nanocomposite with different CNT concentrations

4.5 The influence of curing temperature on the resistance of CB/IN2/AT30S

To discuss the influence of curing temperature on the resistance of CB/IN2/AT30S, four different curing temperatures (70 ℃, 130 ℃, and 180 ℃) are considered at 3 wt.% CB/IN2/AT30 composites and 2.5 wt.% CNTs/IN2/AT30 composites, which are shown in Figure 4.19 and Figure 4.20.

In all samples, the resistivity rapidly decreases as the resin temperature increases. As the resin is heated, the viscosity of samples decreases, which allows the CB nanoparticles to diffuse more rapidly. However, at the same time, the resin is curing, which affects the viscosity and the thermodynamics. Because the curing process is a step-growth polymerisation, high molecular weights are not achieved until high conversions. Therefore, reaction-induced phase separation (RIPS) proceeds slowly, and the early-stage bicontinuous structure is preserved and fixed by vitrification at high conversion in agreement with Soltani [288].

In terms of separate mixtures of CB/IN2 and CB/AT30S, the resistance is stable with time after mixing, as shown in Figure 4.3. In addition, the resistance of graphene/IN2 and graphene/AT30S is also stable in high temperatures. The resistance is stable in monomers but drops in the curing system, which indicates that the aggregation of carbon nanoparticles is not driven by an incompatibility with the resin components but with the

polymer formed from the resin. This phase separation on polymerisation has been widely observed in many systems and is generally termed RIPS [289]. As the degree of polymerisation, *N*, increases, phase separation can be observed. It is driven by *cN,* which is the product of the Flory-Huggins interaction parameter *c* and the degree of polymerisation, *N*.

The decrease in resistivity is primarily due to a decreased separation of the carbon nanoparticles. Figure 4.18 shows that when pure CB particles are heated from room temperature to 170 °C, the resistance will drop with temperature increasing. During the curing process, CB nanoparticles are initially dispersed but still form conductive networks. They tend to coalesce with adjacent nanoparticles and form bicontinuous networks with higher concentrations of carbon nanomaterials. As a result, the resistivity of the sample drops rapidly at the beginning of the curing process. The phase separation proceeds by spinodal decomposition. CB nanoparticles diffuse to areas richer in nanoparticles, and as interparticle distance decreases, the resistance drops.

This fall in resistivity with phase separation would, at first sight, appear to contradict the drop in resistance with improved mixing. However, this decrease in resistance is higher than the compensation for a reduction in volume that carbon nanoparticles occupied because the resistance depends exponentially on tunnelling distance.

Because the curing process is exothermic and generates heat, there is an overshoot in the sample polymerisation process for the low curing temperature CB/IN2/AT30S and CNTs/IN2/AT30S samples (70 and 130 °C). This trend is not observed in the higher curing temperature samples as the heating rate masks it. However, it indicates that curing is complete in all these systems relatively quickly. As the sample temperature stabilises, the sample resistivity plateaus. However, compared with samples at other curing temperatures, in two 70 °C samples, both resistances continue to fall slowly over 300 minutes. DSC measured the glass transition temperature of the IN2/AT30 resin system as 63 °C. Therefore, the curing happens close to the Tg of the formed network, and diffusion is slow due to the higher viscosity at this lower temperature. At 70 °C, this resin system needs approximately 6 hours to cure fully. Because of the temperature coefficient of resistivity, there is a drop in resistance of all samples as they cool to room temperature.

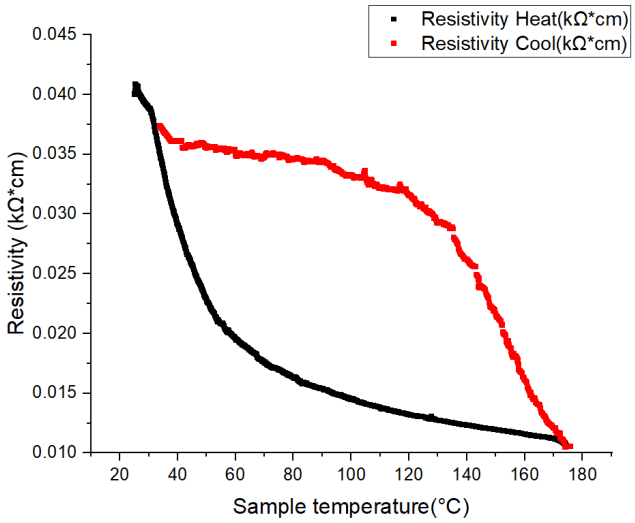

Figure 4.18 The resistivity of CB powder in different temperatures (sample heated to 170 ℃ and cooled down to room temperature). The hysteresis may be due to the loss of water from the surface of the CB.

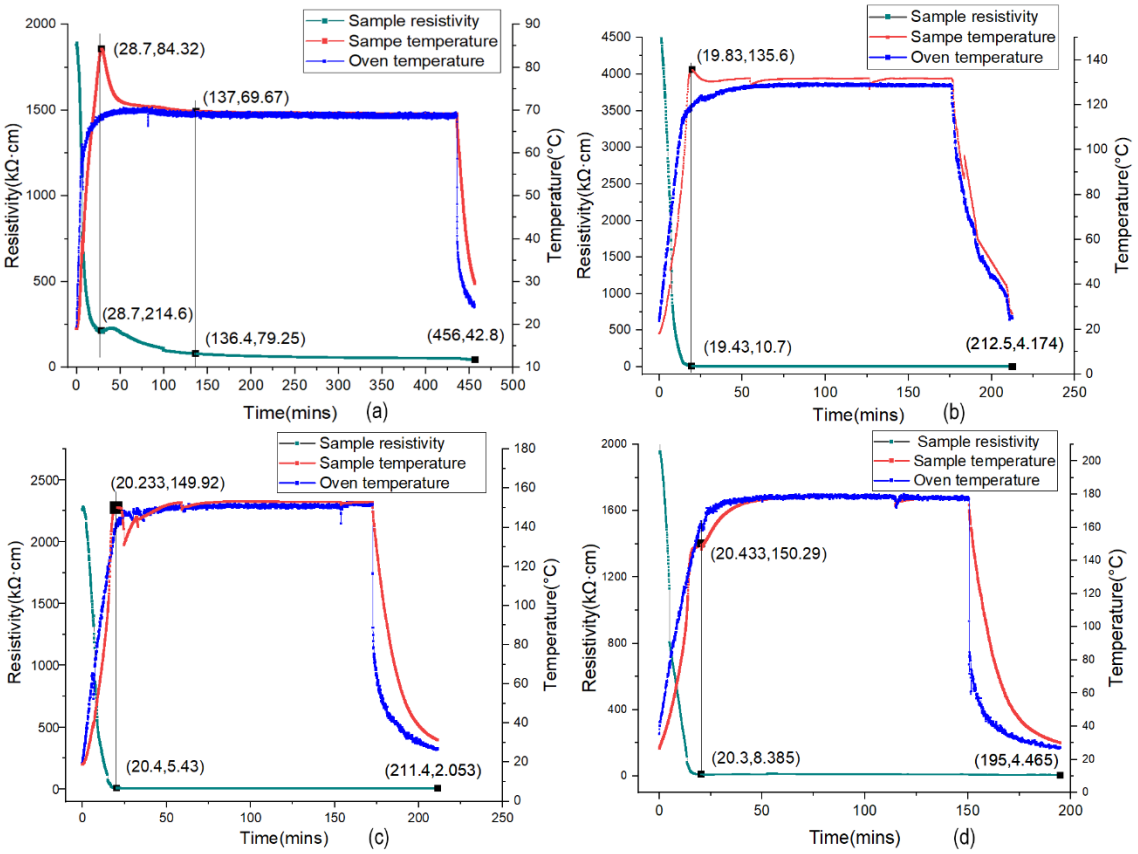

Figure 4.19 The changes of 3 wt.% CB/IN2s temperature (red line), their resistivity (green line), and oven temperature (blue line) during the curing process in different curing temperatures (a) 70 ℃ (b) 130 ℃ (c) 150 ℃ (d) 170 ℃.

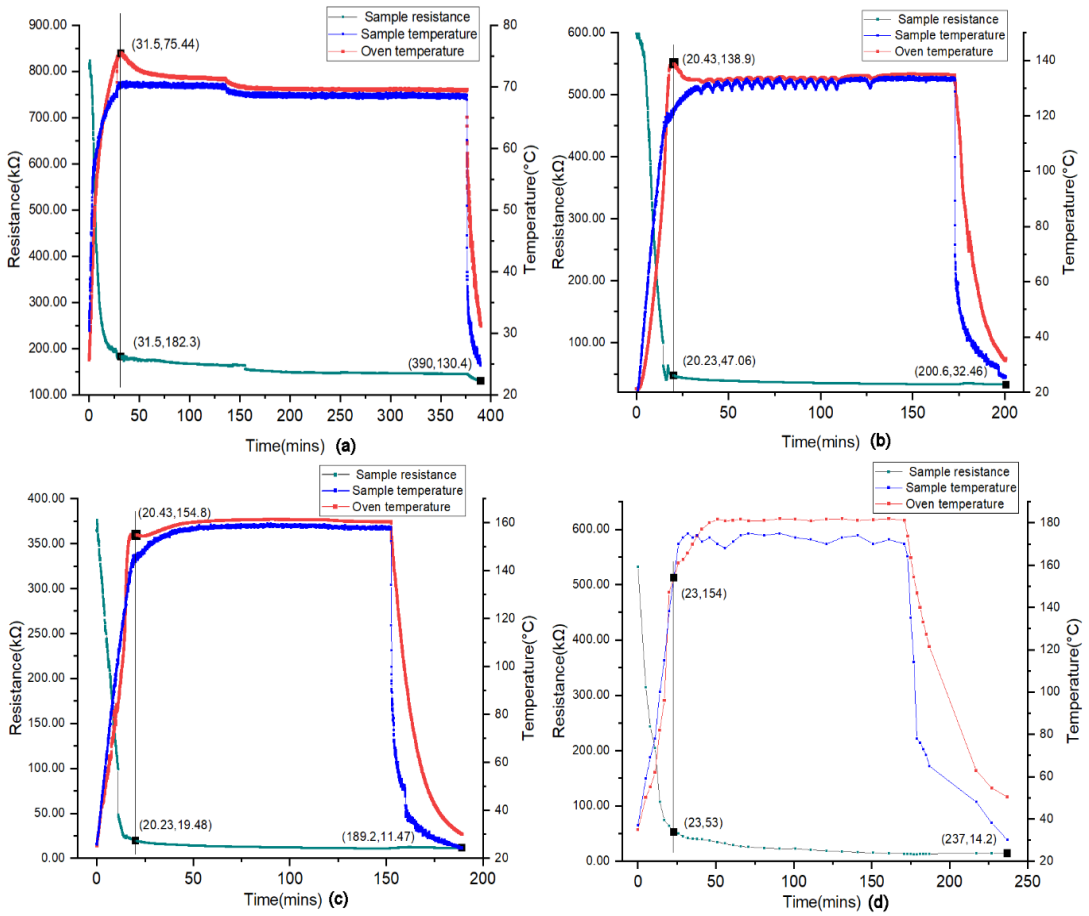

Figure 4.20 The changes of 2.5 wt.% CNT/IN2/AT30S temperature (red line), their resistivity (green line), and oven temperature (blue line) during the curing process in different curing temperatures (a) 70 ℃ (b) 130 ℃ (c) 150 ℃ (d) 170 ℃.

4.6 Tensile test

Compared with CNTs and graphene, CB shows better performance in terms of dispersion and electrical properties in the IN2/AT30S resin system. In this section, the tensile properties (tensile strength and Young's modulus) of CB/IN2/AT30S nanocomposites are examined at different CB concentrations and curing temperatures.

4.6.1 Different CB concentration

Figure 4.21 shows the tensile properties of four different CB concentration samples (0 wt.%, 1 wt.%, 2 wt.%, and 3 wt.%). When concentration is increased, both the tensile strength and Young's modulus increase, reaching peak values at 2 wt.%. Compared with 0 wt.%, the tensile strength and Young's modulus increases by 9% and 20%, respectively. After 2 wt.%, ANOVA test result shows there is no significant difference in tensile strength

and Young's modulus. Compared with the electrical conductivity and fractal dimension, the peak of tensile properties appears at a lower CB concentration (2 wt.%). When the concentration of nanoparticles is high, the dispersion is poor due to the aggregation of nanoparticles. These aggregated nanoparticles are poorly interpenetrated by the epoxy resin, which will act as stress concentrators that negatively affect the tensile properties. Soltani [288] indicates that a nucleation and growth mechanism takes over from spinodal decomposition at a high nanoparticle concentration. Therefore, the isolated islands of CB are created.

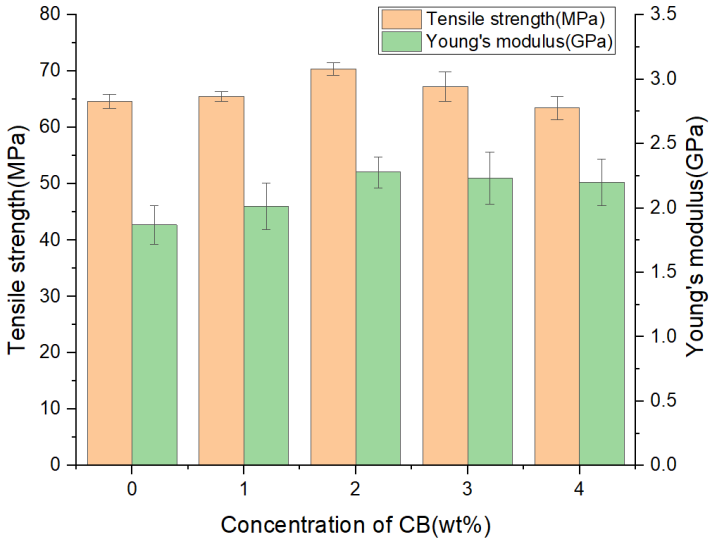

Figure 4.21 The average tensile strength and Young's modulus of CB/IN2 composite (5 samples) with different CB concentrations. The error bar is one standard deviation.

4.6.2 Different curing temperatures at 3 wt.% CB

Figure 4.22 shows the tensile properties of 3 wt% CB at different curing temperatures. Compared with CB concentration, the effect of curing temperature on tensile properties is small. There is no statistically significant difference (ANOVA test) in the tensile strength or Young's modulus of the 3 wt.% CB/IN2/AT30S samples with different CB wt.%.

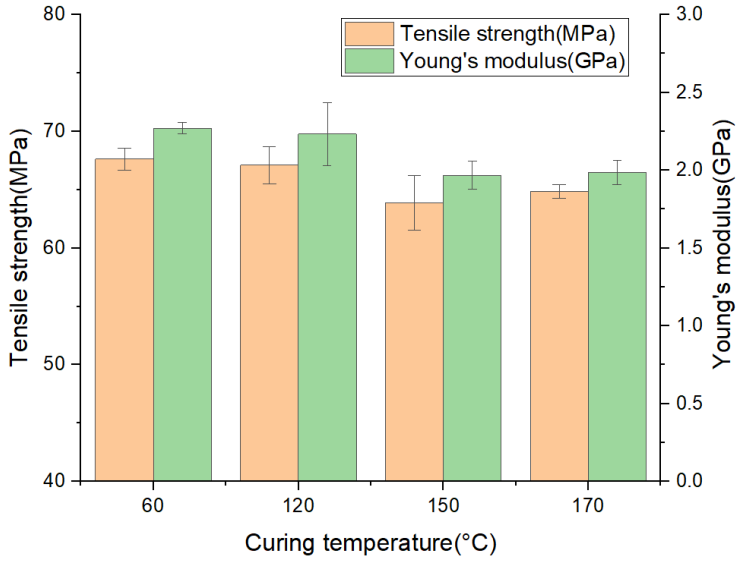

Figure 4.22 The average tensile strength and Young's modulus of 3 wt.% CB/IN2/AT30S composite (5 samples) with different curing temperatures. The error bar is one standard deviation.

4.7 Conclusion

This work investigates the effect of carbon nanomaterials (CB, CNTs, and graphene) on the dispersion in epoxy resin, as well as the electrical and mechanical properties of carbon nanomaterial-modified epoxy resin composites. The structure of carbon nanoparticles and the networks they form, which allow electrical conductivity throughout the resin, is determined by electron (SEM and TEM) and optical microscopy. In addition, the percolation threshold was calculated by examining the resistivity of composites with different concentrations of carbon nanomaterials. An optimal concentration of carbon nanomaterials for electrical conductivity was obtained from this research. The optimal concentration was used to study the influence of the curing temperature and mixing methodology on the electrical conductivity of composites. Finally, the tensile properties (tensile strength and Young's modulus) for different carbon nanomaterial concentrations and curing temperatures were investigated. The most valuable insights are summarised in the below bullet points.

- Compared with CB and CNTs, the structure of graphene is a single layer (monolayer) of carbon atoms. It is unstable and readily aggregates at room temperature.

- Carbon nanoparticles (CB and CNTs) have a high tendency to agglomerate, forming structures that are much larger than those of a particle itself. The high nanoparticle agglomeration boosts the formation of electrical networks, which can reduce the required concentration of nanomaterials for achieving the percolation threshold.
- The fractal dimension values and resistivity measurements indicated that the percolation threshold is 3 wt.% in CB/IN2/AT30S composite and 2.5 wt.% in CNTs/IN2/AT30S composite.
- The overhead stirrer is the optimal mixing technique due to its high working torque and minimal heat generation.
- The curing temperature has a positive effect on the conductivity of the composite. Higher curing temperatures can improve the connectivity between carbon nanoparticles, forming bicontinuous spinodal networks that will enhance conductivity up to 150 ℃.
- In terms of the CB/IN2/AT30S composite, the optimal tensile properties (tensile strength and Young's modulus) are achieved when the CB concentration is 2 wt.%. The tensile strength and Young's modulus are 9% and 20% higher than that of a pure IN/AT30 resin system. When CB wt.% is higher than 2wt.%, there is no noticeable difference in tensile properties. As a result, the percolation threshold should be between 2 and 3 wt.%. This result matches the result of fractal dimension and resistivity measurement. As the CB concentration increases to 4 wt.%, the tensile strength of the composite is 2% lower than the pure resin system due to the stress concentration.
- Compared across CB concentrations, 2 wt.% CB samples show optimal electrical and mechanical performance.
- The influence of curing temperature on the mechanical properties of composites is small.

Chapter 5 Result and Discussion Part 2 – CFRPs with different CB wt.%

Carbon black (CB) particles were incorporated into IN2 resin at 0, 1, 2, 3 wt.% of the epoxy matrix, and the “prepreg” of CFRPs was prepared by hand layup. The samples are manufactured using traditional manufacturing methods (oven and heat press). In this section, the influence of CB on CFRPs' mechanical properties is discussed.

5.1 The structure of CB nanoparticle-filled resin in CFRP

To determine the influence of CB on CFRP, the distribution of CB in a CFRP sample was analysed. The intention was to determine if the CB affected the fibre-matrix interface or only the matrix, as shown previously. The sample with 3 wt.% CB in the matrix was examined using SEM. As depicted in Figure 5.1 (a), the chord length of the carbon fibres’ cross-section ranges from 6 to 8 μm. The variation in size is due to the sample’s sectioning and polishing, which causes the observed fibre width to be a chord of the circular cross-section instead of the diameter. There are a few fragments that can be observed on the fibre surface, which were marked by red circles. However, due to the very low concentration of CB (3 wt.% in matrix), there is insufficient evidence to determine if they are CB nanoparticles or debris from the grinding and polishing process. In addition, the TEM image of CB nanoparticles (Figure 5.1 (b)) indicates that the CB nanoparticles are spherical and approximately 32 nm in diameter. These nanoparticles form larger particles around 500 nm in size. Therefore, it is uncertain whether these fragments are agglomerations of CB nanoparticles, as shown in Figure 5.1(b). In the absence of contrary evidence, it is assumed that all CB nanoparticles are dispersed in the matrix rather than being associated with the carbon fibre.

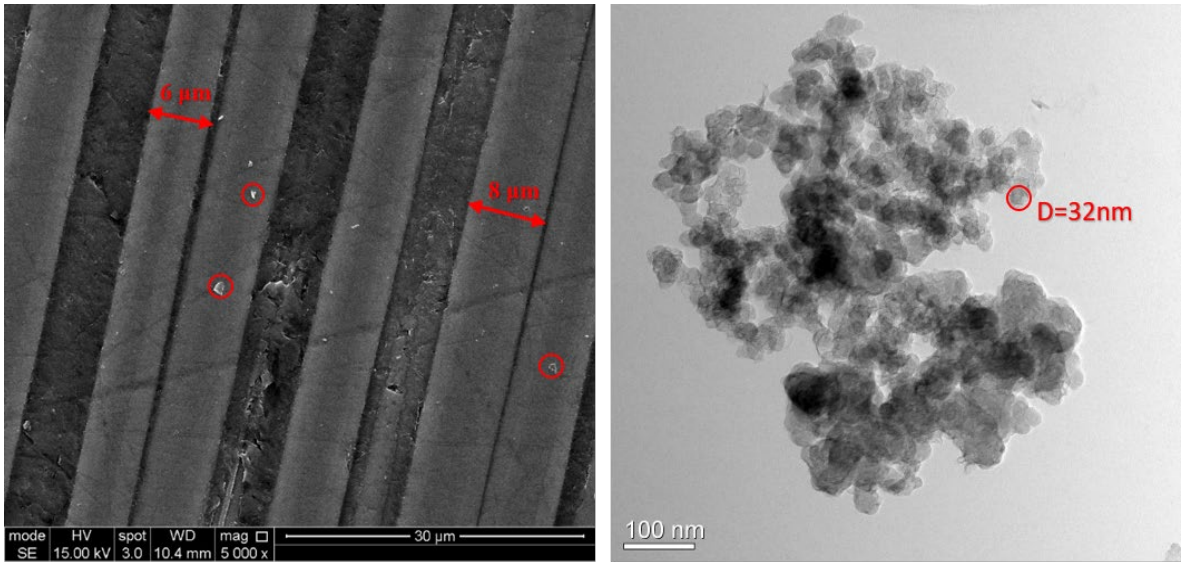

Figure 5.1 The microstructure of (a) CFRP with 3 wt.% CB in the matrix under SEM and (b) CB nanoparticles under TEM.

In addition, there are two SEM images of CFRP with 3 wt.% CB in the matrix shows the quality of CFRP (see Figure 5.2). In Figure 5.2 (b), at high magnification, some cracks can be observed on the surface, which may be caused by cutting and polishing during the sample preparation process.

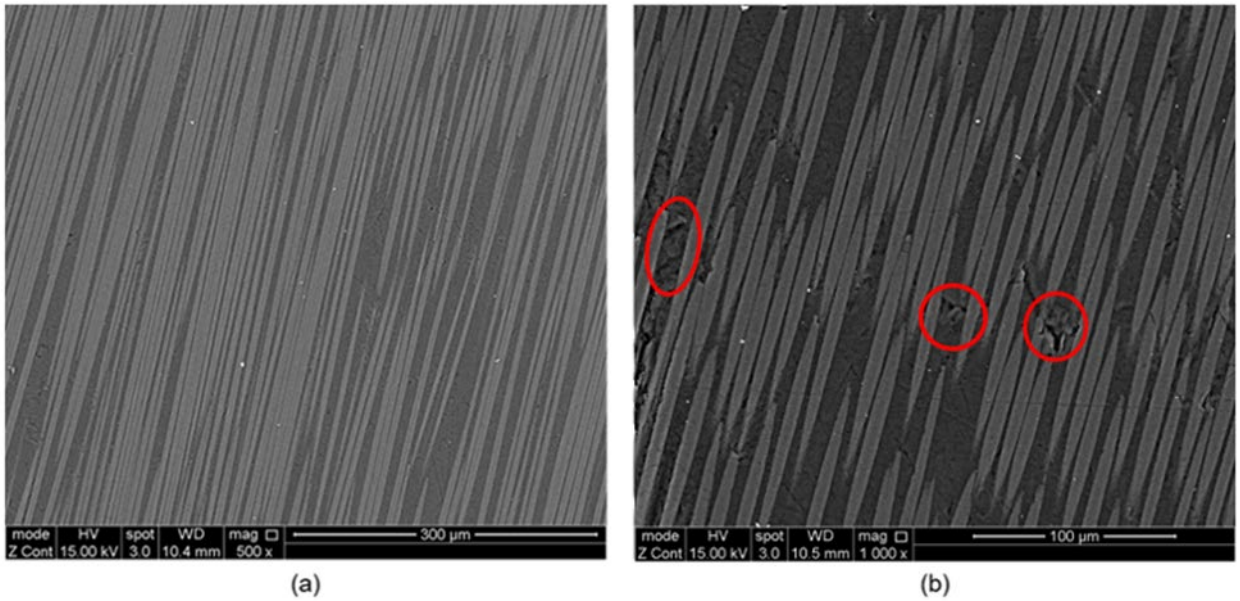

Figure 5.2 SEM images of CFRP with 3 wt.% CB in matrix with different magnification (a) 500x and (b) 1000x.

5.2 Physical properties

To determine the influence of CB on CFRPs (mechanical, thermal and electrical properties), the composite density and fraction of fibre were first examined, which are shown in Table 5.1. With the concentration of CB increasing, the viscosity of the matrix (CB/epoxy resin) will increase. As a result, more matrix will be left in laminate during the vacuum consolidation in the hand layup manufacturing process, which leads to a decrease in the fibre volume fraction. However, this reduction is minimal, with the maximum difference in weight and volume fraction of fibre not exceeding 10%. For unmodified CFRP, the fibre volume fraction is consistently 60 Vol.%. The void volume fraction is estimated to be 6% based on the density readings.

However, the voids are calculated by the density measured from the density balance and helium pycnometry machine. The particle density calculated by the helium pycnometry machine is reliable. However, the bulk density calculated by density balance could be lower than the actual value. When putting the sample in the water in density balance, there are some air bubbles around the sample, which increases the volume of the sample in the calculation. As a result, the calculated void fraction should be regarded as a higher limitation.

Due to the limited volume of the 4-layer carbon fibre CFRP samples, their density was determined using a density balance. The potential influence of voids has been disregarded in this analysis. The resulting density and fibre fraction are presented in Table 5.2. When compared to the 15-layer carbon fibre sample, the fibre fraction in the 5-layer carbon fibre samples is significantly lower. In terms of thinner laminates, the hand layup process may not exert sufficient pressure, resulting in lower effective compaction. Consequently, more resin is deposited in the sample, thereby reducing the fibre fraction.

Table 5.1 The physical properties of CFRP with 15 layers of carbon fibre and different CB wt.% in the matrix. The error is the standard deviation of three samples.

Concentration of CB in matrix (wt.%)	Density[1] (g/cm^3)	Fibre volume fraction (vol.%)	Fibre mass fraction (wt.%)	Void fraction[2] (wt.%)
0	1.46±0.0049	51.26±0.74	62.70±0.69	3.06±0.72
1	1.48±0.0039	53.48±0.59	64.66±0.54	2.95±0.23
2	1.46±0.0009	49.48±0.14	60.83±0.13	2.69±0.52
3	1.45±0.0026	47.20±1.20	59.87±0.38	4.84±0.24

[1]As determined by Helium pycnometry. [2]Determined from helium and density balance data.

Table 5.2 The physical properties of CFRP with 4 layers of carbon fibre and different CB wt.% in the matrix. The error is the standard deviation of three samples.

Concentration of CB in matrix (wt.%)	Density[1] (g/cm^3)	Fibre volume fraction (vol.%)	Fibre mass fraction (wt.%)
0	1.4093±0.0037	43.18±0.57	54.84±0.57
1	1.4073±0.0012	44.02±0.17	54.08±0.17
2	1.4107±0.0025	44.17±0.38	54.12±0.39
3	1.4087±0.0021	43.49±0.31	53.33±0.32

5.3 The resistivity of CFRP under compressive load

Figure 5.3 shows the resistivity of CFRP, with CB, versus pressures. CB, as a conductivity nanoparticle, can efficiently improve the conductivity of CFRP. As expected, at a given pressure, the resistivity of the CFRP with a higher CB concentration is lower. In addition, as the pressure increases, the resistivity of CFRP decreases. This decrease in the resistance is due to the highly sensitive nature of the conduction between the carbon components in the system. The plain weave nature of the composite gives excellent in-plane conductivity. Contacts between the laminate layers in the lower-concentration samples control the through-plane conductivity. For 0 and 1 wt.%, the resistivity versus pressure curve shows similar exponential behaviour. However, for 3 wt.%., the resistivity is considerably lower. The 2 wt.% at low compression pressures follows the 0 and 1 wt.% behaviour. However, as pressure increases, the data more closely resembles that of the 3 wt.% sample. It suggests that at around 3 MPa, a compression of 36.61% percolation is established in the CB in the 2 wt.% sample. Unfortunately, due to the carbon fibre limiting the sideways expansion of the epoxy, Poisson's ratio cannot be determined. Therefore, this result cannot be used to derive a more precise value for the percolation limit in this system.

At the highest concentrations, 3 wt.%, an aspect ratio of around 50 would be expected [290] for the formation of a contacting percolation network within epoxy resin. Conduction, as previously established, is due to electron tunnelling, the probability of which drops exponentially with distance [166]. This tunnelling property of nanomaterials makes them particularly useful for strain-sensing applications.

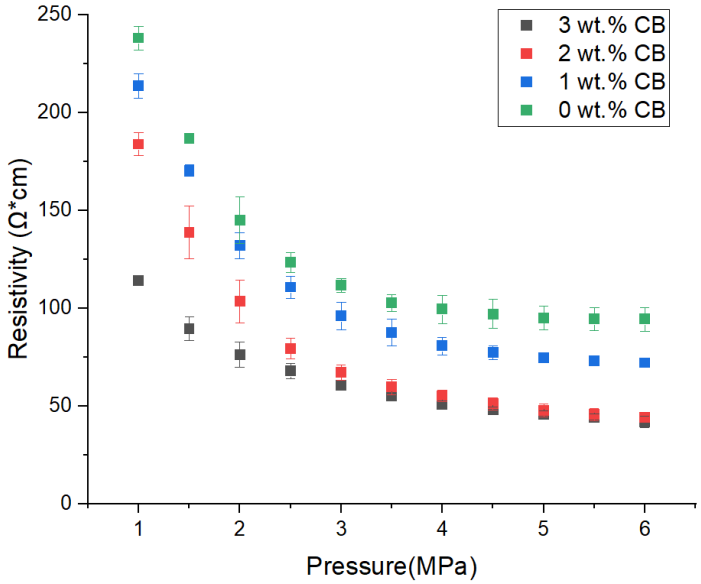

Figure 5.3 The resistivity of cured CFRP with different CB wt.% in the matrix under various pressures. The error bar is the standard deviation of 4 samples.

Figure 5.4 shows the relationship between stress and strain of CFRP with different CB wt.% in the compressing process. In all samples, as the pressure increases, the distance increases linearly. As a result, during the pressing process, the samples are under an elastic deformation region. In addition, the distance is smaller under the same pressure when the CB concentration is higher, though this difference is small, with a maximum value of around 0.2 mm.

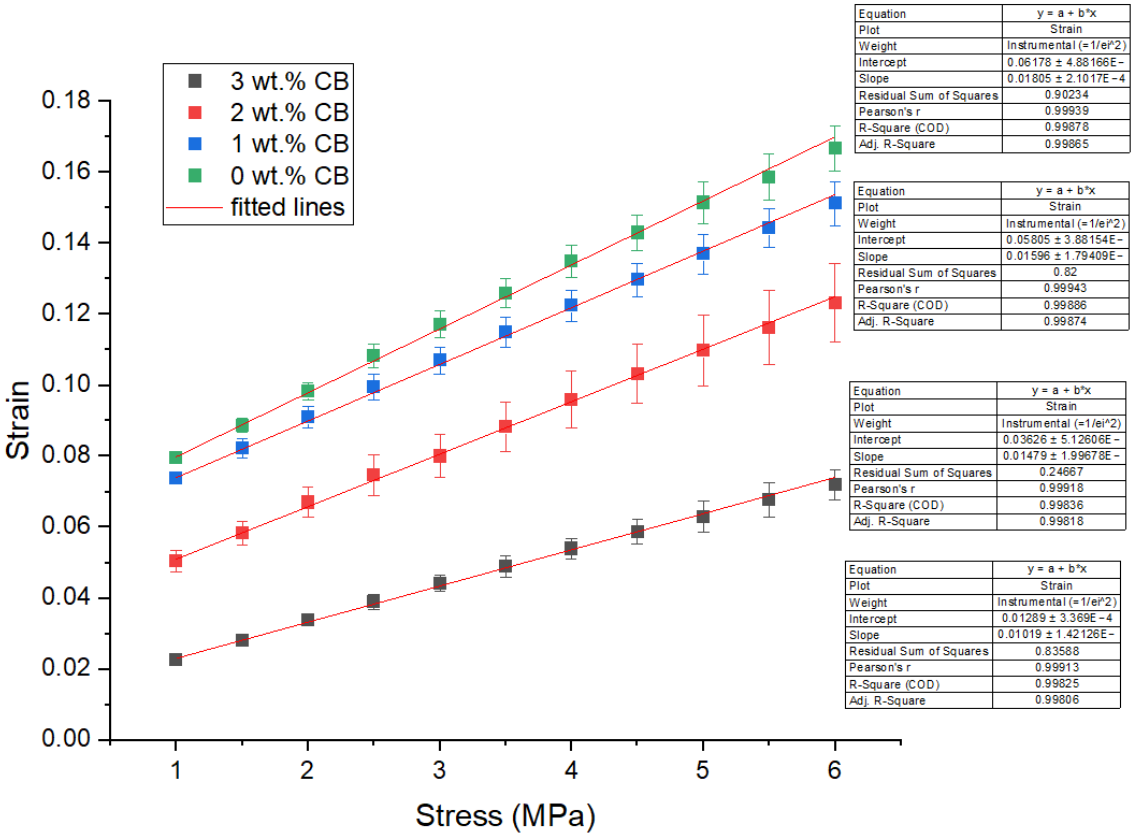

Figure 5.4 The relationship between stress and strain of CFRP with different CB wt.% in the compressing process.

To explain the influence of CB distance on the resistivity of CFRP, the strain value in CFRP with 0 wt.% CB is regarded as a base. Figure 5.5 represents (a) the relationship between resistivity and original strain, and (b) the relationship between resitivity and modified strain During the pressing process, the decrease in sample thickness decreases the spacing between the adjacent two carbon fibre layers, and more conductive CB nanoparticle networks are formed in the matrix between carbon fibre layers. With the strain value increases (CB distance decreases), the resistivity drops exponentially. Conductivity is governed by electron tunnelling, which depends exponentially on the separation of the CB particles. The difference in resistivity at high strain is due to the percolation network. In the low strain, carbon fibre dominates the resistivity. However, in the high strain, CB concentration affects the network formation.

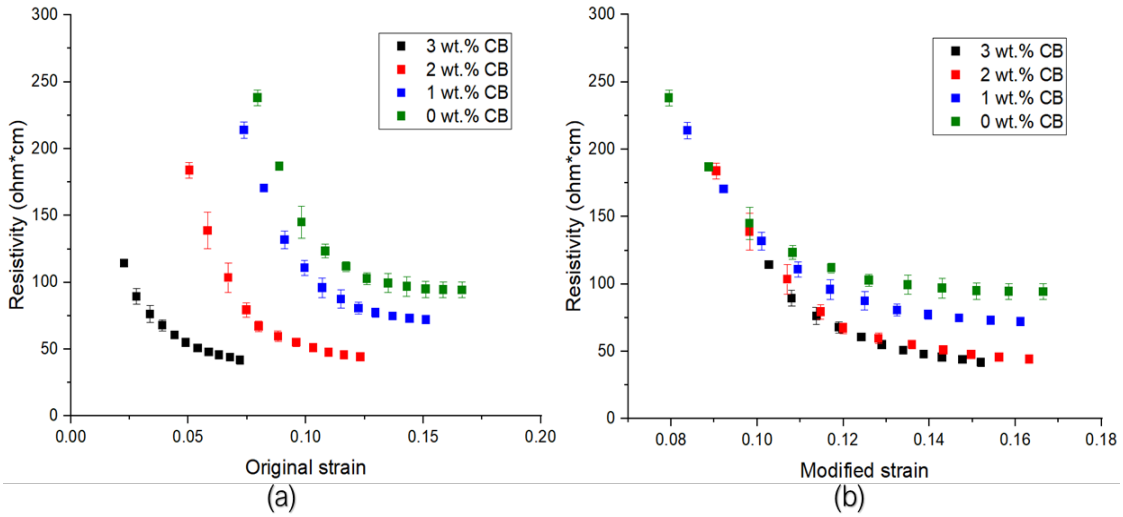

Figure 5.5 (a) The relationship between resistivity and original strain. (b) The relationship between resitivity and modified strain (the data of unmodified CFRP is regarded as the base).

5.4 The mechanical properties of CFRP with different CB wt.%

5.4.1 The tensile properties

The tensile strength and Young's modulus of the cured laminates are shown in Figure 5.6. As expected for a fibre-dominated property, if the CB does not influence the interface, there was no statistically significant change in the tensile strength and Young's modulus of CFRP with different CB wt.% in the matrix. However, to thoroughly test this, an ANOVA test was undertaken. The ANOVA tests show an F value of 0.18613 and 2.16 in tensile strength and Young's modulus, respectively, which is considerably lower than the critical F value of 3.24 when α is 0.05. As a result, there is no statistically significant difference in both the tensile strength and Young's modulus with these different samples.

The results for Young's modulus were compared with the expected values from the rule of mixtures (RoM) (see Equation 5.1 and Table 5.3). As the carbon fibre is a 2×2 twill weave carbon fibre, it is assumed that 50% is tensioned in the loading direction. Young's modulus of the matrix is from the experiment result (see section 4.6.1), and the value of Young's modulus of fibre is from the supplier's datasheet [242]. The experiment result is around 70% of the expected result from RoM. The carbon fabric is a 2x2 Twill, where the warp carbon fibre tow passes under and then over the weft tows, inducing a bend or "crimp" in the tow. In addition, the process of weaving induces damage to the fibres.

These effects have been shown to reduce the tensile properties of the fabric compared to unidirectional fibres [291]–[294]. Therefore, the experiment results are expected to be smaller than the RoM results. As a comparison, in terms of unmodified CFRP, Young's modulus of an out-of-autoclave, vacuum consolidated "2x2 Twill 3k Prepreg Carbon Fibre" of 58 wt.%, or 48 vol.% PYROFILTM TR 30S 3L carbon fibre from Easy Composites, is 55 GPa [295]. The fibre is the same as that used in the experiments. The matrix in this prepreg is not given in the data. However, from the information in the SDS, we can see it is similar to the IN2/AT30 systems (DGEBA/polymeric Amine) and, therefore, would have a modulus similar to that of our matrix.

$$E_c = fE_f + (1-f)E_m \qquad \text{Equation 5.1}$$

Table 5.3 The comparison of the model and experiment result for Young's modulus of CFRP with different CB wt.%

Material	Young's modulus of fibre (Ef)	Young's modulus of the matrix (Em)	volume fraction of fibre(f)	Young's modulus (Gpa)		ratio (experiment result/model result)
				model result	Experiment result	
0wt.%	234	1.86925	0.43	51.38	39.43	0.77
1wt.%	234	2.01335	0.43	51.46	34.52	0.67
2wt.%	234	2.27871	0.43	51.61	33.82	0.66
3wt.%	234	2.2326	0.42	50.43	36.56	0.72

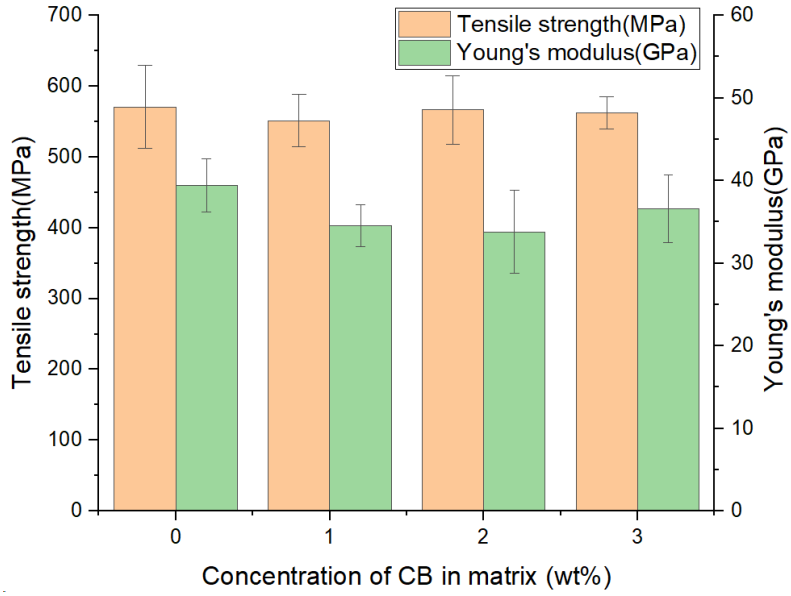

Figure 5.6 The tensile properties of laminate with different CB wt.%. The error bar is the standard deviation of 5 samples.

5.4.2 Fracture toughness of the matrix

Figure 5.7 shows the fracture toughness data for the CB/IN2/AT30S resin composite with different concentrations of CB. Compared with unmodified IN2/AT30S resin, there are significant enhancements in the plane-strain fracture toughness (K_{Ic}) and the critical strain energy release rate (G_{Ic}) of the CB/IN2/AT30S resin composite. 2 wt.%, K_{Ic} reaches its peak, increasing 14% compared with that of unmodified IN2/AT30S resin. When the CB concentration is 3 wt.% CB, G_{Ic} attains its maximum value, increasing by 7% over the resin. As a result, CB nanoparticles can effectively improve fracture toughness and fracture energy release rate of IN2/AT30S resin. The expectation is thus that this will carry over to improved CFRP properties.

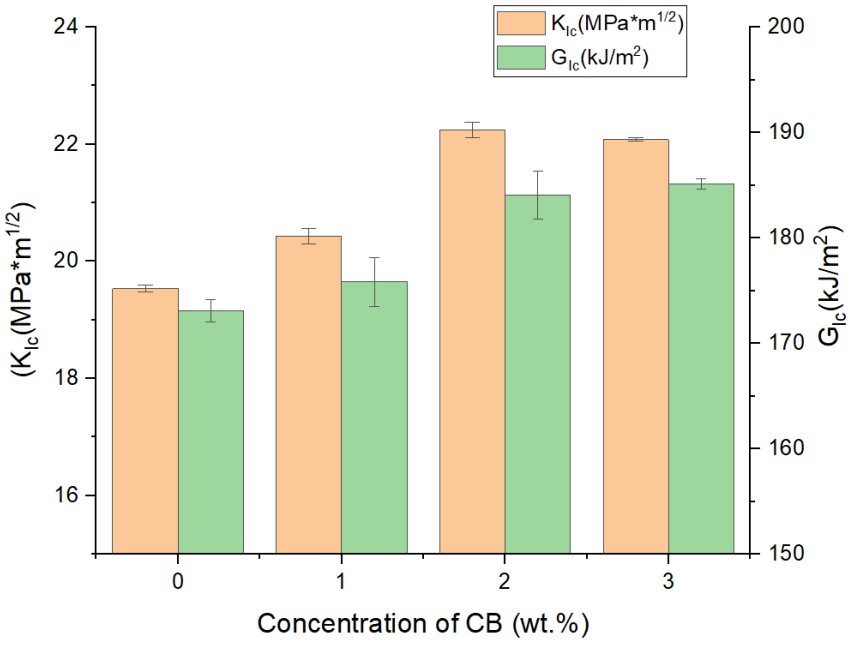

Figure 5.7 The fracture toughness of CB/IN2/AT30S composites. The error bar is the standard deviation of four samples.

5.4.3 Flexural properties

Four-point bend tests determined the flexural strength and flexural modulus of the laminates. The data is presented in Figure 5.8. As the CB concentration increases, the flexural strength increases. When the CB concentration is 2 wt.%, the flexural strength reaches a maximum value of 730.08±12.77 MPa. Compared with the unmodified, 0 wt.% CB laminate, an increase of 31% is observed. When the CB concentration is 3 wt.%, the flexural strength decreases slightly. At higher nanoparticle concentrations, nanoparticles

may aggregate and these act as stress risers, which degrade the properties of the laminate [155]–[157].

Figure 5.8 shows that there is no statistically significant variation in flexural modulus across the series. An ANOVA test gives a p-value of 2.065, which is lower than the critical F value of 3.06 for an α of 0.05. As a result, there is no statistically significant difference in the flexural modulus of elasticity across these samples.

This set of results thus implies that even though the CB particles are expected to have a higher stiffness than the IN2/AT30S resin, the low concentration and fact that the particles are not compressed to the point where they are touching means they do not impede the compression of the resin and thus have no effect on the flexural modulus. However, the CB nanoparticles do impede failure in the system. Nanoparticles are known to prevent crack growth through a variety of mechanisms and thus improve fracture properties, as shown in Figure 5.7. It has also been widely reported in the literature [296]–[300].

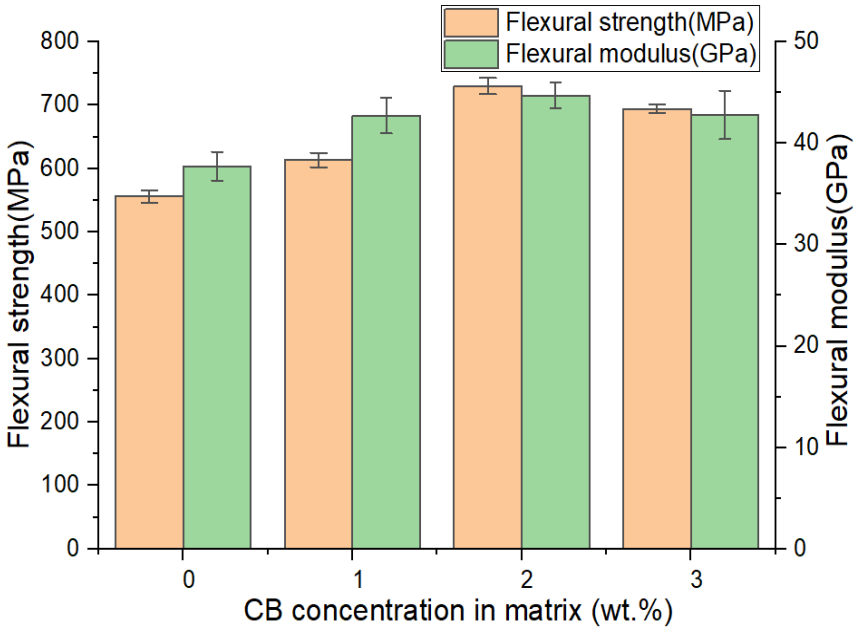

Figure 5.8 The flexural strength and modulus of the laminate with different CB wt.%. The error bar is the standard deviation of 5 samples.

5.5 The through lamella (z-direction) thermal properties

Figure 5.9 (a) and (b) present the z-direction thermal conductivity and thermal capacity of the series of samples over the temperature range 20 to 250 ℃. CB nanoparticles, which have higher thermal capacity and conductivity than epoxy resin, can effectively boost the thermal properties of CFRP at low concentrations. Compared with unmodified CFRP, the thermal conductivity increases by 30% and thermal capacity by 50% of CFRP for 3 wt.%.

For all CFRP samples, there is a significant increase in thermal conductivity and heat capacity with increasing temperature. Compared with the thermal conductivity of laminates at 30 ℃, that of laminates at 250 ℃ increases by 30-40%. The heat capacity of CFRP at 250 ℃ is 80-90% more than that at 30 ℃. There is no noticeable difference in the gradient among different CFRPs; the data shows an offset with some scattering in the data points.

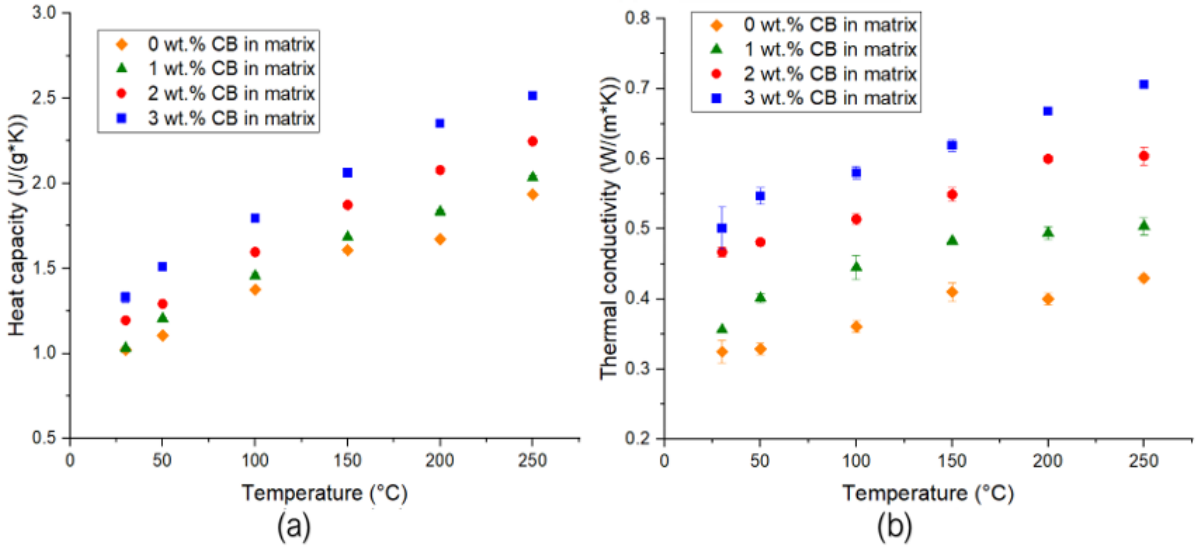

Figure 5.9 (a) The thermal conductivity and (b) the heat capacity of CFRP with different CB wt.% in the matrix as a function of temperature. The error bar is the standard deviation of 3 times measurement, which is no more than 0.03 and not apparent in the graphs.

The experiment data of thermal conductivity was compared to a model result calculated by the rule of mixtures. Equation 5.2 was used to compare the results of the experiment; see Table 5.4. The thermal conductivity of carbon fibre and epoxy resin are taken from the literature [301]–[303], 7 and 0.2 W/(m·K), respectively. As the concentration of CB is small (3 wt.% or 1.74 vol.% maximum in the matrix) compared to that of the carbon fibre (about 50 vol.%), we assumed that the thermal conductivity of CB is the same as that of

carbon fibre. As expected, the thermal conductivity from the experiment is close to the lower bound thermal conductivity from the model. The experiment data measures the thermal conductivity in the z-direction, that is, the direction perpendicular to the fibre axis and should, therefore, be close to the lower bound value.

$$(\frac{f}{k_f}+\frac{1-f}{k_m})^{-1} \leq k_c \leq fk_f+(1-f)k_m \qquad \text{Equation 5.2}$$

Table 5.4 The comparison of model and experiment result for thermal conductivity of CFRP with different CB wt.%

Material	Volume fraction of fibre and CB(f/vol.%)	Thermal conductivity fibre and CB (k_f/ (W/(m·K))	Thermal conductivity matrix (k_m/(W/(m·K))	Thermal conductivity from model (k_c/(W/(m·K))		Thermal conductivity from experiment (k_c)
				lowest	highest	
0wt.%	57	7	0.2	0.45	4.08	0.325
1wt.%	53	7	0.2	0.41	3.80	0.356
2wt.%	50	7	0.2	0.39	3.60	0.467
3wt.%	48	7	0.2	0.37	3.46	0.501

The increase rates of the thermal properties of CFRP with temperature increases are calculated, which are plotted in Figure 5.10. Though the increase rate of thermal properties increases with CB concentration increasing, these increases are not obvious. As a result, the CB nanoparticles improve the thermal conductivity and heat capacity of CFRP by enhancing the properties of the matrix (epoxy resin) and do not significantly affect fibres or the interface between fibres and matrix.

The significant increase in heat capacity around 40% for a 3wt.% addition of CB implies that there is a considerable increase in phonon scattering with the addition of CB. As a result, the CB is well distributed in the resin and not concentrated at the interface.

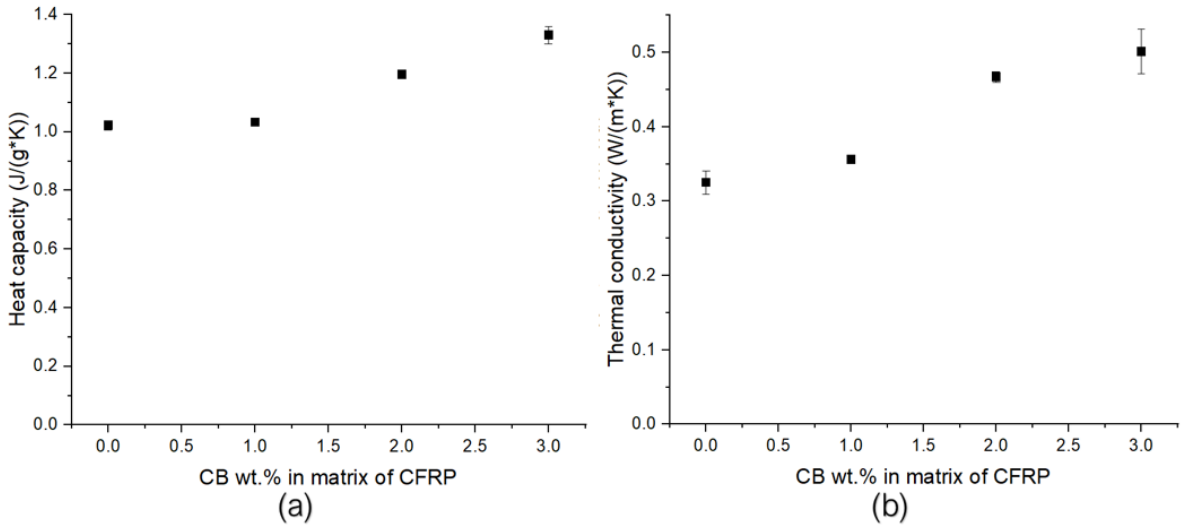

Figure 5.10 (a) The heat capacity. (b) The thermal conductivity of CFRP with different CB wt.% in the matrix at 30 ℃.

5.6 Conclusion

This study investigates the influence of CB on CFRP. SEM analysis is inconclusive as to the location of the CB, but it does not show that CB nanoparticles are agglomerated at the interface. The mechanical and thermal properties suggest that the CB is well dispersed in the matrix and not agglomerated around the fibres. As a result, CB effectively enhances the properties of CFRP by modifying the matrix. When the CB concentration increases to 2 wt.%, CFRP shows the optimal electrical and mechanical performance. This result is consistent with the influence of CB on epoxy resin, as discussed in section Chapter 4.

Chapter 6 Result and Discussion Part 3 – DEC of CFRPs with 2 wt.% CB

The CB particles were incorporated into IN2 resin at 2 wt.% of the epoxy matrix, and the "prepreg" of CFRPs was prepared by hand layup and vacuum consolidation. The samples are manufactured using traditional manufacturing methods (ovens and autoclaves) and direct electrical cure (DEC). The conductivity of the CB fillers enabled four different contact arrangements for DEC. This section discusses the curing process by DEC, the properties of samples manufactured by DEC, and traditional manufacturing methods.

6.1 The physical properties of CFRP with 2 wt.% CB

Table 6.1 represents the physical properties of CFRP samples with 2 wt.% CB, which DEC, autoclave, heat press or oven cured. The fibre volume fraction is elevated in CFRP samples manufactured by the hydraulic press, which includes both the heat press and DEC samples. This is expected as the pressure of the hydraulic press (2 MPa) is higher than that of the oven (0.08 MPa) and autoclave (0.7 MPa). The application of pressure before the curing process leads to some expulsion of the low-viscosity matrix from the samples, with more matrix lost at increased pressures.

Table 6.1 The physical properties of the CFRP samples. (The error is the standard deviation of three samples.)

Curing	Density[1] (g/cm^3)	Fibre volume fraction (vol.%)	Fibre mass fraction (wt.%)	Thickness (mm)	Void fraction[2] (vol.%)
DEC-Inside-Inside	1.42±0.0016	44.36±0.24	55.84±0.24	4.22±0.02	1.54±0.17
DEC-Inside-Outside	1.42±0.0009	44.44±0.14	55.92±0.14	4.38±0.02	3.53±0.27
DEC-Outside-Outside	1.44±0.0079	47.20±1.20	58.63±1.18	4.18±0.04	3.24±0.41
DEC-Top-Bottom	1.45±0.0014	48.41±0.22	59.82±0.21	3.87±0.12	5.09±0.12
Heat press	1.46±0.0009	49.47±0.14	60.83±0.13	3.73±0.03	2.69±0.52
Oven	1.40±0.0125	40.54±1.89	51.95±1.96	4.53±0.05	2.65±0.41
Autoclave	1.41±0.0030	42.20±0.45	53.67±0.46	4.48±0.07	1.47±0.19

[1]As determined by Helium pycnometer. [2]Determined from helium and density balance data, therefore, should be regarded as a higher limitation. See Supplementary Information

As a result of the higher consolidation pressure, the samples manufactured by the hydraulic press have lower thicknesses and higher fibre volume fractions, as shown in Figure 6.1. Although this is not the optimal scenario for comparative analysis, the

maximum discrepancy in the fibre volume fraction is less than 10%. Furthermore, irrespective of the curing method employed, the measured void fraction of the sample remains below 6%. However, it should be noted that this void fraction represents a higher limitation, which has been explained in section 5.2.

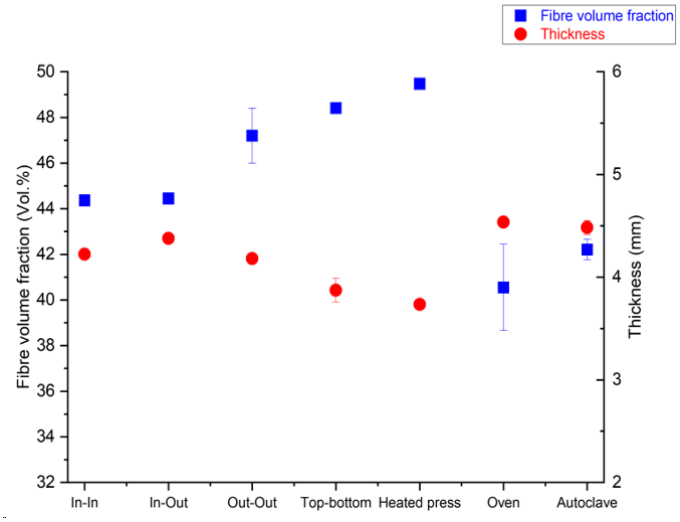

Figure 6.1 The volume fraction of fibre and sample thickness in different manufacturing methods. The value is the average of 3 samples, and the error bar is the standard deviation.

6.2 Resistance changes of 2wt.% CB-CFRP during the DEC process

Figure 6.2 shows that the resistance and central temperature in the middle layer of 2 wt.% CB-CFRPs (see section 3.7.2) in four DEC configurations with time during the curing process. A salient characteristic observed is that during the initial stages of the curing process, there is a sharp decrement in resistance concurrent with the increment in sample temperature. For reasons of health and safety, the rate of temperature increase was confined to about 0.5 ℃/min via manual control and the swift thermal response elicited by minor current adjustments. This rate is inferior to those observed in conventional curing methods, though this can be improved via the implementation of an automated control system.

In this process, Joule heating is responsible for the thermal excitation of the resin, resulting in an initial decline in viscosity as the temperature increases. This lower viscosity accelerated the diffusion of CB nanoparticles. Simultaneously, the polymerization of resin

induced a reaction-induced phase separation (RIPS). In this process, CB nanoparticles form networks that reduce the system's resistance. At a curing time of 75 minutes, the temperature is close to 60 ℃, and the resistance begins to stabilize. At this point, the polymerization degree is elevated, leading to an increase in viscosity and a consequent decrease in the movement of CB nanoparticles. This plateau in resistance is a clear indication that curing is almost complete.

The phenomenon of RIPS is frequently encountered in materials such as polyurethanes, polymer blends, and solutions [304]. The occurrence of phase separation is fundamentally attributed to the decrement in configurational entropy of the polymer in comparison to the monomer [305]–[307]. This phenomenon has been extensively documented in polymer-nanoparticle systems by numerous researchers, thereby establishing its commonality [308]–[310].

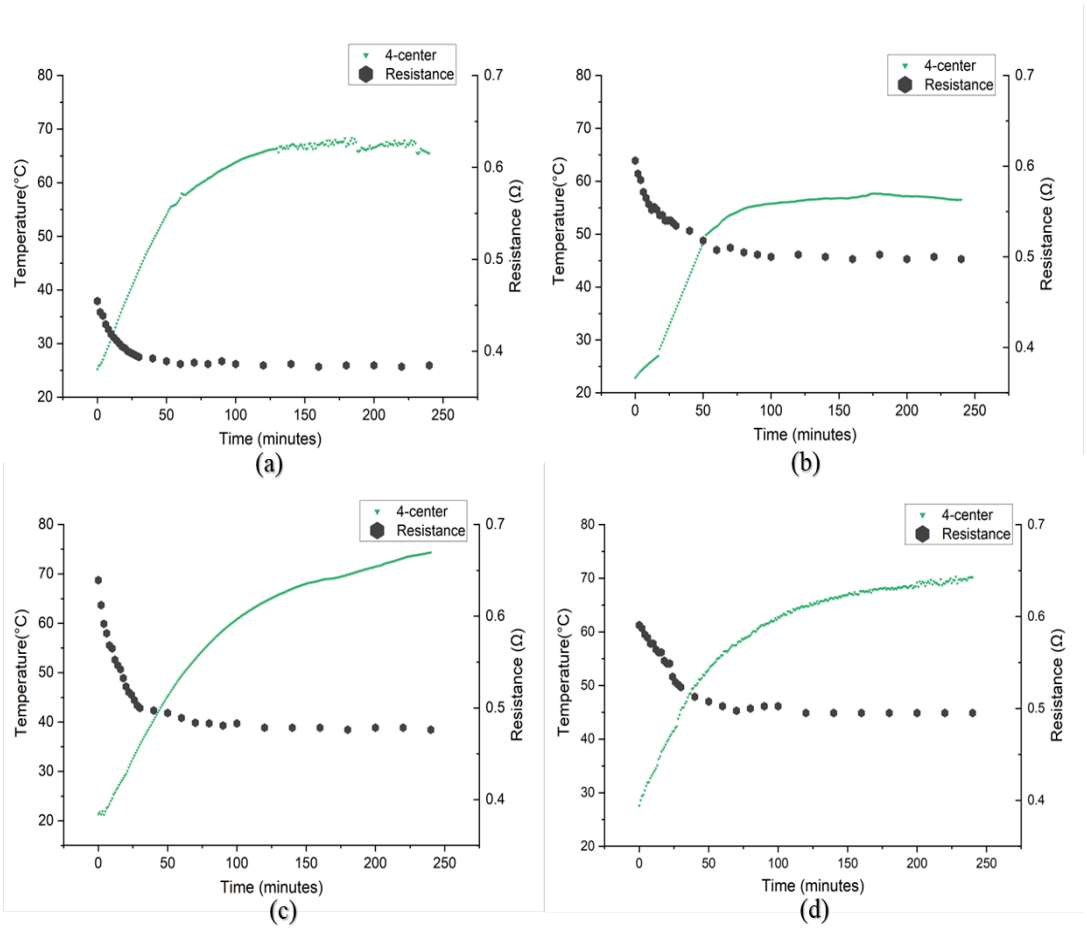

Figure 6.2 The central temperature rise and resistance changes of CFRP with time during the DEC process under different copper contact configurations (a) Inside-Inside (b) Inside-Outside (c) Outside-Outside (d) Top-Bottom.

6.3 The temperature distributions during the DEC process

There is a range of literature that explores the temperature distributions within CFRP during the DEC process. Collinson *et al.* [219] employed an outside-outside configuration of DEC to cure CFRP prepreg. They observed a temperature differential of 11 ℃, marginally exceeding the 7 ℃ differential noted in this study for the same configuration. A 3k plain weave with a vacuum infusion system is utilized, but the consolidation pressure was not mentioned. It is noteworthy that in the study of Hayes [29], there is consolidation pressure with 0.97 bar pressure in the manufacture of CFRP, and the maximum temperature difference is between 15 ℃ and 20 ℃.

Figure 6.3 shows that the temperature differences within a sample are small, with a maximum difference of 10 ℃, which occurs in the Inside-Inside mode. The smallest difference is observed in the Top-Bottom mode, which is half of this at 5℃. As a result, the DEC manufacturing method demonstrates an effective temperature distribution during the curing process.

During the DEC process, the samples are positioned in the heat press, compressed by two unheated steel plates, and electrically insulated by PTFE sheets of 0.3mm thickness. The heat loss is mainly caused by conduction via the PFTE film on the large steel plates. The Top-Bottom configuration situates the large area of electrical contacts immediately adjacent to the PTFE, which, in conjunction with a more uniform current distribution through the thickness of the sample, results in the most uniform temperature distribution. However, even with this configuration, the Top and Bottom temperatures are low due to heat conduction to the platens.

In the Outside-Outside and Inside-Inside modes, the electrodes contact two sides (left and right) of only two carbon fibre plys in Outside-Outside and four plys in Inside-Inside modes. The electrical current predominantly flows through these plys. In the Outside-Inside mode, the current must traverse through the resin layers. Compared with the Top-Bottom mode, the temperature distribution is similar. It implies that the current must flow through most of the sample with the carbon fibre plys at the top and bottom, which effectively function as electrodes. In the Top-Bottom mode, the current permeates through the entire sample. The whole sample thickness generates Joule heating instead of a

localised region. Thus, the temperature distribution in the Top-Bottom mode is more uniform than the other three modes.

Another general feature observed is that in all four DEC modes, the highest temperatures occur in close to positive electrodes, followed by areas close to negative electrodes. This phenomenon is also demonstrated in the DEC study of Collinson *et al.* [219]. The contact resistance at the interface between copper and carbon fibre plays the most significant role here. Furthermore, the elevated temperature of the positive electrode implies that differences in electrochemical potential are influential. Essentially, the positive electrode reverse biases the copper-carbon junction, thereby generating more heat.

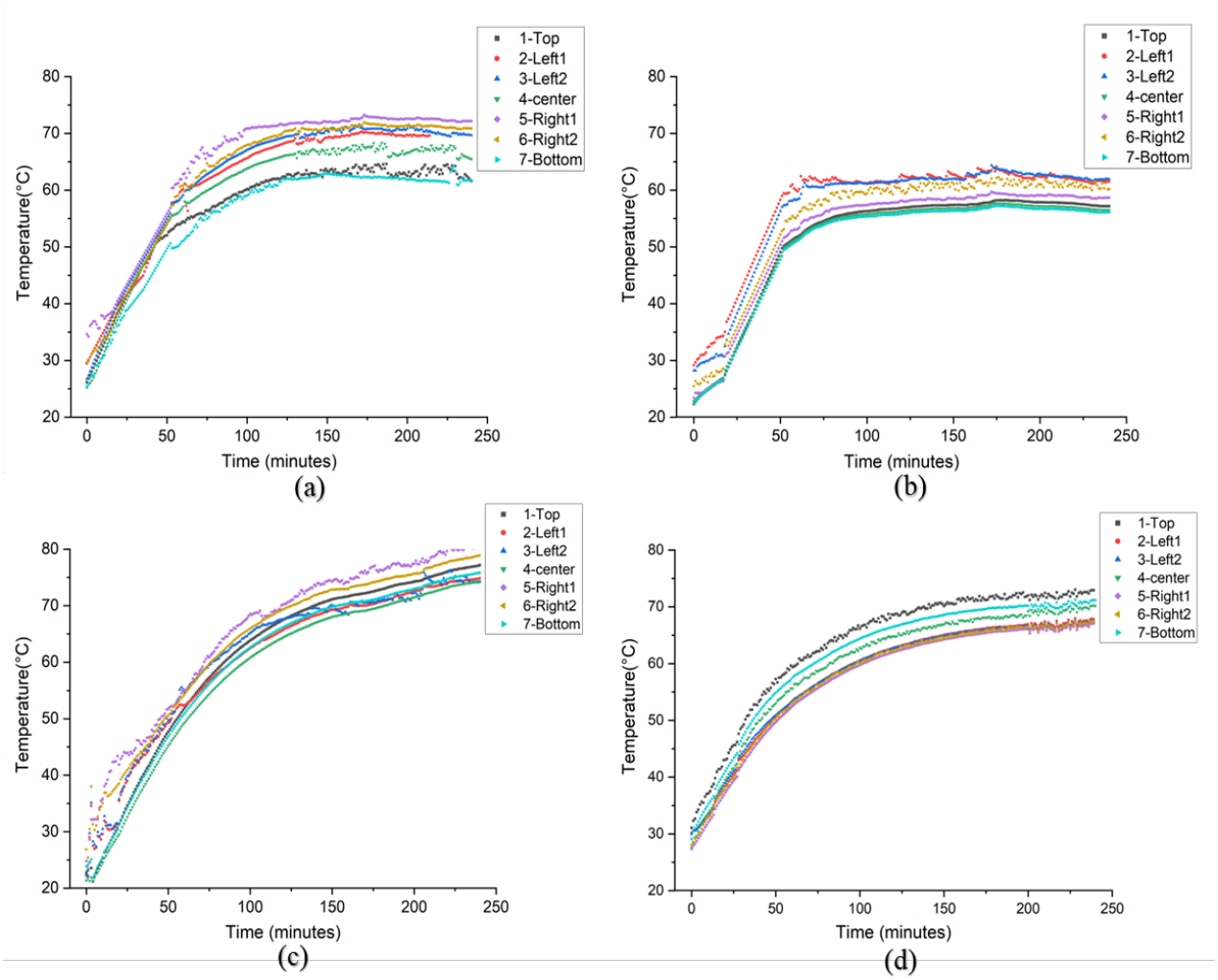

Figure 6.3 The temperature rise of different points in CFRP with time during the DEC process. (a) Inside-Inside (b) Inside-Outside (c) Outside-Outside (d) Top-Bottom

6.4 Comparison of flexural testing for DEC CFRPs with 2 wt.% CB in matrix

Figure 6.4 represents the flexural properties of CFRPs with 2 wt.% CB in matrix. There was no statistically significant change in the flexural strength or modulus of samples manufactured by these different methods. However, to thoroughly test this, an ANOVA test was undertaken. With a significance level, α, set at 0.05, the F-statistics for strength and modulus are 1.55 and 0.72, respectively, falling below the critical F value of 2.69. Consequently, it can be inferred that the flexural strength and modulus of CB-CFRPs manufactured by DEC are commensurate with those manufactured by traditional manufacturing methods.

It is noteworthy that the samples cured in the oven and the autoclave exhibited a slightly greater thickness compared to those subjected to hot pressing and DEC, as depicted in Figure 6.1 and Table 6.1. A review of analogous comparisons in existing literature between DEC and conventional curing methods corroborates the assertion that DEC is on par with traditional methods in terms of flexural properties [29], [224], [311].

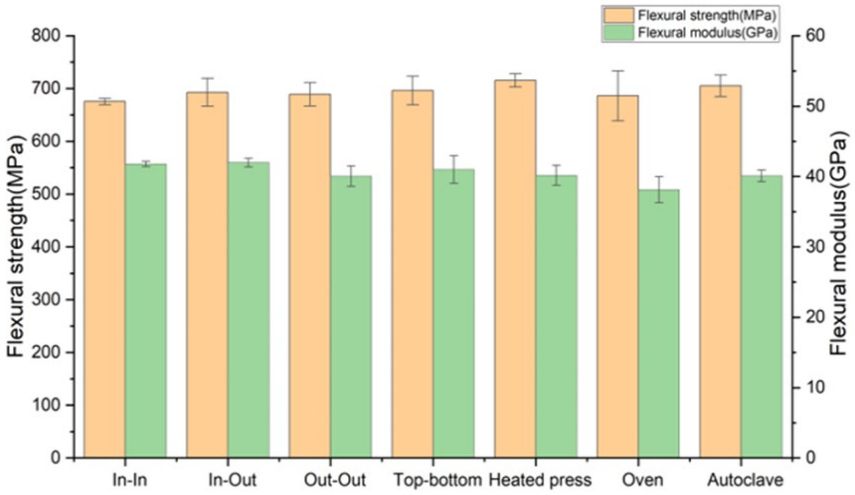

Figure 6.4 The flexural properties of CFRPs with 2 wt.% CB in matrix manufactured by DEC (Inside-Inside, Inside-Outside, Outside-Outside, Top-bottom) and traditional manufacturing methods (Autoclave, Oven, and Heat Press). The average value is from 5 samples, and the error bar is the standard deviation of samples.

6.5 The Degree of Cure (DoC) of CFRPs with 2 wt.% CB

Figure 6.5 shows that the DoC for CFRPs with 2 wt.% CB in matrix. The DoC of samples manufactured by autoclave, oven, and heat press is slightly higher than that of DEC. The

sample manufactured by autoclave has the highest DoC value, which is 99% at the centre and 98% at the edge.

The difference in the DoC between the centre and edge of CFRPs manufactured by traditional manufacturing methods is less than that of DEC, which implies a more uniform time-temperature profile in these systems. For DEC, the maximum difference in DoC between the centre and edge is 2%, corresponding to the sample manufactured by DEC with Inside-Inside mode, which also has the lowest DoC, 90-92%. However, the sample manufactured by Top-Bottom mode has the highest DoC values and the smallest centre-edge difference, about 1%, which compares favourably with the literature [29], [219], [220]. In a comparative study with traditional curing, the Inside-Inside mode resulted in a maximum DoC difference of approximately 2%.

While the incorporation of CB does not entirely rectify the variations in cure, it does reduce differences when combined with the Top-Bottom and Outside-Outside configurations, achieving a level of performance comparable to conventional methods.

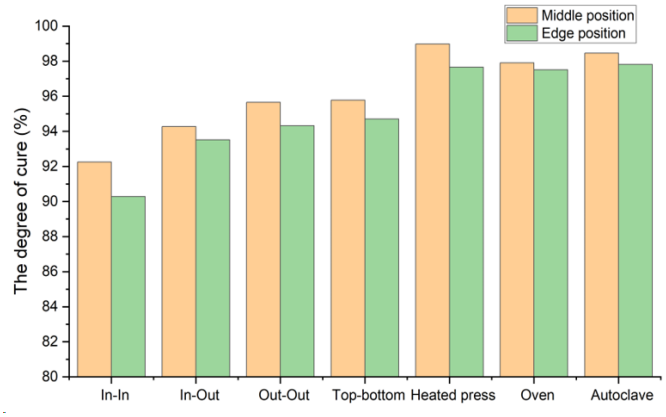

Figure 6.5 The DOC of CFRPs with 2 wt.% CB manufactured in different methods (DEC (Inside-Inside, Inside-Outside, Outside-Outside, Top-bottom) and traditional manufacturing methods (Autoclave, Oven, and Heat Press))

6.6 Energy consumption

Figure 6.6 describes the total energy consumption of CFRP manufacturing using different manufacturing methods. Compared with traditional manufacturing methods, the energy

consumption of the DEC method is significantly lower. As expected, the autoclave is the highest at 559.15 J/mm^3.

In terms of DEC modes, the Outside-Outside and Top-Bottom modes demonstrate the most efficient energy consumption. The energy expenditure in these two modes constitutes 57% and 65% of that in the Inside-Inside mode. The Inside-Inside mode is characterized by a rapid escalation in temperature, an extended high-temperature region, the most substantial temperature fluctuation, and the lowest DoC. This uneven temperature distribution can be attributed to the suboptimal thermal conduction perpendicular to the carbon fibres and the presence of unheated steel plates.

As a result, though DEC can effectively reduce energy consumption, the insulation of the part, as well as electrode placement (avoiding the Inside-Inside mode), needs to be considered more carefully in future work.

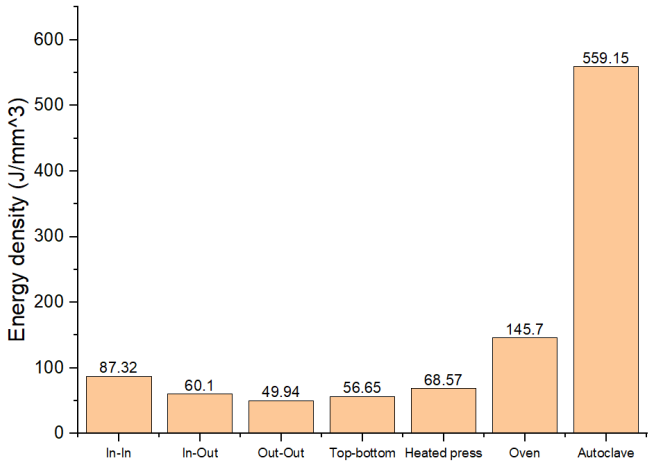

Figure 6.6 The energy density of the curing process in different manufacturing methods

6.7 Conclusion

Direct electrical curing (DEC) emerges as an economically efficient and feasible alternative for the low-energy curing of CFRP. Compared with traditional manufacturing methods, top-bottom modes in DEC significantly reduced energy consumption, which is 8.7% for autoclaves and 33.2% for ovens. The inclusion of 2 wt.% CB into the epoxy resin improves the flexural strength of CFRPs. This addition not only enhances the temperature distribution but also facilitates both the final DoC and the uniformity of cure across an

extensive array of DEC contact modes. In addition, CFRP samples manufactured by DEC show the same good performance on mechanical properties as those by traditional manufacturing methods. The DoC by DEC for equivalent cure times is comparable at 95% but lower than that by traditional curing methods, i.e. 98%.

Chapter 7 Result and Discussion Part 4 – DPIF of CFRPs with 2 wt.% CB

The CB nanoparticles were incorporated into IN2 resin at 2 wt.% of epoxy resin, and the "prepreg" of CFRPs was prepared by hand layup and vacuum consolidation. In this section, a novel CFRP manufacturing method, double-point incremental forming (DPIF) with direct electrical curing (DEC), was proposed. The temperature distribution and changes during the curing process were discussed. The numerical result calculated by finite element analysis is used to compare with the experiment result. In addition, DPIF was compared with traditional manufacturing methods (autoclave and oven) in terms of energy consumption, DoC of the cured sample, and mechanical properties of the cured sample.

7.1 The curing reaction equation building

The DSC curves of the IN2/AT30S resin are shown in Figure 7.1. With increasing heating rate, the exothermic peak narrows; the temperature (T_p) of the peak heat release and the heat flow at this peak increase. When the same curing degree is reached, the corresponding temperature of the sample with a faster heating rate is higher. As a result, the exothermic peak of the curing reaction shifts to the high-temperature direction.

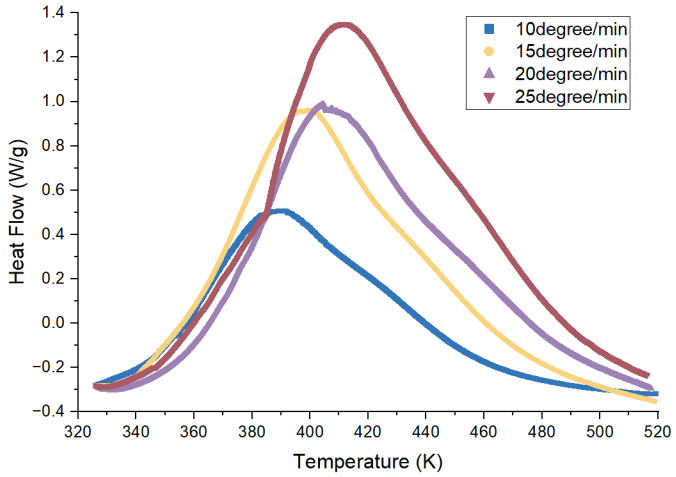

Figure 7.1 DSC curves of IN2/AT30S resin at different heating rates

7.1.1 Kissinger equation

From the DSC data, Kissinger details how the relevant kinetic parameters can be determined [312]. Table 7.1 shows the kinetic parameters of the curing. Then, the plot of $\ln(\beta/T_p^2)$ against $1000/T_p$ and its fit line can be drawn, which is shown in Figure 7.2 (a). The E_a and A values can be calculated, which are 52877±6235.5 J/mol and 0.4866±0.0412 $\times 10^6$ $s^{-1,}$ respectively.

Table 7.1 The kinetics parameters of curing reaction different heating rates

Speed rate β (℃/min)	Peak point temperature T_p (K)	$1000/T_p$	$\ln(\beta/(T_p^2))$
10	390.39	2.56	-9.63
15	401.30	2.49	-9.28
20	404.65	2.47	-9.01
25	411.37	2.43	-8.82

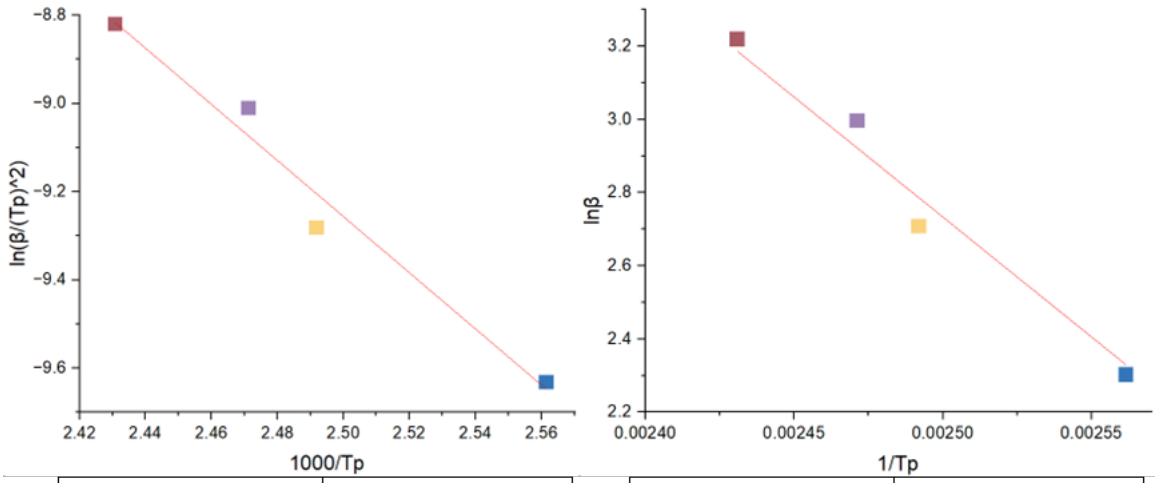

Equation	y = a + b*x
Plot	ln(β/(Tp)^2)
Weight	No Weighting
Intercept	6.64 ± 1.87
Slope	-6.36 ± 0.75
Residual Sum of Squares	0.01013
Pearson's r	-0.9863
R-Square (COD)	0.97279
Adj. R-Square	0.95919

(a)

Equation	y = a + b*x
Plot	lnβ
Weight	No Weighting
Intercept	19.12 ± 1.52
Slope	-6554.79 ± 13.45
Residual Sum of Squares	0.01344
Pearson's r	0.99017
R-Square (COD)	0.99958
Adj. R-Square	0.99944

(b)

Figure 7.2 (a) The plot of $\ln(\beta/Tp^2)$ against (1000/Tp) and (b) the plot of ln(β) against (1000/Tp). Fit to straight lines, the output to the fit is in the tables below the figures (OriginPro).

7.1.2 Crane equation

The Crane equation is used to determine the order of reaction (n). The plot of $ln(\beta)$ against $1/T_p$ and its fit line can be drawn, which is shown in Figure 7.2 (b). The n value is 0.97±0.02. This data is close to the reference [313], [314].

As a result, the curing reaction equation can be built as Equation 3.8.

$$\frac{d\alpha}{dt} = 486600 \cdot e^{\left(\frac{52877}{8.314 \cdot T}\right)} \cdot (1-\alpha)^{0.97} \qquad \text{Equation 7.1}$$

7.2 The consolidation load changes during the DPIF process.

Figure 7.3 shows the consolidation load changes in the curing process when the copper tools press the sample to 160N and keep it in the same position. As the composite is cured, the epoxy resin's density increases. It is a common occurrence in polymerisation and is referred to commercially as "shrinkage". If the external tools are kept at fixed positions during this process, the force they experience will reduce as this shrinkage occurs. Thus, the change of force over time gives a measure of the process of curing. However, it does not provide a reliable measure of the degree of polymerisation, but it is sufficient to indicate that the tools can move to the next step in the process. In this process, the DoC of the sample and the stiffness of the sample increase. After 60 seconds, the DoC of the sample is high, and the change in stiffness is small. As a result, the decrease in load is slight. If increasing the time, the curve will be close to stable.

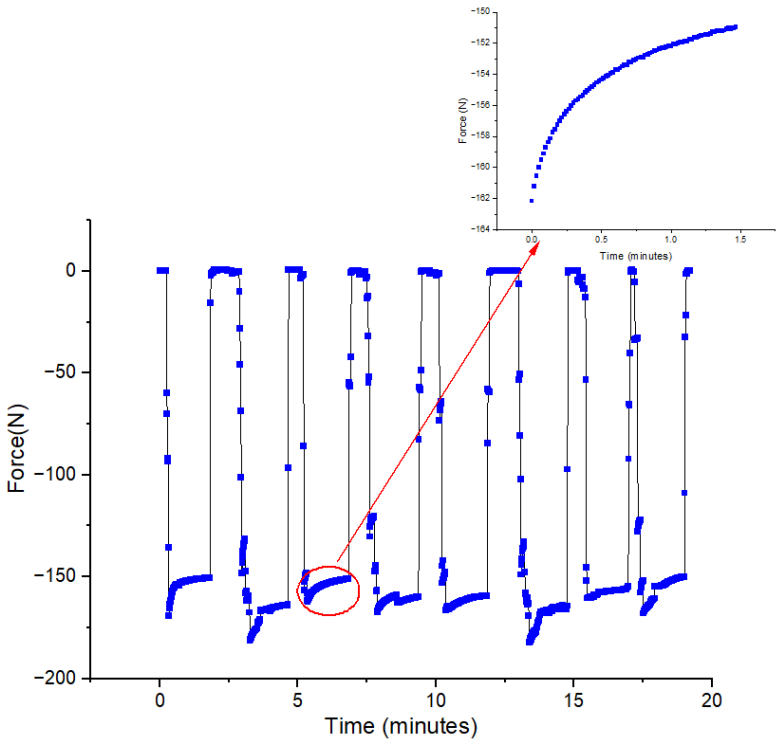

Figure 7.3 The load change during the DPIF process in the first 60 minutes.

7.3 The temperature changes during the DPIF process.

The temperature changes of the copper tools for one DPIF point are discussed to analyse the temperature control and heat transfer of the sample during the DPIF process.

7.3.1 The temperature changes on the inside of copper tools.

Figure 7.4 shows the temperature changes inside the copper tools during the DPIF process. In the first 20 mins, the temperature, as measured by the thermocouples on the copper tools, increases to 80 ℃ and 70 ℃ for the top and bottom tools, respectively. Then, the temperature was controlled at 70-90 ℃ for the top tool and 60-80 ℃ for the bottom tool. This temperature fluctuation is due to the manual power control. The temperature quickly reduced when the tools were moved away from the sample. In addition, the higher temperatures for the top tool, which is connected to a positive electrode, suggest that differences in electrochemical potential play a part. In essence, the positive electrode reverse biases the copper-carbon junction and thus generates more heat.

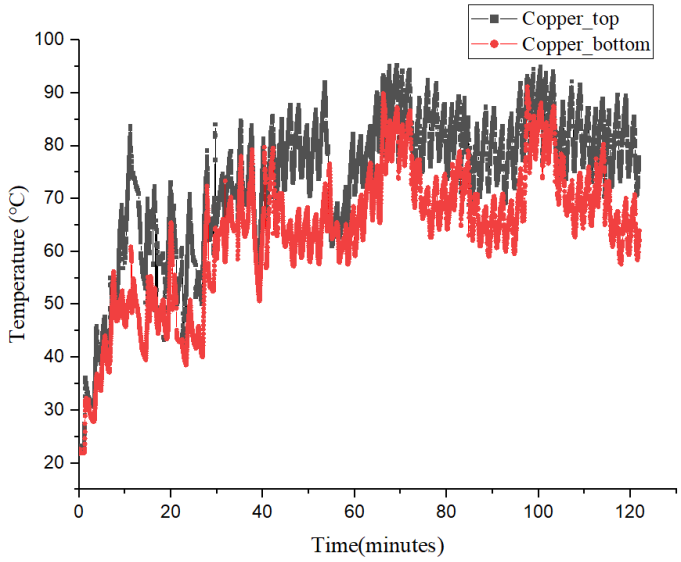

Figure 7.4 The temperature changes of copper tools during the DPIF process in the first 120 min (there is no noticeable change after 120 min).

7.3.2 The temperature changes of a fixed point in the sample

Figure 7.5 shows the top, middle, and bottom temperature changes of a point in the sample, which is about 30mm in the x direction from the start cure point. In the red circle, the copper tools directly contacted the electrically insulated thermocouple. In the blue circle, the tools passed close to the thermocouple. The thermocouples show both a rapid temperature rise (130 ℃/min) and a rapid cooling (100 ℃/min). The thermocouples also show a significant difference between the top and middle contacts, 185 and 165 ℃, respectively. As it already stated and observed by other authors, the difference in temperature between the top (closed to the positive electrode) and bottom (closed to the negative electrode) is seen in the DC electrically cured systems [219], [311].

According to a simplified numerical analysis that only considers the heat transfer between the sample surface and its middle from a heated tool, the temperature difference is expected to be 70 ℃. However, the clear advantage of Joule heating is that it reduces this to the observed 20 ℃. As a result, the DoC distribution in the z direction is more uniform (the specific analysis can be seen in section 7.4).

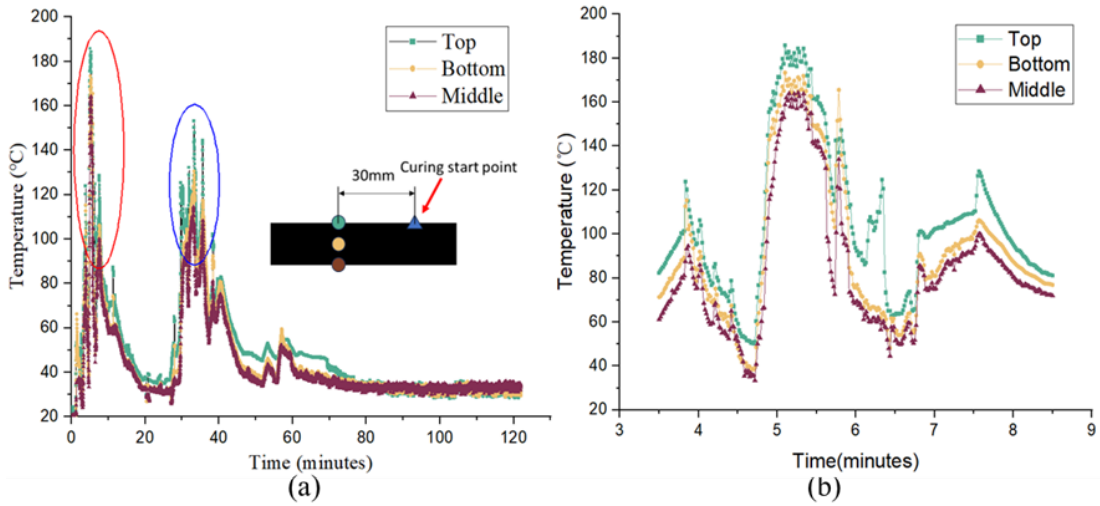

Figure 7.5 The temperature recorded by the thermocouples at the top, middle, and bottom positions of a fixed point in the sample, which is 30 mm in the x direction from the start point during the DPIF process. (b)The magnified image for the red circle in Fig (a) is from 3.5 to 8.5 minutes.

7.4 The DoC changes at a fixed point during the DPIF process.

From the Arrhenius equation (see Equation 7.1), derived from the DSC analysis, and the temperature profiles in Figure 7.5, the DoC changes at a fixed point during the DPIF process can be estimated, which is shown in Figure 7.6. When the prepreg was prepared, it was left to cure at 20 ℃ for 16 hours partially. Thus, the initial DoC is 62%. In the curing process, there are two rapid growth periods in DoC, which are marked by red and blue circles, corresponding to those in Figure 7.5. In the first period, when the copper tools directly contact the fixed point, the DoC of the surface position is over 90%, and the DoC of the middle position is 85%. When the tool moved through one loop and returned to a position close to the fixed point, the DoC of the points increased for all positions to over 90%.

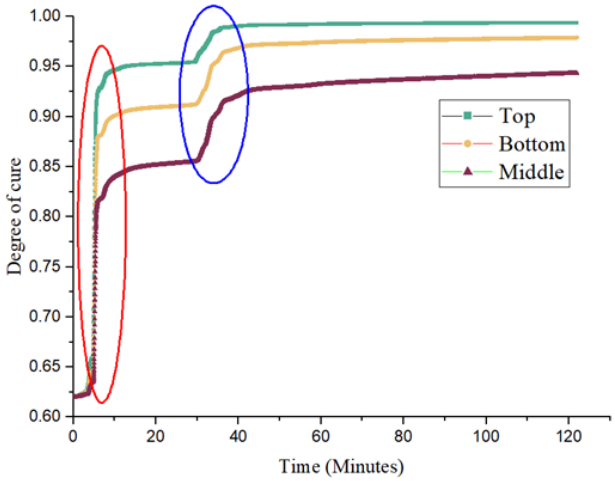

Figure 7.6 The DoC changes at the fixed point during the DPIF process

7.5 The numerical simulation compared with the experiment.

7.5.1 The temperature change of a fixed point

The time evolution of temperature in a fixed point 30 mm from the start position is shown in Figure 7.7. The simplified numerical simulation is shown as the blue open symbols, and the experiment recorded by the thermocouple is the red closed symbols. The difference between the two results is small in the heating process. As a result, the numerical result of CFRP can be used to estimate the temperature distribution during the DPIF process. The simulation does not model the heat loss effectively, as can be seen in comparisons of the cooling profiles between 15 and 25 minutes and after 40 minutes. Due to the simplified model, this numerical result can only be regarded as a crude approximation.

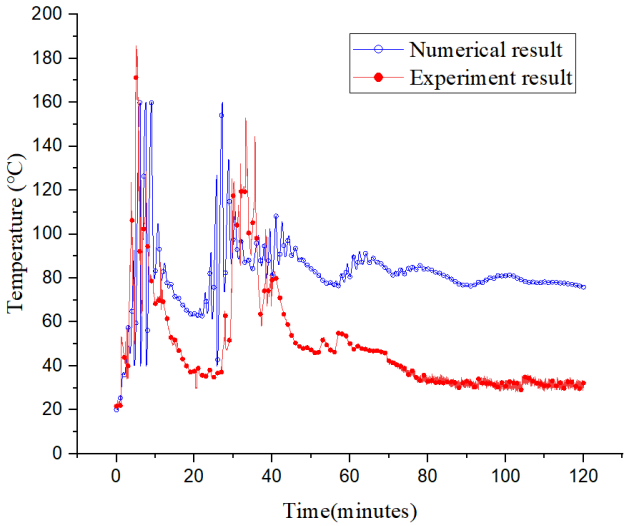

Figure 7.7 The experimental (red closed symbols) and simulation (blue open symbols) temperature changes at the fixed point during the DPIF process

Figure 7.8 shows the DoC from the experiment result and numerical result. In the numerical result, the DoC value rapidly increases and is close to 1 in a short time. However, the increased speed in the DoC of the experiment result is lower. The difference in DoC indicates that the numerical result did not consider the heat loss effectively. As a result, to reduce the difference, the FEA module will need to consider the heat loss of the sample in the curing process.

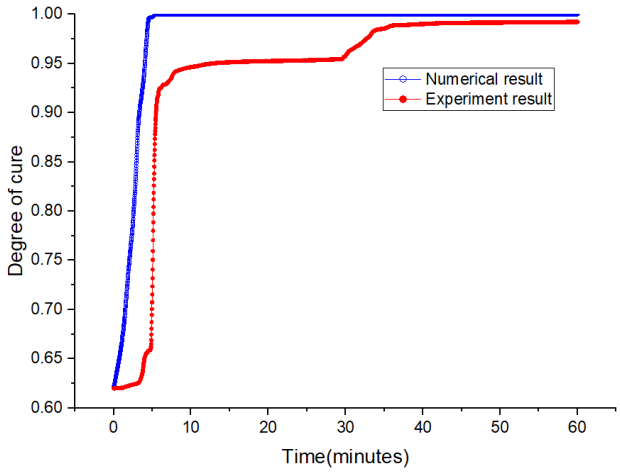

Figure 7.8 The DoC from the experiment result and numerical result

7.5.2 The temperature distribution of the sample surface

Figure 7.9 shows the temperature distribution of the sample during the DPIF process, as measured by a FLIR thermal imaging camera (left) and the simulation results (right). The images from the thermal imaging camera show that the heat distribution from the cure point is a cross, although this feature is weak. Due to the woven nature of the carbon fibre, the thermal conductivity along the fibre (K_{11} and K_{22}) are higher (about 7 W/(m·k)), but at 45 ° to the fibre axis (K_{12}) is much lower (about 0.3 W/(m·k)). In the simulation, K_{12} and K_{23} are defined as the thermal conductivity of resin, which did not consider the influence of carbon fibre. Figure 7.10 describes the temperature data from the numerical result and IR image at different positions when the heating position is 60 mm X. There is no significant difference between the two data groups. As a result, numerical results can be used to simulate the temperature distribution around heating resources.

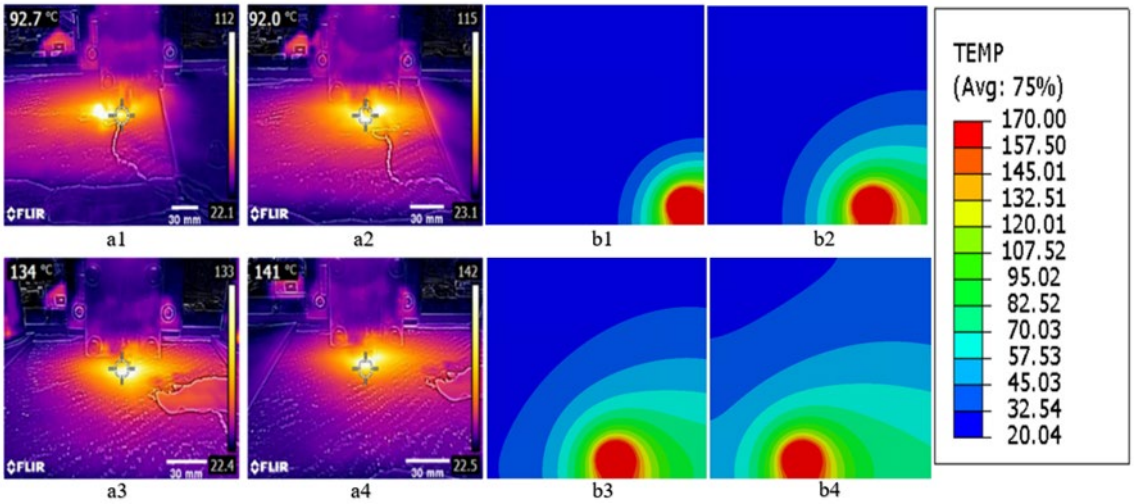

Figure 7.9 The temperature distribution measured by the thermal imaging camera and the numerical result when heating points at (1)0 mm, (2)20 mm, (3)40 mm, and (4)60 mm. The camera cannot image the area directly beneath the tool, which is the red area in the simulation.

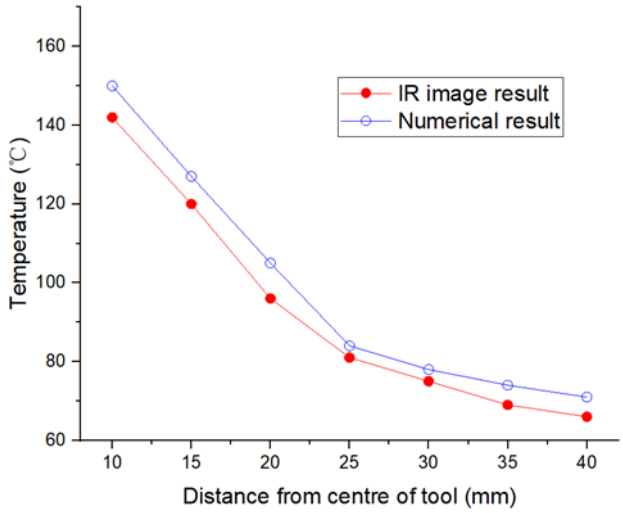

Figure 7.10 The temperature distribution from the numerical result and IR image results when the heating point at 60 mm

7.6 The cure problem in the DPIF process

In the DPIF process, the sample is consolidated, and this leads to a deformation of the surface. Figure 7.11 shows that there is obvious deformation at the top, where the tools first contact the sample, due to the consolidation pressure. Here, a 45° orientation was chosen to highlight the effect. However, this deformation is not apparent in the second and later rows in the curing path. Figure 7.12 shows the temperature changes measured

by the simulation result and DoC changes calculated by temperature and Arrhenius function at three different points: 0, 15 and 30 mm (marked in Figure 7.11, as red, blue and green points, respectively). When consolidating the points in the first row (0 mm), the DoC and stiffness of these points are low. As a result, high pressure leads to the deformation of the sample. However, when heating the points in the 2nd and later row (15 and 30 mm), due to the heat transfer from the tools passing on the 0 mm pass, the initial DoC is higher, and the deformation is not observed. This effect is present in all but the first row of curing. When curing the point at 15 mm and the point at 30 mm, the initial DoC is around 0.8 compared with 0.62 for the first point. As a result, when pressing points in the 2nd or later row, the stiffness is higher and no obvious deformation at the same external load.

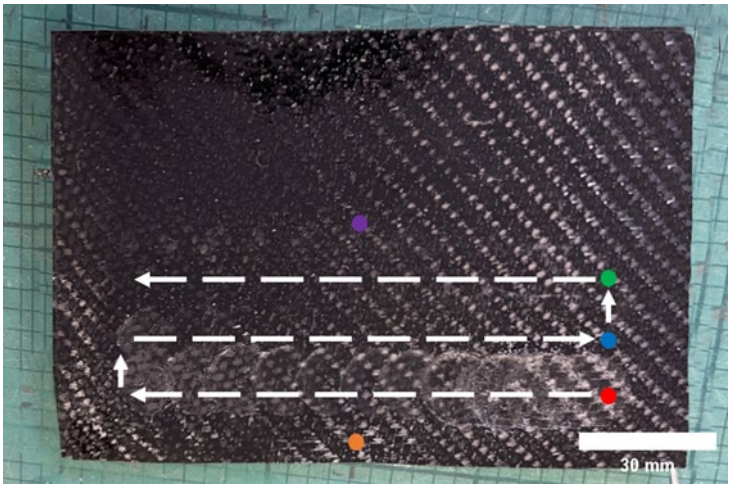

Figure 7.11 The back profile of the CFRP sample cured by DPIF (red:0 mm, blue:15 mm, green: 30 mm, orange is on edge, purple is in the centre. The white dash line with arrow shows the movement path of tools).

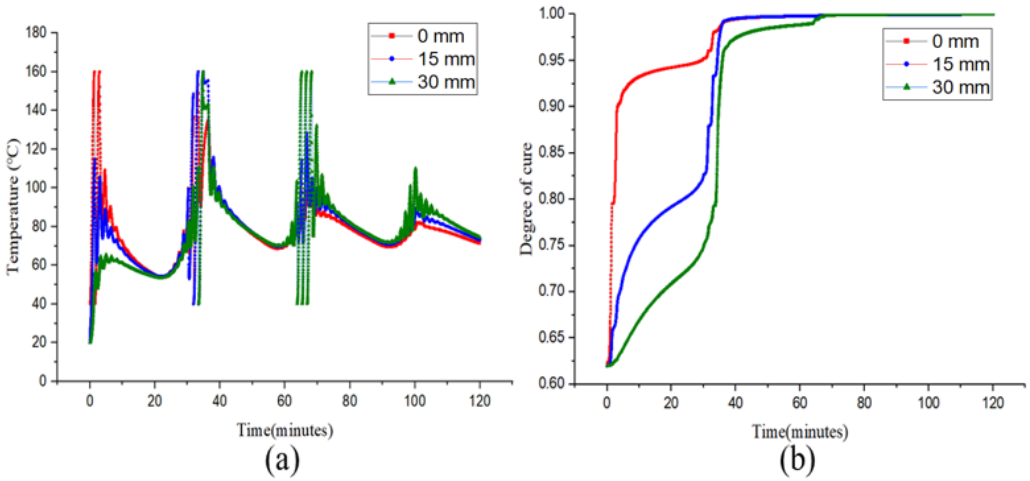

Figure 7.12 (a) The temperature changes collected from the numerical result and (b) DoC changes calculated by temperature and Arrhenius function at three different points 0, 15 and 30 mm during the DPIF process.

7.7 Physical properties

Table 7.2 compares the physical properties (composite density and volume and mass fraction of fibre) of DPIF aminates versus those manufactured by traditional techniques. Samples manufactured by DPIF have the same physical performance as those manufactured using traditional manufacturing methods.

Compared with other manufacturing methods, due to the high pressure in the curing process, the void content of the autoclave cured samples is the lowest, at around 1 vol.%. Due to the effect of the contact arrangement, the void content is higher in the DEC manufacturing method than in other manufacturing methods. In addition, the voids are calculated by the density measured from density balance and helium pycnometer. The density calculated by the helium pycnometer is the more reliable, as the helium penetrates small crevices and holes in the sample. However, the bulk density calculated by density balance could be lower than the actual value. When immersing the sample in the water in density balance, there are probably some air bubbles trapped around the sample, which increases the volume of the sample in the calculation. As a result, the calculated void fraction should be regarded as a higher limitation.

Table 7.2 The physical properties of CFRP with different manufacturing methods. The error is the standard deviation of three samples.

Manufacturing methods	Composite density (g/cm^3)	Fibre volume fraction (vol.%)	Fibre mass fraction (vol.%)	Thickness (mm)	Void fraction (vol.%)
DPIF	1.39±0.008	39.3±1.24	50.6±1.3	4.25±0.01	2.19±0.80
Oven	1.40±0.0125	40.54±1.89	51.95±1.96	4.53±0.05	2.65±0.41
Autoclave	1.41±0.0030	42.20±0.45	53.67±0.46	4.48±0.07	1.47±0.19

7.8 Mechanical properties

This study considered tensile tests and flexural tests to discuss the influence of different manufacturing methods on the mechanical properties of CFRP.

7.8.1 Tensile properties

The tensile properties (tensile strength and Young's modulus) of CFRP are shown in Figure 7.13. In this project, the fibre used is 2x2 twill weave fibre, and the loading direction is along the fibre in the tensile test. As a result, this is a fibre-dominated property. As expected, there was no statistically significant difference in the tensile strength and Young's modulus of CFRP samples. The ANOVA tests show an F value of 2.5 and 0.06 for the tensile strength and Young's modulus data, respectively, with critical F values of 3.48 for a level of significance, α of 0.05. Thus, there is no statistically significant difference in both the tensile strength and Young's modulus in these samples. Therefore, DPIF manufacturing does not significantly damage the carbon fibre and does not degrade its mechanical performance.

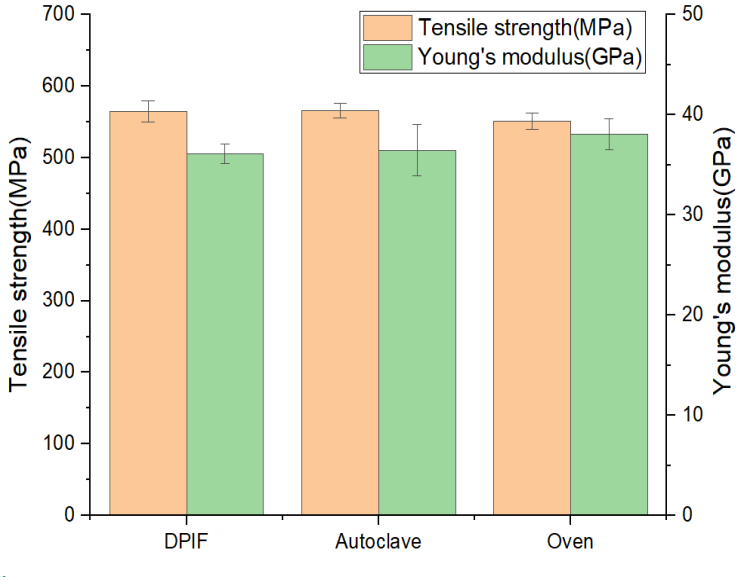

Figure 7.13 The tensile properties (tensile strength and Young's modulus) of CFRP with 2wt.% in the matrix manufactured in different methods. The average value is from 5 samples, and the error bar is the standard deviation of samples.

7.8.2 Flexural properties

Figure 7.14 shows the flexural properties (Flexural strength and Flexural modulus of elasticity) of CFRP samples with 2 wt.% CB in the matrix. ANOVA test was used to analyse the difference in flexural strength and flexural modulus of 12 samples between the manufacturing methods. For an α of 0.05, the F value is 1.248 and 1.959 in flexural strength and modulus, respectively. Both are far lower than the critical F value of 4.07. As a result, compared with the traditional manufacturing methods, DPIF shows no statistically significant difference in flexural properties.

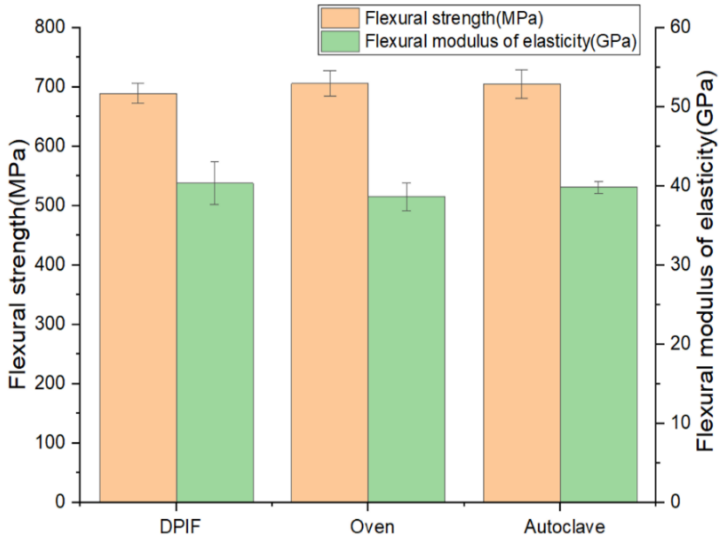

Figure 7.14 The flexural properties (flexural strength and modulus) of CFRP with 2wt.% in matrix manufactured in different methods. The average value is from 4 samples, and the error bar is the standard deviation of samples.

7.9 The DoC of samples manufactured in different methods

Figure 7.15 shows the DoC of middle and edge positions in samples manufactured by the different methods. The DoC of the middle in all samples is high, over 0.95. However, the DoC of the edge position in the sample manufactured by DPIF is the lowest of the three manufacturing methods, which is only 0.87, and is significantly lower by about 0.09 than that of the other manufacturing methods. The reason for this is discussed in section 7.6 and Figure 7.12 above. In the edge position (purple circle), the sample was not directly heated by tools. The heat energy is from the heat transfer when heating the 1st row in the sample, which is lower than that in the centre position. However, due to the chamber heating, this difference is tiny, close to 0.02, in the autoclave and oven. All in all, DPIF shows good uniformity in DoC beyond the first passes of the tool.

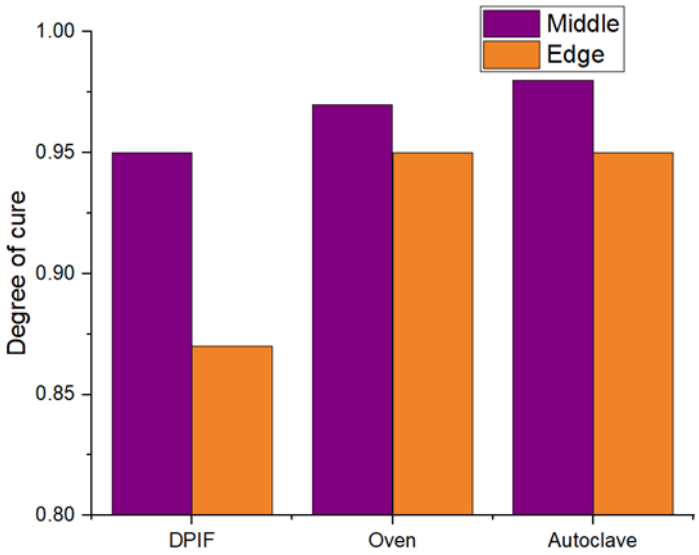

Figure 7.15 The DoC of the middle and edge in the sample manufactured by different methods.

7.10 Energy consumption

Energy consumption is an essential economic factor when considering manufacturing operations. Whilst it must be recognised that the highest greenhouse gas contribution is in the manufacture of carbon fibre, any method that limits greenhouse gas emissions in manufacturing is beneficial. The energy consumption of the different manufacturing methods is shown in Figure 7.16. Compared with autoclave and oven curing, the energy consumption of DPIF is low. In terms of 15 plies, the energy consumption of DPIF is only 4% and 15% of that of autoclave and oven, respectively. In addition, when comparing the energy consumption for different sample thicknesses, i.e. between 15 and 5 plies, the energy consumption was reduced by 57.5%. However, this change is negligible for oven and autoclave cure, which is only 6.1% and 6.9%, respectively. Indicating the significant energy expended to heat the ovens and autoclaves as opposed to the part. As a result, DPIF is a cost-effective method to produce parts using carbon fibre.

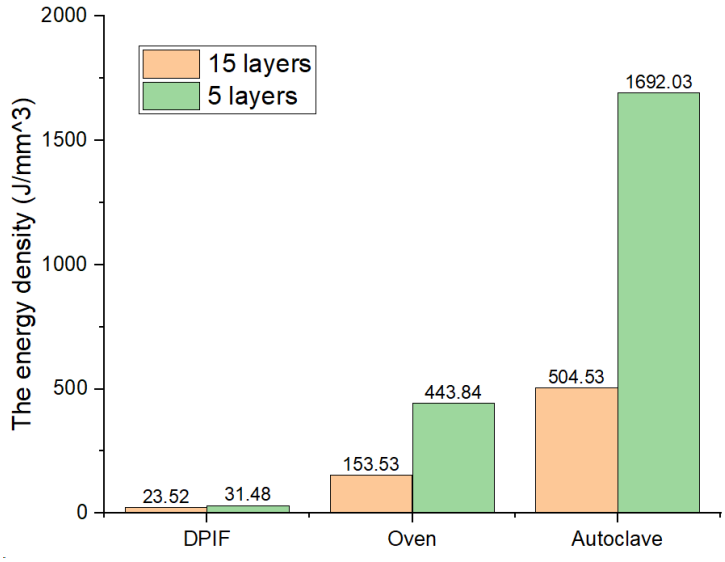

Figure 7.16 The energy density of different manufacturing methods.

7.11 PID control

To control the curing temperature, a PID control system in LabVIEW is used to adjust the current (to a maximum value of 10A) of the power supply to stabilise the temperature of the top copper tool. The PID is proportional gain (K_c) 20, integral time (T_i) 0.008, and derivative time (T_d) 0.001. To preheat the copper tools, the first point is heated for 90 seconds. After this, the first point, each point is heated for 30 seconds. Figure 7.17 shows the temperature changes of the top and bottom tools (see section 3.9.2) during the curing process under PID control. Under PID control, the temperature of the top tool is stabilized. The cyclical fluctuation in temperature is due to the heat loss when the copper tools move away from the sample. In addition, the maximum temperature difference between top and bottom tools also is less than 10 ℃. With the set temperature reduced, this difference is smaller.

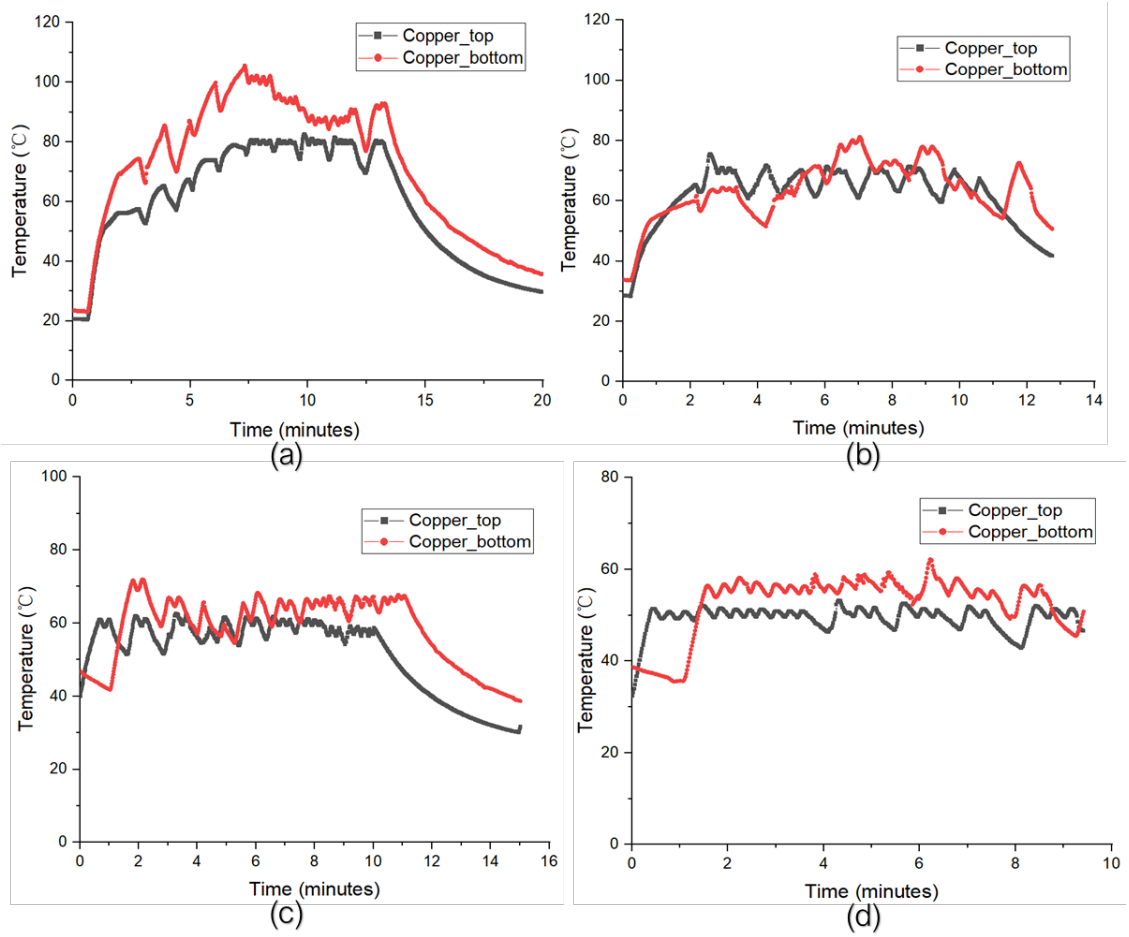

Figure 7.17 The temperature changes of the top and bottom tools during the curing process under PID control, as measured by the two thermocouples. The temperature of the inside copper is set to (a) 80℃, (b) 70℃, (c) 60 ℃, and (d) 50℃.

Table 7.3 shows the surrounding temperature, DoC and cure point temperature. An IR camera measures the surrounding temperature. Because the copper tools block the line of sight of the IR camera, the cure point temperature cannot be measured. Therefore, based on the DoC value and cure time, the cure point temperature is simulated using a numerical approach with the Arrhenius equation. The Arrhenius equation simulates the process of the cure for the DoC prepreg, which starts at 62% cured. As a result, this approach can effectively simulate the cure process. When the copper temperature is 80 ℃, the cure point temperature is predicted to reach around 175 ℃ directly under the tool, and the DoC value is over 85% within 30 seconds. As a result, DPIF can control the curing temperature by PID control and cure the sample in a short time.

Table 7.3 The surrounding temperature, DoC, and cure point temperature at different set temperatures

Copper temperature (℃)	Surrounding temperature (℃)	DoC	Cure point temperature (℃) (from Equation 7.1)
80	140	0.85	175
70	115	0.81	155
60	90	0.68	120
50	65	0.64	90

7.12 Conclusion

In this project, a novel manufacturing method, double-point incremental forming (DPIF) with localised pressure-electrical curing (DEC), is discussed. It manufactures the CFRPs via a localised force and electrical curing. This new method achieves mold-free manufacturing technology. The mechanical tests (tensile test and four-point bending test) and Differential Scanning Calorimetry (DSC) test show that CFRP manufactured by DPIF has the same performance in terms of mechanical properties and DoC as that of traditional manufacturing methods (oven and autoclave). In addition, compared with traditional manufacturing methods, DPIF can effectively reduce energy consumption.

Chapter 8 Conclusion and future work

In this chapter, a summary of the thesis is performed. First, all results and conclusions drawn from this thesis are exposed. Then, the possible improvements to enhance the quality of this project are discussed.

8.1 Conclusion

This thesis's principal aim is to use a novel manufacturing method, double-point incremental forming (DPIF) with direct electrical curing (DEC), to manufacture the carbon fibre-reinforced polymer (CFRP). This novel manufacturing method makes a significant contribution to CFRP manufacturing. Compared with traditional manufacturing methods (oven, heat press, and autoclave), DPIF with DEC can deliver manufacturing without mould and with low energy consumption directly from a computer-generated design. In addition, the CFRPs manufactured by DPIF have the same excellent performance as those by traditional manufacturing methods. The main contributions of this thesis can be separated into four sections, which are shown below.

- The dispersion of carbon nanomaterials in epoxy resin

This project studied the influence of carbon nanomaterials, including carbon black (CB), carbon nanotubes (CNTs), and graphene, on the dispersion in epoxy resin. In addition, the electrical and mechanical properties of carbon nanomaterial-modified epoxy resin composites are studied. Graphene particles are unstable and quickly aggregate at room temperature. The SEM and TEM images show that the carbon nanoparticles have a high tendency to agglomerate, forming more significant structures. The high nanoparticle agglomeration can boost the formation of electrical networks, which can reduce the required concentration of nanomaterials to achieve percolation. It is consistent with the result of fractal dimension and resistivity measurements, which indicates that the percolation threshold is between 2 and 3 wt.% in CB/IN2/AT30 composite and around 2.5 wt.% in CNTs/IN2/AT30 composite. Due to the large aspect ratios in CNTs, they prove difficult to mix and create highly viscous mixtures. Compared with other nanoparticle dispersion methods, the overhead stirrer is the optimal mixing technique due to its high working torque and minimal heat generation.

During the curing process, the temperature is a critical factor. Higher curing temperatures can boost the phase separation and improve the connectivity between carbon nanoparticles. As a result, bicontinous spinodal networks can be formed, which enhances conductivity at temperatures up to 150 ℃. In terms of CB/IN2/AT30S composites, the optimal tensile properties are reached at 2 wt.% CB, which matches the result of the percolation threshold value (between 2 wt.% and 3 wt.%). As the CB concentration increases to 4 wt.%, the tensile strength of the composite decreases by 2% compared to that of the pure resin system. In addition, curing temperature has no apparent influence on tensile properties.

- The influence of carbon black (CB) on CFRPs

This project investigates the influence of CB on CFRP. SEM images cannot determine the location of the CB in CFPRs and do not show CB nanoparticles agglomerated at the interface of CFRP. As a result, the mechanical and thermal properties suggest that the CB is well dispersed in the matrix and not agglomerated around the fibres. CB effectively enhances the properties of CFRP by modifying the matrix. When the concentration of CB is 2 wt.%, CFRP shows optimal performance in terms of electrical and mechanical properties. Compared with unmodified CFRP, the resistivity decreases by 52%, and the flexural strength increases by 57%. These results are consistent with the CB in epoxy resin results. CB significantly improves the thermal properties of CFRP beyond the rule of mixtures.

- The carbon black (CB) modified carbon fibre reinforcement polymers (CFRPs) are manufactured by direct electrical curing (DEC)

This project used the hand layup method to fabricate the CFRP “prepreg” with 2 wt.% CB in matrix. The “prepreg” was cured by DEC with four different contact arrangements and traditional curing methods (oven, heat press, and autoclave). The result shows that DEC is a cost-effective and viable option for the low-energy cure of CFRP. Compared with previous DEC research, the new contact arrangement (top-bottom mode, through the ply stack) and external pressure on the sample improve the temperature distribution and both the final degree of cure (DoC) and uniformity of cure. In addition, in terms of energy consumption, DEC is 8.7% of the autoclave and 33.2% of the oven. However, DEC shows

similar mechanical properties and DoC in comparison to traditional manufacturing methods.

- Carbon black (CB) modified carbon fibre reinforcement polymers (CFRPs) are manufactured by double-point incremental forming (DPIF)

This project explored a novel manufacturing method, double-point incremental forming (DPIF) with localized pressure-electrical curing, which involves the production of CFRPs via a localised force and electrical curing. This new manufacturing method can achieve a mould-free manufacturing process. The mechanical tests (tensile test and four-point bending tests) and DSC tests indicate that CFRP manufactured by DPIF shows comparable mechanical properties and DoC to those manufactured by traditional manufacturing methods (autoclave and oven). Compared with traditional manufacturing methods, there is no obvious difference in mechanical properties. In terms of DoC, in the middle position, there is no obvious change (about 0.98). In the edge position, the value of DPIF is 0.09 lower than that of traditional manufacturing methods. Furthermore, in comparison to traditional manufacturing methods, DPIF shows notable energy saving, with a particularly significant reduction in energy consumption observed in small-size samples, where energy use can be as low as 2% in comparison to the autoclave process.

8.2 Future work

- The Quantification of nanoparticle dispersion in epoxy resin

In this project, the quantification of nanoparticle dispersion is discussed by the fractal dimension value and the resistivity of nanocomposites. However, these two methods have apparent limitations. Fractal dimension values were obtained by analysing the optical microscope images. However, the number of images is limited, and they may not be representative.

In terms of resistivity, the project only shows a lower resistivity with a better dispersion. However, the relationship between the resistivity, dispersion and the concentration of nanoparticles has not been analysed. In future work, the quantification of nanoparticle dispersion by the relationship among the above three factors will be investigated.

Additionally, RIPS leads to a reduction in resistivity. This phase separation that creates a network of conductive fibrils has not been determined. TEM and X-ray and Neutron scattering may be helpful in determining the exact nature of this structure.

- The integration of the electrical curing control system

When electrical curing is used to cure CFRP sheets in DPIF, the power supplier is controlled by a PID control system to stabilise the curing temperature. However, the monitored temperature is the inside temperature of copper tools, not the surface temperature of samples. As a result, in future work, an infrared camera will be used to monitor the surface temperature of samples, and PID will be used to control the power supply. In addition, the curing time and curing temperature of each curing point will be modelled and optimized to save energy and time.

- Communication in DPIF machine

In this project, DPIF uses low-cost and open-source motion control. The critical issue is the communication between the motion controller and LabVIEW. The buffer area of the motion controller can only support limited characters and not real-time communication.

To overcome the above limitation, ethernet is one suitable communication performance [315], which is most popular in industrial communication. It includes different communication protocols, such as Ether CAT, Ethernet, ProfNet, and Modbus. They are used in industrial applications such as robots, high-performance PLC systems, motor control systems and input-output systems [316]. Compared with buffer communication, real-time communication is better for motion with a closed-loop system.

- Large size sample

Due to the limitation of the clamp for the sample, the copper tool size, and the maximum power of the power supplier, the CFRP samples manufactured by the DPIF are limited, and the maximum size is 150mm × 150mm. If DPIF should manufacture CFRP samples with larger sizes, the design of the clamp and tools should be considered, and the power supplier with higher power should be provided.

- Monitoring the temperature and DoC distribution

In this project, when DPIF manufactures the CFRP sample, there are only three thermocouples (two are on the top and bottom surface, and one is in the middle at a fixed position) to observe the temperature changes during the curing process. Then, according to these data, the numerical result was calculated by Abaqus and used to simulate the curing process. Though numerical results can present the temperature distribution, which can calculate the DoC distribution by the Arrhenius equation, it is built in ideal conditions, and its data is different from the data in experiments.

An infrared camera and thermocouple mesh can be used to monitor the temperature and DoC distribution during the curing process, which can observe the surface temperature and middle layer temperature of the samples, respectively. In addition, the temperature recorded by an infrared camera and thermocouple mesh can be used to figure out the DoC distribution using the Arrhenius equation.

- Complicated geometry shape sample.

In this project, CFRP samples manufactured by DPIF are laminated sheets. Due to only three axes (x,y,z) and a low maximum press load (about 160N), it is challenging to manufacture CFRP samples with complicated geometry shapes. To solve the above issue, two five-axis CNC machines or two parallel robots can be used in DPIF, which has two more axes (x and y rotation axes), which can help to manufacture curves or other complicated shape samples. In addition, hydraulic actuation can be used to replace the traditional mechanical actuation in DPIF. Hydraulic press can provide more flexibility and control for complex forming processes. It can adjust the pressure and speed at any time and can apply different forces to different parts of the workpiece. It can also press thick samples and make obvious deformations in the samples to help manufacture complicated shape samples [317].

Chapter 9 Bibliography

[1] B. Parveez, M. I. Kittur, I. A. Badruddin, S. Kamangar, M. Hussien, and M. A. Umarfarooq, 'Scientific Advancements in Composite Materials for Aircraft Applications: A Review', *Polymers (Basel)*, vol. 14, no. 22, p. 5007, Nov. 2022, doi: 10.3390/polym14225007.

[2] Mike and P. Brady, 'Technology developments in automotive composites', *Reinforced Plastics*, vol. 54, no. 6, pp. 25–29, Nov. 2010, doi: 10.1016/S0034-3617(10)70213-7.

[3] R. Nelson, 'Bike frame races carbon consumer goods forward', *Reinforced Plastics*, vol. 47, no. 7, pp. 36–40, Jul. 2003, doi: 10.1016/S0034-3617(03)00728-8.

[4] I. Bianchi, A. Forcellese, M. Simoncini, A. Vita, V. Castorani, D. Cafagna, and G. Buccoliero, 'Comparative life cycle assessment of safety shoes toe caps manufacturing processes', *The International Journal of Advanced Manufacturing Technology*, vol. 120, no. 11–12, pp. 7363–7374, Jun. 2022, doi: 10.1007/s00170-022-09240-x.

[5] I. Bianchi, A. Forcellese, M. Simoncini, A. Vita, V. Castorani, M. Arganese, and C. De Luca, 'Life cycle impact assessment of safety shoes toe caps realized with reclaimed composite materials', *J Clean Prod*, vol. 347, p. 131321, May 2022, doi: 10.1016/j.jclepro.2022.131321.

[6] I. Bianchi, A. Forcellese, M. Marconi, M. Simoncini, A. Vita, and V. Castorani, 'Environmental impact assessment of zero waste approach for carbon fiber prepreg scraps', *Sustainable Materials and Technologies*, vol. 29, p. e00308, Sep. 2021, doi: 10.1016/j.susmat.2021.e00308.

[7] P. Bere, C. Neamtu, and R. Udroiu, 'Novel Method for the Manufacture of Complex CFRP Parts Using FDM-based Molds', *Polymers (Basel)*, vol. 12, no. 10, p. 2220, Sep. 2020, doi: 10.3390/polym12102220.

[8] F. Van Der Klift, Y. Koga, A. Todoroki, M. Ueda, Y. Hirano, and R. Matsuzaki, '3D Printing of Continuous Carbon Fibre Reinforced Thermo-Plastic (CFRTP) Tensile

Test Specimens', *Open Journal of Composite Materials*, vol. 06, no. 01, pp. 18–27, Dec. 2016, doi: 10.4236/ojcm.2016.61003.

[9] M. T. Mastura, M. R. Alkahari, and A. K. Syahibudil Ikhwan, 'Life cycle analysis of fused filament fabrication: A review', in *Design for Sustainability*, Elsevier, 2021, pp. 415–434.

[10] C. Yang, X. Tian, T. Liu, Y. Cao, and D. Li, '3D printing for continuous fiber reinforced thermoplastic composites: mechanism and performance', *Rapid Prototyp J*, vol. 23, no. 1, pp. 209–215, Jan. 2017, doi: 10.1108/RPJ-08-2015-0098.

[11] N. van de Werken, H. Tekinalp, P. Khanbolouki, S. Ozcan, A. Williams, and M. Tehrani, 'Additively manufactured carbon fiber-reinforced composites: State of the art and perspective', *Addit Manuf*, vol. 31, p. 100962, Jan. 2020, doi: 10.1016/j.addma.2019.100962.

[12] G. Ginger, 'Three new 3D printing technologies for composites', *CompositesWorld*. https://www.compositesworld.com/articles/three-new-3d-printing-technologies-for-composites (accessed Nov. 11, 2023).

[13] B. Karaş, P. J. Smith, J. P. A. Fairclough, and K. Mumtaz, 'Additive manufacturing of high density carbon fibre reinforced polymer composites', *Addit Manuf*, vol. 58, p. 103044, Oct. 2022, doi: 10.1016/j.addma.2022.103044.

[14] M. Ramesh, L. Rajeshkumar, and D. Balaji, 'Influence of Process Parameters on the Properties of Additively Manufactured Fiber-Reinforced Polymer Composite Materials: A Review', *J Mater Eng Perform*, vol. 30, no. 7, pp. 4792–4807, Jul. 2021, doi: 10.1007/s11665-021-05832-y.

[15] H. L. Tekinalp, V. Kunc, G. M. Velez-Garcia, C. E. Duty, L. J. Love, A. K. Naskar, C. A. Blue, and S. Ozcan, 'Highly oriented carbon fiber–polymer composites via additive manufacturing', *Compos Sci Technol*, vol. 105, pp. 144–150, Dec. 2014, doi: 10.1016/j.compscitech.2014.10.009.

[16] J. Justo, L. Távara, L. García-Guzmán, and F. París, 'Characterization of 3D printed long fibre reinforced composites', *Compos Struct*, vol. 185, pp. 537–548, Feb. 2018, doi: 10.1016/j.compstruct.2017.11.052.

[17] M. Handwerker, J. Wellnitz, and H. Marzbani, 'Review of mechanical properties of and optimisation methods for continuous fibre-reinforced thermoplastic parts manufactured by fused deposition modelling', *Progress in Additive Manufacturing*, vol. 6, no. 4, pp. 663–677, Dec. 2021, doi: 10.1007/s40964-021-00187-1.

[18] S. Adil and I. Lazoglu, 'A review on additive manufacturing of carbon fiber-reinforced polymers: Current methods, materials, mechanical properties, applications and challenges', *J Appl Polym Sci*, vol. 140, no. 7, p. e53476, Feb. 2023, doi: 10.1002/APP.53476.

[19] Y. Li, X. Chen, Z. Liu, J. Sun, F. Li, J. Li, and G. Zhao, 'A review on the recent development of incremental sheet-forming process', *The International Journal of Advanced Manufacturing Technology*, vol. 92, no. 5–8, pp. 2439–2462, Sep. 2017, doi: 10.1007/s00170-017-0251-z.

[20] J. R. Duflou, A.-M. Habraken, J. Cao, R. Malhotra, M. Bambach, D. Adams, H. Vanhove, A. Mohammadi, and J. Jeswiet, 'Single point incremental forming: state-of-the-art and prospects', *International Journal of Material Forming*, vol. 11, no. 6, pp. 743–773, Nov. 2018, doi: 10.1007/s12289-017-1387-y.

[21] A. K. Behera, R. A. de Sousa, G. Ingarao, and V. Oleksik, 'Single point incremental forming: An assessment of the progress and technology trends from 2005 to 2015', *J Manuf Process*, vol. 27, pp. 37–62, Jun. 2017, doi: 10.1016/j.jmapro.2017.03.014.

[22] A. K. Behera, R. A. de Sousa, G. Ingarao, and V. Oleksik, 'Single point incremental forming: An assessment of the progress and technology trends from 2005 to 2015', *J Manuf Process*, vol. 27, pp. 37–62, Jun. 2017, doi: 10.1016/J.JMAPRO.2017.03.014.

[23] M. B. Silva, M. Skjoedt, P. A. F. Martins, and N. Bay, 'Revisiting the fundamentals of single point incremental forming by means of membrane analysis', *Int J Mach Tools Manuf*, vol. 48, no. 1, pp. 73–83, Jan. 2008, doi: 10.1016/J.IJMACHTOOLS.2007.07.004.

[24] R. Emami, M. J. Mirnia, M. Elyasi, and A. Zolfaghari, 'An experimental investigation into single point incremental forming of glass fiber-reinforced polyamide sheet with different fiber orientations and volume fractions at elevated temperatures', *Journal of Thermoplastic Composite Materials*, vol. 36, no. 5, pp. 1893–1917, May 2023, doi: 10.1177/08927057221074266.

[25] M. Okada, T. Kato, M. Otsu, H. Tanaka, and T. Miura, 'Development of optical-heating-assisted incremental forming method for CFRTP sheet - Fundamental forming characteristics in spot-forming -', *Procedia Eng*, vol. 207, pp. 813–818, Jan. 2017, doi: 10.1016/j.proeng.2017.10.834.

[26] V. M. Cedeno-Campos, P. A. Jaramillo, C. M. Fernyhough, and J. P. A. Fairclough, 'Towards mould free composites manufacturing of thermoset prepregs. Incremental curing with localised pressure-heat (ICULPH)', *Procedia CIRP*, vol. 85, pp. 237–242, Jan. 2019, doi: 10.1016/j.procir.2019.09.020.

[27] N. Moser, D. Leem, K. Ehmann, and J. Cao, 'A high-fidelity simulation of double-sided incremental forming: Improving the accuracy by incorporating the effects of machine compliance', *J Mater Process Technol*, vol. 295, p. 117152, Sep. 2021, doi: 10.1016/j.jmatprotec.2021.117152.

[28] H. Fukuda, 'Processing of carbon fiber reinforced plastics by means of Joule heating', *Advanced Composite Materials*, vol. 3, no. 3, pp. 153–161, Jan. 1994, doi: 10.1163/156855194X00015.

[29] S. A. Hayes, A. D. Lafferty, G. Altinkurt, P. R. Wilson, M. Collinson, and P. Duchene, 'Direct electrical cure of carbon fiber composites', *Advanced Manufacturing: Polymer & Composites Science*, vol. 1, no. 2, pp. 112–119, Apr. 2015, doi: 10.1179/2055035915Y.0000000001.

[30] C. Joseph and C. Viney, 'Electrical resistance curing of carbon-fibre/epoxy composites', *Compos Sci Technol*, vol. 60, no. 2, pp. 315–319, Feb. 2000, doi: 10.1016/S0266-3538(99)00112-8.

[31] P. E. Irving and C. Thiagarajan, 'Fatigue damage characterization in carbon fibre composite materials using an electrical potential technique', *Smart Mater Struct*, vol. 7, no. 4, pp. 456–466, Aug. 1998, doi: 10.1088/0964-1726/7/4/004.

[32] A. Todoroki, M. Tanaka, and Y. Shimamura, 'Measurement of orthotropic electric conductance of CFRP laminates and analysis of the effect on delamination monitoring with an electric resistance change method', *Compos Sci Technol*, vol. 62, no. 5, pp. 619–628, Apr. 2002, doi: 10.1016/S0266-3538(02)00019-2.

[33] A. Buketov, S. Smetankin, E. Lysenkov, K. Yurenin, O. Akimov, S. Yakushchenko, and I. Lysenkova, 'Electrophysical Properties of Epoxy Composite Materials Filled with Carbon Black Nanopowder', *Advances in Materials Science and Engineering*, vol. 2020, 2020, doi: 10.1155/2020/6361485.

[34] A. S. Krieg, J. A. King, D. C. Jaszczak, I. Miskoglu, O. P. Mills, and G. M. Odegard, 'Tensile and conductivity properties of epoxy composites containing carbon black and graphene nanoplatelets', *J Compos Mater*, vol. 52, no. 28, pp. 3909–3918, Dec. 2018, doi: 10.1177/0021998318771460.

[35] C. Lester and S. Nutt, 'Composite Materials: Advantages and Cost Factors', 2018, Accessed: Jan. 04, 2024. [Online].

[36] T. von Reden and D. Schüppel, 'Developments Toward Cost-effective CFRP', *Lightweight Design worldwide 2019 12:1*, vol. 12, no. 1, pp. 60–63, Mar. 2019, doi: 10.1007/S41777-018-0062-4.

[37] J. R. Fekete and J. N. Hall, 'Design of auto body: Materials perspective', *Automotive Steels: Design, Metallurgy, Processing and Applications*, pp. 1–18, Jan. 2017, doi: 10.1016/B978-0-08-100638-2.00001-8.

[38] S. A. Mirdehghan, 'Fibrous polymeric composites', *Engineered Polymeric Fibrous Materials*, pp. 1–58, Jan. 2021, doi: 10.1016/B978-0-12-824381-7.00012-3.

[39] S. Kurbanoglu, B. Uslu, and S. A. Ozkan, 'Carbon-based nanostructures for electrochemical analysis of oral medicines', *Nanostructures for Oral Medicine*, pp. 885–938, Jan. 2017, doi: 10.1016/B978-0-323-47720-8.00029-8.

[40] A. M. Pawlak, T. Górny, Ł. Dopierała, and P. Paczos, 'The Use of CFRP for Structural Reinforcement—Literature Review', *Metals (Basel)*, vol. 12, no. 9, p. 1470, Sep. 2022, doi: 10.3390/met12091470.

[41] R. Gogoi, A. K. Maurya, and G. Manik, 'A review on recent development in carbon fiber reinforced polyolefin composites', *Composites Part C: Open Access*, vol. 8, p. 100279, Jul. 2022, doi: 10.1016/j.jcomc.2022.100279.

[42] H. Zheng, W. Zhang, B. Li, J. Zhu, C. Wang, G. Song, G. Wu, X. Yang, Y. Huang, and L. Ma, 'Recent advances of interphases in carbon fiber-reinforced polymer composites: A review', *Compos B Eng*, vol. 233, p. 109639, Mar. 2022, doi: 10.1016/J.COMPOSITESB.2022.109639.

[43] H. Sharma, A. Kumar, S. Rana, and L. Guadagno, 'An Overview on Carbon Fiber-Reinforced Epoxy Composites: Effect of Graphene Oxide Incorporation on Composites Performance', *Polymers (Basel)*, vol. 14, no. 8, p. 1548, Apr. 2022, doi: 10.3390/polym14081548.

[44] N. Forintos and T. Czigany, 'Multifunctional application of carbon fiber reinforced polymer composites: Electrical properties of the reinforcing carbon fibers – A short review', *Compos B Eng*, vol. 162, pp. 331–343, Apr. 2019, doi: 10.1016/J.COMPOSITESB.2018.10.098.

[45] J. Chen and Y. Ji, 'The Application of Carbon Fiber Reinforced Material in Sports Equipments', *Adv Mat Res*, vol. 568, pp. 372–375, Sep. 2012, doi: 10.4028/www.scientific.net/AMR.568.372.

[46] M. V. Seica and J. A. Packer, 'FRP materials for the rehabilitation of tubular steel structures, for underwater applications', *Compos Struct*, vol. 80, no. 3, pp. 440–450, Oct. 2007, doi: 10.1016/J.COMPSTRUCT.2006.05.029.

[47] A. I. Danilov, 'Some Aspects of CFRP Steel Structures Reinforcement in Civil Engineering', *Procedia Eng*, vol. 153, pp. 124–130, Jan. 2016, doi: 10.1016/J.PROENG.2016.08.091.

[48] J. P. Davim and R. Cardoso, 'Effect of the reinforcement (carbon or glass fibres) on friction and wear behaviour of the PEEK against steel surface at long dry sliding', *Wear*, vol. 266, no. 7–8, pp. 795–799, Mar. 2009, doi: 10.1016/j.wear.2008.11.003.

[49] S.-J. Park, M.-H. Kim, J.-R. Lee, and S. Choi, 'Effect of Fiber–Polymer Interactions on Fracture Toughness Behavior of Carbon Fiber-Reinforced Epoxy Matrix Composites', *J Colloid Interface Sci*, vol. 228, no. 2, pp. 287–291, Aug. 2000, doi: 10.1006/jcis.2000.6953.

[50] L. Dong, W. Zhou, X. Sui, Z. Wang, P. Wu, J. Zuo, H. Cai, and X. Liu, 'Thermal, mechanical, and dielectric properties of epoxy resin modified using carboxyl-terminated polybutadiene liquid rubber', *Journal of Elastomers & Plastics*, vol. 49, no. 4, pp. 281–297, Jun. 2017, doi: 10.1177/0095244316653261.

[51] J. Bentley, 'Organic film formers', *Paint and Surface Coatings*, pp. 19–90, Jan. 1999, doi: 10.1533/9781855737006.19.

[52] G. Gibson, 'Epoxy Resins', in *Brydson's Plastics Materials*, Elsevier, 2017, pp. 773–797.

[53] N. Karak, 'Overview of Epoxies and Their Thermosets', in *ACS Symposium Series*, vol. 1385, American Chemical Society, 2021, pp. 1–36.

[54] N. Prileschajew, 'Oxydation ungesättigter Verbindungen mittels organischer Superoxyde', *Berichte der deutschen chemischen Gesellschaft*, vol. 42, no. 4, pp. 4811–4815, Nov. 1909, doi: 10.1002/cber.190904204100.

[55] P. V. Reddy, R. Thiagarajan, M. C. Ratra, and N. M. N. Gowda, 'Transition metal chelates as accelerators for epoxy resin systems—studies with cobalt (III) acetylacetonate', *J Appl Polym Sci*, vol. 41, no. 1–2, pp. 319–328, Jan. 1990, doi: 10.1002/app.1990.070410124.

[56] K. P. Unnikrishnan and E. T. Thachil, 'Toughening of epoxy resins', *Des Monomers Polym*, vol. 9, no. 2, pp. 129–152, Jan. 2006, doi: 10.1163/156855506776382664.

[57] S. Nikafshar, O. Zabihi, S. Hamidi, Y. Moradi, S. Barzegar, M. Ahmadi, and M. Naebe, 'A renewable bio-based epoxy resin with improved mechanical

performance that can compete with DGEBA', *RSC Adv*, vol. 7, no. 14, pp. 8694–8701, 2017, doi: 10.1039/C6RA27283E.

[58] C. Chen, B. Li, M. Kanari, and D. Lu, 'Epoxy Adhesives', in *Adhesives and Adhesive Joints in Industry Applications*, IntechOpen, 2019.

[59] C. O. Tuck, E. Pérez, I. T. Horváth, R. A. Sheldon, and M. Poliakoff, 'Valorization of Biomass: Deriving More Value from Waste', *Science (1979)*, vol. 337, no. 6095, pp. 695–699, Aug. 2012, doi: 10.1126/science.1218930.

[60] A. Gandini, 'The irruption of polymers from renewable resources on the scene of macromolecular science and technology', *Green Chemistry*, vol. 13, no. 5, p. 1061, May 2011, doi: 10.1039/c0gc00789g.

[61] W. Peng, X. Chen, and J. Wang, 'Study on the curing behavior of polythiol/phenolic/epoxy resin and the mechanical and thermal properties of the composites', *Mater Res Express*, vol. 8, no. 5, p. 055302, May 2021, doi: 10.1088/2053-1591/abeb4a.

[62] S.-J. Park, M.-K. Seo, and J.-R. Lee, 'Isothermal cure kinetics of epoxy/phenol-novolac resin blend system initiated by cationic latent thermal catalyst', *J Polym Sci A Polym Chem*, vol. 38, no. 16, pp. 2945–2956, Aug. 2000, doi: 10.1002/1099-0518(20000815)38:16<2945::AID-POLA120>3.0.CO;2-6.

[63] B. Guo, D. Jia, W. Fu, and Q. Qiu, 'Hygrothermal stability of dicyanate-novolac epoxy resin blends', *Polym Degrad Stab*, vol. 79, no. 3, pp. 521–528, Mar. 2003, doi: 10.1016/S0141-3910(02)00368-3.

[64] J. J. Licari and D. W. Swanson, 'Chemistry, Formulation, and Properties of Adhesives', in *Adhesives Technology for Electronic Applications*, Elsevier, 2011, pp. 75–141.

[65] A. Isa, N. Nosbi, M. Che Ismail, H. Md Akil, W. F. F. Wan Ali, and M. F. Omar, 'A Review on Recycling of Carbon Fibres: Methods to Reinforce and Expected Fibre Composite Degradations', *Materials*, vol. 15, no. 14, p. 4991, Jul. 2022, doi: 10.3390/ma15144991.

[66] S. Shi, Y. Wang, T. Jiang, X. Wu, B. Tang, Y. Gao, N. Zhong, K. Sun, Y. Zhao, W. Li, and J. Yu, 'Carbon Fiber/Phenolic Composites with High Thermal Conductivity Reinforced by a Three-Dimensional Carbon Fiber Felt Network Structure', *ACS Omega*, vol. 7, no. 33, pp. 29433–29442, Aug. 2022, doi: 10.1021/acsomega.2c03848.

[67] D. Li, Y. Feng, F. Li, J. Tang, and T. Hua, 'Carbon Fibers for Bioelectrochemical: Precursors, Bioelectrochemical System, and Biosensors', *Advanced Fiber Materials*, vol. 5, no. 3, pp. 699–730, Jun. 2023, doi: 10.1007/s42765-023-00256-w.

[68] 'High Performance Carbon Fibers', *American Chemical Society National Historic Chemical Landmarks*, 2003. http://www.acs.org/content/acs/en/education/whatischemistry/landmarks/carbonfibers.html (accessed May 07, 2023).

[69] B. A. Newcomb, 'Processing, structure, and properties of carbon fibers', *Compos Part A Appl Sci Manuf*, vol. 91, pp. 262–282, Dec. 2016, doi: 10.1016/j.compositesa.2016.10.018.

[70] Qilin Wu and Ding Pan, 'A New Cellulose Based Carbon Fiber from a Lyocell Precursor', *Textile Research Journal*, vol. 72, no. 5, pp. 405–410, May 2002, doi: 10.1177/004051750207200506.

[71] K. Acatay, 'Carbon fibers', in *Fiber Technology for Fiber-Reinforced Composites*, Elsevier, 2017, pp. 123–151.

[72] J. Moosburger-Will, M. Bauer, E. Laukmanis, R. Horny, D. Wetjen, T. Manske, F. Schmidt-Stein, J. Töpker, and S. Horn, 'Interaction between carbon fibers and polymer sizing: Influence of fiber surface chemistry and sizing reactivity', *Appl Surf Sci*, vol. 439, pp. 305–312, May 2018, doi: 10.1016/j.apsusc.2017.12.251.

[73] B. Cornelissen, M. B. de Rooij, B. Rietman, and R. Akkerman, 'Frictional behavior of carbon fiber tows: a contact mechanics model of tow–tow friction', *Textile Research Journal*, vol. 84, no. 14, pp. 1476–1488, Sep. 2014, doi: 10.1177/0040517514525876.

[74] E. Frank, F. Hermanutz, and M. R. Buchmeiser, 'Carbon Fibers: Precursors, Manufacturing, and Properties', *Macromol Mater Eng*, vol. 297, no. 6, pp. 493–501, Jun. 2012, doi: 10.1002/mame.201100406.

[75] A. Chaudhary, V. Gupta, S. Teotia, S. Nimanpure, and D. K. Rajak, 'Electromagnetic Shielding Capabilities of Metal Matrix Composites', in *Encyclopedia of Materials: Composites*, vol. 1, Elsevier, 2021, pp. 428–441.

[76] J. Pusch and B. Wohlmann, 'Carbon Fibers', in *Inorganic and Composite Fibers*, Elsevier, 2018, pp. 31–51.

[77] H. Hu and Y. Liu, 'High modulus, high tenacity yarns', in *Technical Textile Yarns*, Elsevier, 2010, pp. 329–386.

[78] DragonPlate, 'Carbon Fiber 101: Understanding Weaves and Fabrics'. https://dragonplate.com/carbon-fiber-101-understanding-weaves-and-fabrics (accessed Apr. 01, 2024).

[79] PENTA PATTERN & MODEL LTD, 'Different carbon fibre weave pattern and their strengths'. https://www.pentapatterns.co.uk/carbon-fibre-weave-patterns/ (accessed Apr. 01, 2024).

[80] Rohan, 'Ultimate Guide: 5 Carbon Fiber Fabric Patterns', *Knowing Fabric*, 2024. https://knowingfabric.com/ultimate-guide-5-carbon-fiber-fabric-patterns/?utm_content=cmp-true (accessed May 03, 2024).

[81] Y. Zhang, Y. Li, J. Zhang, J. Pan, L. Zhang, F. Tan, H. Wei, and W. Zhang, 'High-Temperature Effect on the Tensile Mechanical Properties of Unidirectional Carbon Fiber-Reinforced Polymer Plates', *Materials*, vol. 14, no. 23, p. 7214, Nov. 2021, doi: 10.3390/ma14237214.

[82] L. Tarallo, R. Mugnai, R. Adani, F. Zambianchi, and F. Catani, 'A new volar plate made of carbon-fiber-reinforced polyetheretherketon for distal radius fracture: analysis of 40 cases', *Journal of Orthopaedics and Traumatology*, vol. 15, no. 4, pp. 277–283, Dec. 2014, doi: 10.1007/s10195-014-0311-1.

[83] J. Liu, X. Huang, Y. Ren, L. M. Wong, H. Liu, and S. Wang, 'Galvanic corrosion protection of Al-alloy in contact with carbon fibre reinforced polymer through

plasma electrolytic oxidation treatment', *Sci Rep*, vol. 12, no. 1, p. 4532, Mar. 2022, doi: 10.1038/s41598-022-08727-7.

[84] S. Das, 'Life cycle assessment of carbon fiber-reinforced polymer composites', *Int J Life Cycle Assess*, vol. 16, no. 3, pp. 268–282, Mar. 2011, doi: 10.1007/s11367-011-0264-z.

[85] S. Nunna, P. Blanchard, D. Buckmaster, S. Davis, and M. Naebe, 'Development of a cost model for the production of carbon fibres', *Heliyon*, vol. 5, no. 10, p. e02698, Oct. 2019, doi: 10.1016/j.heliyon.2019.e02698.

[86] T. von Reden and D. Schüppel, 'Developments Toward Cost-effective CFRP', *Lightweight Design worldwide*, vol. 12, no. 1, pp. 60–63, Mar. 2019, doi: 10.1007/s41777-018-0062-4.

[87] A. F. Johnson, R. S. Thomson, M. David, and M. W. Joosten, 'Design and testing of crashworthy aerospace composite components', in *Polymer Composites in the Aerospace Industry*, Elsevier, 2015, pp. 261–293.

[88] I. Shakir Abbood, S. aldeen Odaa, K. F. Hasan, and M. A. Jasim, 'Properties evaluation of fiber reinforced polymers and their constituent materials used in structures – A review', *Mater Today Proc*, vol. 43, pp. 1003–1008, Jan. 2021, doi: 10.1016/j.matpr.2020.07.636.

[89] S. Karuppannan Gopalraj and T. Kärki, 'A review on the recycling of waste carbon fibre/glass fibre-reinforced composites: fibre recovery, properties and life-cycle analysis', *SN Appl Sci*, vol. 2, no. 3, pp. 1–21, Mar. 2020, doi: 10.1007/S42452-020-2195-4/TABLES/5.

[90] J. Zhang, G. Lin, U. Vaidya, and H. Wang, 'Past, present and future prospective of global carbon fibre composite developments and applications', *Compos B Eng*, vol. 250, p. 110463, Feb. 2023, doi: 10.1016/j.compositesb.2022.110463.

[91] David Isaiah, 'Carbon fibre: the fabric of the future?', May 2014. https://www.automotiveworld.com/articles/carbon-fibre-the-fabric-of-the-future/ (accessed May 09, 2023).

[92] R. Othman, M. Hisyam Basri, I. Ismail, M. A. Ab, H. Pahmi, M. Hisyam, M. Basri, H. Sharudin, and A. Rahman Hemdi, 'APPLICATION OF CARBON FIBER REINFORCED PLASTICS IN AUTOMOTIVE INDUSTRY: A REVIEW Morphing MAV View project Sustainable Manufacturing View project APPLICATION OF CARBON FIBER REINFORCED PLASTICS IN AUTOMOTIVE INDUSTRY: A REVIEW', *Journal of Mechanical Manufacturing (J-MFac)*, vol. 1, 2018, Accessed: May 10, 2023. [Online]. Available: https://www.researchgate.net/publication/337917403.

[93] Y. Lin, J. Min, H. Teng, J. Lin, J. Hu, and N. Xu, 'Flexural Performance of Steel–FRP Composites for Automotive Applications', *Automotive Innovation*, vol. 3, no. 3, pp. 280–295, Sep. 2020, doi: 10.1007/s42154-020-00109-x.

[94] F.-J. Sun, S.-H. Pang, Z.-W. Zhang, F. Fu, and K. Qian, 'Retrofitting seismically damaged steel sections encased concrete composite walls using externally bonded CFRP strips', *Compos Struct*, vol. 236, p. 111927, Mar. 2020, doi: 10.1016/j.compstruct.2020.111927.

[95] F. Yu, H. Zhou, N. Jiang, Y. Fang, J. Song, C. Feng, and Y. Guan, 'Flexural experiment and capacity investigation of CFRP repaired RC beams under heavy pre-damaged level', *Constr Build Mater*, vol. 230, p. 117030, Jan. 2020, doi: 10.1016/j.conbuildmat.2019.117030.

[96] S.-W. Kim, W.-C. Choi, and H.-D. Yun, 'Strengthening methods for reinforced concrete infrastructure using FRP composites in Korea', *Proceedings of the Institution of Civil Engineers - Structures and Buildings*, vol. 171, no. 11, pp. 898–907, Nov. 2018, doi: 10.1680/jstbu.17.00057.

[97] U. Meier, 'Carbon Fiber Reinforced Polymer Cables: Why? Why Not? What If?', *Arab J Sci Eng*, vol. 37, no. 2, pp. 399–411, Mar. 2012, doi: 10.1007/s13369-012-0185-6.

[98] R. J. Young and M. Liu, 'The microstructure of a graphene-reinforced tennis racquet', *J Mater Sci*, vol. 51, no. 8, pp. 3861–3867, Apr. 2016, doi: 10.1007/s10853-015-9705-6.

[99] A. Kumar, K. Sharma, and A. R. Dixit, 'Carbon nanotube- and graphene-reinforced multiphase polymeric composites: review on their properties and applications', *J Mater Sci*, vol. 55, no. 7, pp. 2682–2724, Mar. 2020, doi: 10.1007/s10853-019-04196-y.

[100] R. Usamentiaga, C. Ibarra-Castanedo, M. Klein, X. Maldague, J. Peeters, and A. Sanchez-Beato, 'Nondestructive Evaluation of Carbon Fiber Bicycle Frames Using Infrared Thermography', *Sensors*, vol. 17, no. 11, p. 2679, Nov. 2017, doi: 10.3390/s17112679.

[101] N. Anzar, R. Hasan, M. Tyagi, N. Yadav, and J. Narang, 'Carbon nanotube - A review on Synthesis, Properties and plethora of applications in the field of biomedical science', *Sensors International*, vol. 1, p. 100003, Jan. 2020, doi: 10.1016/j.sintl.2020.100003.

[102] R. Rauti, M. Musto, S. Bosi, M. Prato, and L. Ballerini, 'Properties and behavior of carbon nanomaterials when interfacing neuronal cells: How far have we come?', *Carbon N Y*, vol. 143, pp. 430–446, Mar. 2019, doi: 10.1016/j.carbon.2018.11.026.

[103] W. Zhang, A. A. Dehghani-Sanij, and R. S. Blackburn, 'Carbon based conductive polymer composites', *J Mater Sci*, vol. 42, no. 10, pp. 3408–3418, May 2007, doi: 10.1007/s10853-007-1688-5.

[104] H. Pan, J. Li, and Y. P. Feng, 'Carbon Nanotubes for Supercapacitor', *Nanoscale Res Lett*, vol. 5, no. 3, pp. 654–668, Mar. 2010, doi: 10.1007/s11671-009-9508-2.

[105] C. Lee, X. Wei, J. W. Kysar, and J. Hone, 'Measurement of the Elastic Properties and Intrinsic Strength of Monolayer Graphene', *Science (1979)*, vol. 321, no. 5887, pp. 385–388, Jul. 2008, doi: 10.1126/science.1157996.

[106] M. Singh and R. Vander Wal, 'Nanostructure Quantification of Carbon Blacks', *C (Basel)*, vol. 5, no. 1, p. 2, Dec. 2018, doi: 10.3390/c5010002.

[107] T. Takamura, 'CHEMISTRY, ELECTROCHEMISTRY, AND ELECTROCHEMICAL APPLICATIONS | Carbon', in *Encyclopedia of Electrochemical Power Sources*, Elsevier, 2009, pp. 709–743.

[108] N. R. Ostyn, J. A. Steele, M. De Prins, S. P. Sree, C. V. Chandran, W. Wangermez, G. Vanbutsele, J. W. Seo, M. B. J. Roeffaers, E. Breynaert, and J. A. Martens, 'Low-temperature activation of carbon black by selective photocatalytic oxidation', *Nanoscale Adv*, vol. 1, no. 8, pp. 2873–2880, Aug. 2019, doi: 10.1039/C9NA00188C.

[109] T. D. Bolt, E. M. Dannenberg, R. E. Dobbin, and R. P. Rossman, 'Carbon Black Structure Effects in Synthetic Rubbers', *Rubber Chemistry and Technology*, vol. 34, no. 4, pp. 1141–1161, Sep. 1961, doi: 10.5254/1.3540273.

[110] P. A. Marsh, A. Voet, T. J. Mullens, and L. D. Price, 'Quantitative micrography of carbon black microstructure', *Carbon N Y*, vol. 9, no. 6, pp. 797–805, Dec. 1971, doi: 10.1016/0008-6223(71)90013-3.

[111] R. L. Vander Wal, A. J. Tomasek, K. Street, D. R. Hull, and W. K. Thompson, 'Carbon Nanostructure Examined by Lattice Fringe Analysis of High-Resolution Transmission Electron Microscopy Images', *Appl Spectrosc*, vol. 58, no. 2, pp. 230–237, Feb. 2004, doi: 10.1366/000370204322842986.

[112] D. Pantea, H. Darmstadt, S. Kaliaguine, and C. Roy, 'Electrical conductivity of conductive carbon blacks: influence of surface chemistry and topology', *Appl Surf Sci*, vol. 217, no. 1–4, pp. 181–193, Jul. 2003, doi: 10.1016/S0169-4332(03)00550-6.

[113] J. Huang, 'Carbon black filled conducting polymers and polymer blends', *Advances in Polymer Technology*, vol. 21, no. 4, pp. 299–313, Dec. 2002, doi: 10.1002/adv.10025.

[114] M. Monthioux and V. L. Kuznetsov, 'Who should be given the credit for the discovery of carbon nanotubes?', *Carbon N Y*, vol. 44, no. 9, pp. 1621–1623, Aug. 2006, doi: 10.1016/j.carbon.2006.03.019.

[115] S. Iijima, 'Helical microtubules of graphitic carbon', *Nature*, vol. 354, no. 6348, pp. 56–58, Nov. 1991, doi: 10.1038/354056a0.

[116] X. Wang, Q. Li, J. Xie, Z. Jin, J. Wang, Y. Li, K. Jiang, and S. Fan, 'Fabrication of Ultralong and Electrically Uniform Single-Walled Carbon Nanotubes on Clean

Substrates', *Nano Lett*, vol. 9, no. 9, pp. 3137–3141, Sep. 2009, doi: 10.1021/nl901260b.

[117] J. Tersoff and R. S. Ruoff, 'Structural Properties of a Carbon-Nanotube Crystal', *Phys Rev Lett*, vol. 73, no. 5, pp. 676–679, Aug. 1994, doi: 10.1103/PhysRevLett.73.676.

[118] M. Sharon, 'An Introduction to Carbon Nanofiber', in *Carbon Nanofibers*, Wiley, 2021, pp. 1–20.

[119] N. Saifuddin, A. Z. Raziah, and A. R. Junizah, 'Carbon Nanotubes: A Review on Structure and Their Interaction with Proteins', *J Chem*, vol. 2013, pp. 1–18, 2013, doi: 10.1155/2013/676815.

[120] B. Yoo, Z. Xu, and F. Ding, 'How Single-Walled Carbon Nanotubes are Transformed into Multiwalled Carbon Nanotubes during Heat Treatment', *ACS Omega*, vol. 6, no. 5, pp. 4074–4079, Feb. 2021, doi: 10.1021/acsomega.0c06133.

[121] E. T. Thostenson, Z. Ren, and T.-W. Chou, 'Advances in the science and technology of carbon nanotubes and their composites: a review', *Compos Sci Technol*, vol. 61, no. 13, pp. 1899–1912, Oct. 2001, doi: 10.1016/S0266-3538(01)00094-X.

[122] M. Russ, S. S. Rahatekar, K. Koziol, B. Farmer, and H.-X. Peng, 'Length-dependent electrical and thermal properties of carbon nanotube-loaded epoxy nanocomposites', *Compos Sci Technol*, vol. 81, pp. 42–47, Jun. 2013, doi: 10.1016/j.compscitech.2013.03.011.

[123] B. Earp, D. Dunn, J. Phillips, R. Agrawal, T. Ansell, P. Aceves, I. De Rosa, W. Xin, and C. Luhrs, 'Enhancement of electrical conductivity of carbon nanotube sheets through copper addition using reduction expansion synthesis', *Mater Res Bull*, vol. 131, p. 110969, Nov. 2020, doi: 10.1016/j.materresbull.2020.110969.

[124] K. Jiang, Q. Li, and S. Fan, 'Spinning continuous carbon nanotube yarns', *Nature*, vol. 419, no. 1999, p. 801, 2002.

[125] T. Kuilla, S. Bhadra, D. Yao, N. H. Kim, S. Bose, and J. H. Lee, 'Recent advances in graphene based polymer composites', *Prog Polym Sci*, vol. 35, no. 11, pp. 1350–1375, Nov. 2010, doi: 10.1016/j.progpolymsci.2010.07.005.

[126] D. Nuvoli, L. Valentini, V. Alzari, S. Scognamillo, S. B. Bon, M. Piccinini, J. Illescas, and A. Mariani, 'High concentration few-layer graphene sheets obtained by liquid phase exfoliation of graphite in ionic liquid', *J. Mater. Chem.*, vol. 21, no. 10, pp. 3428–3431, 2011, doi: 10.1039/C0JM02461A.

[127] M. Notarianni, J. Liu, K. Vernon, and N. Motta, 'Synthesis and applications of carbon nanomaterials for energy generation and storage', *Beilstein Journal of Nanotechnology*, vol. 7, no. 6, pp. 149–196, Feb. 2016, doi: 10.3762/bjnano.7.17.

[128] G. Yang, L. Li, W. B. Lee, and M. C. Ng, 'Structure of graphene and its disorders: a review', *Sci Technol Adv Mater*, vol. 19, no. 1, pp. 613–648, Dec. 2018, doi: 10.1080/14686996.2018.1494493.

[129] A. R. Urade, I. Lahiri, and K. S. Suresh, 'Graphene Properties, Synthesis and Applications: A Review', *JOM*, vol. 75, no. 3, pp. 614–630, Mar. 2023, doi: 10.1007/s11837-022-05505-8.

[130] U. K. Sur, 'Graphene: A Rising Star on the Horizon of Materials Science', *International Journal of Electrochemistry*, vol. 2012, pp. 1–12, 2012, doi: 10.1155/2012/237689.

[131] D. Yang, 'Analysis on the Conductivity of Graphene-based Composite Material', *J Phys Conf Ser*, vol. 2011, no. 1, p. 012002, Sep. 2021, doi: 10.1088/1742-6596/2011/1/012002.

[132] R. J. Young, I. A. Kinloch, L. Gong, and K. S. Novoselov, 'The mechanics of graphene nanocomposites: A review', *Compos Sci Technol*, vol. 72, no. 12, pp. 1459–1476, Jul. 2012, doi: 10.1016/j.compscitech.2012.05.005.

[133] S. S. Ray, L. T. Temane, and J. T. Orasugh, 'Graphene Nanoplatelets in Brief', Springer, Cham, 2024, pp. 7–25.

[134] S. G. Prolongo, A. Jiménez-Suárez, R. Moriche, A. Ureña, R. J. Carlos, and C. / Tulipán, 'Macromolecular Nanotechnology Graphene nanoplatelets thickness and lateral size influence on the morphology and behavior of epoxy composites', 2014, doi: 10.1016/j.eurpolymj.2014.01.019.

[135] S. Kim and L. T. Drzal, 'High latent heat storage and high thermal conductive phase change materials using exfoliated graphite nanoplatelets', *Solar Energy Materials and Solar Cells*, vol. 93, no. 1, pp. 136–142, Jan. 2009, doi: 10.1016/J.SOLMAT.2008.09.010.

[136] L. Yue, G. Pircheraghi, S. A. Monemian, and I. Manas-Zloczower, 'Epoxy composites with carbon nanotubes and graphene nanoplatelets – Dispersion and synergy effects', *Carbon N Y*, vol. 78, pp. 268–278, Nov. 2014, doi: 10.1016/j.carbon.2014.07.003.

[137] A. J. Marsden, D. G. Papageorgiou, C. Vallés, A. Liscio, V. Palermo, M. A. Bissett, R. J. Young, and I. A. Kinloch, 'Electrical percolation in graphene–polymer composites', *2d Mater*, vol. 5, no. 3, p. 032003, Jun. 2018, doi: 10.1088/2053-1583/AAC055.

[138] L. Jing, P. Ma, C. Sze, T. Kai, B. Z. Tang, and J. Kim, 'Percolation threshold of polymer nanocomposites containing graphite nanoplatelets and carbon nanotubes', 2007, Accessed: Sep. 08, 2023. [Online]. Available: https://api.semanticscholar.org/CorpusID:31711118.

[139] D. Carolan, A. Ivankovic, A. J. Kinloch, S. Sprenger, and A. C. Taylor, 'Toughened carbon fibre-reinforced polymer composites with nanoparticle-modified epoxy matrices', *J Mater Sci*, vol. 52, no. 3, pp. 1767–1788, Feb. 2017, doi: 10.1007/s10853-016-0468-5.

[140] A. Kausar, 'Thermally conducting polymer/nanocarbon and polymer/inorganic nanoparticle nanocomposite: a review', *Polymer-Plastics Technology and Materials*, vol. 59, no. 8, pp. 895–909, May 2020, doi: 10.1080/25740881.2019.1708103.

[141] S.-H. Jeong, J.-B. Song, K. L. Kim, Y. H. Choi, and H. Lee, 'Enhanced thermal properties of epoxy composite containing cubic and hexagonal boron nitride fillers for superconducting magnet applications', *Compos B Eng*, vol. 107, pp. 22–28, Dec. 2016, doi: 10.1016/j.compositesb.2016.09.066.

[142] S. R. Mousavi, S. Estaji, H. Kiaei, M. Mansourian-Tabaei, S. Nouranian, S. H. Jafari, H. Ruckdäschel, M. Arjmand, and H. A. Khonakdar, 'A review of electrical and

thermal conductivities of epoxy resin systems reinforced with carbon nanotubes and graphene-based nanoparticles', *Polym Test*, vol. 112, p. 107645, Aug. 2022, doi: 10.1016/j.polymertesting.2022.107645.

[143] C. Zhang, Y. Ling, X. Zhang, M. Liang, and H. Zou, 'Ultra-thin carbon fiber reinforced carbon nanotubes modified epoxy composites with superior mechanical and electrical properties for the aerospace field', *Compos Part A Appl Sci Manuf*, vol. 163, p. 107197, Dec. 2022, doi: 10.1016/j.compositesa.2022.107197.

[144] M. Kamble, A. S. Lakhnot, S. F. Bartolucci, A. G. Littlefield, C. R. Picu, and N. Koratkar, 'Improvement in fatigue life of carbon fibre reinforced polymer composites via a Nano-Silica Modified Matrix', *Carbon N Y*, vol. 170, pp. 220–224, Dec. 2020, doi: 10.1016/j.carbon.2020.08.029.

[145] M. E. Islam, T. H. Mahdi, M. V. Hosur, and S. Jeelani, 'Characterization of Carbon Fiber Reinforced Epoxy Composites Modified with Nanoclay and Carbon Nanotubes', *Procedia Eng*, vol. 105, pp. 821–828, Jan. 2015, doi: 10.1016/j.proeng.2015.05.078.

[146]C. Kostagiannakopoulou, T. H. Loutas, G. Sotiriadis, A. Markou, and V. Kostopoulos, 'On the interlaminar fracture toughness of carbon fiber composites enhanced with graphene nano-species', *Compos Sci Technol*, vol. 118, pp. 217–225, Oct. 2015, doi: 10.1016/j.compscitech.2015.08.017.

[147] Ç. Uzay, 'Studies on mechanical and thermal properties of cubic boron nitride (c-BN) nanoparticle filled carbon fiber reinforced polymer composites', *Polymer-Plastics Technology and Materials*, vol. 61, no. 13, pp. 1439–1455, Sep. 2022, doi: 10.1080/25740881.2022.2069037.

[148] V. Kostopoulos, A. Masouras, A. Baltopoulos, A. Vavouliotis, G. Sotiriadis, and L. Pambaguian, 'A critical review of nanotechnologies for composite aerospace structures', *CEAS Space Journal*, vol. 9, no. 1, pp. 35–57, Mar. 2017, doi: 10.1007/s12567-016-0123-7.

[149] H. W. Zhou, L. Mishnaevsky, H. Y. Yi, Y. Q. Liu, X. Hu, A. Warrier, and G. M. Dai, 'Carbon fiber/carbon nanotube reinforced hierarchical composites: Effect of CNT

distribution on shearing strength', *Compos B Eng*, vol. 88, pp. 201–211, Mar. 2016, doi: 10.1016/j.compositesb.2015.10.035.

[150] S. S. Wicks, W. Wang, M. R. Williams, and B. L. Wardle, 'Multi-scale interlaminar fracture mechanisms in woven composite laminates reinforced with aligned carbon nanotubes', *Compos Sci Technol*, vol. 100, pp. 128–135, Aug. 2014, doi: 10.1016/j.compscitech.2014.06.003.

[151] Y. Lin, M. Gigliotti, M. C. Lafarie-Frenot, J. Bai, D. Marchand, and D. Mellier, 'Experimental study to assess the effect of carbon nanotube addition on the through-thickness electrical conductivity of CFRP laminates for aircraft applications', *Compos B Eng*, vol. 76, pp. 31–37, Jul. 2015, doi: 10.1016/j.compositesb.2015.02.015.

[152] Wei Zhang, R. S. Blackburn, and A. A. Dehghani-Sanij, 'Carbon Black Reinforced Epoxy Resin Nanocomposites as Bending Sensors', *J Compos Mater*, vol. 43, no. 4, pp. 367–376, Feb. 2009, doi: 10.1177/0021998308099308.

[153] R. Dungani, I. Sumardi, E. M. Alamsyah, P. Aditiawati, T. Karliati, J. Malik, and Sulistyono, 'A study on fracture toughness of nano-structured carbon black-filled epoxy composites', *Polymer Bulletin*, vol. 78, no. 12, pp. 6867–6885, Dec. 2021, doi: 10.1007/s00289-020-03444-5.

[154] A.-J. Ma, W. Chen, Y. Hou, and G. Zhang, 'Dispersion, Mechanical and Thermal Properties of Epoxy Resin Composites Filled with the Nanometer Carbon Black', *Polym Plast Technol Eng*, vol. 49, no. 9, pp. 916–920, Jun. 2010, doi: 10.1080/03602551003773122.

[155] M. H. Woldemariam, G. Belingardi, E. G. Koricho, and D. T. Reda, 'Effects of nanomaterials and particles on mechanical properties and fracture toughness of composite materials: a short review', *AIMS Mater Sci*, vol. 6, no. 6, pp. 1191–1212, 2019, doi: 10.3934/matersci.2019.6.1191.

[156] B. Bittmann, F. Haupert, and A. K. Schlarb, 'Ultrasonic dispersion of inorganic nanoparticles in epoxy resin', *Ultrason Sonochem*, vol. 16, no. 5, pp. 622–628, 2009, doi: 10.1016/j.ultsonch.2009.01.006.

[157] K.-W. Nam and C.-K. Moon, 'Evaluation of dispersion degree of nanoparticles in TiO_2/epoxy resin nanocomposites', *Journal of Ocean Engineering and Technology*, vol. 28, no. 4, pp. 338–344, Aug. 2014, doi: 10.5574/KSOE.2014.28.4.338.

[158] D. W. Schaefer, J. M. Brown, D. P. Anderson, J. Zhao, K. Chokalingam, D. Tomlin, and J. Ilavsky, 'Structure and dispersion of carbon nanotubes', *J Appl Crystallogr*, vol. 36, no. 3, pp. 553–557, Jun. 2003, doi: 10.1107/S0021889803005028.

[159] X. Gong, J. Liu, S. Baskaran, R. D. Voise, and J. S. Young, 'Surfactant-Assisted Processing of Carbon Nanotube/Polymer Composites', *Chemistry of Materials*, vol. 12, no. 4, pp. 1049–1052, Apr. 2000, doi: 10.1021/cm9906396.

[160] D. Penumadu, A. Dutta, G. M. Pharr, and B. Files, 'Mechanical properties of blended single-wall carbon nanotube composites', *J Mater Res*, vol. 18, no. 8, pp. 1849–1853, Aug. 2003, doi: 10.1557/JMR.2003.0258.

[161] P. M. Ajayan, L. S. Schadler, C. Giannaris, and A. Rubio, 'Single-Walled Carbon Nanotube-Polymer Composites: Strength and Weakness', *Advanced Materials*, vol. 12, no. 10, pp. 750–753, May 2000, doi: 10.1002/(SICI)1521-4095(200005)12:10<750::AID-ADMA750>3.0.CO;2-6.

[162] H. Machrafi, 'On the chemical potential of nanoparticle dispersion', *Phys Lett A*, vol. 384, no. 19, p. 126485, Jul. 2020, doi: 10.1016/j.physleta.2020.126485.

[163] C. Zhang, H. Li, Y. Liu, P. Li, S. Liu, and C. He, 'Advancement of Polyaniline/Carbon Nanotubes Based Thermoelectric Composites', *Materials*, vol. 15, no. 23, p. 8644, Dec. 2022, doi: 10.3390/ma15238644.

[164] S. R. Broadbent and J. M. Hammersley, 'Percolation processes', *Mathematical Proceedings of the Cambridge Philosophical Society*, vol. 53, no. 3, pp. 629–641, Jul. 1957, doi: 10.1017/S0305004100032680.

[165] S. Kirkpatrick, 'Percolation and Conduction', *Rev Mod Phys*, vol. 45, no. 4, pp. 574–588, Oct. 1973, doi: 10.1103/RevModPhys.45.574.

[166] A. Voet, Wm. N. Whitten, and F. R. Cook, 'Electron tunneling in carbon blacks', *Kolloid-Zeitschrift und Zeitschrift für Polymere*, vol. 201, no. 1, pp. 39–46, Jan. 1965, doi: 10.1007/BF01497077.

[167] R. Taherian, 'Experimental and analytical model for the electrical conductivity of polymer-based nanocomposites', *Compos Sci Technol*, vol. 123, pp. 17–31, Feb. 2016, doi: 10.1016/j.compscitech.2015.11.029.

[168] J. Payandehpeyman, M. Mazaheri, A. S. Zeraati, S. Jamasb, and U. Sundararaj, 'Physics-Based Modeling and Experimental Study of Conductivity and Percolation Threshold in Carbon Black Polymer Nanocomposites', *Applied Composite Materials*, vol. 31, no. 1, pp. 127–147, Feb. 2024, doi: 10.1007/s10443-023-10169-x.

[169] S. Kirkpatrick, 'Percolation and Conduction', *Rev Mod Phys*, vol. 45, no. 4, pp. 574–588, Oct. 1973, doi: 10.1103/RevModPhys.45.574.

[170] I. Y. Forero-Sandoval, A. P. Franco-Bacca, F. Cervantes-Álvarez, C. L. Gómez-Heredia, J. A. Ramírez-Rincón, J. Ordonez-Miranda, and J. J. Alvarado-Gil, 'Electrical and thermal percolation in two-phase materials: A perspective', *J Appl Phys*, vol. 131, no. 23, p. 230901, Jun. 2022, doi: 10.1063/5.0091291.

[171] J. Wei, R. Atif, T. Vo, and F. Inam, 'Graphene Nanoplatelets in Epoxy System: Dispersion, Reaggregation, and Mechanical Properties of Nanocomposites', *J Nanomater*, vol. 2015, no. 1, pp. 1–12, Jan. 2015, doi: 10.1155/2015/561742.

[172] E. A. Grulke, S. B. Rice, J. Xiong, K. Yamamoto, T. H. Yoon, K. Thomson, M. Saffaripour, G. J. Smallwood, J. W. Lambert, A. J. Stromberg, R. Macy, N. J. Briot, and D. Qian, 'Size and shape distributions of carbon black aggregates by transmission electron microscopy', *Carbon N Y*, vol. 130, pp. 822–833, Apr. 2018, doi: 10.1016/j.carbon.2018.01.030.

[173] H. Pathangi, P. M. Vereecken, A. Klekachev, G. Groeseneken, and A. Witvrouw, 'Quantifying the Aggregation Factor in Carbon Nanotube Dispersions by Absorption Spectroscopy', *Journal of Nanoscience*, vol. 2014, pp. 1–13, Apr. 2014, doi: 10.1155/2014/328627.

[174] H. Qiu, W. Zhao, H. Pei, J. Li, and Z.-Y. Sun, 'Highly accurate prediction of viscosity of epoxy resin and diluent at various temperatures utilizing machine learning',

Polymer (Guildf), vol. 256, p. 125216, Sep. 2022, doi: 10.1016/j.polymer.2022.125216.

[175] Y. He, D. Xie, and X. Zhang, 'The structure, microphase-separated morphology, and property of polyurethanes and polyureas', *J Mater Sci*, vol. 49, no. 21, pp. 7339–7352, Nov. 2014, doi: 10.1007/s10853-014-8458-y.

[176] T. G. Fox and P. J. Flory, 'Second-Order Transition Temperatures and Related Properties of Polystyrene. I. Influence of Molecular Weight', *J Appl Phys*, vol. 21, no. 6, pp. 581–591, Jun. 1950, doi: 10.1063/1.1699711.

[177] V. Aseyev, H. Tenhu, and F. M. Winnik, 'Non-ionic Thermoresponsive Polymers in Water', in *Advances in Polymer Science*, vol. 242, no. 1, 2010, pp. 29–89.

[178] Z. P. LUO and J. H. KOO, 'Quantifying the dispersion of mixture microstructures', *J Microsc*, vol. 225, no. 2, pp. 118–125, Feb. 2007, doi: 10.1111/j.1365-2818.2007.01722.x.

[179] B. M. Tyson, R. K. Abu Al-Rub, A. Yazdanbakhsh, and Z. Grasley, 'A quantitative method for analyzing the dispersion and agglomeration of nano-particles in composite materials', *Compos B Eng*, vol. 42, no. 6, pp. 1395–1403, Sep. 2011, doi: 10.1016/j.compositesb.2011.05.020.

[180] J. Sui, P. Zhao, B. Bin-Mohsin, L. Zheng, X. Zhang, Z. Cheng, Y. Chen, and G. Chen, 'Fractal aggregation kinetics contributions to thermal conductivity of nano-suspensions in unsteady thermal convection', *Sci Rep*, vol. 6, no. 1, p. 39446, Dec. 2016, doi: 10.1038/srep39446.

[181] V. Kanniah, P. Wu, N. Mandzy, and E. A. Grulke, 'Fractal analysis as a complimentary technique for characterizing nanoparticle size distributions', *Powder Technol*, vol. 226, pp. 189–198, Aug. 2012, doi: 10.1016/j.powtec.2012.04.041.

[182] S. Ganguly, S. Basu, and S. Sikdar, 'Determination of the aggregate fractal dimensions in colloidal nanofluids', *Proceedings of the Institution of Mechanical Engineers, Part N: Journal of Nanoengineering and Nanosystems*, vol. 226, no. 1, pp. 3–7, Mar. 2012, doi: 10.1177/1740349912444687.

[183] Y. Chen, 'Fractal Modeling and Fractal Dimension Description of Urban Morphology', *Entropy 2020, Vol. 22, Page 961*, vol. 22, no. 9, p. 961, Aug. 2020, doi: 10.3390/E22090961.

[184] A. Ali, H. Rafique, T. Arshad, M. A. Alqarni, S. H. Chauhdary, and A. K. Bashir, 'A fractal-based authentication technique using sierpinski triangles in smart devices', *Sensors (Switzerland)*, vol. 19, no. 3, Feb. 2019, doi: 10.3390/S19030678.

[185] T. Gneiting, H. Ševčíková, and D. B. Percival, 'Estimators of Fractal Dimension: Assessing the Roughness of Time Series and Spatial Data', *Statistical Science*, vol. 27, no. 2, pp. 247–277, May 2012, doi: 10.1214/11-STS370.

[186] T. Vicsek, 'Fractal Geometry', in *Fractal Growth Phenomena*, WORLD SCIENTIFIC, 1992, pp. 9–47.

[187] B. Mandelbrot, 'How Long Is the Coast of Britain? Statistical Self-Similarity and Fractional Dimension', *Science (1979)*, vol. 156, no. 3775, pp. 636–638, May 1967, doi: 10.1126/science.156.3775.636.

[188] K. Foroutan-pour, P. Dutilleul, and D. L. Smith, 'Advances in the implementation of the box-counting method of fractal dimension estimation', *Appl Math Comput*, vol. 105, no. 2–3, pp. 195–210, Nov. 1999, doi: 10.1016/S0096-3003(98)10096-6.

[189] M. Sahini and M. Sahimi, *Applications Of Percolation Theory*. CRC Press, 1994.

[190] S.-H. Kim, 'Fractal dimensions of a green broccoli and a white cauliflower', Nov. 2004, Accessed: Mar. 29, 2024. [Online]. Available: http://arxiv.org/abs/cond-mat/0411597.

[191] K. Falconer, 'Brownian motion and Brownian surfaces', in *Fractal Geometry*, Wiley, 2003, pp. 258–276.

[192] E. M. Anitas, 'Small-Angle Scattering from Mass and Surface Fractals', in *Complexity in Biological and Physical Systems - Bifurcations, Solitons and Fractals*, InTech, 2018.

[193] A. Laaksonen, J. Malila, A. Nenes, H.-M. Hung, and J.-P. Chen, 'Surface fractal dimension, water adsorption efficiency and cloud nucleation activity of insoluble aerosol', *Sci Rep*, vol. 6, no. 1, p. 25504, May 2016, doi: 10.1038/srep25504.

[194] X. ning Liang and W. Li, 'Fractal and digital image processing to determine the degree of dispersion of carbon nanotubes', *Journal of Nanoparticle Research*, vol. 18, no. 5, pp. 1–11, May 2016, doi: 10.1007/S11051-016-3445-7/FIGURES/10.

[195] E. do N. Karasinski, F. D. Sasse, and L. A. F. Coelho, 'Multifractal Analysis of Particle Dispersion and Interphase Percolation in Nanocomposites', *Materials Research*, vol. 21, no. 5, p. 20180265, Aug. 2018, doi: 10.1590/1980-5373-mr-2018-0265.

[196] V. Kanniah, P. Wu, N. Mandzy, and E. A. Grulke, 'Fractal analysis as a complimentary technique for characterizing nanoparticle size distributions', *Powder Technol*, vol. 226, pp. 189–198, Aug. 2012, doi: 10.1016/j.powtec.2012.04.041.

[197] I. A. Morozov, B. Lauke, and G. Heinrich, 'Microstructural analysis of carbon black filled rubbers by atomic force microscopy and computer simulation techniques', *Plastics, Rubber and Composites*, vol. 41, no. 7, pp. 285–289, Sep. 2012, doi: 10.1179/1743289812Y.0000000014.

[198] K. Anane-Fenin, E. T. Akinlabi, and N. Perry, 'A Method for the Quantification of Nanoparticle Dispersion in Nanocomposites Based on Fractal Dimension', in *Advances in Material Sciences and Engineering*, M. Awang, S. S. Emamian, and F. Yusof, Eds. Singapore: Springer Singapore, 2020, pp. 555–564.

[199] A. Lagarias, 'Fractal analysis of the urbanization at the outskirts of the city: Models, measurement and explanation', *Cybergeo*, vol. 2007, Jul. 2007, doi: 10.4000/cybergeo.8902.

[200] A. Shundo, S. Yamamoto, and K. Tanaka, 'Network Formation and Physical Properties of Epoxy Resins for Future Practical Applications', *JACS Au*, vol. 2, no. 7, pp. 1522–1542, Jul. 2022, doi: 10.1021/jacsau.2c00120.

[201] K. J. Laidler, 'The development of the Arrhenius equation', *J Chem Educ*, vol. 61, no. 6, p. 494, Jun. 1984, doi: 10.1021/ed061p494.

[202] S. R. Logan, 'The origin and status of the Arrhenius equation', *J Chem Educ*, vol. 59, no. 4, p. 279, Apr. 1982, doi: 10.1021/ed059p279.

[203] A. Kulczycki and C. Kajdas, 'A New Attempt to Better Understand Arrehnius Equation and Its Activation Energy', in *Tribology in Engineering*, InTech, 2013.

[204] C. Sievers, Y. Noda, L. Qi, E. M. Albuquerque, R. M. Rioux, and S. L. Scott, 'Phenomena Affecting Catalytic Reactions at Solid–Liquid Interfaces', *ACS Catal*, vol. 6, no. 12, pp. 8286–8307, Dec. 2016, doi: 10.1021/acscatal.6b02532.

[205] W. Zhao, L. An, and S. Wang, 'Recyclable High-Performance Epoxy-Anhydride Resins with DMP-30 as the Catalyst of Transesterification Reactions', *Polymers (Basel)*, vol. 13, no. 2, p. 296, Jan. 2021, doi: 10.3390/polym13020296.

[206] T. Triyono, 'Correlation between preexponential factor and activation energy of isoamylalcohol hydrogenolysis on platinum catalysts', *Indonesian Journal of Chemistry*, vol. 4, no. 1, pp. 1–5, Jun. 2010, doi: 10.22146/ijc.21867.

[207] Inc. Thermcraft, 'An Introduction to a Curing Oven', 2018. https://www.azom.com/article.aspx?ArticleID=16950 (accessed Jul. 23, 2021).

[208] A. B. Gadekar, S. K. Biradar, M. Irfan, and P. D. Somavanshi, 'Review on Systematic Approach to Industrial Oven Improvement for Process Performance'. https://ijariie.com/AdminUploadPdf/Review_on_Systematic_Approach_to_Industrial_Oven__Improvement_for_Process_Performance_ijariie15685.pdf (accessed Nov. 09, 2023).

[209] Despatch Ltd., 'THE DIFFERENCE BETWEEN INDUSTRIAL CONVEYOR OVENS AND BATCH OVENS'. https://www.despatch.com/blog/difference-between-conveyor-ovens-and-batch-ovens/ (accessed Nov. 09, 2023).

[210] F. C. Campbell, *Manufacturing technology for aerospace structural materials*. 2006.

[211] V. R. Sastri, 'Material Requirements for Plastics Used in Medical Devices', in *Plastics in Medical Devices*, Elsevier, 2022, pp. 65–112.

[212] Michael Greenwood, 'An Introduction to the Autoclave Sterilization Process', *News Medical* , Feb. 07, 2019. https://www.news-

medical.net/whitepaper/20190207/Introduction-to-Autoclave-Sterilization-Process.aspx (accessed Mar. 29, 2024).

[213] T. R. Schoeb and K. A. Eaton, 'Gnotobiotics', *Gnotobiotics*, pp. 1263–1296, Jan. 2015, doi: 10.1016/B978-0-12-409527-4.00026-2.

[214] G. D. Dockery, 'Aseptic techniques', *Lower Extremity Soft Tissue & Cutaneous Plastic Surgery: Second Edition*, pp. 53–68, Jan. 2012, doi: 10.1016/B978-0-7020-3136-6.00007-2.

[215] H. Koushyar, S. Alavi-Soltani, B. Minaie, and M. Violette, 'Effects of variation in autoclave pressure, temperature, and vacuum-application time on porosity and mechanical properties of a carbon fiber/epoxy composite', *J Compos Mater*, vol. 46, no. 16, pp. 1985–2004, Aug. 2012, doi: 10.1177/0021998311429618.

[216] H. N. Dhakal and S. O. Ismail, 'Design, manufacturing processes and their effects on bio-composite properties', in *Sustainable Composites for Lightweight Applications*, Elsevier, 2021, pp. 121–177.

[217] R. Alagirusamy, 'Hybrid yarns for thermoplastic composites', in *Technical Textile Yarns*, Elsevier, 2010, pp. 387–428.

[218] B. Mas, J. P. Fernández-Blázquez, J. Duval, H. Bunyan, and J. J. Vilatela, 'Thermoset curing through Joule heating of nanocarbons for composite manufacture, repair and soldering', *Carbon N Y*, vol. 63, pp. 523–529, Nov. 2013, doi: 10.1016/j.carbon.2013.07.029.

[219] M. G. Collinson, T. J. Swait, M. P. Bower, B. Nuhiji, and S. A. Hayes, 'Development and implementation of direct electric cure of plain weave CFRP composites for aerospace', *Compos Part A Appl Sci Manuf*, vol. 172, p. 107615, Sep. 2023, doi: 10.1016/j.compositesa.2023.107615.

[220] J. Lee, X. Ni, F. Daso, X. Xiao, D. King, J. S. Gómez, T. B. Varela, S. S. Kessler, and B. L. Wardle, 'Advanced carbon fiber composite out-of-autoclave laminate manufacture via nanostructured out-of-oven conductive curing', *Compos Sci Technol*, vol. 166, pp. 150–159, Sep. 2018, doi: 10.1016/j.compscitech.2018.02.031.

[221] C. Joseph and C. Viney, 'Electrical resistance curing of carbon-fibre/epoxy composites', *Compos Sci Technol*, vol. 60, no. 2, pp. 315–319, Feb. 2000, doi: 10.1016/S0266-3538(99)00112-8.

[222] A.-T. Chien, S. Cho, Y. Joshi, and S. Kumar, 'Electrical conductivity and Joule heating of polyacrylonitrile/carbon nanotube composite fibers', *Polymer (Guildf)*, vol. 55, no. 26, pp. 6896–6905, Dec. 2014, doi: 10.1016/j.polymer.2014.10.064.

[223] M. Çelik, T. Noble, A. Haseeb, J. Maguire, C. Robert, and C. M. Ó Brádaigh, 'Contact resistance heating of unidirectional carbon fibre tows in a powder-epoxy towpregging line', *Plastics, Rubber and Composites*, vol. 51, no. 8, pp. 383–392, Sep. 2022, doi: 10.1080/14658011.2022.2108982.

[224] S. Liu, Y. Li, Y. Shen, and Y. Lu, 'Mechanical performance of carbon fiber/epoxy composites cured by self-resistance electric heating method', *The International Journal of Advanced Manufacturing Technology*, vol. 103, no. 9–12, pp. 3479–3493, Aug. 2019, doi: 10.1007/s00170-019-03707-0.

[225] Y. Gu, X. Qin, M. Li, K. Zhang, and Z. Zhang, 'Temperature Distribution and Curing Behaviour of Carbon Fibre/ Epoxy Composite during Vacuum Assisted Resin Infusion Moulding Using Rapid Heating Methods', *Polymers and Polymer Composites*, vol. 23, no. 1, pp. 11–20, Jan. 2015, doi: 10.1177/096739111502300102.

[226] P. K., M. M., and S. P. P., 'Technologies in additive manufacturing for fiber reinforced composite materials: a review', *Curr Opin Chem Eng*, vol. 28, pp. 51–59, Jun. 2020, doi: 10.1016/j.coche.2020.01.001.

[227] H. L. Tekinalp, V. Kunc, G. M. Velez-Garcia, C. E. Duty, L. J. Love, A. K. Naskar, C. A. Blue, and S. Ozcan, 'Highly oriented carbon fiber–polymer composites via additive manufacturing', *Compos Sci Technol*, vol. 105, pp. 144–150, Dec. 2014, doi: 10.1016/J.COMPSCITECH.2014.10.009.

[228] J. Justo, L. Távara, L. García-Guzmán, and F. París, 'Characterization of 3D printed long fibre reinforced composites', *Compos Struct*, vol. 185, pp. 537–548, Feb. 2018, doi: 10.1016/J.COMPSTRUCT.2017.11.052.

[229] E. Leszak, 'Apparatus and process for incremental dieless forming. Patent US3342051A1', published 1967–09-19, 1967.

[230] X. Xiao, J.-J. Kim, S.-H. Oh, and Y.-S. Kim, 'Study on the incremental sheet forming of CFRP sheet', *Compos Part A Appl Sci Manuf*, vol. 141, p. 106209, Feb. 2021, doi: 10.1016/j.compositesa.2020.106209.

[231] M. Fiorotto, M. Sorgente, and G. Lucchetta, 'Preliminary studies on single point incremental forming for composite materials', *International Journal of Material Forming*, vol. 3, no. S1, pp. 951–954, Apr. 2010, doi: 10.1007/s12289-010-0926-6.

[232] P. K, V. R. N, C. S. A. Assuad, and K. Martinsen, 'Optimal process planning for energy consumption and product quality during double-sided incremental forming', *The International Journal of Advanced Manufacturing Technology*, vol. 125, no. 7–8, pp. 3305–3327, Apr. 2023, doi: 10.1007/s00170-023-10948-7.

[233] H. Meier, C. Magnus, and V. Smukala, 'Impact of superimposed pressure on dieless incremental sheet metal forming with two moving tools', *CIRP Annals*, vol. 60, no. 1, pp. 327–330, Jan. 2011, doi: 10.1016/j.cirp.2011.03.134.

[234] Y. Li, X. Chen, Z. Liu, J. Sun, F. Li, J. Li, and G. Zhao, 'A review on the recent development of incremental sheet-forming process', *The International Journal of Advanced Manufacturing Technology 2017 92:5*, vol. 92, no. 5, pp. 2439–2462, Apr. 2017, doi: 10.1007/S00170-017-0251-Z.

[235] R. Malhotra, J. Cao, F. Ren, V. Kiridena, Z. Cedric Xia, and N. V. Reddy, 'Improvement of Geometric Accuracy in Incremental Forming by Using a Squeezing Toolpath Strategy With Two Forming Tools', *J Manuf Sci Eng*, vol. 133, no. 6, Dec. 2011, doi: 10.1115/1.4005179.

[236] Easy Composites Ltd., 'IN2 EPOXY INFUSION RESIN-Technical Datasheet'. https://media.easycomposites.co.uk/datasheets/EC-TDS-IN2-Infusion-Resin.pdf (accessed May 19, 2023).

[237] B. Marinho, M. Ghislandi, E. Tkalya, C. E. Koning, and G. de With, 'Electrical conductivity of compacts of graphene, multi-wall carbon nanotubes, carbon black,

and graphite powder', *Powder Technol*, vol. 221, pp. 351–358, May 2012, doi: 10.1016/j.powtec.2012.01.024.

[238] Alfa Chemistry, 'CAS 1333-86-4 Carboxylic Multi-walled Carbon Nanotubes'. https://www.alfa-chemistry.com/product/carboxylic-multi-walled-carbon-nanotubes-cas-1333-86-4-283882.html (accessed May 19, 2023).

[239] D. Mattia, M. P. Rossi, B. M. Kim, G. Korneva, H. H. Bau, and Y. Gogotsi, 'Effect of Graphitization on the Wettability and Electrical Conductivity of CVD-Carbon Nanotubes and Films', *J Phys Chem B*, vol. 110, no. 20, pp. 9850–9855, May 2006, doi: 10.1021/jp061138s.

[240] First Graphene, 'Puregraph Products'. https://firstgraphene.net/puregraph-products/ (accessed Apr. 02, 2024).

[241] PYROFIL, 'Typical Properties of carbon fiber'. https://media.easycomposites.co.uk/datasheets/Pyrofil-TRSeries.pdf (accessed Apr. 03, 2024).

[242] Easy Composites Ltd., '210g Plain Weave 3k Carbon Fibre Cloth'. https://www.easycomposites.co.uk/200g-plain-weave-3k-carbon-fibre-cloth (accessed May 19, 2023).

[243] M. Loos, 'Processing of Polymer Matrix Composites Containing CNTs', in *Carbon Nanotube Reinforced Composites*, Elsevier, 2015, pp. 171–188.

[244] Aimee O'Driscoll, 'How to Choose a Magnetic Stir Bar (Stirring Flea)', May 2018. https://stirrers.net/blogs/blog/how-to-choose-a-magnetic-stir-bar-stirring-flea (accessed Jan. 09, 2024).

[245] B. Bhanvase and D. Barai, 'Stability of nanofluids', in *Nanofluids for Heat and Mass Transfer*, Elsevier, 2021, pp. 69–97.

[246] Edward L. Paul, Victor A. Atiemo-Obeng, and Suzanne M. Kresta, *Handbook of Industrial Mixing*. Hoboken, NJ, USA: Wiley, 2003.

[247] R. R. Retamal Marín, F. Babick, and M. Stintz, 'Ultrasonic dispersion of nanostructured materials with probe sonication – practical aspects of sample

preparation', *Powder Technol*, vol. 318, pp. 451–458, Aug. 2017, doi: 10.1016/j.powtec.2017.05.049.

[248] C. E. Brennen, 'Cavitation in medicine', *Interface Focus*, vol. 5, no. 5, p. 20150022, Oct. 2015, doi: 10.1098/rsfs.2015.0022.

[249] J. S. Taurozzi, V. A. Hackley, and M. R. Wiesner, 'Ultrasonic dispersion of nanoparticles for environmental, health and safety assessment – issues and recommendations', *Nanotoxicology*, vol. 5, no. 4, pp. 711–729, Dec. 2011, doi: 10.3109/17435390.2010.528846.

[250] Hielscher ultrasound technology, 'Ultrasonic Dispersing and Deagglomeration', 2020. https://www.hielscher.com/disperse.htm (accessed Feb. 26, 2021).

[251] J. S. Mamaradlo, 'Four-Wire Sensing Can Make or Break Your Measurements', *Electronicdesign*, 2015. https://www.electronicdesign.com/blogs/guest-blogger/article/21802776/fourwire-sensing-can-make-or-break-your-measurements (accessed Mar. 20, 2021).

[252] H. Chandra, S. Allen, S. Oberloier, N. Bihari, J. Gwamuri, and J. Pearce, 'Open-Source Automated Mapping Four-Point Probe', *Materials*, vol. 10, no. 2, p. 110, Jan. 2017, doi: 10.3390/ma10020110.

[253] 'Kelvin Sensing', *Reed Relays and Electronics India Limited*. www.reed-sensor.com/glossary/kelvin-sensing/ (accessed Mar. 21, 2021).

[254] J. P. Martin, 'Measuring Resistance/Impedance with the Four-Wire Kelvin Method', *"WATTS CURRENT" TECHNICAL BULLETIN*, no. 1, 2014, Accessed: May 20, 2023. [Online]. Available: https://www.aemc.com/userfiles/files/resources/applications/micro-ohmmeter/APP-4WireKelvin.pdf.

[255] V. Vance, 'Open- vs. closed-loop control', *Control Engineering*, Aug. 28, 2014. https://www.controleng.com/articles/open-vs-closed-loop-control/ (accessed Sep. 10, 2023).

[256] Spark Concepts, 'CNC xPRO Driver', *OpenBuilds*, Oct. 09, 2017. https://openbuilds.com/builds/cnc-xpro-driver.643/ (accessed Sep. 10, 2023).

[257] W. Bob, ‘How to Use GRBL in Your CNC Machine for 2023’, *CNC Cookbook*, Jun. 21, 2023. https://www.cnccookbook.com/how-to-use-grbl-in-your-cnc-machine-for-2023/ (accessed Sep. 10, 2023).

[258] M. S. Grant, ‘Data Acquisition (DAQ) - The Ultimate Guide’, *Dewesoft*, 2022. https://dewesoft.com/blog/what-is-data-acquisition (accessed Sep. 12, 2023).

[259] ‘Use NI DAQ Devices for Load, Pressure, and Torque Measurements’, *National Instruments*. https://knowledge.ni.com/KnowledgeArticleDetails?id=kA03q000000x1jjCAA&l=en-GB (accessed Sep. 11, 2023).

[260]‘Piezoelectric Wireless Sensors: The Future of Technology and How It Will Affect Us’, *Sensor-Works Ltd*. https://www.sensor-works.com/piezoelectric-wireless-sensors-the-future-of-technology/ (accessed Nov. 14, 2023).

[261] ‘K type thermocouple Working principle’, *SHANGHAI MKYD INSTRUMENT*. https://www.k-thermocouple.com/news/k-type-thermocouple-working-principle (accessed Sep. 12, 2023).

[262] N. C. Knowles, ‘Finite element analysis’, *Computer-Aided Design*, vol. 16, no. 3, pp. 134–140, May 1984, doi: 10.1016/0010-4485(84)90036-8.

[263] S. Han and D. D. L. Chung, ‘Increasing the through-thickness thermal conductivity of carbon fiber polymer–matrix composite by curing pressure increase and filler incorporation’, *Compos Sci Technol*, vol. 71, no. 16, pp. 1944–1952, Nov. 2011, doi: 10.1016/j.compscitech.2011.09.011.

[264] S. Li, X. Yu, H. Bao, and N. Yang, ‘High Thermal Conductivity of Bulk Epoxy Resin by Bottom-Up Parallel-Linking and Strain: A Molecular Dynamics Study’, *The Journal of Physical Chemistry C*, vol. 122, no. 24, pp. 13140–13147, Jun. 2018, doi: 10.1021/acs.jpcc.8b02001.

[265] H. Schulz, ‘From the Kissinger equation to model-free kinetics: reaction kinetics of thermally initiated solid-state reactions’, *ChemTexts*, vol. 4, no. 3, p. 9, Oct. 2018, doi: 10.1007/s40828-018-0062-3.

[266] S. Vyazovkin, 'Kissinger Method in Kinetics of Materials: Things to Beware and Be Aware of', *Molecules*, vol. 25, no. 12, p. 2813, Jun. 2020, doi: 10.3390/molecules25122813.

[267] S. Vyazovkin, 'Kissinger Method in Kinetics of Materials: Things to Beware and Be Aware of', *Molecules*, vol. 25, no. 12. MDPI AG, Jun. 01, 2020, doi: 10.3390/molecules25122813.

[268] T. U. of S. Electronic and Electrical Engineering, 'Kroto Centre for High Resolution Imaging and Analysis'. https://www.sheffield.ac.uk/eee/research/semiconductor-materials-devices/kroto-centre-high-resolution-imaging-and-analysis (accessed Sep. 05, 2023).

[269] Scanservice, 'Inspect-F'. https://www.semservice.com/inspect-f/ (accessed Sep. 05, 2023).

[270] 'FEI Quanta 650 FEG SEM | Natural History Museum'. https://www.nhm.ac.uk/our-science/departments-and-staff/core-research-labs/imaging-and-analysis/electron-microscopy/fei-quanta.html (accessed Sep. 05, 2023).

[271] F. Coupette, L. Zhang, B. Kuttich, A. Chumakov, S. V. Roth, L. González-García, T. Kraus, and T. Schilling, 'Percolation of rigid fractal carbon black aggregates', *J Chem Phys*, vol. 155, no. 12, p. 124902, Sep. 2021, doi: 10.1063/5.0058503.

[272] S. Keily, 'Digital image correlation (DIC): the why and the how-to - Simcenter'. https://blogs.sw.siemens.com/simcenter/digital-image-correlation-2021_1/ (accessed Sep. 15, 2023).

[273] 'Pike F-505B - Vital Vision Technology Pte Ltd'. https://vitalvisiontechnology.com/machine-vision-components/firewire-cameras/pike-f-505b/ (accessed Sep. 15, 2023).

[274] N. Kuppusamy and R. A. Tomlinson, 'Repeatable pre-cracking preparation for fracture testing of polymeric materials', *Eng Fract Mech*, vol. 152, pp. 81–87, Feb. 2016, doi: 10.1016/j.engfracmech.2015.12.007.

[275] A. Suri, S. K. Yadav, and A. Dasari, 'A simple chemical treatment for easy dispersion of carbon nanotubes in epoxy matrix for improving mechanical properties', *J Mater*

Sci, vol. 51, no. 24, pp. 10775–10781, Dec. 2016, doi: 10.1007/s10853-016-0289-6.

[276] A. Bajpai, R. Martin, H. Faria, E. Ibarboure, and S. Carlotti, 'Epoxy based hybrid nanocomposites: Fracture mechanisms, tensile properties and electrical properties', *Mater Today Proc*, vol. 34, pp. 210–216, 2021, doi: 10.1016/j.matpr.2020.02.797.

[277] PerkinElmer Inc., 'Optimize Process Conditions of Resins and Composites'. https://resources.perkinelmer.com/lab-solutions/resources/docs/app-optimize-process-conditions-of-resins-and-composites.pdf (accessed Sep. 03, 2023).

[278] O. P. Stebeleva, L. V. Kashkina, and O. A. Vshivkova, 'Structure and Morphology of Carbon-Black Particles Formed during the Evaporation of Aqueous Suspensions', *Nanobiotechnology Reports*, vol. 17, no. 4, pp. 489–494, Aug. 2022, doi: 10.1134/S2635167622040255.

[279] Yu. V. Surovikin, A. G. Shaitanov, I. V. Rezanov, and A. V. Syrieva, 'Formation the Properties of Carbon Black Particles by Gas-Phase Thermochemical Modification', *Inorganic Materials: Applied Research*, vol. 10, no. 2, pp. 480–495, Mar. 2019, doi: 10.1134/S2075113319020370.

[280] J. Lee, J. Bae, W. Kim, and S. Lee, 'A Study on Aqueous Dispersing of Carbon Black Nanoparticles Surface-Coated with Styrene Maleic Acid (SMA) Copolymer', *Polymers (Basel)*, vol. 14, no. 24, p. 5455, Dec. 2022, doi: 10.3390/polym14245455.

[281] S. Mo, X. Shao, Y. Chen, and Z. Cheng, 'Increasing entropy for colloidal stabilization', *Sci Rep*, vol. 6, no. 1, p. 36836, Nov. 2016, doi: 10.1038/srep36836.

[282] S. C. Leguizamon, J. Powers, J. Ahn, S. Dickens, S. Lee, and B. H. Jones, 'Polymerization-Induced Phase Separation in Rubber-Toughened Amine-Cured Epoxy Resins: Tuning Morphology from the Nano- to Macro-scale', *Macromolecules*, vol. 54, no. 17, pp. 7796–7807, Sep. 2021, doi: 10.1021/acs.macromol.1c01208.

[283] G. Zhang and G. Qiao, 'Polymerization-induced spinodal decomposition of ethylene glycol/phenolic resin solutions under electric fields', *J Chem Phys*, vol. 139, no. 13, p. 134903, Oct. 2013, doi: 10.1063/1.4822295.

[284] S. P. Nunes and T. Inoue, 'Evidence for spinodal decomposition and nucleation and growth mechanisms during membrane formation', *J Memb Sci*, vol. 111, no. 1, pp. 93–103, Mar. 1996, doi: 10.1016/0376-7388(95)00281-2.

[285] A. N. Naik, S. Patra, D. Sen, and A. Goswami, 'Evaluating the mechanism of nucleation and growth of silver nanoparticles in a polymer membrane under continuous precursor supply: tuning of multiple to single nucleation pathway', *Physical Chemistry Chemical Physics*, vol. 21, no. 8, pp. 4193–4199, Feb. 2019, doi: 10.1039/C8CP06202A.

[286] B. Zhang and T. Chen, 'Study of Ultrasonic Dispersion of Graphene Nanoplatelets', *Materials*, vol. 12, no. 11, p. 1757, May 2019, doi: 10.3390/ma12111757.

[287] L. Mohan, P. N. Kumar, S. Karakkad, and S. T. Krishnan, 'Determination of electrical percolation threshold of carbon nanotube-based epoxy nanocomposites and its experimental validation', *IET Science, Measurement & Technology*, vol. 13, no. 9, pp. 1299–1304, Nov. 2019, doi: 10.1049/iet-smt.2019.0011.

[288] S. Soltani, S. A. Razinobakht, and R. Asmatulu, 'Effect of carbon black silanization on isothermal curing kinetics of epoxy nanocomposites', *J Appl Polym Sci*, vol. 137, no. 37, Oct. 2020, doi: 10.1002/app.49106.

[289] F. Chen, Y. Zhang, T. Sun, and C. C. Han, 'Miscibility, Phase Separation, and Mechanism of Phase Separation in Epoxy/Thermoplastic Blends', in *Handbook of Epoxy Blends*, Cham: Springer International Publishing, 2015, pp. 1–35.

[290] A. Plyushch, P. Lamberti, G. Spinelli, J. Macutkevič, and P. Kuzhir, 'Numerical Simulation of the Percolation Threshold in Non-Overlapping Ellipsoid Composites: Toward Bottom-Up Approach for Carbon Based Electromagnetic Components Realization', *Applied Sciences*, vol. 8, no. 6, p. 882, May 2018, doi: 10.3390/app8060882.

[291] M. Dahale, G. Neale, R. Lupicini, L. Cascone, C. McGarrigle, J. Kelly, E. Archer, E. Harkin-Jones, and A. McIlhagger, 'Effect of weave parameters on the mechanical properties of 3D woven glass composites', *Compos Struct*, vol. 223, p. 110947, Sep. 2019, doi: 10.1016/J.COMPSTRUCT.2019.110947.

[292] A. P. Mouritz and B. N. Cox, 'A mechanistic interpretation of the comparative in-plane mechanical properties of 3D woven, stitched and pinned composites', *Compos Part A Appl Sci Manuf*, vol. 41, no. 6, pp. 709–728, Jun. 2010, doi: 10.1016/J.COMPOSITESA.2010.02.001.

[293] S. Dai, P. R. Cunningham, S. Marshall, and C. Silva, 'Influence of fibre architecture on the tensile, compressive and flexural behaviour of 3D woven composites', *Compos Part A Appl Sci Manuf*, vol. 69, pp. 195–207, Feb. 2015, doi: 10.1016/J.COMPOSITESA.2014.11.012.

[294] E. Archer, S. Buchanan, A. McIlhagger, and J. Quinn, 'The effect of 3D weaving and consolidation on carbon fiber tows, fabrics, and composites', *Journal of Reinforced Plastics and Composites*, vol. 29, no. 20, pp. 3162–3170, Oct. 2010, doi: 10.1177/0731684410371405.

[295] Easy Composites Ltd, 'XC130 | AUTOCLAVE CURE COMPONENT PREPREG SYSTEM'. https://media.easycomposites.co.uk/datasheets/EC-TDS-XPREG-XC130-Component-Prepreg.pdf (accessed Apr. 10, 2024).

[296] S. Al Wakeel, J. Němeček, L. Li, Y. Xi, and M. Hubler, 'The effect of introducing nanoparticles on the fracture toughness of well cement paste', *International Journal of Greenhouse Gas Control*, vol. 84, pp. 147–153, May 2019, doi: 10.1016/j.ijggc.2019.03.009.

[297] Y. Sasaki, Y. Nishizawa, T. Watanabe, T. Kureha, K. Uenishi, K. Nakazono, T. Takata, and D. Suzuki, 'Nanoparticle-Based Tough Polymers with Crack-Propagation Resistance', *Langmuir*, vol. 39, no. 26, pp. 9262–9272, Jul. 2023, doi: 10.1021/acs.langmuir.3c01226.

[298] Y.-M. Jen and Y.-C. Huang, 'Improvement in Tensile Quasi-Static and Fatigue Properties of Carbon Fiber-Reinforced Epoxy Laminates with Matrices Modified by

Carbon Nanotubes and Graphene Nanoplatelets Hybrid Nanofillers', *Nanomaterials*, vol. 11, no. 12, p. 3459, Dec. 2021, doi: 10.3390/nano11123459.

[299] H. R. Azimi, R. A. Pearson, and R. W. Hertzberg, 'Fatigue of rubber-modified epoxies: effect of particle size and volume fraction', *J Mater Sci*, vol. 31, no. 14, pp. 3777–3789, Jul. 1996, doi: 10.1007/BF00352793.

[300] M. Imanaka, S. Motohashi, K. Nishi, Y. Nakamura, and M. Kimoto, 'Crack-growth behavior of epoxy adhesives modified with liquid rubber and cross-linked rubber particles under mode I loading', *Int J Adhes Adhes*, vol. 29, no. 1, pp. 45–55, Jan. 2009, doi: 10.1016/j.ijadhadh.2007.11.004.

[301] G. J. Shin, D. H. Kim, J.-W. Kim, S. H. Kim, and J. H. Lee, 'Enhancing vertical thermal conductivity of carbon fiber reinforced polymer composites using cauliflower-shaped copper particles', *Mater Today Commun*, vol. 35, p. 105792, Jun. 2023, doi: 10.1016/j.mtcomm.2023.105792.

[302] Y. Guo, K. Ruan, X. Shi, X. Yang, and J. Gu, 'Factors affecting thermal conductivities of the polymers and polymer composites: A review', *Compos Sci Technol*, vol. 193, p. 108134, Jun. 2020, doi: 10.1016/j.compscitech.2020.108134.

[303] S.-L. Chung and J.-S. Lin, 'Thermal Conductivity of Epoxy Resin Composites Filled with Combustion Synthesized h-BN Particles', *Molecules*, vol. 21, no. 5, p. 670, May 2016, doi: 10.3390/molecules21050670.

[304] Christopher W. Macosko, *Fundamentals of Reaction Injection Molding*. Oxford University Press, 1989.

[305] E. R. Soulé, J. Borrajo, and R. J. J. Williams, 'Thermodynamic Analysis of a Polymerization-Induced Phase Separation in Nanoparticle−Monomer−Polymer Blends', *Macromolecules*, vol. 40, no. 22, pp. 8082–8086, Oct. 2007, doi: 10.1021/ma071369c.

[306] M. L. Huggins, 'Solutions of Long Chain Compounds', *J Chem Phys*, vol. 9, no. 5, pp. 440–440, May 1941, doi: 10.1063/1.1750930.

[307] P. J. Flory, 'Thermodynamics of High Polymer Solutions', *J Chem Phys*, vol. 10, no. 1, pp. 51–61, Jan. 1942, doi: 10.1063/1.1723621.

[308] I. A. Zucchi, M. J. Galante, R. J. J. Williams, E. Franchini, J. Galy, and J.-F. Gérard, 'Monofunctional Epoxy-POSS Dispersed in Epoxy–Amine Networks: Effect of a Prereaction on the Morphology and Crystallinity of POSS Domains', *Macromolecules*, vol. 40, no. 4, pp. 1274–1282, Feb. 2007, doi: 10.1021/ma062188y.

[309] H. Liu, S. Zheng, and K. Nie, 'Morphology and Thermomechanical Properties of Organic–Inorganic Hybrid Composites Involving Epoxy Resin and an Incompletely Condensed Polyhedral Oligomeric Silsesquioxane', *Macromolecules*, vol. 38, no. 12, pp. 5088–5097, Jun. 2005, doi: 10.1021/ma0504318.

[310] M. M. Demir, P. Castignolles, Ü. Akbey, and G. Wegner, 'In-Situ Bulk Polymerization of Dilute Particle/MMA Dispersions', *Macromolecules*, vol. 40, no. 12, pp. 4190–4198, Jun. 2007, doi: 10.1021/ma070142e.

[311] S. Liu, Y. Li, Y. Shen, and Y. Lu, 'Mechanical performance of carbon fiber/epoxy composites cured by self-resistance electric heating method', *International Journal of Advanced Manufacturing Technology*, vol. 103, no. 9–12, pp. 3479–3493, Aug. 2019, doi: 10.1007/s00170-019-03707-0.

[312] H. Schulz, 'From the Kissinger equation to model-free kinetics: reaction kinetics of thermally initiated solid-state reactions', *ChemTexts*, vol. 4, no. 3, pp. 1–10, Oct. 2018, doi: 10.1007/S40828-018-0062-3/FIGURES/4.

[313] T. Zhou, M. Gu, Y. Jin, and J. Wang, 'Mechanism and Kinetics of Epoxy-Imidazole Cure Studied with Two Kinetic Methods', doi: 10.1295/polymj.37.833.

[314] D. Lascano, A. Lerma-canto, V. Fombuena, R. Balart, N. Montanes, and L. Quiles-carrillo, 'Kinetic Analysis of the Curing Process of Biobased Epoxy Resin from Epoxidized Linseed Oil by Dynamic Differential Scanning Calorimetry', *Polymers (Basel)*, vol. 13, no. 8, Apr. 2021, doi: 10.3390/POLYM13081279.

[315] G. Prytz, 'A performance analysis of EtherCAT and PROFINET IRT', *IEEE International Conference on Emerging Technologies and Factory Automation, ETFA*, pp. 408–415, 2008, doi: 10.1109/ETFA.2008.4638425.

[316] P. Danielis, J. Skodzik, V. Altmann, E. B. Schweissguth, F. Golatowski, D. Timmermann, and J. Schacht, 'Survey on real-time communication via ethernet in industrial automation environments', *19th IEEE International Conference on Emerging Technologies and Factory Automation, ETFA 2014*, Jan. 2014, doi: 10.1109/ETFA.2014.7005074.

[317] Shane, 'Mechanical Press vs. Hydraulic Press: The Differences Explained | MachineMFG', *MachineMFG*, Jul. 2023. https://www.machinemfg.com/mechanical-press-vs-hydraulic-press/ (accessed Nov. 26, 2023).